



# **Polypyridyl Transition Metal Complexes with Application in Water Oxidation Catalysis and Dye-Sensitised Solar Cells**

**Inauguraldissertation**

zur

Erlangung der Würde eines Doktors der Philosophie

vorgelegt der

Philosophisch-Naturwissenschaftlichen Fakultät

der Universität Basel

von

**Jennifer A. Rudd**

aus England

Basel 2012

Genehmigt von der Philosophisch-Naturwissenschaftlichen Fakultät der Universität  
Basel auf Antrag der Herren Professoren und Herr Doktor

Prof. Dr. E. C. Constable

Dr. N. Robertson

Basel, den 13.11.2012

Prof. Dr. J. Schibler  
Dekan

Original document stored on the publication server of the University of Basel  
**edoc.unibas.ch**



This work is licenced under the agreement „Attribution Non-Commercial No Derivatives – 2.5 Switzerland“. The complete text may be viewed here:  
**[creativecommons.org/licenses/by-nc-nd/2.5/ch/deed.en](https://creativecommons.org/licenses/by-nc-nd/2.5/ch/deed.en)**



## Attribution-Noncommercial-No Derivative Works 2.5 Switzerland

---

**You are free:**



to Share — to copy, distribute and transmit the work

**Under the following conditions:**



**Attribution.** You must attribute the work in the manner specified by the author or licensor (but not in any way that suggests that they endorse you or your use of the work).



**Noncommercial.** You may not use this work for commercial purposes.



**No Derivative Works.** You may not alter, transform, or build upon this work.

- For any reuse or distribution, you must make clear to others the license terms of this work. The best way to do this is with a link to this web page.
- Any of the above conditions can be waived if you get permission from the copyright holder.
- Nothing in this license impairs or restricts the author's moral rights.

**Your fair dealing and other rights are in no way affected by the above.**

This is a human-readable summary of the Legal Code (the full license) available in German:  
<http://creativecommons.org/licenses/by-nc-nd/2.5/ch/legalcode.de>

**Disclaimer:**

The Commons Deed is not a license. It is simply a handy reference for understanding the Legal Code (the full license) — it is a human-readable expression of some of its key terms. Think of it as the user-friendly interface to the Legal Code beneath. This Deed itself has no legal value, and its contents do not appear in the actual license. Creative Commons is not a law firm and does not provide legal services. Distributing of, displaying of, or linking to this Commons Deed does not create an attorney-client relationship.

*„Und Gott sprach: Es werde Licht! und es ward Licht.  
Und Gott sah, daß das Licht gut war.  
Da schied Gott das Licht von der Finsternis“*

1 Mose 1 vs 3-4, Luther Bibel 1545

*“God spoke “Light!” and light appeared.  
God saw that light was good and separated light from dark.”*

Genesis 1 vs 3-4, The Message translation

## Acknowledgements

First and foremost thank you to Prof. Ed. Constable for giving me a place in the research group, for freedom to explore the world of chemistry and for all his help, support and kindness over the last three years.

I can no longer count the number of hours of discussion Prof. Catherine Housecroft and I have had sat in her office. Thank you for all of them and all of your proof-reading of this manuscript.

Thank you to Dr Robertson for agreeing to be my examiner and travelling from Edinburgh to do so.

Thank you to Prof. Markus Meuwly for giving me a place in his research group for a few months to run my own calculations and for the countless subsequent discussions on basis sets, calculating absorption spectra and how to please referees when publishing.

Dr. Jennifer Zampese and Dr. Markus Neuburger have measured all my crystals and have done their best to help me understand where the results come from and what they mean.

Dr. Michael Devereux was kind enough to run the DFT calculations on my ruthenium complexes and was very patient in teaching me how to read output files, use GaussSum and Molekel.

Dr Emma Dunphy got me started on the ruthenium project and has always been a massive encouragement and a great photophysics teacher. Thanks for all of our Skype, lab and gmail conversations about all things chemistry.

Thank you to Dr. Biljana Bozic-Weber, Liselotte Siegfried and Ewald Schönhofer for all of their work making and measuring the solar cells.

Thanks must also go to Prof. Craig Hill, Dr. Yurii Geletii and Hongjin Lv of Emory University (Atlanta) for the water oxidation collaboration.

Dr. Niamh Murray, Dr. Colin Martin and Dr. Iain Wright have been great post-docs and have also spent their time checking and suggesting improvements for this manuscript. Thank you. Iain is thanked particularly for help with the spectroelectrochemistry.

The old members of lab 217 made the Constable group a very amusing and interesting place to be in my first couple of years here.

Dr Kate Harris, I still miss you sitting on the opposite side of the lab to me.

Thank you to Constable group members past and present, particularly for ESI/MALDI and VT-NMR measurements, to the Meuwly group and to all of the chemistry department support team.

Beatrice without you I wouldn't have my Ausländerausweis in the first place (do you remember shouting at the people in the Spiegelhof down the phone?) and your help with the ever present Swiss paperwork has been invaluable throughout the last three years.

Thanks to the Swiss National Science Foundation and the European Research Council (Advanced Grant 267816 LiLo) for financial support.

A massive thank you to the Rock Solid youth and team past and present. My Basel experience would not have been the same without you and I have been blessed throughout my time with all of you. Zech. 4 vs 6 "Not by might, nor by power, but by my Spirit, says the Lord Almighty"

My parents have supported me throughout and it's great knowing you're always there.

Thomas thanks for always making me feel better about my research and Clare, thank you for all your crazy texts, post and encouragement along the way.

Last but certainly not least - Jason, thank you for saying "yes dear" to all of my PhD neuroses and all of your support through every stage. With you by my side everything is better.

## Abstract

This thesis contains complementary synthetic and computational studies of transition metal complexes with polypyridyl ligands for use either as water oxidation catalysts or for application in dye-sensitised solar cells (DSSCs).

**Chapter 1** introduces the reasons for researching water splitting catalysts and describes a number of current techniques used to do so; from photoelectrochemical cells to the use of transition metal polypyridyl complexes. It also introduces three commercially available types of solar cells; silicon, thin film and the dye-sensitised solar cell.

**Chapter 2** describes the synthesis of seven ruthenium(II) complexes with substituted 4'-(4-pyridyl)-2,2':6,2''-terpyridine ligands and their photophysical and electrochemical properties. Density Functional Theory (DFT) calculations were used to explore the compositions of the highest occupied- and lowest unoccupied molecular orbitals (HOMO and LUMO, respectively) and Time Dependent DFT (TD-DFT) was used to predict the absorption spectra of the complexes.

**Chapter 3** contains information on water soluble ruthenium(II) complexes, their synthesis, photophysical and electrochemical properties and their activity as water splitting co-catalysts. A mechanism to explain the variable activities of the complexes is also put forward.

**Chapter 4** describes the synthesis of two homoleptic Cu(I) complexes. One complex involves a simple 6,6'-dimethyl-2,2'-bipyridine ligand. The other complex contains a ligand with extended  $\pi$ -conjugation. The properties of the Cu(I) complexes are studied in terms of their suitability for use in DSSCs. A strategy of ligand-exchange on the surface of titanium dioxide ( $\text{TiO}_2$ ) is then utilised to form surface-bound heteroleptic Cu(I) complexes and efficiencies of these complexes in DSSCs were measured.



**Chapter 5** details the development of a suitable basis set to be used in both DFT and TD-DFT to predict the absorption spectra of the homoleptic Cu(I) complexes in Chapter 4 and the accuracies of the predicted spectra are assessed. The properties of the uncharacterised, heteroleptic Cu(I) complexes were then predicted and the effects of the anchoring ligands on the overall properties of the complexes were assessed.

**Chapter 6** describes the synthesis of two mono-substituted bipyridine-based ligands and their corresponding homoleptic chiral copper(I) complexes. Variable temperature nuclear magnetic resonance (VT-NMR) experiments are described, along with the photophysical properties of the ligands and complexes.

**Chapter 7** consists of the overall conclusions and an outlook.

Parts of this work have been published in:

“Water-soluble alkylated bis{4'-(4-pyridyl)-2,2':6',2''-terpyridine}ruthenium(II) complexes for use as photosensitizers in water oxidation: a complementary experimental and TD-DFT investigation”

Edwin C. Constable, Michael Devereux, Emma L. Dunphy, Catherine E. Housecroft, Jennifer A. Rudd and Jennifer A. Zampese, *Dalton Trans.*, 2011, **40**, 5505-5515

“Exploring copper(I)-based dye-sensitized solar cells: a complementary experimental and TD-DFT investigation”

Biljana Bozic-Weber, Valerie Chaurin, Edwin C. Constable, Catherine E. Housecroft, Markus Meuwly, Markus Neuburger, Jennifer A. Rudd, Ewald Schönhofer and Liselotte Siegfried, *Dalton Trans.*, 2012, **41**, 14157-14169

## Abbreviations

Å	Angstrom
bpy	2,2'-bipyridine
<sup>n</sup> Bu	n-Butyl
<sup>t</sup> Bu	t-Butyl
calc.	calculated
COSY	correlation spectroscopy
CPCM	conductor-like polarisable continuum model
CV	cyclic voltammetry
δ	chemical shift
D	deuterium
DFT	density functional theory
dmbpy	6,6'-dimethyl-2,2'-bipyridine
DSSC	dye-sensitised solar cell
E	standard half-cell potential
ε	absorption coefficient in mol dm <sup>-3</sup> cm <sup>-1</sup>
EA	elemental analysis
Eh	Hartree
eq.	equivalent
ESI	electrospray ionization
Et	ethyl
eV	electron volt
ff	fill factor
η	overall conversion efficiency from solar to electrical energy for a photovoltaic device
HF	Hartree-Fock
HMBC	heteronuclear multiple bond configuration
HMQC	heteronuclear multiple quantum coherence
HOMO	highest occupied molecular orbital
Hz	hertz
ic	internal conversion
ILCT	intra-ligand charge transfer

$I_{sc}$	short circuit current
isc	intersystem crossing
IR	infra-red (s, strong; m, medium; w, weak)
ITO	indium tin oxide
$J$	coupling constant
K	Kelvin
$\lambda_{em}$	emission wavelength
$\lambda_{ex}$	excitation wavelength
$\lambda_{max}$	wavelength at maximum absorbance
L	ligand
LC	ligand centered transition
LLCT	ligand to ligand charge transfer
LMCT	ligand to metal charge transfer
LUMO	lowest unoccupied molecular orbital
M	parent ion
MALDI-TOF	matrix assisted laser desorption ionisation – time of flight
MC	metal centred transition
MLCT	metal to ligand charge transfer
mmol	milimol
MO	molecular orbital
MS	mass spectrometry
mV	millivolt
$m/z$	mass to charge ratio
N3	[Ru(4,4'-(dicarboxy)-2,2'-bipyridine) <sub>2</sub> (SCN) <sub>2</sub> ]
N719	[Ru(4,4'-(dicarboxy)-2,2'-bipyridine) <sub>2</sub> (SCN) <sub>2</sub> ][TBA] <sub>2</sub>
nHOMO	next highest occupied molecular orbital
NIST	National Institute of Standards and Technology
nm	nanometre
NMR	nuclear magnetic resonance (signals identified as d, dd, t, m, br which mean doublet, doublet of doublets, triplet, multiplet and broad, respectively)
NOESY	nuclear Overhauser enhancement spectroscopy
PCM	polarisable continuum model

Ph	phenyl
ppm	parts per million
qpy	2,2':6',2'':6'',2'''-quaterpyridine
rt	room temperature
SCN	thiocyanate
TBA	tetrabutylammonium
TBAPF <sub>6</sub>	tetrabutylammonium hexafluoridophosphate
<sup>t</sup> Bu	<i>tert</i> -butyl
TD-DFT	time dependent density functional theory
TFL	Transport for London
THF	tetrahydrofuran
TiO <sub>2</sub>	titanium dioxide
TLC	thin layer chromatography
TMS	trimethylsilane
tpy	2,2';6',6''-terpyridine
UV	ultraviolet
V	volt
vis	visible
V <sub>oc</sub>	open circuit voltage
vs.	Versus
VT-NMR	variable temperature NMR
WOC	water oxidation catalyst

## General Experimental Section

$^1\text{H}$  and  $^{13}\text{C}$  NMR spectra were recorded on a Bruker DRX-500 MHz NMR spectrometer; chemical shifts are referenced to residual solvent peaks with TMS =  $\delta$  0 ppm.

MALDI-TOF mass spectra were recorded on a PerSeptive Biosystems Voyager spectrometer. Electrospray mass spectra were recorded on a Bruker esquire 3000plus.

Electronic absorption and emission spectra were recorded using an Agilent 8453 spectrophotometer and Shimadzu RF-5301 PC spectrofluorometer, respectively. Solution lifetime measurements were made using an Edinburgh Instruments mini- $\tau$  apparatus equipped with an Edinburgh Instruments EPLED-300 pico-second pulsed diode laser ( $\lambda_{\text{ex}}$  = 467 or 404 nm, pulse width = 75.5 or 48.2 ps, respectively) with the appropriate wavelength filter. The quantum yields were measured with an absolute PL quantum yield spectrometer C11347 Quantaaurus\_QY from Hamamatsu.

Solid state electronic absorption spectra of Cu(I)-containing dyes on  $\text{TiO}_2$  were measured using a Varian Cary 5000 with a conducting glass with a  $\text{TiO}_2$  layer as a blank.

TGA-MS measurements were carried out on a Mettler Toledo TGA/SDTA851e with Pfeiffer Vacuum Thermostar<sup>TM</sup>.

IR spectra were recorded on a Shimadzu FTIR-8400S spectrophotometer (solid samples on a Golden Gate diamond ATR accessory).

In chapter 2 electrochemical measurements were carried out using an Eco Chemie Autolab PGSTAT system with glassy carbon working and platinum auxiliary electrodes; a silver wire was used as a pseudo-reference electrode. Solvent was dry, purified MeCN and 0.1M [ $n\text{Bu}_4\text{N}$ ][ $\text{PF}_6$ ] was used as supporting electrolyte. An internal reference of  $\text{Cp}_2\text{Fe}$  was added at the end of each experiment.

In chapter 3 electrochemical measurements were carried out using an Eco Chemie Autolab PGSTAT system with a Ag/AgCl working electrode and a Pt counter electrode. Solvent was deionised water and  $\text{NaHSO}_4$  was used as the supporting electrolyte.

In chapter 4 electrochemical data were recorded using a CH Instruments potentiostat (model 900B) with glassy carbon working and platinum auxiliary electrodes; a silver wire was used as a pseudo-reference electrode. Solvents for the electrochemistry were dry and purified, and the supporting electrolyte was 0.1 M [<sup>n</sup>Bu<sub>4</sub>N][PF<sub>6</sub>]; an external reference of Cp<sub>2</sub>Fe was measured at the start and again at the end of each experiment.

## Table of Contents

Chapter 1	Introduction	
1.1	General Introduction	1
1.2	Water Splitting	1
1.3	Solar Cells	6
1.4	References	10
Chapter 2	Alkylated bis {4'-(4-pyridyl)-2,2':6',2''-terpyridine}ruthenium(II) complexes	
2.1	Introduction	12
2.2	Synthesis of [Ru(R-pytpy) <sub>2</sub> ][PF <sub>6</sub> ] <sub>4</sub> Complexes	16
2.3	Results and Discussion	18
2.3.1	<sup>1</sup> H NMR Spectroscopy	18
2.3.2	<sup>13</sup> C{ <sup>1</sup> H} NMR Spectroscopy	21
2.3.3	Mass Spectrometry	23
2.3.4	Absorption Spectroscopy	23
2.3.5	Emission Spectroscopy	25
2.3.6	Electrochemistry	27
2.3.7	Crystal Structures	30
2.4	DFT and TD-DFT Calculations	40
2.5	Conclusion	46
2.6	Experimental	47
2.7	References	53
Chapter 3	Water soluble alkylated bis{4'-(4-pyridyl)-2,2':6',2''} - terpyridine}ruthenium(II) complexes for application as water oxidation catalysts.	
3.1	Introduction	55
3.2	Synthesis of [Ru(R-pytpy) <sub>2</sub> ][HSO <sub>4</sub> ] <sub>4</sub> Complexes	61

3.3	Results and Discussion	62
3.3.1	$^1\text{H}$ NMR Spectroscopy	62
3.3.2	$^{13}\text{C}\{^1\text{H}\}$ NMR Spectroscopy	64
3.3.3	Mass Spectrometry	65
3.3.4	Elemental Analysis and Thermogravimetric Analysis	65
3.3.5	Absorption Spectroscopy	66
3.3.6	Emission Spectroscopy	68
3.3.7	Electrochemistry	70
3.3.8	Water Oxidation Activity	72
3.4	Conclusion	75
3.5	Experimental	76
3.6	References	81

#### Chapter 4 Copper(I) Polypyridyl Complexes for Application in DSSCs.

4.1	Introduction	83
4.2	Synthesis of ligand <b>9</b> and corresponding Cu(I) complexes	91
4.3	Results and Discussion	93
4.3.1	$^1\text{H}$ NMR Spectroscopy	93
4.3.2	$^{13}\text{C}\{^1\text{H}\}$ NMR Spectroscopy	100
4.3.3	Mass Spectrometry	103
4.3.4	Absorption Spectroscopy	104
4.3.5	Excitation and Emission Spectroscopy	106
4.3.6	Electrochemistry	110
4.3.7	Crystal Structures	114
4.3.8	DSSCs Incorporating the Cu(I) Complexes	121
4.4	Conclusions	123
4.5	Experimental	124
4.6	References	128

#### Chapter 5 A DFT and TD-DFT investigation of Cu(I) polypyridyl complexes with application in DSSCs



5.1	Introduction	130
5.2	Calculation Details	134
5.3	Results and Discussion	135
5.4	Conclusions	155
5.5	References	156
5.6	Appendix	157

Chapter 6      Cu(I) complexes with pendant pyridyl functionalities for application in DSSCs

6.1	Introduction	166
6.2	Synthesis – Ligands	168
6.3	Results and Discussion (I)	170
6.3.1	<sup>1</sup> H NMR Spectroscopy – Ligands	170
6.3.2	<sup>13</sup> C{ <sup>1</sup> H} NMR Spectroscopy- Ligands	172
6.3.3	Mass Spectrometry – Ligands	174
6.3.4	Absorption Spectroscopy – Ligands	175
6.3.5	Emission and Excitation Spectroscopy – Ligands	176
6.3.6	Crystal Structures – Ligands	177
6.4	Synthesis - Cu(I) Complexes	182
6.5	Results and Discussion (II)	182
6.5.1	Section Introduction	182
6.5.2	<sup>1</sup> H NMR Spectroscopy – Cu(I) Complexes	183
6.5.3	Mass Spectrometry – Cu(I) Complexes	189
6.5.4	Absorption Spectroscopy – Cu(I) Complexes	189
6.5.5	Emission and Excitation Spectroscopy – Cu(I) Complexes	191
6.5.6	Crystal Structures – Cu(I) Complexes	191
6.6	Conclusions	194
6.7	Experimental	195
6.8	References	199

Chapter 7	Conclusions and Outlook	200
-----------	-------------------------	-----

# Chapter 1

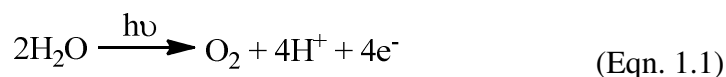
## Introduction

### 1.1 General Introduction

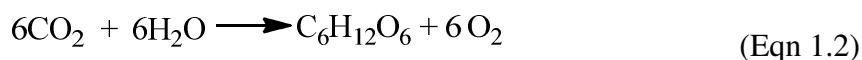
The world's fossilised energy resources are finite and the impact of their use is already being felt worldwide. Global warming, melting ice caps and repeated flash flooding are all symptoms of human dependence on fossil fuels to provide the 14 terawatts (TW) of power that are used every year<sup>1</sup>. In order to reduce such dependence, alternative fuel sources, such as hydrogen gas for use in fuel cells, are being developed by means of the catalytic splitting of water – a focus of this thesis. Nuclear power, wind turbines, tidal barriers, geothermal energy, hydroelectric dams and biogas are also in use, along with the other focus of this thesis: solar cells.

### 1.2 Water Splitting

Water splitting (Eqn. 1.1) is a process carried out in plants by means of photosynthesis.



In photosynthesis sunlight is absorbed by a plant and the energy from the sunlight is converted into chemical energy whereupon carbon dioxide and water are converted into sugars and molecular oxygen (Eqn. 1.2).



This process provides ~130 TW of power per year<sup>2</sup>, which is far more than is consumed by the human race. For this reason research has recently blossomed in the area of artificial photosynthesis – chemically mimicking photosynthesis. This process is a way of producing hydrogen that can then be stored and used as a source of fuel.

Hydrogen is becoming more common as a fuel source for road transport. BMW recently manufactured 100 test cars (BMW Hydrogen 7) which can be powered by either petrol or hydrogen<sup>3</sup>. The cars have conventional internal combustion engines, which can burn either petrol or hydrogen in the cylinders. Honda have developed a car (Honda FX Clarity) which runs on electricity, which is produced from the combination of hydrogen and oxygen (Eqn. 1.3) by means of a fuel cell<sup>4</sup>. A fuel cell is a device that converts chemical energy from a fuel to electrical energy by means of a chemical reaction with oxygen or another oxidising agent<sup>5</sup>.



The same technology is used in the newest fleet of London buses, which were introduced in 2011<sup>6</sup>. The fuel cell that combines the hydrogen and oxygen works at 40-60 % efficiency and the only emission from the bus is water vapour.

Hydrogen is also used as a feedstock for the synthesis of fertilisers, pharmaceuticals and plastics.

As the demand for hydrogen grows, more efficient ways of generating hydrogen are needed. There are multiple ways of photochemically splitting water (Eqn. 1.1) to generate molecular hydrogen and molecular oxygen<sup>7-14</sup>, for example: photoelectrochemical cells, heterogeneous catalysis involving semiconductor particles with co-catalysts attached, quantum dots and homogeneous catalysis using dyes.

The workings of a photoelectrochemical cell are depicted in Fig. 1.1.

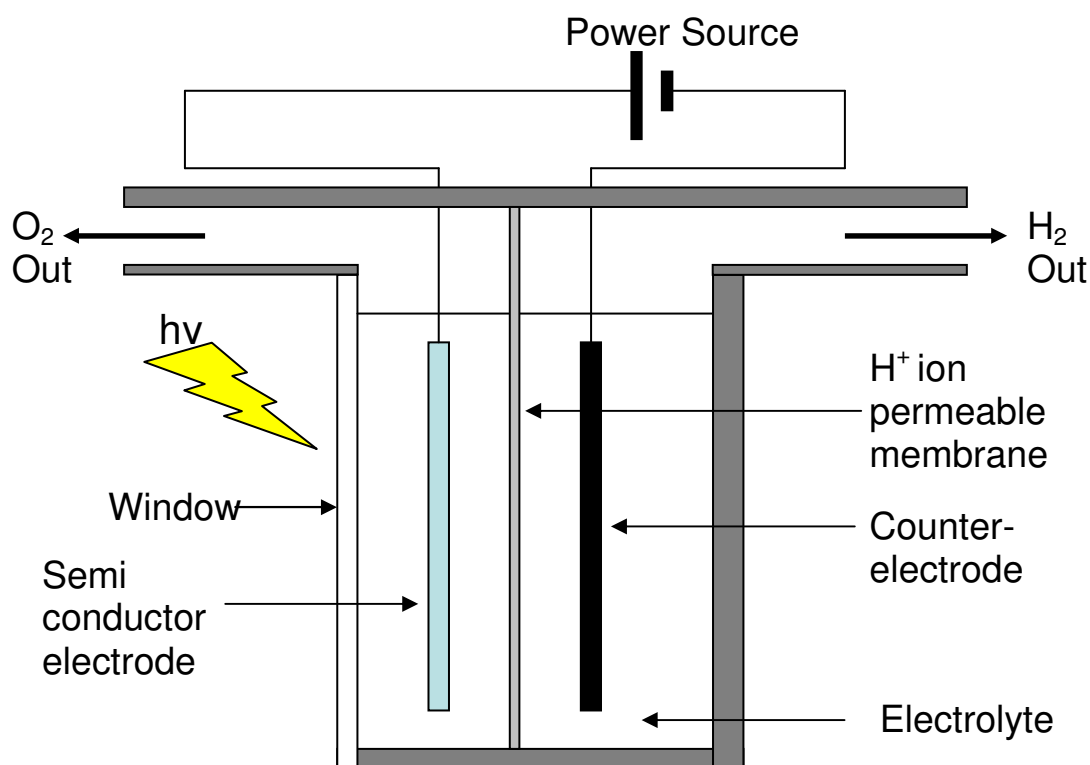


Fig. 1.1 Schematic of a photoelectrochemical cell redrawn from ref [10].

Fujishima and Honda were the first to report this method of water splitting<sup>15</sup>. Titanium dioxide (TiO<sub>2</sub>) in the rutile form was used as the semiconductor electrode in conjunction with nanoparticulate platinum (Pt) as the counter electrode. On illumination there is hole-electron separation within the TiO<sub>2</sub> nanoparticles. The holes oxidise water to molecular oxygen and protons. The electrons migrate to the Pt counter electrode where the protons are reduced to molecular hydrogen. The photoelectrochemical cell only absorbs light in the UV region of the spectrum as TiO<sub>2</sub> has such a large bandgap energy (3 eV).

Since the discovery by Fujishima and Honda, work has been carried out on substituting the TiO<sub>2</sub> in the photoelectrochemical cell for another substrate or substrates which will absorb visible light. This work has been the subject of recent reviews<sup>7,9</sup>. Methods such as chemical doping or the use of more than one semiconductor in parallel are being developed. The advantage of these newer systems is that they absorb visible light and therefore have a higher efficiency than the Fujishima/Honda system. However, the chemically doped and parallel systems tend to be much less stable.

Another approach to splitting water is the use of heterogeneous catalysts. The advantages of heterogeneous catalysis over the photoelectrochemical cell are that there is no need for direct illumination or transparent materials, which can often be expensive.

The heterogeneous catalyst can be prepared in one of two ways<sup>16</sup>;

- (i) Both the water oxidation catalyst and the water reduction catalyst are grafted onto the same semiconductor particle or one semiconductor part (Fig. 1.2, left).
- (ii) The semiconductor particles have only a water oxidation catalyst or a water reduction catalyst grafted onto them and the water splitting takes place in the presence of an electrolyte (Fig. 1.2, right).

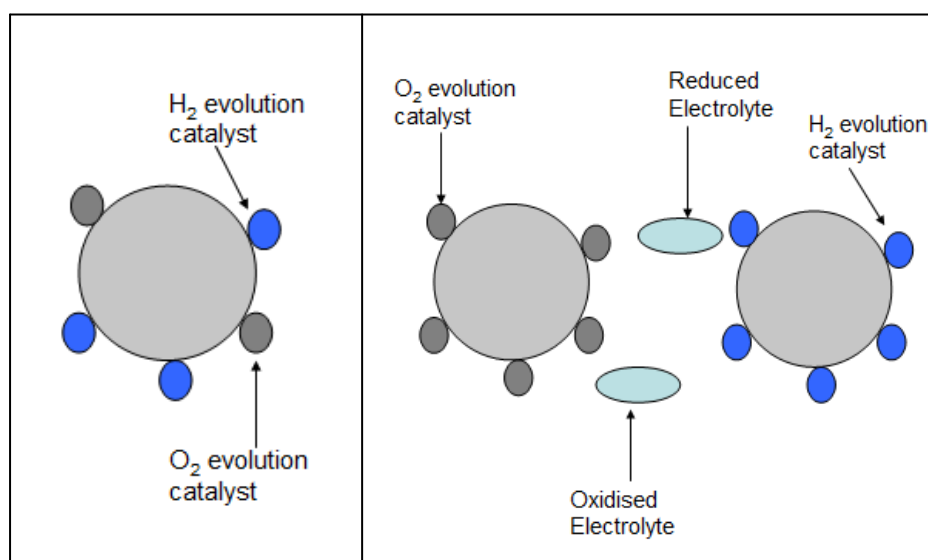


Fig. 1.2 The two types of heterogeneous catalyst for water splitting catalysis, redrawn from reference [16].

The one-step system (Fig. 1.2, left) is problematic as oxygen and hydrogen are produced simultaneously and the mixture of the two gases is explosive, so energy consuming separation of the gases is required. Also, catalysts that are efficient at water splitting are often efficient at the back reaction; the reaction between hydrogen and oxygen to form water, and so a steady state system can be reached.

For these reasons a two step system (Fig. 1.2, right) is preferred<sup>9, 14</sup>. As water oxidation and water reduction are happening at different sites, the reaction products can be collected separately, removing the possibility of the recombination reaction. However, the two step system is more complicated as it necessitates the use of a redox couple.

Quantum dots are small semiconductor particles whose band gap energy depends on the size of the dot. The absorption spectrum of a quantum dot (QD) can therefore be tuned by engineering the size of said QD. An emerging area of research is to use these QDs to sensitise large band gap semi-conductors, such as ZnO or TiO<sub>2</sub>, which are known to be good water splitting catalysts (Fig. 1.3). This enables the overall system to absorb visible light.

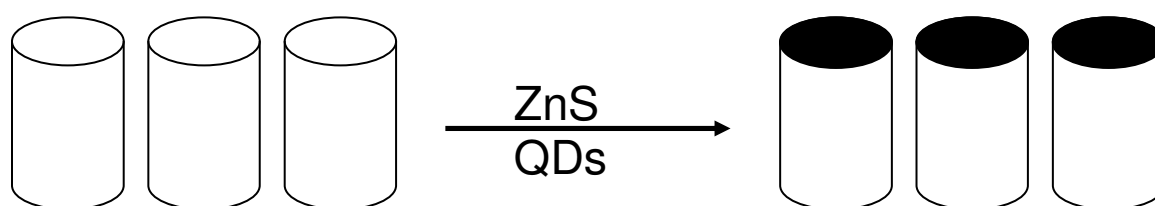


Fig. 1.3 The deposition of ZnS quantum dots onto ZnO nanorods<sup>17, 18</sup>.

The advantage of this type of water splitting catalysis is:  
 (i) the simple engineering of the absorption spectrum of the quantum dot  
 (ii) on acceptance of a photon a quantum dot can generate multiple hole-electron pairs<sup>19</sup>, which can lead to increased efficiency of the system.

However, charge carriers which have been photogenerated can react with other quantum dots, instead of water, which decreases the overall efficiency of the system.

The use of quantum dots is not the only way to sensitise a large band-gap semiconductor. In 1979 Graetzel *et al.* discovered that by using [Ru(bpy)<sub>3</sub>]<sup>2+</sup> (bpy = 2,2'-bipyridine) as a sensitiser for TiO<sub>2</sub> and Pt as a counter-electrode, visible light could be used to produce both hydrogen and oxygen from water<sup>20, 21</sup>. This type of water splitting catalysis involves both homogeneous and heterogeneous catalysis, which adds complexity. As such, research into the use of dyes for solely homogeneous water splitting catalysis is also being carried out. In 1978 Graetzel *et al.* reported the use of [Ru(bpy)<sub>3</sub>]<sup>2+</sup> as a photosensitiser to evolve hydrogen from water<sup>22</sup>. Research into the use of dyes as water reduction agents continues to date and has recently been reviewed by Bernhard *et al.*<sup>23</sup>. The more challenging side of water splitting, the four electron water oxidation process, is one of the subjects of this thesis and is introduced in detail in Chapter 3.

### 1.3 Solar Cells

The working principles of water splitting are shared in some cases by solar cells. Both involve the irradiation of large band-gap semiconductors with visible light to induce a flow of electrons and holes, which can then carry out “work”.

Solar cells were first used on a large scale in space to power satellites. Now, with increasing research in the field and decreasing costs of the solar cells themselves, they can be found in a plethora of different electrically powered devices (examples in Fig. 1.4).

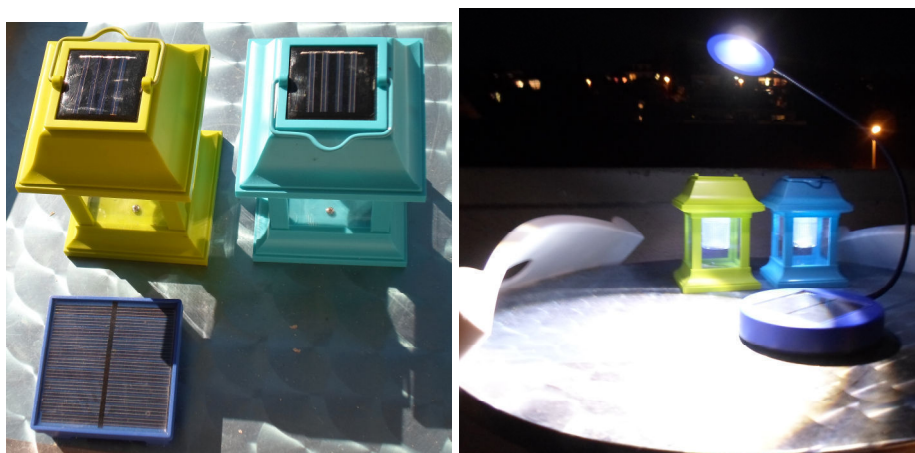


*Fig. 1.4 Left, two solar lanterns (B&Q) and one solar battery pack (IKEA) charging in the sunlight. Right, as night falls the solar lanterns switch themselves on using the energy gained during the daytime, the battery pack can be used to power a light.*

*Photographs taken by J. Rudd October 2012.*

The most prevalent type of solar cell today is the silicon solar cell. The manufacturing costs have decreased dramatically since they were first invented and the cost per Watt of electricity from solar panels in places such as California and Japan is decreasing towards the cost per Watt of electricity from the grid (this is termed, approaching grid parity)<sup>24</sup>. The working principles of a silicon solar cell are depicted in Fig. 1.5.

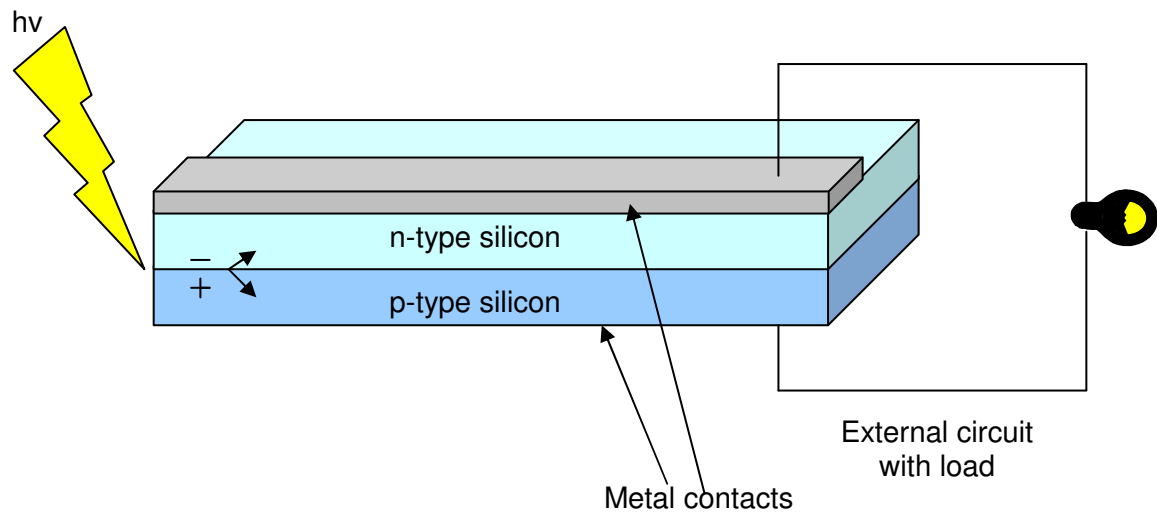


Fig. 1.5 The working principles of a silicon solar cell<sup>25</sup>.

Silicon itself is a poor conductor as its electrons are all involved in bonding the silicon atoms together to form a lattice. However, it is possible to dope silicon, which results in a silicon lattice with defects. For use in a solar cell one silicon wafer is n-doped (n = negative); that is, atoms such as phosphorus, which have five electrons in their outer shell, are introduced into the lattice. The other silicon wafer is p-doped (p = positive) with an atom such as boron, which only has three electrons in its outer shell. An electric field is formed when the two wafers come into contact with one another. On irradiation electrons start to flow towards the n-side of the cell and the resulting holes flow towards the p-side of the cell. This results in a current, which can be used to do ‘work’.

The overall efficiency of the cell is limited as some wavelengths do not have enough energy to displace an electron and some wavelengths have more energy than is required, so the excess energy is lost.

With the recent rapid uptake of silicon for both solar panels and for use in electronics, the demand and therefore cost of silicon has started to rise. For this reason another type of solar cell using thin film technology is becoming more competitive<sup>26</sup>. Thin film solar cells have been used in calculators for many years but the production cost and lower efficiencies (compared to silicon cells) have prohibited the development of large scale arrays. Thin film solar cells work on the same principle as the silicon solar cells with p-type and n-type doping facilitating the flow of current. Thin film cells have an additional *i* layer which is photovoltaically active<sup>27</sup>. Thin layers of photovoltaic material are



deposited sequentially onto a substrate, commonly glass resulting in a cell with a thickness of approximately ten micrometres<sup>27</sup>. Thin film solar cells can but do not always incorporate silicon and the most efficient cells so far (17.3%) are manufactured from cadmium and tellurium by a company called First Solar<sup>28</sup>. Other thin film cells are made from copper indium diselenide (CIS) and copper indium gallium diselenide (CIGS).

A further type of solar cell that is becoming competitive is the dye-sensitised solar cell (DSSC). This research was pioneered by Michael Graetzel in the late 1980s and has resulted in a solar cell that is made of low cost materials and has a simple structure<sup>29</sup>. A further advantage of this type of solar cell is that it can be flexible and therefore has a greater range of uses than the silicon solar cells. Originally, the dye tris(2,2'-bipyridyl-4,4'-carboxylate)ruthenium(II) (Fig 1.5) was used to sensitise TiO<sub>2</sub> in order to convert sunlight into current. A ruthenium compound was used as it was capable of absorbing visible light and the carboxylate groups were used to anchor the ruthenium complex to the TiO<sub>2</sub>. In 1991 the reported efficiency of the DSSC was 7.1%<sup>30</sup>. Over the years research to optimise the TiO<sub>2</sub> and other components of the DSSC have lead to incremental rises in efficiency<sup>29</sup>. Research into the optimisation of the ruthenium dye itself had also been underway with the aim of synthesising a dye that could absorb over the entire visible spectrum. This was achieved in 2001 with the synthesis of the “black dye” (Fig 1.5) and the efficiency at that time was reported to be 10.4%<sup>31</sup>. Further development of the DSSC has increased this efficiency to 11%<sup>32</sup> and DSSCs are now commercially available<sup>33</sup>.

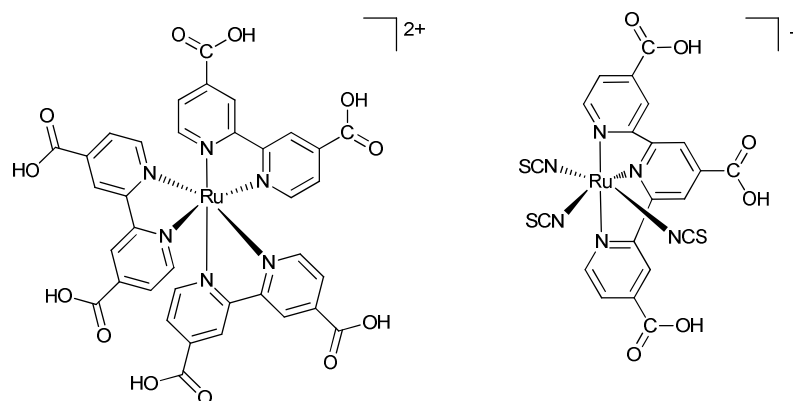


Fig. 1.5 Left, the cation in tris(2,2'-bipyridyl-4,4'-carboxylate)ruthenium(II), right, the ruthenium complex known as the “black dye”.

In an effort to make DSSCs even more cost-effective and environmentally friendly, research into the use of earth-abundant first-row transition metals is underway. To date polypyridyl iron<sup>34</sup>, zinc<sup>35</sup> and copper<sup>36</sup> complexes for the sensitisation of TiO<sub>2</sub> have been reported and it is under this umbrella that the second topic of this thesis falls. For further introductory information see Chapter 4.

## 1.4 References

1. *Statistical Review of World Energy (BP)*, <http://www.bp.com/sectionbodycopy.do?categoryId=7500&contentId=7068481>, Accessed 5th October, 2012.
2. J. Whitmarsh and Govindjee, *Photosynthesis*, Kluwer Academic Publishers, Dordrecht, 1999.
3. *BMW Hydrogen 7*, [http://www.bmw.com/com/en/insights/technology/efficient\\_dynamics/phase\\_2/clean\\_energy/bmw\\_hydrogen\\_7.html](http://www.bmw.com/com/en/insights/technology/efficient_dynamics/phase_2/clean_energy/bmw_hydrogen_7.html), Accessed 28th September, 2012.
4. *Honda FX Clarity*, <http://automobiles.honda.com/fcx-clarity/how-fcx-works.aspx>, Accessed 28th September, 2012.
5. C. E. Housecroft and A. G. Sharpe, *Inorganic Chemistry*, 4 edn., Prentice Hall, Gosport, 2012.
6. *TFL Buses*, <http://www.tfl.gov.uk/corporate/projectsandschemes/environment/8449.aspx>, Accessed 28th September, 2012.
7. X. Chen, S. Shen, L. Guo and S. S. Mao, *Chem. Rev.*, 2010, **110**, 6503-6570.
8. H. M. Chen, C. K. Chen, R.-S. Liu, L. Zhang, J. Zhang and D. P. Wilkinson, *Chem. Soc. Rev.*, 2012, **41**, 5654-5671.
9. A. Kudo and Y. Miseki, *Chem. Soc. Rev.*, 2009, **38**, 253-278.
10. F. E. Osterloh, *Chem. Mater.*, 2007, **20**, 35-54.
11. N. S. Lewis and D. G. Nocera, *P. Natl. Acad. Sci. USA*, 2006, **103**, 15729-15735.
12. M. Ni, M. K. H. Leung, D. Y. C. Leung and K. Sumathy, *Renew. Sustainable Energy Rev.*, 2007, **11**, 401-425.
13. J. Nowotny, C. C. Sorrell, T. Bak and L. R. Sheppard, *Solar Energy*, 2005, **78**, 593-602.
14. R. Abe, *J. Photochem. Photobiol. C*, 2010, **11**, 179-209.
15. A. Fujishima and K. Honda, *Nature*, 1972, **238**, 37-38.
16. Y. Tachibana, L. Vayssieres and J. R. Durrant, *Nat. Photonics*, 2012, **6**, 511-518.
17. H. M. Chen, C. K. Chen, Y.-C. Chang, C.-W. Tsai, R.-S. Liu, S.-F. Hu, W.-S. Chang and K.-H. Chen, *Angew. Chem. Int. Ed.*, 2010, **49**, 5966-5969.
18. H. M. Chen, C. K. Chen, R.-S. Liu, C.-C. Wu, W.-S. Chang, K.-H. Chen, T.-S. Chan, J.-F. Lee and D. P. Tsai, *Adv. Energy Mater.*, 2011, **1**, 742-747.
19. J. B. Sambur, T. Novet and B. A. Parkinson, *Science*, 2010, **330**, 63-66.
20. J. Kiwi and M. Grätzel, *Nature*, 1979, **281**, 657-658.
21. M. Graetzel, *Acc. Chem. Res.*, 1981, **14**, 376-384.
22. K. Kalyanasundaram, J. Kiwi and M. Grätzel, *Helv. Chim. Acta*, 1978, **61**, 2720-2730.
23. L. L. Tinker, N. D. McDaniel and S. Bernhard, *J. Mater. Chem.*, 2009, **19**, 3328-3337.
24. *Gaining on the Grid*, [www.bp.com](http://www.bp.com), Accessed 3rd October, 2012.
25. S. R. Wenham and M. A. Green, *Prog. Photovoltaics: Res. Appl.*, 1996, **4**, 3-33.
26. M. Green, *J. Mater. Sci.-Mater. El.*, 2007, **18**, 15-19.
27. A. Shah, P. Torres, R. Tscharnner, N. Wyrsh and H. Keppner, *Science*, 1999, **285**, 692-698.
28. *First Solar*, [www.firstsolar.com](http://www.firstsolar.com), Accessed 3rd October, 2012.
29. M. Grätzel, *J. Photochem. Photobiol. C*, 2003, **4**, 145-153.
30. B. O'Regan and M. Grätzel, *Nature*, 1991, **335**, 737-740.

31. P. Péchy, T. Renouard, S. M. Zakeeruddin, R. Humphry-Baker, P. Comte, P. Liska, L. Cevey, E. Costa, V. Shklover, L. Spiccia, G. B. Deacon, C. A. Bignozzi and M. Grätzel, *J. Am. Chem. Soc.*, 2001, **123**, 1613-1624.
32. M. A. Green, K. Emery, Y. Hishikawa and W. Warta, *Prog. Photovoltaics: Res. Appl.*, 2008, **16**, 435-440.
33. *Commercially available DSSCs from G24i*, [www.g24i.com](http://www.g24i.com), Accessed 5th October, 2012.
34. S. Ferrere and B. A. Gregg, *J. Am. Chem. Soc.*, 1998, **120**, 843-844.
35. B. Bozic-Weber, E. C. Constable, N. Hostettler, C. E. Housecroft, R. Schmitt and E. Schönhofer, *Chem. Commun.*, 2012, **48**, 5727-5729.
36. S. Sakaki, T. Kuroki and T. Hamada, *J. Chem. Soc. Dalton Trans.*, 2002, 840-842.

## Chapter 2

### Alkylated bis{4'-(4-pyridyl)-2,2':6',2''-terpyridine}ruthenium(II) complexes

#### 2.1 Introduction

For decades, ruthenium complexes with 2,2'-bipyridine derivatives have dominated the field of photochemistry, with long lifetimes, high quantum yields and a variety of applications from solar cells to water-splitting catalysts<sup>1-4</sup>. However, *cis*-bis(bipyridine) and tris(bipyridine) complexes are chiral and can, therefore, be present in reactions as enantiomers, which are difficult to separate<sup>5</sup>. In the more recent past, research has moved towards ruthenium complexes with achiral, tridentate, 2,2':6',2''-terpyridine (tpy) ligands. Synthesis of these tpy ligands is facile using a one-pot synthesis method developed by Hanan and coworkers in 2005<sup>6</sup>. However, the complex  $[\text{Ru}(\text{tpy})_2]^{2+}$  is photophysically inferior to  $[\text{Ru}(\text{bpy})_3]^{2+}$  in many ways; the quantum yield is much poorer ( $<0.00002^7$  compared to  $0.04^1$ ), the lifetime is shorter (0.25 ns compared to  $\sim 850$  ns)<sup>8, 9</sup> and the complex does not emit light, in fluid solution, at room temperature. Subsequently, much research has been carried out into tuning the tpy ligand to improve the photophysical properties of the corresponding Ru(II) complex<sup>10-12</sup>.

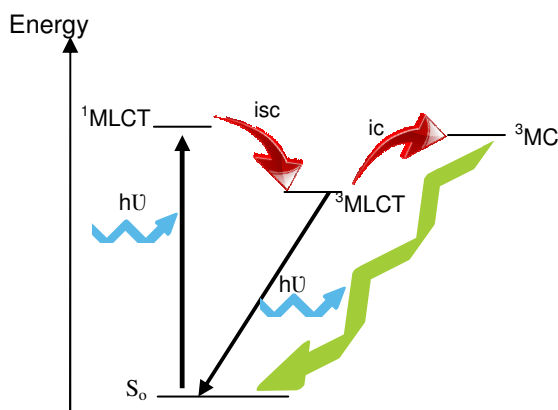


Fig. 2.1 A simplified Jablonski diagram, representing the effect of light on a Ru(II) complex. Green line denotes radiationless decay.

In order to tune a complex, the photophysical properties of said complex must first be understood (Fig. 2.1).

On absorption of light, an electron is promoted from a *d*-orbital centred on ruthenium to a vacant  $\pi^*$  orbital on the ligand. This is known as a metal-to-ligand charge transfer

(MLCT). The triplet (<sup>3</sup>) MLCT state is populated through intersystem crossing (isc), which involves a change in spin state. For ruthenium complexes, the intersystem crossing is so fast, compared to the subsequent internal conversion (ic), that it can be thought of as instantaneous. From the <sup>3</sup>MLCT there are two possibilities:

- 1) internal conversion (ic) to a <sup>3</sup>MC state and then non-radiative decay back to the ground state;
- 2) radiative decay from the <sup>3</sup>MLCT state back to the ground state, which is known as phosphorescence.

In the case of [Ru(tpy)<sub>2</sub>]<sup>2+</sup>, the <sup>3</sup>MC lies very close in energy to the <sup>3</sup>MLCT<sup>1</sup>. This is due to the distorted octahedral geometry around the ruthenium ion, caused by the presence of the terpyridine ligands. As the potential wells of the <sup>3</sup>MC and <sup>3</sup>MLCT overlap, movement of electrons allows population of the <sup>3</sup>MC state, making all decay non-radiative, which means that the complex does not emit light<sup>1</sup>.

The amount of radiative decay is quantified by the quantum yield, which is the amount of radiative decay divided by the amount of light absorbed. For a {Ru(tpy)<sub>2</sub>}-based complex, as the light emitted can only be measured if it came from the <sup>3</sup>MLCT state, the quantum yield gives a good indication of how much electron density has undergone IC and decayed from the <sup>3</sup>MC state. The lifetime of a complex quantifies the decay of intensity of the luminescent emission.

The tuning of the complex is necessary to optimise the energy gap between the <sup>3</sup>MC and the <sup>3</sup>MLCT states. The ideal complex would have a high energy <sup>3</sup>MC and a low energy <sup>3</sup>MLCT, thus maximising radiative decay and minimising IC. To this end many different substituents have been attached to tpy and the resulting ligand complexed to ruthenium<sup>12</sup>.

A paper by Maestri *et al.* detailing the effects of addition of different electron-donating and electron-withdrawing substituents to the tpy moiety was published in 1995<sup>13</sup>. A range of tpy ligands with different electron-accepting and -donating substituents were complexed to ruthenium and the photophysical and electrochemical properties were studied. It was found that the ligand-centered bands of the tpy were considerably shifted to shorter wavelengths by the presence of electron-donating substituents in the absorption spectrum. The spin-allowed MLCT band undergoes an increase in intensity and a red-shift, regardless of the nature of the substituent.

Electron-accepting substituents increased the luminescence quantum yield and the excited state lifetime but electron-donating substituents had the opposite effect. Through correlation of the Hammett  $\sigma$ -parameters, the electrochemical redox properties and the energy of the luminescent level it was found that:

- electron-accepting substituents have a larger stabilisation effect on the LUMO  $\pi^*$  ligand-centred orbital than on the HOMO  $t_{2g}$  metal orbital.
- electron-donating substituents have a larger destabilisation on the HOMO  $t_{2g}$  metal orbital than on the LUMO  $\pi^*$  ligand-centred orbital.

Just over ten years later, a paper by Beves *et al.* reporting the substitution of tpy in the 4'-position with a further 4-pyridyl moiety and the subsequent methylation of the pyridyl moiety was published<sup>14</sup>. The MLCT absorbance of the pyridyl-substituted complexes was red-shifted ( $\lambda_{\text{max}} = 487\text{-}492\text{ nm}$ ) compared to the  $[\text{Ru}(\text{tpy})_2]^{2+}$  complex ( $\lambda_{\text{max}} = 475\text{ nm}$ )<sup>9</sup> and one of the methylated complexes was even more red-shifted ( $\lambda_{\text{max}} = 507\text{ nm}$ ).

Following these two studies, it was decided to alkylate bis{4'-(4-pyridyl)-2,2':6,2''-terpyridine}ruthenium(II) complexes, henceforth denoted as  $[\text{Ru}(\text{pytpy})_2]^{2+}$ , at the terminal pyridyl moiety with a range of electron-donating and electron-withdrawing substituents, (Fig 2.2).

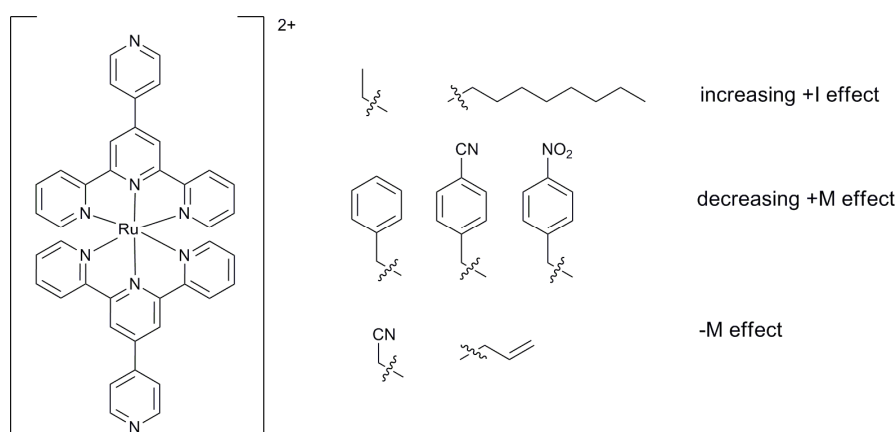


Fig. 2.2. The substituents were added to the  $[\text{Ru}(\text{pytpy})_2]^{2+}$  complex (left), annotated with their electronic contribution to the complex (right)

In adding these various substituents, it was hoped that the properties of the cation could be tuned, increasing the quantum yield and lifetime, and red-shifting both the absorbance and the emission of the complex. To aid our understanding of the effect (or lack of effect) that these substituents have on the {Ru(tpy)<sub>2</sub>} core both density functional theory (DFT) and time-dependent density functional theory (TD-DFT) calculations have been carried out. The results of the calculations are discussed later in this chapter.

DFT calculations are starting to be used more and more to complement and elaborate on experimental observations. Both DFT and TD-DFT calculations have recently been used to investigate the HOMO-LUMO gaps and predict the absorption spectra of Ru(II) complexes, with bpy-type ligands, for application in Dye-Sensitised Solar Cells (DSSCs)<sup>15-17</sup>. In the published work<sup>17</sup>, the agreement between the experimentally obtained and the calculated UV-vis spectra was poor, with disagreement of  $\lambda_{\text{max}}$  up to 90 nm for the MLCT but valuable information about the composition of the HOMO and LUMO on the complex was obtained. This information included where the HOMO and LUMO were localised, showing that the LUMO resides on the bipyridine with the anchoring group substituent, which means that the complex will be capable of binding to and injecting an electron into the TiO<sub>2</sub> layer in a DSSC. The calculations also predicted the energy levels of the HOMO and LUMO of the complex, which is also important for prediction of the complex's use in DSSCs. If the energies of the HOMO and LUMO of the dye are not compatible with the band energies of the TiO<sub>2</sub>, the DSSC will be inefficient<sup>18</sup>.

Investigations into {Ru(tpy)<sub>2</sub>}-type complexes using DFT and TD-DFT calculations have also been carried out<sup>19-23</sup>. Generally the works referenced use the calculations to corroborate experimental data or explore the experimental data in more depth. Work carried out by Berlinguette *et al*<sup>21</sup> used DFT and TD-DFT to explain the effect of a conjugate spacer between a tpy moiety and a triphenylamine moiety. Batista *et al*<sup>19</sup> combined experiment and theory to investigate the triplet potential energy surfaces of three Ru-tpy containing complexes and found that there were several <sup>3</sup>MC and <sup>3</sup>MLCT states close in energy. They also found that the inclusion of solvent in the calculations was critical in order to correctly describe these triplet excited states.



A recent publication details the effect of protonation of  $[\text{Ru}(\text{pytpy})_2]^{2+}$ .<sup>23</sup> Calculations were performed on  $[\text{Ru}(\text{pytpy})_2]^{2+}$ ,  $[\text{Ru}(\text{Hpytpy})(\text{pytpy})]^{3+}$  and  $[\text{Ru}(\text{Hpytpy})_2]^{4+}$  and the predicted UV-vis spectra showed good agreement (within 20 nm) with the experimental data. The energy gap between the  $^3\text{MLCT}$  and the  $^3\text{MC}$  was also investigated and it was found that “population of lower-lying MC states [were] held responsible for the reduced quantum yields and emission lifetimes observed for the nonprotonated Ru(II) compound.”<sup>23</sup>

The work in this chapter was completed in collaboration with Dr. Michael Devereux and is published in:

E.C. Constable, M. Devereux, E.L. Dunphy, C.E. Housecroft, J.A. Rudd and J.A. Zampese, *Dalton Trans.*, **2011**, 40, 5505-5515.

## 2.2 Synthesis of $[\text{Ru}(\text{R-pytpy})_2][\text{PF}_6]_4$ Complexes

Ruthenium complexes of the ligands depicted in Fig. 2.3, are described in this section.

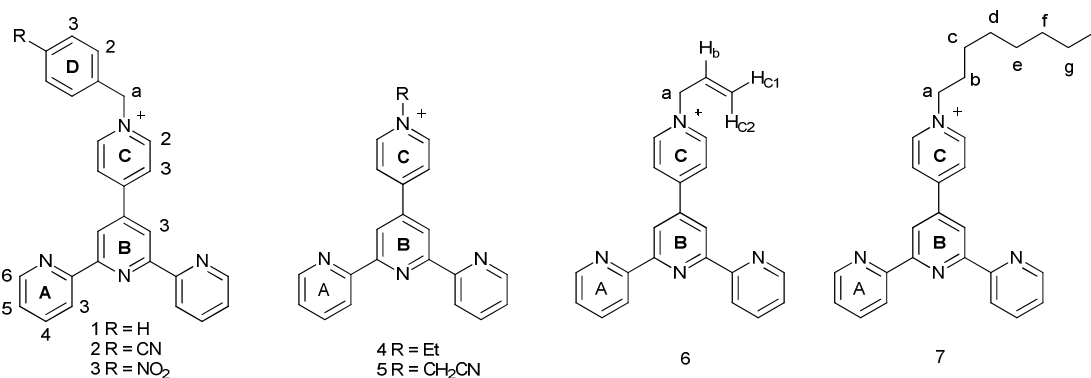
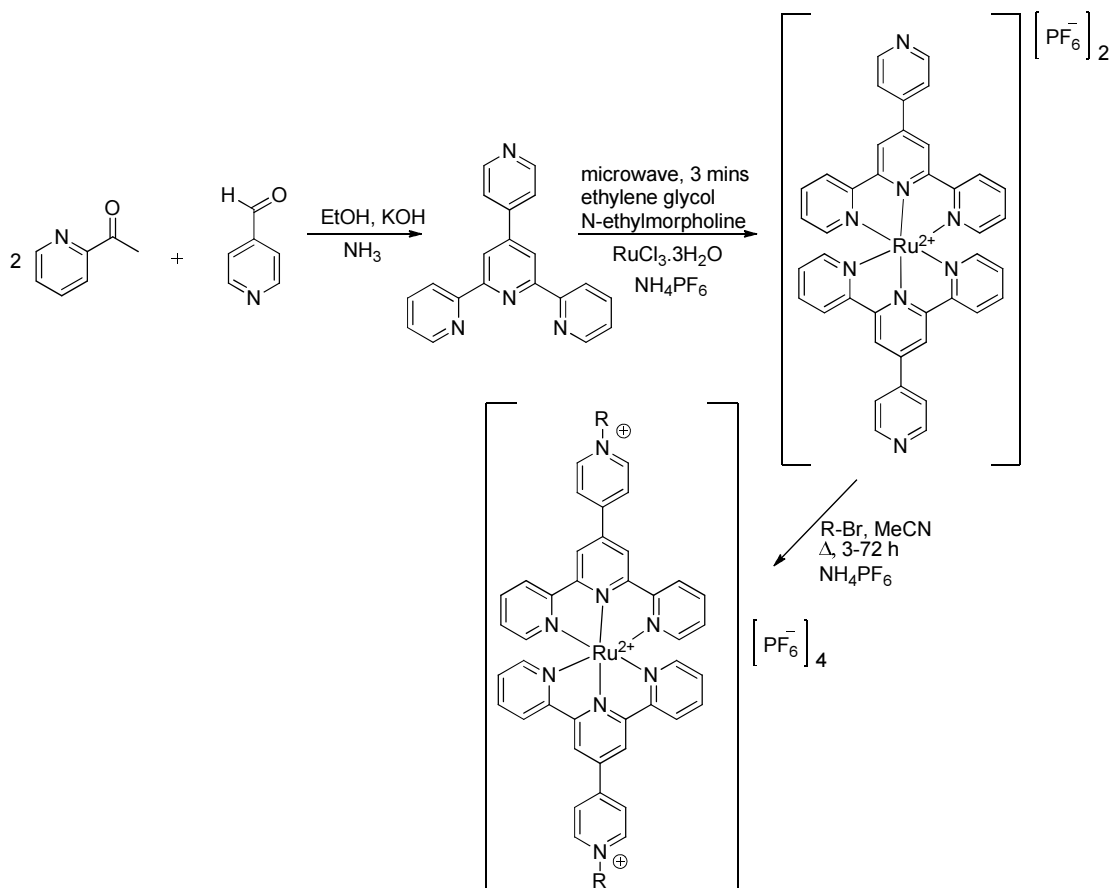


Fig. 2.3 Ligands 1-7 with labelling for  $^1\text{H}$  NMR spectroscopic assignments.

The starting material for the complexes  $[\text{Ru}(\text{L})_2][\text{PF}_6]_4$  was  $[\text{Ru}(\text{pytpy})_2][\text{PF}_6]_2$ . This was synthesised by reacting two equivalents of 4'-(4-pyridyl)-2,2':6',2''-terpyridine with one equivalent of  $\text{RuCl}_3 \cdot 3\text{H}_2\text{O}$ , in ethylene glycol, in a microwave oven for three minutes (Scheme 2.1)<sup>14</sup>. A catalytic amount of N-ethylmorpholine is required to reduce the oxidation state of the ruthenium from +3 to +2. This method of synthesising  $[\text{Ru}(\text{pytpy})_2][\text{PF}_6]_2$  greatly reduces the reaction time compared to the method of Cargill Thompson, which required refluxing pytpy and  $\text{RuCl}_3 \cdot 6\text{H}_2\text{O}$  in

ethanol for six hours<sup>24</sup>. The  $[\text{Ru}(\text{pytpy})_2][\text{PF}_6]_2$  complex was then alkylated by heating it at reflux in acetonitrile with 120 equivalents of the appropriate alkylating agent. (Table 2.1) A large excess of the alkylating agent was required to alkylate both pendant pyridines and the progress of the reaction was monitored using spot TLC.



*Scheme 2.1 Synthesis of a  $[\text{Ru}(\text{R-pytpy})_2][\text{PF}_6]_4$  complex.*

When the reaction was judged complete, the product of the reaction was purified chromatographically. After work-up, the product was isolated as a red powder in moderate to good yield (Table 2.1).

Complex	Reaction Time (h)	Yield (%)
[Ru( <b>1</b> )]PF <sub>6</sub> ] <sub>4</sub>	12	70
[Ru( <b>2</b> )]PF <sub>6</sub> ] <sub>4</sub>	12	79
[Ru( <b>3</b> )]PF <sub>6</sub> ] <sub>4</sub>	12	42
[Ru( <b>4</b> )]PF <sub>6</sub> ] <sub>4</sub>	72	64
[Ru( <b>5</b> )]PF <sub>6</sub> ] <sub>4</sub>	12	62
[Ru( <b>6</b> )]PF <sub>6</sub> ] <sub>4</sub>	4	73
[Ru( <b>7</b> )]PF <sub>6</sub> ] <sub>4</sub>	48	38

*Table 2.1 Reaction times and yields of the Ru(II) complexes of ligands 1-7 with PF<sub>6</sub> counter-anions*

## 2.3 Results and Discussion

### 2.3.1 <sup>1</sup>H NMR Spectroscopy

For solubility reasons, complexes [Ru(L)<sub>2</sub>](PF<sub>6</sub>)<sub>4</sub> L<sup>+</sup> = **2-6** were measured in d<sub>6</sub>-DMSO and complexes [Ru(L)<sub>2</sub>](PF<sub>6</sub>)<sub>4</sub> L<sup>+</sup> = **1, 7** were measured in d<sub>3</sub>-MeCN (Tables 2.2 and 2.3)

Complex (substituted with)	B <sup>3</sup>	C <sup>2</sup>	C <sup>3</sup>	A <sup>3</sup>	A <sup>4</sup>	A <sup>6</sup>	A <sup>5</sup>	H <sub>a</sub>
[Ru(pytpy) <sub>2</sub> ][PF <sub>6</sub> ] <sub>2</sub> (unsubstituted)	9.62	9.14	9.02	8.47	8.11	7.57	7.30	N/A
[Ru( <b>2</b> ) <sub>2</sub> ][PF <sub>6</sub> ] <sub>4</sub> (cyanobenzyl)	9.77	9.65	9.20	9.10	8.17	7.59	7.34	6.13
[Ru( <b>3</b> ) <sub>2</sub> ][PF <sub>6</sub> ] <sub>4</sub> (nitrobenzyl)	9.77	9.66	9.21	9.09	8.17	7.59	7.34	6.18
[Ru( <b>4</b> ) <sub>2</sub> ][PF <sub>6</sub> ] <sub>4</sub> (ethyl)	9.78	9.52	9.17	9.12	8.17	7.58	7.33	4.80
[Ru( <b>5</b> ) <sub>2</sub> ][PF <sub>6</sub> ] <sub>4</sub> (cyano)	9.80	9.61	9.25	9.12	8.17	7.58	7.33	6.08
[Ru( <b>6</b> ) <sub>2</sub> ][PF <sub>6</sub> ] <sub>4</sub> (allyl)	9.79	9.48	9.19	9.12	8.17	7.58	7.33	6.35

*Table 2.2 Comparison of shifts ( $\delta/ppm$ ) on alkylation and between alkylations for complexes measured in *d*<sub>6</sub>-DMSO at room temperature. (N/A means not applicable.)*

Complex (substituted with)	B <sup>3</sup>	C <sup>2</sup>	C <sup>3</sup>	A <sup>3</sup>	A <sup>4</sup>	A <sup>6</sup>	A <sup>5</sup>	H <sub>a</sub>
[Ru(pytpy) <sub>2</sub> ][PF <sub>6</sub> ] <sub>2</sub> (unsubstituted)	9.06	8.98	8.67	8.16	7.97	7.42	7.20	N/A
[Ru( <b>1</b> ) <sub>2</sub> ][PF <sub>6</sub> ] <sub>4</sub> (benzyl)	9.16	9.12	8.79	8.72	8.03	7.45	7.26	5.93
[Ru( <b>7</b> ) <sub>2</sub> ][PF <sub>6</sub> ] <sub>4</sub> (octyl)	9.14	9.01	8.77	8.70	8.02	7.46	7.25	4.69

*Table 2.3 Comparison of shifts ( $\delta/ppm$ ) on alkylation and between alkylations for complexes measured in CD<sub>3</sub>CN at room temperature. (N/A means not applicable.)*

A representative spectrum of [Ru(**7**)<sub>2</sub>][PF<sub>6</sub>]<sub>4</sub> is depicted (Fig. 2.4).

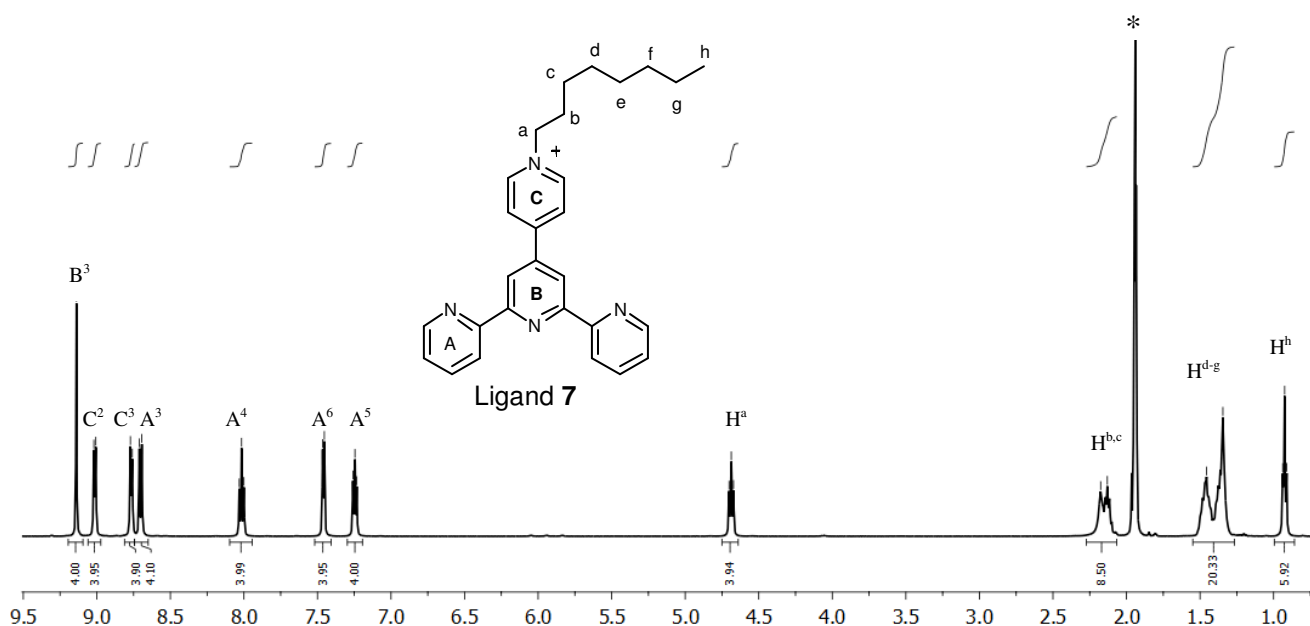


Fig. 2.4  $^1\text{H}$  NMR spectrum of  $[\text{Ru}(\mathbf{7})_2][\text{PF}_6]_4$ , in  $\text{CD}_3\text{CN}$ ; 500 MHz,  $\text{CD}_2\text{HCN}^*$ ,  $25^\circ\text{C}$ .

The appearance of only one set of pytpy signals (**A**, **B**, **C**) indicates successful alkylation of both pyridyl moieties. The majority of the pytpy signals can easily be assigned using the splitting patterns and by comparing the spectra of the product and the parent  $[\text{Ru}(\text{pytpy})_2][\text{PF}_6]_2$  (Tables 2.2 and 2.3). The singlet at  $\delta$  9.14 ppm is ascribed to proton **B**<sup>3</sup>. To assign the other peaks, a COSY spectrum was measured. The spectrum showed couplings between the AB doublets at  $\delta$  9.01 and 8.76 ppm, which meant that these signals could be ascribed to the **C** ring. COSY analysis showed couplings between the signals at  $\delta$  8.69, 8.02, 7.45 and 7.25 ppm and these signals were ascribed to the **A** ring. The triplet splitting of the signal at  $\delta$  8.02 and doublet of doublets splitting at  $\delta$  7.25 ppm determined the assignment of **A**<sup>4</sup> and **A**<sup>5</sup> and the specific assignment was achieved by comparing the shifts to the parent  $[\text{Ru}(\text{pytpy})_2][\text{PF}_6]_2$  complex. The same process was followed to ascribe **A**<sup>3</sup> and **A**<sup>6</sup>. The assignment of **C**<sup>2</sup> and **C**<sup>3</sup> required the use of a NOESY spectrum to assign these signals unambiguously. A NOESY correlation between the singlet at  $\delta$  9.14 ppm (ascribed to **B**<sup>3</sup>) and the AB doublet at  $\delta$  8.76 ppm meant that the AB doublet at  $\delta$  8.76 ppm could be ascribed to **C**<sup>3</sup>.

Relative to the parent  $[\text{Ru}(\text{pytpy})_2][\text{PF}_6]_2$  complex, upon alkylation all pytpy signals were deshielded and the signals due to protons  $\text{A}^3$ ,  $\text{C}^2$  and  $\text{C}^3$  were most affected, regardless of substituent (Tables 2.2, 2.3). The chemical shift of the signal ascribed to  $\text{A}^3$  was shifted downfield, compared to the parent complex, to  $\delta$  9.11 ppm for all complexes, regardless of the substituent. The chemical shifts of the signals ascribed to  $\text{C}^2$  and  $\text{C}^3$  were shifted downfield, compared to the parent complex, but their specific chemical shift depended on the substituent. When the substituent was electron-withdrawing the  $\text{C}^2$  and  $\text{C}^3$  signals were downfield, compared to when the substituent was electron-donating.

New signals, due to the substituent, were also observed in the NMR spectra of the alkylated complexes. The signal for  $\text{H}_a$  (the  $-\text{NCH}_2-$  protons), which occurs between  $\delta$  4.69 and 6.18 ppm is characteristic for this set of complexes (Table 2.3 and 2.4). The shift of this signal depends on the electronegativity of the substituent. For example, the  $\text{H}_a$  signal for complex  $[\text{Ru}(\mathbf{3})_2][\text{PF}_6]_4$  is downfield ( $\delta$  6.18 ppm) relative to the  $\text{H}^a$  signal of  $[\text{Ru}(\mathbf{4})_2][\text{PF}_6]_4$  ( $\delta$  4.80 ppm) due to deshielding effects from the phenyl and the cyano group at the para position. However, complex  $[\text{Ru}(\mathbf{7})_2][\text{PF}_6]_4$  has an octyl substituent, which is much less electron-withdrawing, therefore more shielded and the signal, correspondingly, is at  $\delta$  4.69 ppm. The parent complex  $[\text{Ru}(\text{pytpy})_2][\text{PF}_6]_2$  was compared with compounds  $[\text{Ru}(\text{L})_2][\text{PF}_6]_2$  ( $\text{L}^+ = \mathbf{2-6}$ ) in  $d_6$ -DMSO (Table 2.2) and compounds  $[\text{Ru}(\text{L})_2][\text{PF}_6]_2$  ( $\text{L}^+ = \mathbf{1, 6}$ ) in  $d_3$ -MeCN for solubility reasons (Table 2.3). The splitting and integrals of the peaks in the aliphatic region confirmed the octyl chain.

### 2.3.2 $^{13}\text{C}\{^1\text{H}\}$ NMR Spectroscopy

The  $^{13}\text{C}$  NMR spectrum for  $[\text{Ru}(\mathbf{7})_2][\text{PF}_6]_4$  is depicted in Fig. 2.5. The signals were assigned using DEPT, HMQC and HMBC techniques. Again, the appearance of only one set of pytpy signals confirmed the alkylation of both pendant pyridyl moieties and eight signals in the aliphatic region of the spectrum also confirmed that the complex had an octyl substituent. However, it was not possible to unambiguously ascribe all signals in the aliphatic region of the spectrum because the signals in the proton spectrum appeared so close together that distinguishing between cross peaks in the HMQC and HMBC spectra was not feasible.

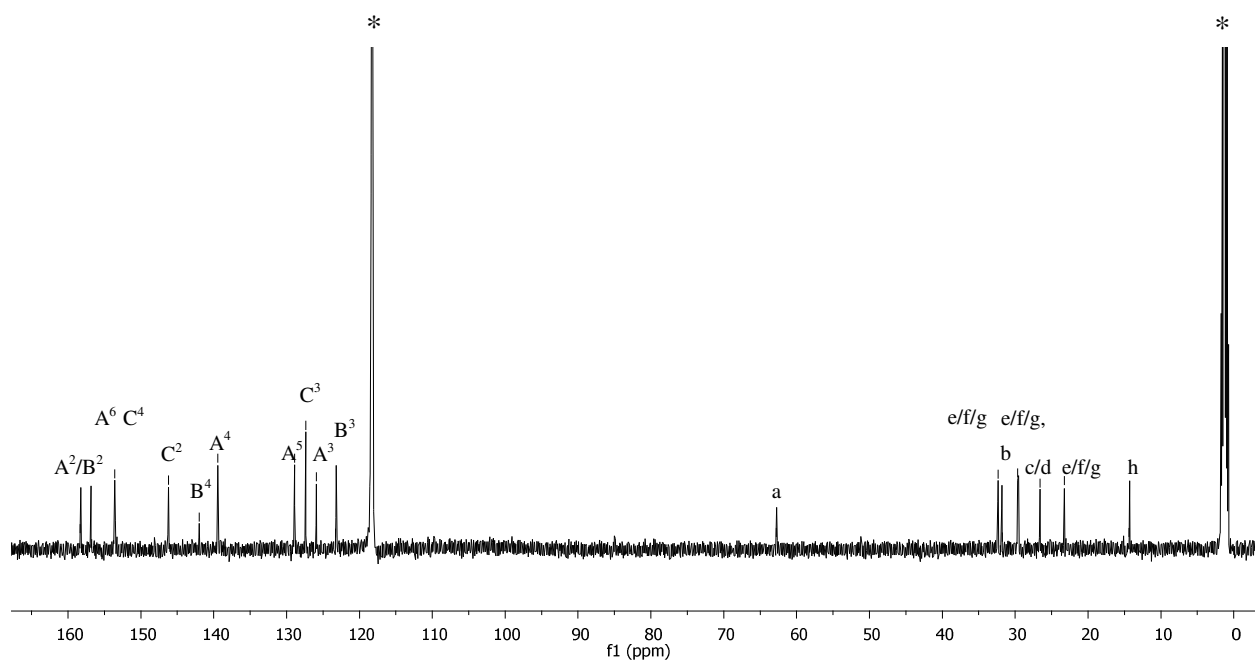


Fig. 2.5  $^{13}\text{C}\{^1\text{H}\}$  NMR spectrum of  $[\text{Ru}(\mathbf{7})_2][\text{PF}_6]_4$  in  $\text{CD}_3\text{CN}$ ; 500 MHz,  $\text{CD}_3\text{CN}^*$ ,  $25^\circ\text{C}$ .

The signal for *a*, which occurs between  $\delta$  47.6 and 62.7 ppm across the series of complexes, is characteristic for this set of complexes (Tables 2.4 and 2.5). As observed for the  $\text{H}^a$  proton signal, the shift of the *a* signal in the carbon spectrum is dependent on the electronegativity of the substituent; the more electronegative the substituent, the more downfield the signal (Tables 2.4 and 2.5). For solubility reasons, complexes  $[\text{Ru}(\text{L})_2][\text{PF}_6]_4$   $\text{L}^+ = \mathbf{1}, \mathbf{7}$  were measured in  $\text{d}_3\text{-MeCN}$  and complexes  $[\text{Ru}(\text{L})_2][\text{PF}_6]_4$   $\text{L}^+ = \mathbf{2-6}$  were measured in  $\text{d}_6\text{-DMSO}$ .

	$[\text{Ru}(\mathbf{1})_2][\text{PF}_6]_4$ (benzyl)	$[\text{Ru}(\mathbf{7})_2][\text{PF}_6]_4$ (octyl)
<i>a</i>	65.4	62.7
( $\delta/\text{ppm}$ )		

Table 2.4 Comparison of shifts of *a* between complexes measured in  $\text{d}_3\text{-MeCN}$ .

	[Ru( <b>2</b> ) <sub>2</sub> ][PF <sub>6</sub> ] <sub>4</sub> (cyanobenzyl)	[Ru( <b>3</b> ) <sub>2</sub> ][PF <sub>6</sub> ] <sub>4</sub> (nitrobenzyl)	[Ru( <b>4</b> ) <sub>2</sub> ][PF <sub>6</sub> ] <sub>4</sub> (ethyl)	[Ru( <b>5</b> ) <sub>2</sub> ][PF <sub>6</sub> ] <sub>4</sub> (cyano)	[Ru( <b>6</b> ) <sub>2</sub> ][PF <sub>6</sub> ] <sub>4</sub> (allyl)
a	62.5	62.0	56.2	47.6	62.1

( $\delta$ /ppm)

Table 2.5 Comparison of shifts of a between complexes measured in *d*<sub>6</sub>-DMSO.

### 2.3.3 Mass Spectrometry

An attempt to characterise the complexes using ESI mass spectrometry (positive mode) was made. However, the only peak observed in the spectrum was that of the parent [Ru(pytpy)<sub>2</sub>]<sup>2+</sup> complex. As NMR spectroscopy had confirmed formation of the product, it was assumed that, although a soft technique, ESI was detaching the substituent from the {Ru(pytpy)<sub>2</sub>} core. For this reason, MALDI-TOF mass spectrometry was used. It was possible to observe peaks corresponding to [M - 3PF<sub>6</sub>]<sup>+</sup> in all cases, as well as either [M - 4PF<sub>6</sub>]<sup>+</sup> or [M - 2PF<sub>6</sub>]<sup>+</sup>. It was also possible to observe fragmentation by loss of alkyl substituents. This gave rise to peaks ascribed to [Ru(L)(Hpytpy)]<sup>+</sup> and [Ru(Hpytpy)<sub>2</sub>]<sup>+</sup>.

### 2.3.4 Absorption Spectroscopy

The complexes described in this chapter were designed with different electron-donating and electron-withdrawing substituents, in order to tune the energy gap between the <sup>3</sup>MLCT and <sup>3</sup>MC states. Absorption spectroscopy was used to investigate these complexes and ascertain the extent to which the <sup>3</sup>MLCT energy level was affected by each substituent.

It has previously been reported that both protonation and methylation of a [Ru(pytpy)<sub>2</sub>]<sup>2+</sup> complex cause the MLCT to red-shift to  $\lambda_{\text{max}} = 507$  nm, from 488nm for the parent complex<sup>14</sup>. This same red-shift occurred for all complexes [Ru(L)<sub>2</sub>][PF<sub>6</sub>]<sub>4</sub> (L<sup>+</sup> = 1-7). However, little change in between complexes was observed (range of  $\lambda_{\text{max}} = 509$ -516 nm), as depicted in Fig. 2.6. The only difference between complexes was the molar absorption coefficient ( $\epsilon$ ) which, for the MLCT band, ranged from  $48.7 \times 10^3$  (L<sup>+</sup> = 7) to  $29.7 \times 10^3$  (L<sup>+</sup> = 3) dm<sup>3</sup> mol<sup>-1</sup> cm<sup>-1</sup>.



The most intense bands were due to ligand  $\pi \rightarrow \pi^*$  transitions. Of these the band centred at 277 nm (276 nm for  $L^+ = 4$ ) was the most intense for all complexes. There was also a marked difference in the  $\epsilon$  values of this band, which ranged from  $10.4 \times 10^4$  ( $L^+ = 2$ ) to  $63.3 \times 10^3$  ( $L^+ = 1$ )  $\text{dm}^3 \text{mol}^{-1} \text{cm}^{-1}$ .

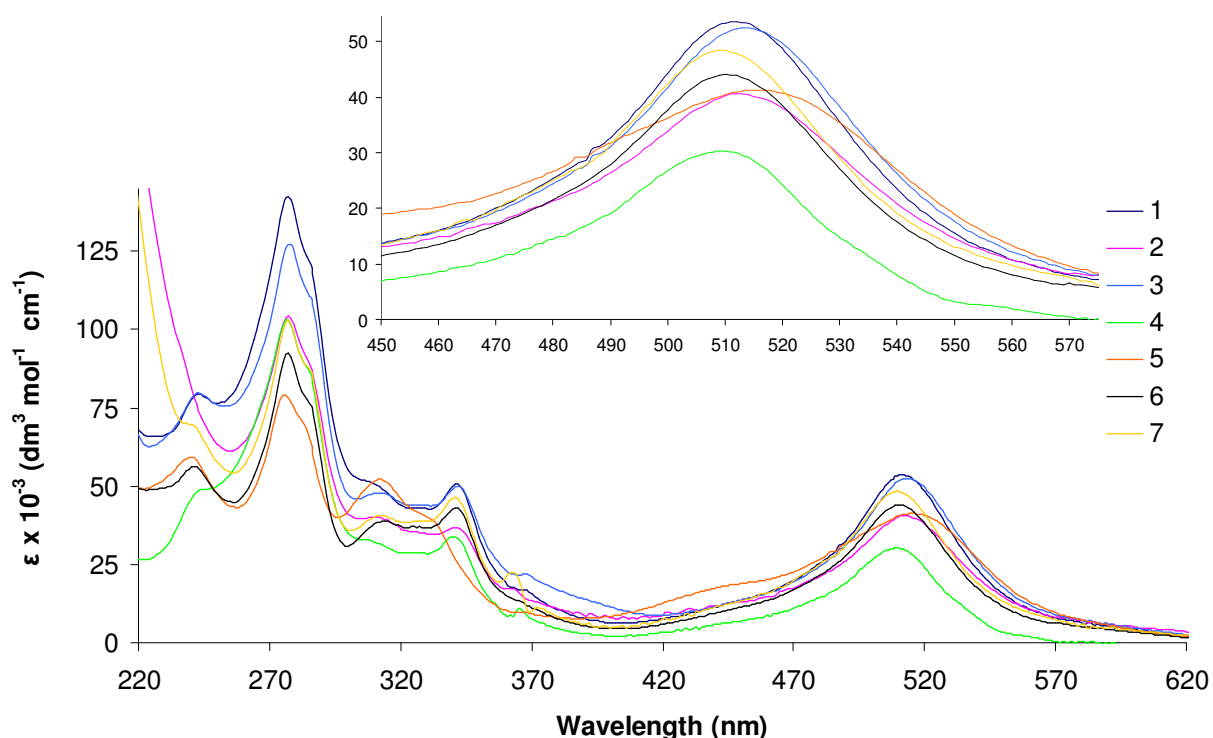


Fig. 2.6 Absorption spectra for  $[\text{Ru}(\text{L})_2][\text{PF}_6]_4$  ( $L^+ = 1-7$ ), measured in acetonitrile. All solutions are of  $10^{-6} \text{ mol dm}^{-3}$  concentration.

The data recorded for the MLCT and the ligand centred transitions are summarised and compared to the parent  $[\text{Ru}(\text{pytpy})_2][\text{PF}_6]_2$  complex (Table 2.6). The results demonstrate that changing the substituent not only has very little effect on the shift of the MLCT band but also no effect on the absorption maximum of any of the  $\pi \rightarrow \pi^*$  bands. The lack of MLCT shift suggests that changing the substituent has no effect of the  $\{\text{Ru}(\text{tpy})_2\}$  core. This could be due to the  $N\text{-CH}_2$  group preventing delocalisation of the  $\pi$  character from the terminal pyridyl moiety, which is explored in greater depth later in a TD-DFT study.

Complex	MLCT		$\lambda_{\text{max}}$			
	$(\epsilon/10^3 \text{ dm}^3 \text{ mol}^{-1} \text{ cm}^{-1})$		$(\epsilon/10^3 \text{ dm}^3 \text{ mol}^{-1} \text{ cm}^{-1})$			
Ru(pytpy) <sub>2</sub> ][PF <sub>6</sub> ] <sub>2</sub>	488 (30.9)	312 (61.6)		273 (78.4)		238 (43.5)
[Ru( <b>1</b> ) <sub>2</sub> ][PF <sub>6</sub> ] <sub>4</sub>	511 (34.3)	341 (26.4)	313 (21.1)	292 sh (46.8)	277 (63.3)	241 (29.9)
[Ru( <b>2</b> ) <sub>2</sub> ][PF <sub>6</sub> ] <sub>4</sub>	512 (40.6)	341 (36.8)	312 (40.6)	285 sh (87.6)	277 (104.2)	
[Ru( <b>3</b> ) <sub>2</sub> ][PF <sub>6</sub> ] <sub>4</sub>	513 (29.7)	342 (26.3)	312 (23.3)	288 sh (68.0)	277 (85.7)	240 sh (46.2)
[Ru( <b>4</b> ) <sub>2</sub> ][PF <sub>6</sub> ] <sub>4</sub>	509 (30.3)	341 (34.0)	309 sh (29.6)	284 sh (88.4)	276 (103.0)	241 sh (47.3)
[Ru( <b>5</b> ) <sub>2</sub> ][PF <sub>6</sub> ] <sub>4</sub>	516 (41.9)	333 sh (39.4)	312 (52.0)	283 sh (69.8)	275 (93.7)	242 sh (36.9)
[Ru( <b>6</b> ) <sub>2</sub> ][PF <sub>6</sub> ] <sub>4</sub>	510 (44.0)	341 (43.3)	313 (38.9)	285 sh (76.6)	277 (92.7)	241 (56.4)
[Ru( <b>7</b> ) <sub>2</sub> ][PF <sub>6</sub> ] <sub>4</sub>	510 (48.7)	341 (46.7)	313 (40.6)	285 sh (87.6)	277 (103.4)	240 sh (69.6)

Table 2.6 A summary of the photophysical data, recorded in MeCN, for the Ru(II) complexes of ligands 1-7.

### 2.3.5 Emission Spectroscopy

Further investigation into the effect of alkylating the [Ru(pytpy)<sub>2</sub>]<sup>2+</sup> complex was carried out using emission spectroscopy. If the gap between the <sup>3</sup>MLCT and the <sup>3</sup>MC states had been increased, the complexes would emit at room temperature with a longer lifetime and a higher quantum yield, compared to the parent [Ru(pytpy)<sub>2</sub>]<sup>2+</sup> complex.

MeCN solutions of the complexes were excited in the MLCT band ( $\lambda_{\text{ex}} = 510 \text{ nm}$ ), which resulted in a broad emission between 620 and 850 nm. Compared to the parent [Ru(pytpy)<sub>2</sub>][PF<sub>6</sub>]<sub>2</sub> complex, the emission was red-shifted and  $\lambda_{\text{em}}$  was generally

centered around 728 nm, with two obvious outliers;  $L^+ = 7$  where  $\lambda_{em} = 701$  nm and  $L^+ = 2$ , where  $\lambda_{em} = 741$  nm. The emission intensities do not differ greatly from one another. The spectra are depicted in Fig. 2.7.

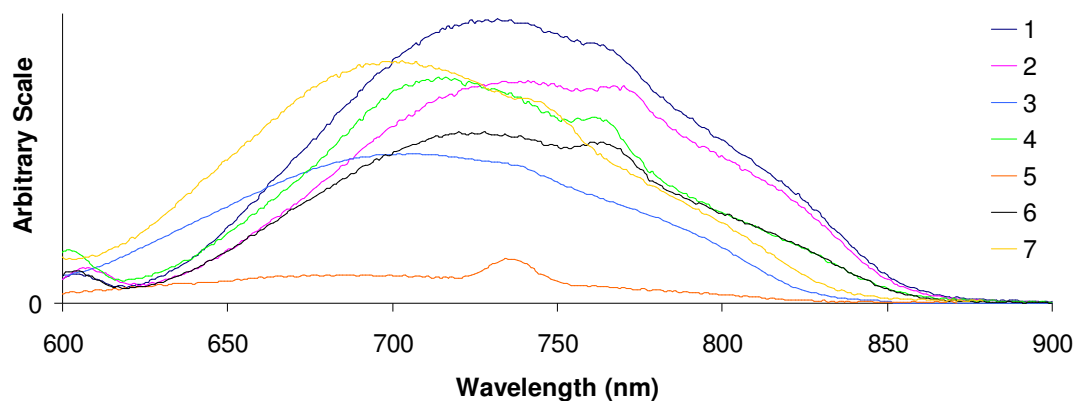


Fig. 2.7 Emission spectra for  $[Ru(L)_2][PF_6]$  ( $L^+ = 1-7$ ) measured in acetonitrile. All solutions are of  $10^{-6}$  mol  $dm^{-3}$  concentration.

As with the absorption spectra, there are no obvious differences between the emission spectra of the complexes. There are also no overt differences between either the lifetimes or the quantum yields of the complexes (Table 2.7). However, there are many differences between the parent  $[Ru(pytpy)_2][PF_6]_2$  complex and the alkyl-substituted complexes. Firstly, the emission maxima of the alkyl-substituted complexes are red-shifted by up to 86 nm. Secondly, the lifetime of the complex has been extended by up to 163 ns. Finally, the quantum yield has increased by a minimum of a factor of 2.5 ( $L^+=3$ ) and up to a factor of 200 ( $L^+=1$ ).

The emission maxima, lifetimes and quantum yields are summarised in Table 2.7.

Complex	Emission Max (nm)	$\tau$ (ns)	Quantum Yield (%) ( $\pm$ 0.1%)
Ru(pytpy) <sub>2</sub> ][PF <sub>6</sub> ] <sub>2</sub> <sup>25</sup>	655	3	0.04
[Ru( <b>1</b> ) <sub>2</sub> ][PF <sub>6</sub> ] <sub>4</sub>	728	160 <sup>a</sup>	0.73
[Ru( <b>2</b> ) <sub>2</sub> ][PF <sub>6</sub> ] <sub>4</sub>	741	115 <sup>a</sup>	0.38
[Ru( <b>3</b> ) <sub>2</sub> ][PF <sub>6</sub> ] <sub>4</sub>	730	105 <sup>a</sup>	0.01
[Ru( <b>4</b> ) <sub>2</sub> ][PF <sub>6</sub> ] <sub>4</sub>	715	162 <sup>a</sup>	0.35
[Ru( <b>5</b> ) <sub>2</sub> ][PF <sub>6</sub> ] <sub>4</sub>	703	129 <sup>a</sup>	0.05
[Ru( <b>6</b> ) <sub>2</sub> ][PF <sub>6</sub> ] <sub>4</sub>	727	145 <sup>a</sup>	0.45
[Ru( <b>7</b> ) <sub>2</sub> ][PF <sub>6</sub> ] <sub>4</sub>	701	166 <sup>a</sup>	0.44

Table 2.7 A summary of the photophysical properties of Ru(II) complexes with ligands **1-7**, recorded in MeCN, <sup>a</sup> means the error is  $\pm$  15 ns.

### 2.3.6 Electrochemistry

Cyclic voltammetry was used to examine the oxidation and reduction potentials of each complex. Oxidation of the complex is the removal of an electron from the highest occupied molecular orbital (HOMO). Reduction is the insertion of an electron into the lowest unoccupied molecular orbital (LUMO) of the complex. For the complex to do work, such as water splitting, the oxidation potential needs to be appropriate; high enough to be above the oxidation potential of water but not so high that oxidation of the complex is impossible.

The measurements were carried out in an MeCN solution of the complex using 0.1M TBAPF<sub>6</sub> as the supporting electrolyte. Ferrocene was added at the end of each measurement as a reference. A square wave voltammogram was also measured as a 'check'; data are not shown.

For all complexes a reversible one-electron oxidation was observed around 1.0 V (vs Fc/Fc<sup>+</sup>), which is attributed to the oxidation of Ru<sup>II</sup> to Ru<sup>III</sup>. Two reversible one-electron ligand-centred reductions around -1.05 V and -1.45 V (vs Fc/Fc<sup>+</sup>), were also observed for all complexes. The two reductions are attributed to the injection of an electron into an unoccupied ligand  $\pi^*$  orbital, to form a radical anion. Fig. 2.8 depicts a representative cyclic voltammogram; [Ru(**1**)<sub>2</sub>][PF<sub>6</sub>]<sub>4</sub>.

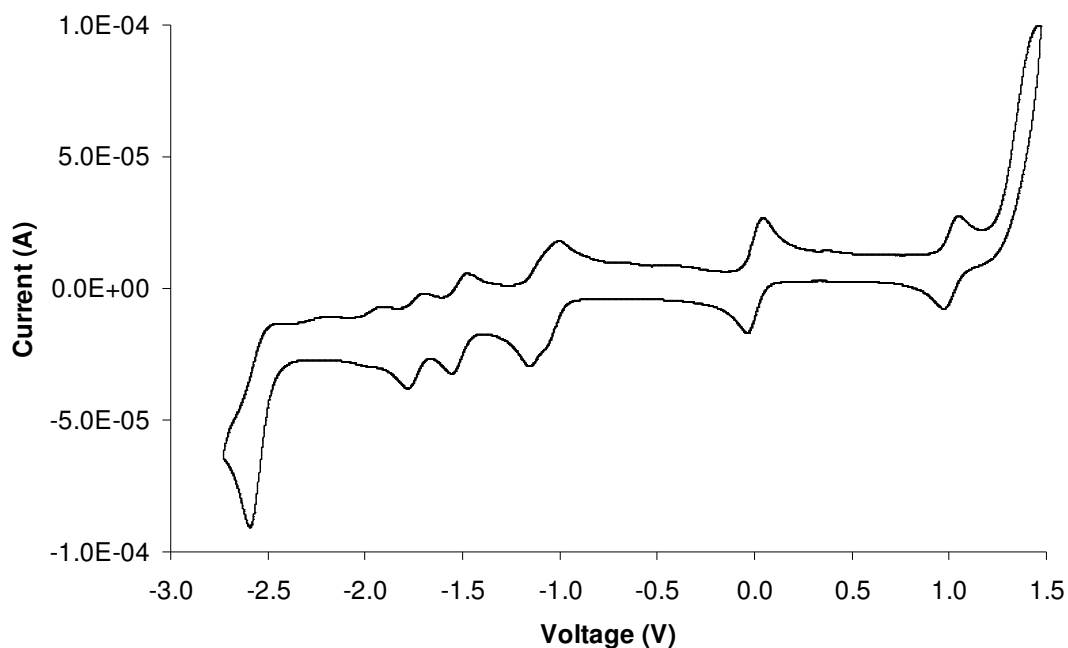


Fig. 2.8 Cyclic Voltammogram for  $[Ru(I)_2][PF_6]_4$  (MeCN, 0.1M TBAPF<sub>6</sub>, internal reference; ferrocene).

The data for all of the complexes are summarised in Table 2.8. Further ligand-centred reductions are observed for each complex, around -1.7 V, but in the case of  $L^+ = 3$  this reduction is irreversible and in the cases of  $L^+ = 5, 7$  the reduction is quasi-reversible. For complex  $L^+ = 1$  (Fig. 2.8) the asymmetry of the reduction peak at -1.0 V suggests the possibility of two reduction processes at close potentials. For complexes  $L^+ = 3, 5$  and  $7$  a further reduction around -2.0 V is observed and this is irreversible in all cases.

Complex	Ru <sup>2+</sup> /Ru <sup>3+</sup>		Ligand centred reductions (V)		
	(V)				
[Ru(pytpy) <sub>2</sub> ][PF <sub>6</sub> ] <sub>2</sub>	+0.95		-1.54	-1.80	
[Ru( <b>1</b> ) <sub>2</sub> ][PF <sub>6</sub> ] <sub>4</sub>	+1.07/ +0.96	-0.98/ -1.17	-1.45/ -1.58	-1.68/ -1.81	
[Ru( <b>2</b> ) <sub>2</sub> ][PF <sub>6</sub> ] <sub>4</sub>	+1.06/ +0.96	-0.97/ -1.13	-1.44/ -1.56	-1.67/ -1.79	
[Ru( <b>3</b> ) <sub>2</sub> ][PF <sub>6</sub> ] <sub>4</sub>	+1.12/ +0.98	-1.00/ -1.20	-1.30/ -1.49	-1.69 <sup>irr</sup>	-2.22 <sup>irr</sup>
[Ru( <b>4</b> ) <sub>2</sub> ][PF <sub>6</sub> ] <sub>4</sub>	+1.05/ +0.95	-1.04/ -1.23	-1.52/ -1.62	-1.73/ -1.84	
[Ru( <b>5</b> ) <sub>2</sub> ][PF <sub>6</sub> ] <sub>4</sub>	+1.08/ +0.96	-0.87/ -1.04	-1.35/ -1.46	-1.56/ -1.71 <sup>qr</sup>	-1.99 <sup>irr</sup>
[Ru( <b>6</b> ) <sub>2</sub> ][PF <sub>6</sub> ] <sub>4</sub>	+1.07/ +0.97	-1.03/ -1.17	-1.50/ -1.57	-1.71/ -1.80	
[Ru( <b>7</b> ) <sub>2</sub> ][PF <sub>6</sub> ] <sub>4</sub>	+1.06/ 0.94	-1.05/ -1.21	-1.51/ -1.61	-1.73/ -1.84 <sup>qr</sup>	-1.94 <sup>irr</sup>

Table 2.8 A summary of the redox potentials for Ru(II) complexes with ligands **1-7**. Measurements carried out in MeCN, using 0.1M TBAPF<sub>6</sub> as the electrolyte and referenced to Fc/Fc<sup>+</sup>. <sup>qr</sup>Quasi-reversible; <sup>irr</sup>Irreversible

The alkyl-substituted complexes have a higher Ru(II)/Ru(III) redox potential than that of the parent [Ru(pytpy)<sub>2</sub>][PF<sub>6</sub>]<sub>2</sub> complex. This means that abstraction of an electron from the HOMO of the alkylated complexes requires more energy than for the parent complex. The negligible change in redox potentials between complexes complements the photophysical data leading to the conclusion that changing the substituent has a negligible effect on the {Ru(tpy)<sub>2</sub>} core.

### 2.3.7 Crystal Structures

Crystal structures of the following complexes were obtained:

- $[\text{Ru}(\mathbf{1})_2][\text{PF}_6]_4 \cdot \text{H}_2\text{O}$
- $[\text{Ru}(\mathbf{3})_2][\text{PF}_6]_4$
- $[\text{Ru}(\mathbf{4})_2][\text{PF}_6]_4 \cdot \text{H}_2\text{O}$
- $[\text{Ru}(\mathbf{6})_2][\text{PF}_6]_4 \cdot 2\text{MeCN}$
- $[\text{Ru}(\mathbf{7})_2][\text{PF}_6]_4$

Red blocks of  $[\text{Ru}(\mathbf{1})_2][\text{PF}_6]_4 \cdot \text{H}_2\text{O}$  were grown by slow evaporation of an acetonitrile solution of the complex and the structure confirmed benzylation at both terminal pyridine rings. The crystal structure solves in the  $P-1$  space group, with a poor R factor of 15.0 %. The asymmetric unit contains 2 independent cations with 7 whole  $\text{PF}_6$  counter-anions, 2 half  $\text{PF}_6$  counter-anions and two water molecules.

The structure of one of the  $[\text{Ru}(\mathbf{1})_2]^{4+}$  cations is depicted in Fig. 2.9 and selected bond lengths and angles are listed in the caption.

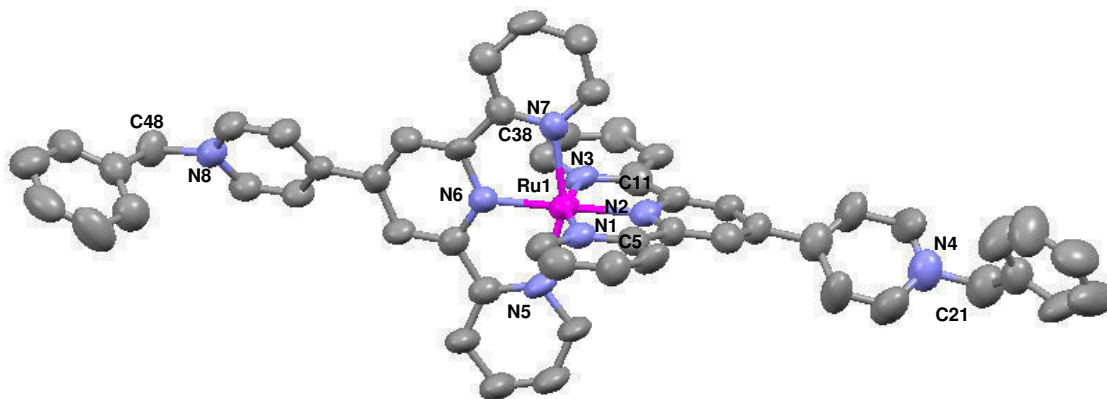


*Fig. 2.9 Structure of one of the  $[\text{Ru}(\mathbf{1})_2]^{4+}$  cations with ellipsoids plotted at 50% probability and hydrogen atoms omitted for clarity. Selected bond parameters:  $\text{Ru1-N1} = 2.07(1)$ ,  $\text{Ru1-N2} = 1.97(1)$ ,  $\text{Ru1-N3} = 2.06(1)$ ,  $\text{Ru1-N5} = 2.07(1)$ ,  $\text{Ru1-N6} = 1.969(7)$ ,  $\text{Ru1-N7} = 2.06(1)$ ,  $\text{N4-N21} = 1.50(2)$ ,  $\text{N8-C48} = 1.46(2)$  Å;  $\text{N2-Ru1-N1} = 79.5(4)$ ,  $\text{N2-Ru1-N3} = 78.9(4)$ ,  $\text{N5-Ru1-N6} = 79.4(4)$ ,  $\text{N6-Ru1-N7} = 78.5(4)^\circ$ .*

As expected for a  $[\text{Ru}(\text{X-tpy})_2]^{n+}$  ( $\text{X} = \text{any substituent}$ ) complex the ruthenium atom coordinates two ligands through the nitrogen atoms of the terpyridine moieties. The terpyridine ligands are almost orthogonal to one another; the angle between the planes is  $89.03^\circ$  (plane 1: N1, C5, ring containing N2 and C11, N3, plane 2: N5, C32, ring containing N6 and C38, N7). The  $\text{N}_{\text{central}}\text{-Ru-N}_{\text{central}}$  vector was expected to be linear, with an N4-Ru1-N8 angle of  $180^\circ$ , however, a bowing of the  $[\text{Ru}(\mathbf{1})_2]^{4+}$  cation is observed. This bowing is also present for  $[\text{Ru}(\text{pytpy})_2][\text{PF}_6][\text{NO}_3]\cdot\text{DMSO}$ <sup>26</sup> and  $[\text{Ru}(\text{pytpy})][\text{PF}_6][\text{NO}_3]$ <sup>27</sup> (N4-Ru1-N8 angles are  $169.11(4)^\circ$  and  $176.03(7)^\circ$ , respectively). Compared to these two complexes the bowing of  $[\text{Ru}(\mathbf{1})_2][\text{PF}_6]_4$  is much greater ( $163.4^\circ$ ), which is probably due to the effect that the benzyl substituent has on the packing (see later). The bond lengths and angles within the Ru-tpy unit are unexceptional. The N4-C21 and N8-C48 bond lengths of  $1.50(2)$  and  $1.46(2)$  Å, respectively, are consistent with single bonds between each pendant pyridine N atom and the benzyl group.

Two independent cations reside in the asymmetric unit. The cations differ most greatly in the orientation of the benzyl substituents. For comparison, the two complexes have been overlaid and are depicted in Fig. 2.10.

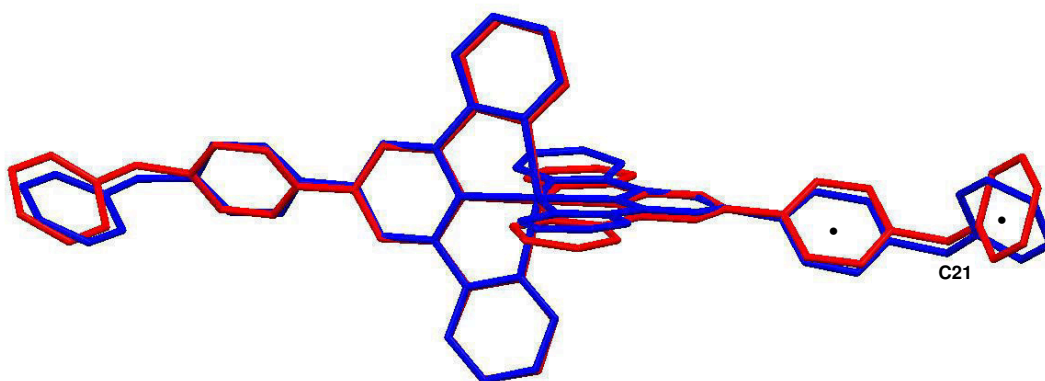


*Fig. 2.10 An overlay of the two independent cations in the asymmetric unit, black dots denote the centroids.*

The core  $\{\text{Ru}(\text{tpy})_2\}$  regions of the cations are similar. In one complex (blue) both of the benzyl substituents are orientated in the same direction. In the other complex (red) one benzyl substituent is almost orthogonal (angle between planes  $86.8^\circ$ ) to the terminal pyridyl moiety, to which it is attached. (Plane 1 is the terminal pyridine ring,



plane 2 is the benzyl ring.) The distance between the centroids of the two rings is 4.8Å and the centroid-C21-centroid angle is 111.3°. The other benzyl group is roughly perpendicular to the terminal pyridyl group, with the angle between the planes of 74.8°. The distance between the two centroids is also 4.8Å, and the centroid-C48-centroid angle, 111.5°, is effectively the same as for the previously described substituent. The centroid to centroid bond lengths and angles are consistent with the carbon atom being constrained to tetrahedral geometry by bonding to four different groups. (Plane 1 is the terminal pyridine ring, plane 2 is the benzyl ring.)

The complexes pack with intermeshing benzyl groups. Within the crystal lattice there are extensive short contacts between hydrogen atoms and fluorine atoms of the hexafluorophosphate counter-anions (e.g. H4-F4 2.56Å).

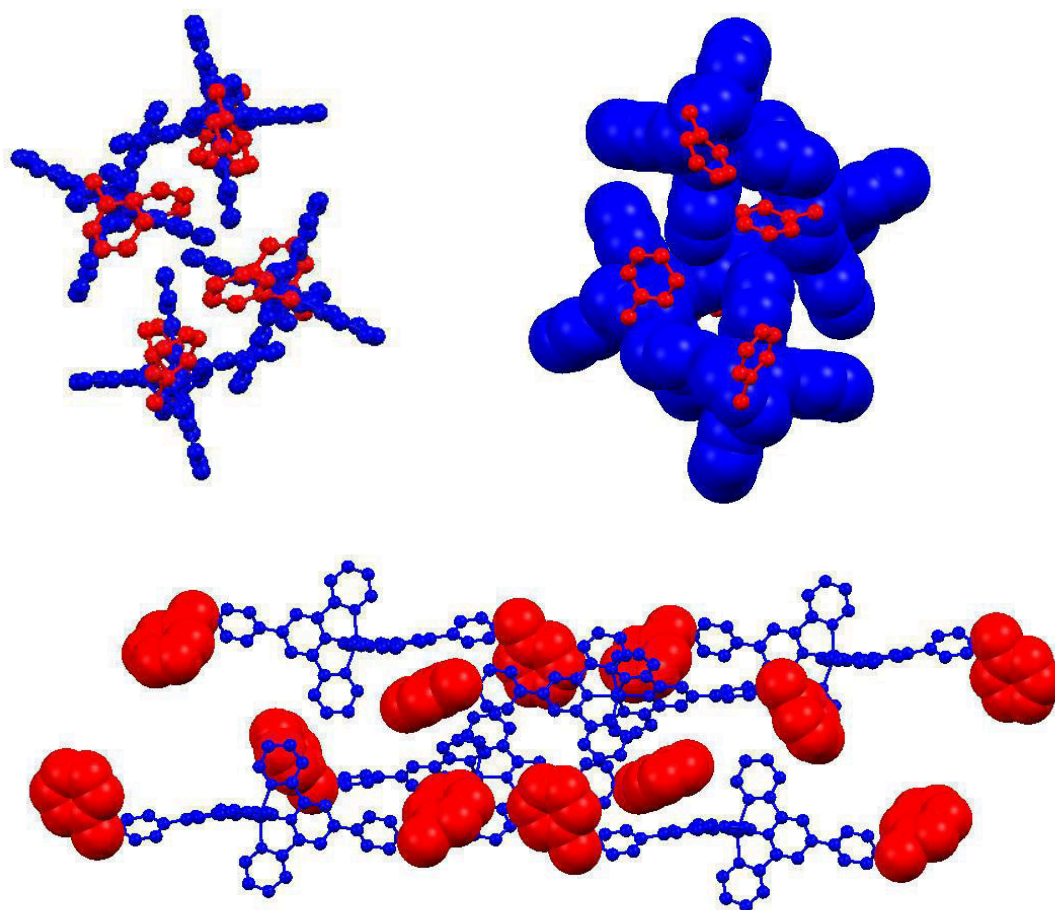


*Fig. 2.11 Packing of the cations in  $[Ru(\mathbf{1})_2][PF_6]_4 \cdot H_2O$  with the  $\{Ru(pytpy)_2\}$ - core in blue and the pendant benzyl groups in red.*

The cations were expected to pack with two dimensional tpy embrace layers<sup>28-32</sup> and some intercalation of the cations can be observed (Fig 1.11 top). However, the benzyl substituent distorts the tpy-tpy embrace by occupying the space between the tpy units, forcing them apart (Fig. 2.11 bottom). This also prohibits  $\pi$ -stacking throughout the lattice.

Red blocks of  $[\text{Ru}(\mathbf{3})_2][\text{PF}_6]_4$  were grown by diffusing diethyl ether into a nitromethane solution of the complex. The structure has an R factor of 10.6%, which has been improved from 16.8% by using SQUEEZE<sup>33</sup> to remove disordered anions and solvent molecules. The unit cell contains four independent cations and, like  $[\text{Ru}(\mathbf{1})_2][\text{PF}_6]_4 \cdot \text{H}_2\text{O}$ , the crystal solves in the  $P - 1$  space group. Although the two complexes solve in the same space group, the unit cell of  $[\text{Ru}(\mathbf{3})_2][\text{PF}_6]_4$  has a c-axis length almost double that of  $[\text{Ru}(\mathbf{1})_2][\text{PF}_6]_4 \cdot \text{H}_2\text{O}$  (50.95 Å compared to 27.76 Å, respectively). This is due to the number of cations in the asymmetric unit; four cations of  $[\text{Ru}(\mathbf{3})_2]^{4+}$  vs two cations of  $[\text{Ru}(\mathbf{1})_2]^{4+}$ . The structure of one of the independent  $[\text{Ru}(\mathbf{3})_2]^{4+}$  cations is depicted in Fig. 2.12 and selected bond lengths and angles are described in the caption.

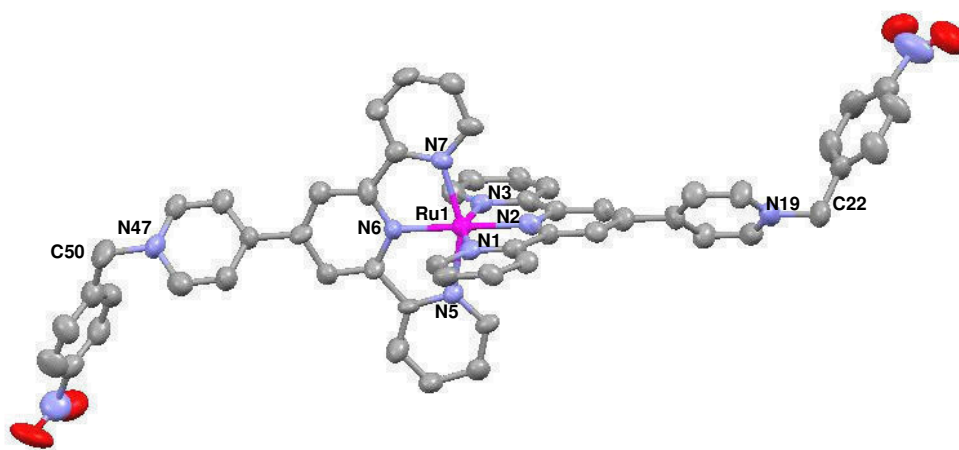
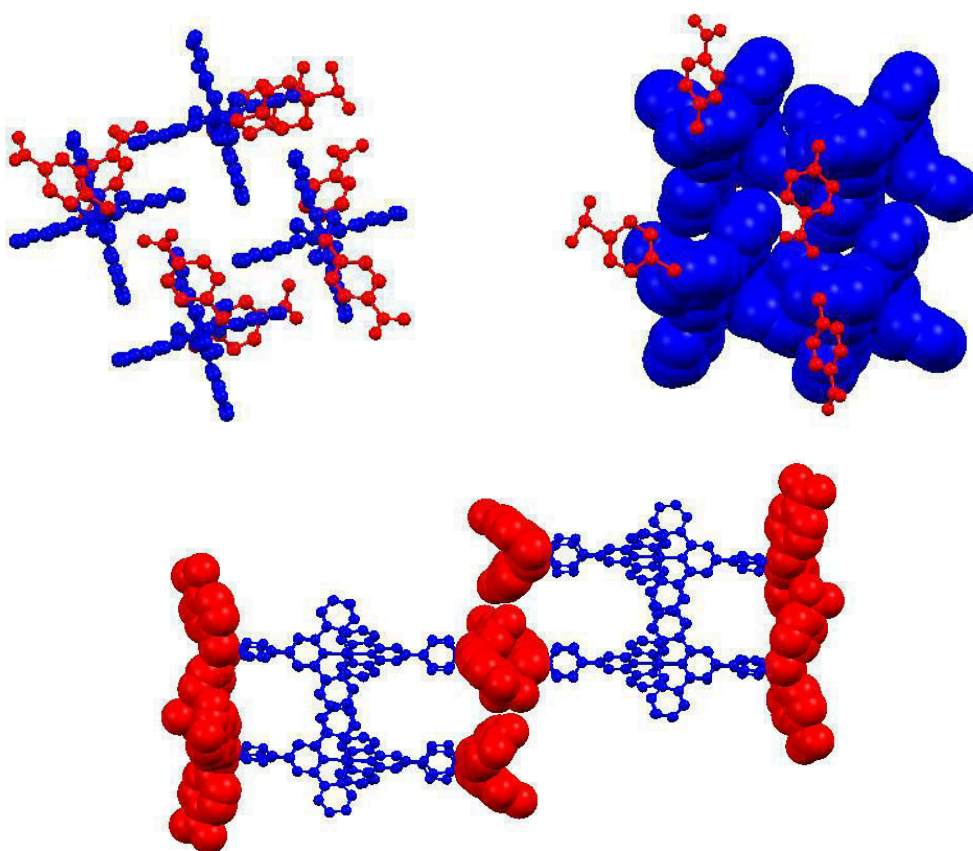


Fig 2.12 Structure of the  $[\text{Ru}(\mathbf{3})_2]^{4+}$  cation with ellipsoids plotted at 50% probability and hydrogens omitted for clarity. Selected bond parameters:  $\text{Ru1-N1} = 2.099(7)$ ,  $\text{Ru1-N2} = 1.986(8)$ ,  $\text{Ru1-N3} = 2.095(7)$ ,  $\text{Ru1-N5} = 2.0082(7)$ ,  $\text{Ru1-N6} = 1.995(5)$ ,  $\text{Ru1-N7} = 2.088(7)$ ,  $\text{N19-N22} = 1.493(7)$ ,  $\text{N47-C50} = 1.523(8)$  Å;  $\text{N2-Ru1-N1} = 79.0(2)$ ,  $\text{N2-Ru1-N3} = 77.8(2)$ ,  $\text{N5-Ru1-N6} = 78.1(2)$ ,  $\text{N6-Ru1-N7} = 79.2(2)^\circ$ .

Two ligands are coordinated to the ruthenium atom, resulting in an octahedral geometry. The two terpyridines are close to orthogonal; the angle between the planes is 89.7°. As for  $[\text{Ru}(\mathbf{1})_2]^{4+}$  there is a bowing of the cation backbone away from linearity but, by comparison, for  $[\text{Ru}(\mathbf{3})_2]^{4+}$  this bowing is less pronounced ( $\text{N4-Ru1-N8} = 173.4^\circ$ ). The bond lengths and angles around the  $\{\text{Ru}(\text{tpy})_2\}$  core are unremarkable. The N19-C22 and N47-C50 bond lengths of 1.493(7) and 1.485(7) Å respectively, are consistent with single bonds between the N atom of the pendant pyridine and the nitrobenzyl substituent. These bond lengths are also very similar to the analogous bonds in  $[\text{Ru}(\mathbf{1})_2][\text{PF}_6]_4 \cdot \text{H}_2\text{O}$ .



*Fig. 2.13 Packing of the cations with the  $\{\text{Ru}(\text{pytpy})_2\}$ -core in blue and the pendant nitrobenzyl groups in red.*

Typical tpy-tpy embraces<sup>28-32</sup> are observed in the packing of  $[\text{Ru}(\mathbf{3})_2]^{4+}$ , with both face-to-face and edge-to-face interactions. The edge-to-face distances range from 2.35 to 2.93 Å and the face-to-face distances are longer, 3.61-3.85 Å. The majority of nitrobenzyl substituents pack orthogonally to the  $\{\text{Ru}(\text{pytpy})_2\}$  core and, therefore, do

not disrupt the packing. Some  $\pi$ -stacking<sup>34</sup> is observed between the nitrobenzyl groups, centroid-centroid distance = 3.76 Å, (Fig 2.14). No  $\pi$ -stacking is observed between the pyridylterpyridine units.

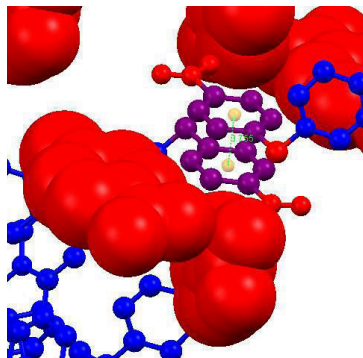


*Fig. 2.14  $\pi$ -stacking between the two benzyl rings of the nitrobenzyl substituents (benzyl rings depicted in purple, centroids in yellow).*

Red needles of  $[\text{Ru}(\mathbf{4})_2][\text{PF}_6]_4 \cdot \text{H}_2\text{O}$  were grown by diffusing diethyl ether into an acetone solution of the complex. The structure has a reasonable R factor of 6.6 % and solves in the space group  $P 2_1/c$ . The asymmetric unit contains one  $[\text{Ru}(\mathbf{4})_2]^{4+}$  cation, four  $\text{PF}_6^-$  counter-anions and one water molecule. One ethyl group is disordered over two positions and has been modelled over two sites with fractional occupancies of 0.76 and 0.24. All four  $\text{PF}_6^-$  counter-anions and the water molecule are disordered.

The two ligands coordinate orthogonally to the central ruthenium atom (angle between the tpy planes is  $87.8^\circ$ ) causing an octahedral geometry of the cation. There is a slight bowing of the cation from linearity; N4-Ru1-N8 angle =  $171.5^\circ$ , more than that of  $[\text{Ru}(\mathbf{3})_2]^{4+}$  but less than that of  $[\text{Ru}(\mathbf{1})_2]^{4+}$ . The bond lengths and angles are standard for this type of complex. The N4-C21 and N8-C43 bond lengths are consistent with analogous bond lengths for the aforementioned  $[\text{Ru}(\text{L})_2]^{4+}$  complexes.

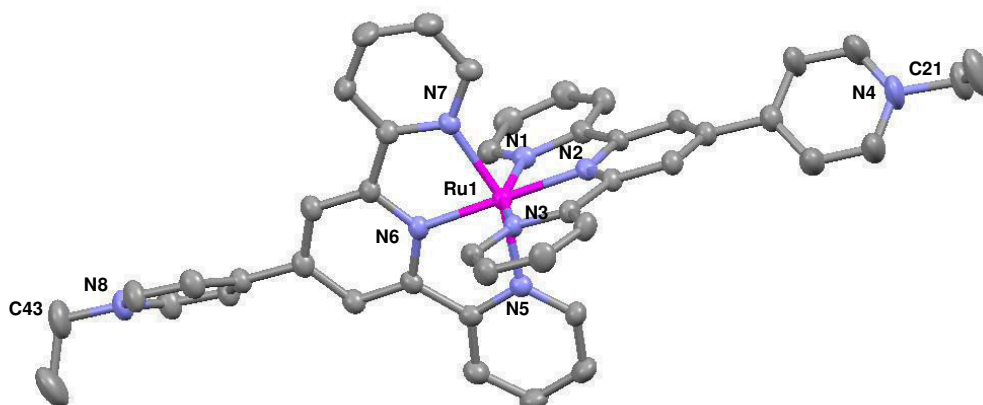


Fig. 2.15 Structure of the  $[Ru(4)_2]^{4+}$  cation with ellipsoids plotted at 50% probability and hydrogens omitted for clarity. Ethyl groups shown in the major occupancy position. Selected bond parameters:  $Ru1-N1 = 2.076(4)$ ,  $Ru1-N2 = 1.981(3)$ ,  $Ru1-N3 = 2.088(4)$ ,  $Ru1-N5 = 2.082(3)$ ,  $Ru1-N6 = 1.976(3)$ ,  $Ru1-N7 = 2.075(3)$ ,  $N4-N21 = 1.49(2)$ ,  $N8-C43 = 1.486(7)$  Å;  $N2-Ru1-N1 = 79.4(1)$ ,  $N2-Ru1-N3 = 78.4(1)$ ,  $N5-Ru1-N6 = 78.7(1)$ ,  $N6-Ru1-N7 = 78.9(1)^\circ$ .

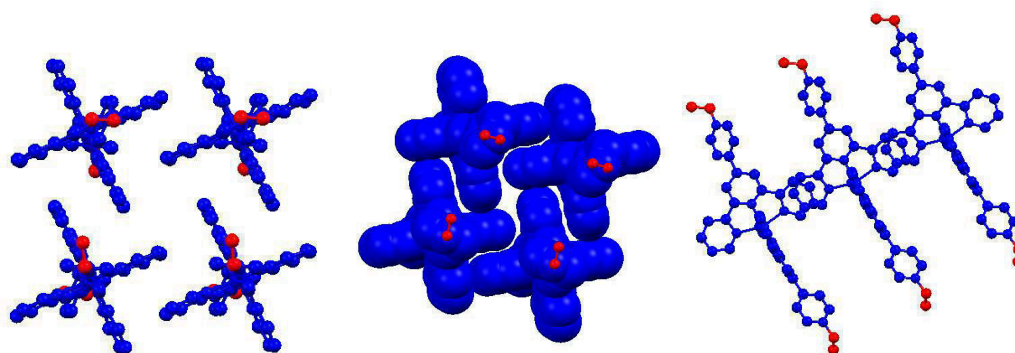
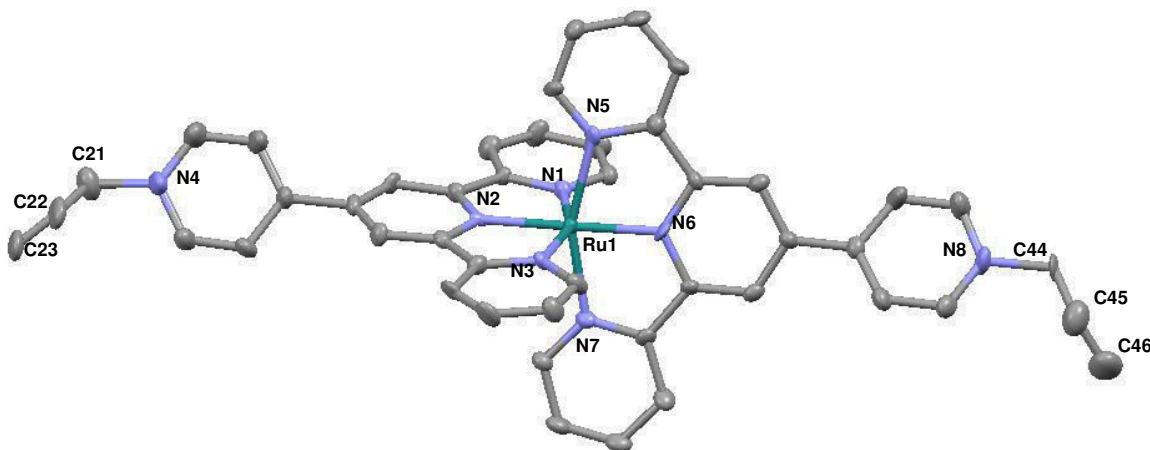


Fig. 2.16 (left and centre) Packing of the cations. (right) Intermeshing of the ethyl groups.  $\{Ru(pytpy)_2\}$ -core in blue, pendant ethyl substituents in red.

The cations pack with typical tpy-tpy Dance embraces<sup>28-32</sup>. There are face-to-face and edge-to-face interactions between the terpyridine moieties, uninterrupted by the ethyl substituents. The ethyl groups are directed above and below the plane and are all oriented in the same direction. There are also extensive CH...F packing interactions throughout the lattice (e.g. H24-F31 2.64 Å).

Small red blocks of  $[\text{Ru}(\mathbf{6})_2][\text{PF}_6]_4$  were grown by slow evaporation of an acetonitrile solution of the complex. The structure solves in the Cc space group with a good R factor of 4.7 %. The asymmetric unit contains one  $[\text{Ru}(\mathbf{6})]^{4+}$  cation, four  $\text{PF}_6^-$  anions, one of which is disordered, two molecules of acetonitrile and one water molecule. The structure of the  $[\text{Ru}(\mathbf{6})_2]^{4+}$  cation is depicted below and selected bond lengths and angles are listed in the caption.



*Fig. 2.17 Structure of the  $[\text{Ru}(\mathbf{6})_2]^{4+}$  cation with ellipsoids plotted at 50% probability and hydrogens omitted for clarity. Allyl groups shown in the major occupancy positions. Selected bond parameters:  $\text{Ru1-N1} = 2.058(2)$ ,  $\text{Ru1-N2} = 1.981(2)$ ,  $\text{Ru1-N3} = 2.067(2)$ ,  $\text{Ru1-N5} = 2.096(2)$ ,  $\text{Ru1-N6} = 1.981(3)$ ,  $\text{Ru1-N7} = 2.097(3)$ ,  $\text{N4-C21} = 1.57(1)$ ,  $\text{C21-C22} = 1.50(2)$ ,  $\text{C22-C23} = 1.13(2)$ ,  $\text{N8-C44} = 1.536(6)$ ,  $\text{C44-C45} = 1.471(7)$ ,  $\text{C45-C46} = 1.28(1)$  Å ;  $\text{N1-Ru1-N2} = 78.56(9)$ ,  $\text{N2-Ru1-N3} = 78.93(9)$ ,  $\text{N5-Ru1-N6} = 78.5(1)$ ,  $\text{N6-Ru1-N7} = 78.9(1)^\circ$ .*

The two ligands are coordinated orthogonally to the central ruthenium atom and the angle between the two terpyridine planes is  $79.0^\circ$ . The ligand is disordered, and the fractional occupancies of the C21-C22-C23 allyl chain are 0.289 (4) and 0.711(4). The occupancies of the C44-C45-C46 chain are 0.80 and 0.20. The structure confirms successful alkylation at the pendant pyridyl moieties and the N4-C21 and C21-C22 bond lengths indicate single bonds. The C22-C23 and C45-C46 bond lengths are shorter, 1.13(2) Å and 1.28(1) respectively, which are consistent with double bonds between the two carbon atoms. The ruthenium – nitrogen bond lengths are typical of  $\{\text{Ru}(\text{tpy})_2\}$ - based complexes.

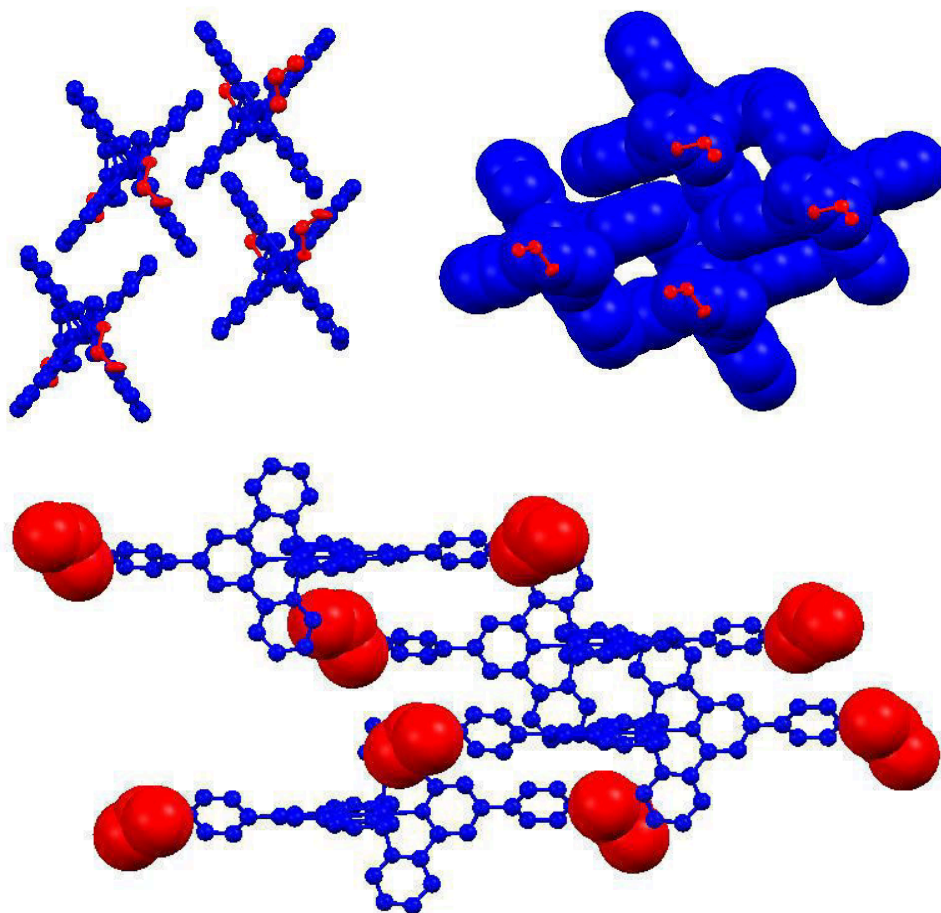


*Fig. 2.18 Packing of the cations with the  $\{Ru(pytpy)_2\}$ - core in blue and the pendant allyl groups in red*

As previously discussed, these types of complexes are expected to pack with tpy-tpy embraces<sup>28-32</sup>. This  $[Ru(\mathbf{6})_2][PF_6]_4$  complex is an exception, similar to  $[Ru(\mathbf{1})_2][PF_6]_4$ , because the allyl substituents occupy the spaces between the tpy units, forcing them apart, thereby distorting the usual tpy-tpy embrace. As such, there are no interactions between the terpyridine moieties. There are, however, short contacts between the acetonitrile molecule and the pendant pyridyl group (e.g. H43A – N200, 2.543Å) and between various hydrogen atoms and fluorine atoms of the hexafluorophosphate anions (e.g. H1A-F23, 2.386Å).

Red needles of  $[Ru(\mathbf{7})_2][PF_6]_4 \cdot H_2O \cdot MeCN$  were grown by very slow evaporation of a deuterated acetonitrile solution of the complex. The crystal structure solves in the P -1 space group, with a poor R factor of 13.1% due to the poor quality of the crystals.

The asymmetric unit contains one cation, two ordered  $\text{PF}_6^-$  anions, two disordered  $\text{PF}_6^-$  counter-anions, one acetonitrile molecule and one water molecule.

The unit cell has similar dimensions to that of  $[\text{Ru}(\mathbf{1})_2][\text{PF}_6]_4$ . It is shorter in a, 8.7018 (7) Å, compared to 13.488 (3) Å, and b, 12.5549 (10) Å compared to 16.934 (3) Å and slightly longer in c, 30.067 (3) Å compared to 27.758 (6) Å. The decrease in the length of the a and b axes is due to the asymmetric unit containing one cation for  $[\text{Ru}(\mathbf{7})_2][\text{PF}_6]_4 \cdot \text{H}_2\text{O} \cdot \text{MeCN}$  compared to two for  $[\text{Ru}(\mathbf{1})_2][\text{PF}_6]_4 \cdot \text{H}_2\text{O}$ . The structure of the  $[\text{Ru}(\mathbf{7})_2]^{4+}$  cation is depicted in Fig. 2.19 and selected bond lengths and angles are listed in the caption. One of the terminal pyridyl moieties is disordered and modelled over two positions, with fractional occupancies of 0.43 and 0.57, only the major occupancies shown in Fig. 2.19.

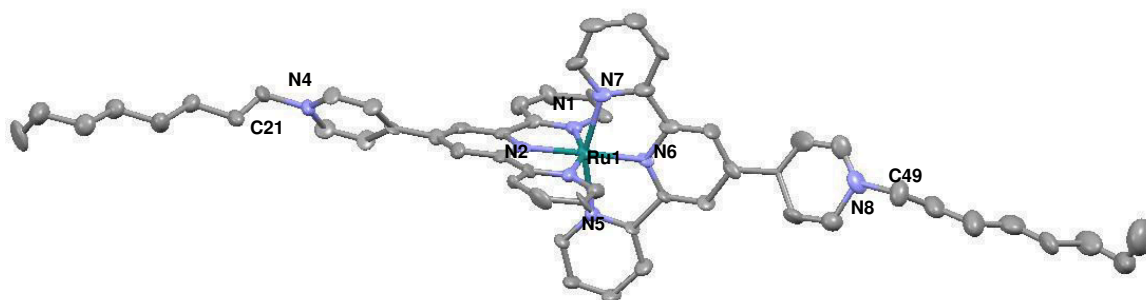
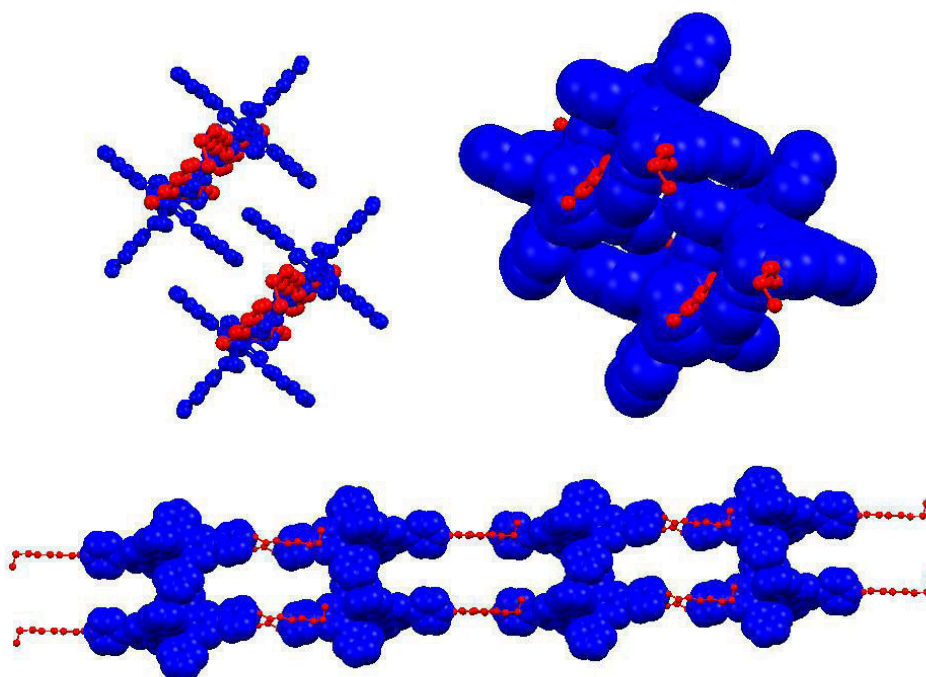


Fig. 2.19. Structure of the  $[\text{Ru}(\mathbf{7})_2]^{4+}$  cation with ellipsoids plotted at 50% probability and hydrogens omitted for clarity. Selected bond parameters:  $\text{Ru1-N1} = 2.085$  (7),  $\text{Ru1-N2} = 1.975$  (7),  $\text{Ru1-N3} = 2.062$  (7),  $\text{Ru1-N5} = 2.069$  (7),  $\text{Ru1-N6} = 1.960$  (6),  $\text{Ru1-N7} = 2.078$  (7)  $\text{N4-C21} = 1.50$  (1),  $\text{N8-C49} = 1.46$  (3) Å;  $\text{N2-Ru1-N1} = 78.5$  (3),  $\text{N2-Ru1-N3} = 78.7$  (3),  $\text{N5-Ru1-N6} = 77.5$  (3),  $\text{N6-Ru1-N7} = 79.4$  (3)°.

The bond lengths and angles of the cation are unexceptional and the two ligands coordinate to the central ruthenium atom in the expected, orthogonal, manner. The angle between the two terpyridine planes is 89.6°. The C-C bond lengths of the octyl chain are all typical of single bonds and are in the range of 1.47(1) to 1.57(1) Å, with an average C-C bond length of 1.52 Å. The bowing of the cation away from linearity ( $\text{N4-Ru1-N8} = 170.5^\circ$ ) is of a similar magnitude to that observed for  $[\text{Ru}(\mathbf{4})_2][\text{PF}_6]_4$ .





*Fig. 2.20 Packing of the cations with the  $\{Ru(pytpy)_2\}$ - core in blue and the pendant octyl groups in red*

Van der Waals interactions are dominant causing the octyl chains to align themselves, which greatly influences the packing of the complex. As such, neither face-to-edge and edge-to-edge interactions, nor  $\pi$ -stacking between the terpyridine units are observed. There are extensive CH...F interactions throughout the crystal lattice (e.g. H32 -F45 2.63Å) and interactions between the acetonitrile molecule and the octyl chain (e.g. H50-N100 2.73Å).

## 2.4 DFT and TD-DFT Calculations

The findings of the experimental data were that the photophysical and electrochemical properties of the complexes did not change, regardless of the nature of the substituent. To investigate the reason for the lack of effect of the substituent DFT and TD-DFT calculations were carried out on the set of complexes. The LANL2DZ basis set was used to describe the Ru and the 6-31G\* basis set was used to describe the other (non-metal) atoms. The solvent was added into the calculations using the standard Gaussian 09 polarizable continuum model (PCM), specifying acetonitrile as the solvent and

predicted TD-DFT transitions were calculated using the *ab initio*, B3LYP method. (see experimental section for more details.)

To validate the calculations a comparison between the calculated bond lengths and the bond lengths determined by crystallography was done for three of the cations. These were  $[\text{Ru}(\mathbf{1})_2]^{4+}$ ,  $[\text{Ru}(\mathbf{3})_2]^{4+}$  and  $[\text{Ru}(\mathbf{4})_2]^{4+}$  although less can be learnt by comparing the data for  $[\text{Ru}(\mathbf{3})_2]^{4+}$  as the crystallographic R factor was so poor. The comparison is tabulated in Table 2.9 and the values of *x* and *y* are given in the table description. (*x* and *y* refer to the numbers of the terminal pendant pyridyl nitrogens as defined in the crystallography section of this chapter. §Section 2.3.7.)

Parameter	$L^+ = \mathbf{1}$ (DFT)	$L^+ = \mathbf{1}$ (exp)	$L^+ = \mathbf{3}$ (DFT)	$L^+ = \mathbf{3}$ (exp)	$L^+ = \mathbf{4}$ (DFT)	$L^+ = \mathbf{4}$ (exp)
Ru1-N1	2.129	2.099(7)	2.127	2.099(7)	2.128	2.076(3)
Ru1-N2	2.017	1.986(8)	2.015	1.986(8)	2.015	1.981(3)
Ru1-N3	2.127	2.095(7)	2.128	2.095(7)	2.128	2.088(3)
Ru1-N5	2.127	2.0082(7)	2.126	2.0082(7)	2.128	2.082(4)
Ru1-N6	2.016	1.995(5)	2.015	1.995(5)	2.015	1.976(3)
Ru1-N7	2.129	2.088(7)	2.128	2.088(7)	2.128	2.075(4)
N4-C21	1.518	1.50(2)	1.497	1.501(7)	1.494	1.487(19)
N <sub>x</sub> -C <sub>y</sub>	1.518	1.46(2)	1.500	1.501(7)	1.494	1.486(6)
N2-Ru1-N1	78.27	79.5(4)	78.31	77.8(2)	78.33	79.37(14)
N2-Ru1-N3	78.24	78.9(4)	78.30	79.3(2)	78.30	78.44(14)
N5-Ru1-N6	78.30	79.4(4)	78.34	78.8(2)	78.33	78.70(14)
N6-Ru1-N7	78.27	78.5(4)	78.24	78.1(2)	78.30	78.95(14)

Table 2.9 Comparison between calculated and X-ray crystal structure determined bond lengths and angles for complexes  $[\text{Ru}(\mathbf{L})_2]^{4+}$  where  $L^+ = \mathbf{1}$  ( $x=8$ ,  $y=48$ ),  $\mathbf{3}$  ( $x=47$ ,  $y=50$ ),  $\mathbf{4}$  ( $x=8$ ,  $y=43$ ). Atom numbering corresponds to figs 2.9, 2.13 and 2.16.

The agreement between the calculated and experimental structures is good. The calculated bond lengths are generally slightly over-estimated by  $<0.1\text{\AA}$  and the calculated bond angles agree with the crystal structure data to within  $1.1^\circ$ . The calculations predict that the substituent at the terminal pyridyl moiety will have a small effect on the C-N bond length but this is not reproduced experimentally. As the

agreement between the calculated and experimental data is good the level of calculation chosen is correct. The energy and structure of the complexes were then minimised again in the presence of the solvent and pictures of the highest lying occupied and lowest lying unoccupied molecular orbitals were generated using the program Molekel<sup>35</sup>.

The lowest lying unoccupied molecular orbitals are purely ligand based and the highest lying occupied molecular orbitals are metal based. The localisation of the molecular orbitals on each complex explained the lack of difference in the photophysical and electrochemical properties in the series. The HOMO and (HOMO-1) are predominantly metal based and do not change from complex to complex and, therefore, cannot effect a change between the properties of the complexes. Furthermore, the LUMO and (LUMO+1) do not extend beyond the terminal pyridyl moiety, due to the break in conjugation caused by the  $-CH_2-$  group. As neither the metal orbitals nor the ligand orbitals change with substituent the MLCT would not be expected to change either. Molecular orbitals of representative complexes are depicted in Figs. 2.21 and 2.22.

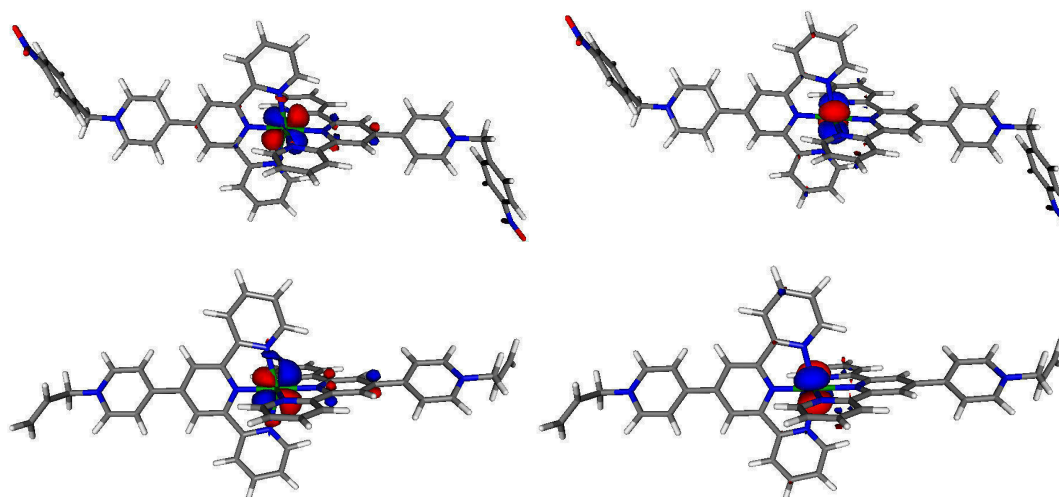
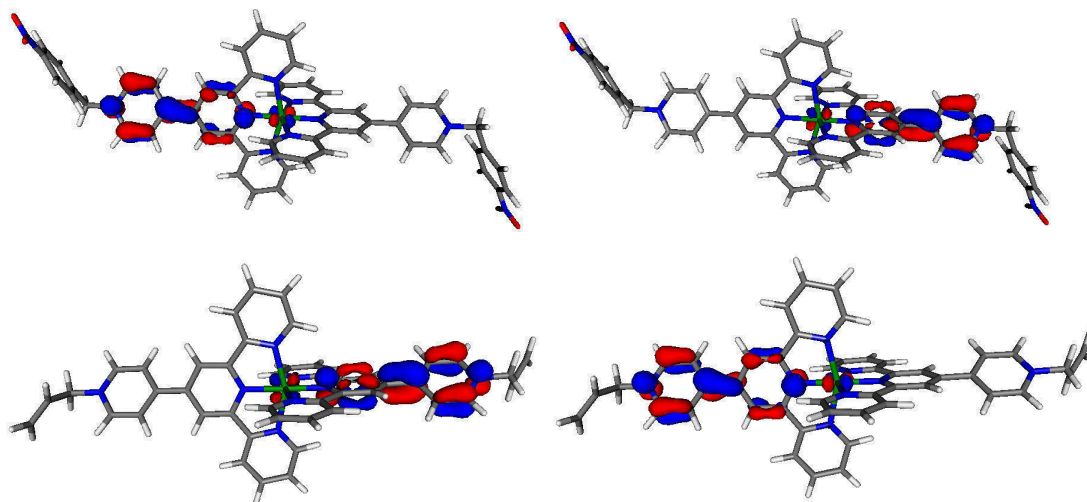


Fig. 2.21 Top left,  $[Ru(3)_2]^{4+}$  (HOMO-1), top right,  $[Ru(3)_2]^{4+}$  HOMO  
Bottom left  $[Ru(6)_2]^{4+}$  (HOMO-1), bottom right,  $[Ru(6)_2]^{4+}$  HOMO



*Fig. 2.22. Top left,  $[Ru(3)_2]^{4+}$  LUMO, top right,  $[Ru(3)_2]^{4+}$  (LUMO+1)  
Bottom left  $[Ru(6)_2]^{4+}$  LUMO, bottom right,  $[Ru(6)_2]^{4+}$  (LUMO+1)*

As can be observed in Fig 2.22 the LUMO and (LUMO+1) are related in their orbital character. They are very close in energy but are not degenerate, which is known as being ‘accidentally degenerate’. This is true for all of the complexes in this study.

TD-DFT was also used to further investigate the set of complexes. The predicted absorption spectra are depicted in Fig. 2.23

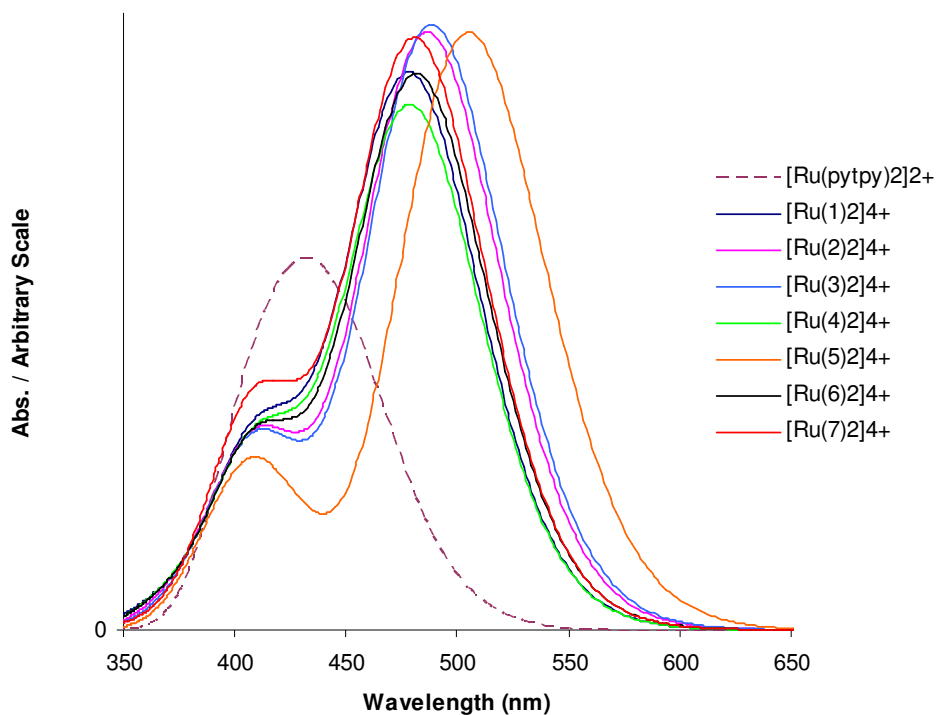


Fig. 2.23 The predicted absorption spectra for  $[\text{Ru}(\text{pytpy})_2][\text{PF}_6]_2$  and  $[\text{Ru}(\text{L})_2][\text{PF}_6]_4$  ( $L^+ = 1-7$ ).

The calculated spectra accurately reproduce the red shift upon alkylation of the parent  $[\text{Ru}(\text{pytpy})_2]^{2+}$  complex. The calculations predict one major peak around 500 nm (depending on substituent) and a shoulder at ~450 nm. The predicted shoulder at ~450 nm explains the non-gaussian shaped MLCT peak observed experimentally. The calculations do not reproduce  $\lambda_{\text{max}}$  exactly but the difference between the experimental and calculated values is a maximum of 44 nm. This is acceptable considering previously published calculations on ruthenium polypyridyl complexes where the predicted experimental and calculated UV-vis spectra differ by up to 100 nm<sup>15-17, 22</sup>. The agreement between the spectra is depicted more clearly in Fig. 2.24, which contains the calculated and experimental UV-vis spectra of  $[\text{Ru}(\mathbf{4})_2]^{4+}$ .

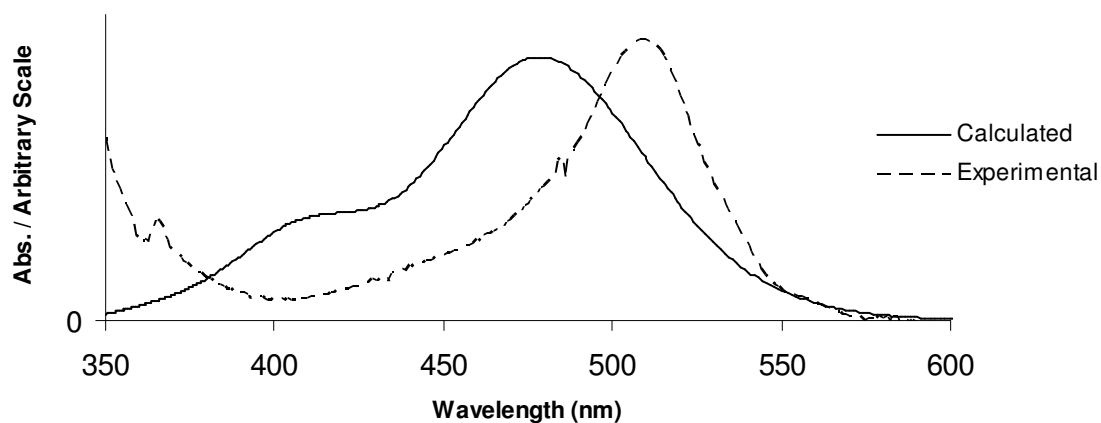


Fig. 2.24 Comparison of calculated and experimental MLCT band of complex  $[Ru(\mathbf{4})_2]^{4+}$

The transitions which contribute to the MLCT band, for all complexes, are summarised (Table 2.10).

Complex	$\lambda_{\text{max}} / \text{nm}$	Orbital Contributions
[Ru(1) <sub>2</sub> ] <sup>4+</sup>	478.4	48% (LUMO+1)←(HOMO-1) 47% LUMO←(HOMO-2)
[Ru(2) <sub>2</sub> ] <sup>4+</sup>	486.3	38% LUMO←(HOMO-2) 34% (LUMO+1)←(HOMO-1) 13% LUMO←(HOMO-1) 10% (LUMO+1)←(HOMO-2)
[Ru(3) <sub>2</sub> ] <sup>4+</sup>	488.3	38% LUMO←(HOMO-2) 34% (LUMO+1)←(HOMO-1) 13% LUMO←(HOMO-1) 10% (LUMO+1)←(HOMO-2)
[Ru(4) <sub>2</sub> ] <sup>4+</sup>	478.8	48% (LUMO+1)←(HOMO-1) 47% LUMO←(HOMO-2)
[Ru(5) <sub>2</sub> ] <sup>4+</sup>	504.6	46% LUMO←(HOMO-2) 45% (LUMO+1)←(HOMO-1)
[Ru(6) <sub>2</sub> ] <sup>4+</sup>	481.6	36% LUMO←(HOMO-1) 31% (LUMO+1)←(HOMO-2) 14% LUMO←(HOMO-2) 13% (LUMO+1)←(HOMO-1)
[Ru(7) <sub>2</sub> ] <sup>4+</sup>	480.9	53% LUMO←(HOMO-1) 38% (LUMO+1)←(HOMO-2)

Table 2.10 A summary of the transitions making up the MLCT band for all complexes.

## 2.5 Conclusion

Functionalisation of the previously known [Ru(pytpy)<sub>2</sub>][PF<sub>6</sub>]<sub>2</sub> complex with a variety of *n*-alkyl and *n*-aryl substituents resulted in complexes with red-shifted MLCT and emission bands and higher oxidation potentials, when compared to the parent complex. The type of substituent had a negligible effect on the photophysical and electrochemical properties of the molecule and this was explored using DFT. The DFT lead to the conclusion that the -CH<sub>2</sub>- bridge between the pendant pyridyl ring and the substituent broke the  $\pi$ -conjugation system. These complexes could have application as water oxidation catalysts, which is discussed in the next chapter.

## 2.6 Experimental

General Synthesis of  $[\text{Ru}(\text{L})_2][\text{PF}_6]_4$ :

$[\text{Ru}(\text{pytpy})_2][\text{PF}_6]_2$  and the appropriate alkylating reagent (120 eq.) were dissolved in acetonitrile ( $50 \text{ cm}^3$ ) and refluxed at  $90 \text{ }^\circ\text{C}$  for between 3 and 72 hours. The reaction was monitored by spot TLC. The volume of solvent was then reduced to c.a.  $5 \text{ cm}^3$  and the complex was purified using column chromatography ( $\text{SiO}_2$ , see text for eluent). Acetonitrile was removed under reduced pressure.  $[\text{NH}_4][\text{PF}_6]$  was added to precipitate  $[\text{Ru}(\text{L})_2][\text{PF}_6]_4$ . The salt was collected on celite, washed with copious amounts of water, EtOH and  $\text{Et}_2\text{O}$ . It was then redissolved in MeCN, dried *in vacuo* and the product was isolated as a red powder.

The eluents are defined as follows:

A Sol = 7:1:0.5 MeCN:  $\text{H}_2\text{O}$ : sat.  $\text{KNO}_3$

B Sol = 7:2:2 MeCN:  $\text{H}_2\text{O}$ : sat.  $\text{KNO}_3$

C Sol = 10:0.5:1.5 MeCN:  $\text{H}_2\text{O}$ : sat.  $\text{KNO}_3$

### $[\text{Ru}(\mathbf{1})_2][\text{PF}_6]_4$

Reaction time: 12 hours

Column Eluent: B Sol ( $R_f = 0.33$ )

Yield: 153.3 mg, 69.7 % (starting with mg  $[\text{Ru}(\text{pytpy})_2][\text{PF}_6]_2$ )

$^1\text{H}$  NMR: (500 MHz,  $\text{CD}_3\text{CN}$ ,  $25^\circ\text{C}$ , TMS)  $\delta/\text{ppm}$ : 9.12 (4H, s,  $\mathbf{B}^3$ ), 9.08 (4H, d,  $J = 6.5 \text{ Hz}$ ,  $\mathbf{C}^2$ ), 8.75 (4H, d,  $J = 6.6 \text{ Hz}$ ,  $\mathbf{C}^3$ ), 8.68 (4H, d,  $J = 8.1 \text{ Hz}$ ,  $\mathbf{A}^3$ ), 8.00 (4H, t,  $J = 7.9 \text{ Hz}$ ,  $\mathbf{A}^4$ ) 7.59 (10H, m,  $\mathbf{D}$ ), 7.42 (4H, d,  $J = 5.4 \text{ Hz}$ ,  $\mathbf{A}^6$ ), 7.23 (4H, t,  $J = 7.5 \text{ Hz}$ ,  $\mathbf{A}^5$ ), 5.89 (4H, s,  $a$ );

$^{13}\text{C}$  NMR: (126 MHz,  $\text{CD}_3\text{CN}$ ,  $25^\circ\text{C}$ , TMS)  $\delta/\text{ppm}$ : 158.24 ( $\mathbf{A}^2$ ), 156.82 ( $\mathbf{B}^2$ ), 154.00 ( $\mathbf{C}^4$ ), 153.55 ( $\mathbf{A}^6$ ), 146.28 ( $\mathbf{C}^2$ ), 139.49 ( $\mathbf{A}^4$ ), 133.77 ( $\mathbf{D}$ ), 130.58 ( $\mathbf{D}$ ), 130.29 ( $\mathbf{D}^1$ ), 128.91 ( $\mathbf{A}^5$ ), 127.63 ( $\mathbf{C}^3$ ), 125.95 ( $\mathbf{A}^3$ ), 123.25 ( $\mathbf{B}^3$ ), 65.27 ( $a$ );

Found: C, 42.29; H, 3.00; N, 7.45;  $\text{C}_{54}\text{H}_{42}\text{F}_{24}\text{N}_8\text{P}_4\text{Ru}\cdot 3\text{H}_2\text{O}$

requires C, 42.17; H, 3.15; N, 7.29;

MALDI-TOF (MeCN):  $m/z$  1340.5  $[\text{M}-\text{PF}_6]^+$  (calc. 1339.2), 1196.3  $[\text{M}-2\text{PF}_6]^+$  (calc. 1194.2), 1050.3  $[\text{M}-3\text{PF}_6]^+$  (calc. 1049.2)



### [Ru(2)<sub>2</sub>][PF<sub>6</sub>]<sub>4</sub>

Reaction time: 12 hours

Column Eluent: B Sol, (R<sub>f</sub> = 0.30)

Yield: 215.5 mg, 78.9 % (starting with 180 mg [Ru(pytpy)<sub>2</sub>][PF<sub>6</sub>]<sub>2</sub>)

<sup>1</sup>H NMR: (500 MHz, d<sub>6</sub>-DMSO, 25°C, TMS) δ/ppm: 9.77 (4H, s, **B**<sup>3</sup>),  
9.65 (4H, br d, J = 6.3 Hz, **C**<sup>2</sup>), 9.20 (4H, br d, J = 6.3 Hz, **C**<sup>3</sup>),  
9.10 (4H, d, J = 8.1 Hz, **A**<sup>3</sup>), 8.17 (4H, t, J = 7.6 Hz, **A**<sup>4</sup>), 8.05 (4H, d, J = 8.2 Hz, **D**<sup>3</sup>),  
7.82 (4H, d, J = 8.2 Hz, **D**<sup>2</sup>), 7.59 (4H, d, J = 5.3 Hz, **A**<sup>6</sup>), 7.34 (4H, m, **A**<sup>5</sup>),  
6.13 (4H, s, *a*);

<sup>13</sup>C NMR: (126 MHz, d<sub>6</sub>-DMSO, 25°C, TMS) δ/ppm: 157.4 (**A**<sup>2</sup>/**B**<sup>2</sup>), 155.4 (**A**<sup>2</sup>/**B**<sup>2</sup>),  
152.5 (**A**<sup>6</sup>), 151.8 (**C**<sup>4</sup>), 146.1 (**C**<sup>2</sup>), 139.9 (**B**<sup>4</sup>), 139.6 (**D**<sup>1</sup>), 138.6 (**A**<sup>4</sup>), 133.2 (**D**<sup>3</sup>),  
129.5 (**D**<sup>2</sup>), 128.1 (**A**<sup>5</sup>), 126.0 (**C**<sup>3</sup>), 125.2 (**A**<sup>3</sup>), 122.3 (**B**<sup>3</sup>), 118.4 (**D**<sup>4</sup>),  
112.2 (**D**-C≡N), 62.54 (*a*);

Found: C, 41.64; H, 2.86; N, 8.86; C<sub>56</sub>H<sub>40</sub>F<sub>24</sub>N<sub>10</sub>P<sub>4</sub>Ru.4H<sub>2</sub>O

requires C, 41.88; H, 3.01; N, 8.72;

MALDI-TOF (MeCN): *m/z* 1245.0 [M-2PF<sub>6</sub>]<sup>+</sup> (calc. 1244.2), 1100.0 [M-3PF<sub>6</sub>]<sup>+</sup>  
(calc. 1099.2)

### [Ru(3)<sub>2</sub>][PF<sub>6</sub>]<sub>4</sub>

Reaction time: 12 hours

Column Eluent: A Sol, (R<sub>f</sub> = 0.29)

Yield: 67.2 mg, 41.6 % (starting with 100 mg [Ru(pytpy)<sub>2</sub>][PF<sub>6</sub>]<sub>2</sub>)

<sup>1</sup>H NMR: (500 MHz, d<sub>6</sub>-DMSO, 25°C, TMS) δ/ppm: 9.77 (4H, s, **B**<sup>3</sup>),  
9.66 (4H, d, J = 6.5 Hz, **C**<sup>2</sup>), 9.21 (4H, d, J = 6.6 Hz, **C**<sup>3</sup>),  
9.09 (4H, d, J = 8.1 Hz, **A**<sup>3</sup>), 8.41 (4H, d, J = 8.7 Hz, **D**<sup>2</sup>), 8.17 (4H, t, J = 7.7 Hz, **A**<sup>4</sup>),  
7.90 (4H, d, J = 8.7 Hz, **D**<sup>2</sup>), 7.59 (4H, d, J = 5.5 Hz, **A**<sup>6</sup>), 7.34 (4H, m, **A**<sup>5</sup>),  
6.18 (4H, s, *a*);

<sup>13</sup>C NMR: (126 MHz, d<sub>6</sub>-DMSO, 25°C, TMS) δ/ppm: 157.6 (**A**<sup>2</sup>/**B**<sup>2</sup>), 155.6 (**A**<sup>2</sup>/**B**<sup>2</sup>),  
152.3 (**A**<sup>6</sup>), 152.0 (**C**<sup>4</sup>), 145.1 (**C**<sup>2</sup>), 141.6 (**D**<sup>1</sup>), 141.3 (**D**<sup>4</sup>), 129.8 (**D**<sup>2</sup>), 128.0 (**A**<sup>5</sup>),  
125.8 (**C**<sup>3</sup>), 125.0 (**A**<sup>3</sup>), 124.2 (**D**<sup>3</sup>), 122.1 (**B**<sup>3</sup>), 62.0 (*a*);

Found: C, 39.62; H, 3.06; N, 8.65; C<sub>54</sub>H<sub>40</sub>F<sub>24</sub>N<sub>10</sub>P<sub>4</sub>Ru.3H<sub>2</sub>O

requires C, 39.84; H, 2.85; N, 8.60.

MALDI-TOF (MeCN): *m/z* 1431.7 [M-PF<sub>6</sub>]<sup>+</sup> (calc. 1429.1), 1285.6 [M-2PF<sub>6</sub>]<sup>+</sup> (calc. 1284.2), 1150.4 [Ru(3)(Hpytpy)(PF<sub>6</sub>)<sub>2</sub>]<sup>+</sup> (calc. 1149.1), 1005.3 [Ru(3)(Hpytpy)(PF<sub>6</sub>)]<sup>+</sup> (calc. 1004.2), 995.5 [M-4PF<sub>6</sub>]<sup>+</sup> (calc. 994.2), 723.2 [Ru(pytpy)(Hpytpy)]<sup>+</sup> (calc. 723.3).

### [Ru(4)<sub>2</sub>][PF<sub>6</sub>]<sub>4</sub>

Reaction time: 72 hours

Column Eluent: B Sol, (R<sub>f</sub> = 0.30)

Yield: 80.6 mg, 64.3 % (starting with 80 mg [Ru(pytpy)<sub>2</sub>][PF<sub>6</sub>]<sub>2</sub>)

<sup>1</sup>H NMR: (500 MHz, d<sub>6</sub>-DMSO, 25°C, TMS) δ/ppm: 9.78 (4H, s, B<sup>3</sup>), 9.52 (4H, d, J = 6.6 Hz, C<sup>2</sup>), 9.17 (4H, d, J = 6.6 Hz, C<sup>3</sup>), 9.12 (4H, d, J = 8.1 Hz, A<sup>3</sup>), 8.17 (4H, t, J = 7.7 Hz, A<sup>4</sup>), 7.58 (4H, d, J = 5.4 Hz, A<sup>6</sup>), 7.33 (4H, t, J = 6.5 Hz, A<sup>5</sup>), 4.80 (4H, m, a), 1.73 (6H, t, J = 7.3 Hz, b);

<sup>13</sup>C NMR: (126 MHz, d<sub>6</sub>-DMSO, 25°C, TMS) δ/ppm: 157.6 (A<sup>2</sup>/B<sup>2</sup>), 155.6 (A<sup>2</sup>/B<sup>2</sup>), 152.6 (A<sup>6</sup>), 150.8 (C<sup>4</sup>), 145.4 (C<sup>2</sup>), 140.0 (B<sup>4</sup>), 138.5 (A<sup>4</sup>), 128.0 (A<sup>5</sup>), 125.2 (C<sup>3</sup>), 125.1 (A<sup>3</sup>), 122.0 (B<sup>3</sup>), 56.2 (a), 16.0 (b);

Found C, 36.96; H, 2.75; N, 8.07; C<sub>44</sub>H<sub>38</sub>F<sub>24</sub>N<sub>8</sub>P<sub>4</sub>Ru.3H<sub>2</sub>O

requires C, 37.38; H, 3.14; N, 7.93;

MALDI-TOF (MeCN): *m/z* 1216.8 [M-PF<sub>6</sub>]<sup>+</sup> (calc. 1215.1), 1071.6 [M-2PF<sub>6</sub>]<sup>+</sup> (calc. 1070.2), 926.8 [M-3PF<sub>6</sub>]<sup>+</sup> (calc. 925.2), 782.1 [M-4PF<sub>6</sub>]<sup>+</sup> (calc. 780.2)

### [Ru(5)<sub>2</sub>][PF<sub>6</sub>]<sub>4</sub>

Reaction time: 12 hours

Column Eluent: B Sol, (R<sub>f</sub> = 0.54)

Yield: 67.3 mg, 61.6 % (starting with 100 mg [Ru(pytpy)<sub>2</sub>][PF<sub>6</sub>]<sub>2</sub>)

$^1\text{H}$  NMR: (500 MHz,  $d_6$ -DMSO, 25°C, TMS)  $\delta$ /ppm: 9.80 (4H, s,  $\mathbf{B}^3$ ), 9.61 (4H, d,  $J = 6.5$  Hz,  $\mathbf{C}^2$ ), 9.25 (4H, d,  $J = 6.5$  Hz,  $\mathbf{C}^3$ ), 9.12 (4H, d,  $J = 8.1$  Hz,  $\mathbf{A}^3$ ), 8.17 (4H, t,  $J = 7.7$  Hz,  $\mathbf{A}^4$ ), 7.58 (4H, d,  $J = 5.4$  Hz,  $\mathbf{A}^6$ ), 7.33 (4H, t,  $J = 6.5$  Hz,  $\mathbf{A}^5$ ), 6.08 (4H, s,  $a$ );

$^{13}\text{C}$  NMR: (126 MHz,  $d_6$ -DMSO, 25°C, TMS)  $\delta$ /ppm: 157.4 ( $\mathbf{A}^2/\mathbf{B}^2$ ), 155.5 ( $\mathbf{A}^2/\mathbf{B}^2$ ), 152.5 ( $\mathbf{A}^6+\mathbf{C}^4$ ), 146.4 ( $\mathbf{C}^2$ ), 139.5 ( $\mathbf{B}^4$ ), 138.6 ( $\mathbf{A}^4$ ), 128.1 ( $\mathbf{A}^5$ ), 125.4 ( $\mathbf{C}^3$ ), 125.2 ( $\mathbf{A}^3$ ), 122.2 ( $\mathbf{B}^3$ ), 114.3 ( $\text{C}\equiv\text{N}$ ), 47.6 ( $a$ );

Found: C, 36.35; H, 2.55; N, 9.84,  $\text{C}_{44}\text{H}_{32}\text{F}_{24}\text{N}_{10}\text{P}_4\text{Ru}\cdot 4\text{H}_2\text{O}$

requires C, 36.35; H, 2.77; N, 9.63;

MALDI-TOF (MeCN):  $m/z$  1092.4 [ $\text{M}-2\text{PF}_6$ ] $^+$  (calc. 1092.1), 947.4 [ $\text{M}-3\text{PF}_6$ ] $^+$  (calc. 947.2), 908.6 [ $\text{Ru}(\mathbf{5})(\text{Hpytpy})(\text{PF}_6)$ ] $^+$  (calc. 908.1), 869.3 [ $\text{Ru}(\text{Hpytpy})_2(\text{PF}_6)$ ] $^+$  (calc. 869.1)

### [Ru(6)<sub>2</sub>][PF<sub>6</sub>]<sub>4</sub>

Reaction time: 4 hours

Column Eluent: B Sol, ( $R_f = 0.20$ )

Yield: 100.4 mg, 73.2 % (starting with 100 mg [ $\text{Ru}(\text{pytpy})_2$ ][PF<sub>6</sub>]<sub>2</sub>)

$^1\text{H}$  NMR: (500 MHz,  $d_6$ -DMSO, 25°C, TMS)  $\delta$ /ppm: 9.79 (4H, s,  $\mathbf{B}^3$ ), 9.48 (4H, d,  $J = 6.7$  Hz,  $\mathbf{C}^2$ ), 9.19 (4H, d,  $J = 6.7$  Hz,  $\mathbf{C}^3$ ), 9.12 (4H, d,  $J = 8.2$  Hz,  $\mathbf{A}^3$ ), 8.17 (4H, t,  $J = 7.8$  Hz,  $\mathbf{A}^4$ ), 7.58 (4H, d,  $J = 5.5$  Hz,  $\mathbf{A}^6$ ), 7.33 (4H, t,  $J = 6.8$  Hz,  $\mathbf{A}^5$ ), 6.35 (2H, ddt,  $b$ ), 5.59 (2H, d,  $J = 10.2$  Hz,  $c_1$ ), 5.51 (2H, d,  $J = 17.2$  Hz,  $c_2$ ), 5.43 (4H, d,  $J = 5.9$  Hz,  $a$ );

$^{13}\text{C}$  NMR: (126 MHz,  $d_6$ -DMSO, 25°C, TMS)  $\delta$ /ppm: 157.4 ( $\mathbf{A}^2/\mathbf{B}^2$ ), 155.6 ( $\mathbf{A}^2/\mathbf{B}^2$ ), 152.5 ( $\mathbf{A}^6$ ), 151.3 ( $\mathbf{C}^4$ ), 145.7 ( $\mathbf{C}^2$ ), 139.9 ( $\mathbf{B}^4$ ), 138.5 ( $\mathbf{A}^4$ ), 131.5 ( $b$ ), 128.0 ( $\mathbf{A}^5$ ), 125.3 ( $\mathbf{C}^3$ ), 125.1 ( $\mathbf{A}^3$ ), 122.1 ( $\mathbf{B}^3$ ), 121.6 ( $c$ ), 62.1 ( $a$ );

Found: C, 38.68; H, 2.92; N, 8.44;  $\text{C}_{46}\text{H}_{38}\text{F}_{24}\text{N}_8\text{P}_4\text{Ru}\cdot 2\text{H}_2\text{O}$

requires C, 38.91; H, 2.98; N, 8.44;

MALDI-TOF (MeCN):  $m/z$  1240.7 [ $\text{M}-\text{PF}_6$ ] $^+$  (calc. 1239.1), 1093.7 [ $\text{M}-2\text{PF}_6$ ] $^+$  (calc. 1094.2), 1055.7 [ $\text{Ru}(\mathbf{6})(\text{Hpytpy})(\text{PF}_6)_2$ ] $^+$  (calc. 1054.1), 949.7 [ $\text{M}-3\text{PF}_6$ ] $^+$  (calc. 949.2), 910.6 [ $\text{Ru}(\mathbf{6})(\text{Hpytpy})(\text{PF}_6)$ ] $^+$  (calc. 909.2), 764.5 [ $\text{Ru}(\mathbf{6})(\text{Hpytpy})$ ] $^+$  (calc. 764.2)

## [Ru(7)<sub>2</sub>][PF<sub>6</sub>]<sub>4</sub>

Reaction time: 48 hours

Column Eluent: C Sol, (R<sub>f</sub> = 0.36)

Yield: 121.7 mg, 38.4 % (starting with 200 mg [Ru(pytpy)<sub>2</sub>][PF<sub>6</sub>]<sub>2</sub>)

<sup>1</sup>H NMR: (500 MHz, CD<sub>3</sub>CN, 25°C, TMS) δ/ppm: 9.14 (4H, s, **B**<sup>3</sup>), 9.01 (4H, d, J = 6.6 Hz, **C**<sup>2</sup>), 8.77 (4H, d, J = 6.5 Hz **C**<sup>3</sup>), 8.70 (4H, d, J = 8.1 Hz, **A**<sup>3</sup>), 8.02 (4H, t, J = 7.9 Hz **A**<sup>4</sup>), 7.46 (4H, d, J = 5.5 Hz **A**<sup>6</sup>), 7.25 (4H, m, **A**<sup>5</sup>), 4.69 (4H, t, J = 7.6 Hz, *a*), 2.13 (4H, s, *b*), 1.46 (8H, m, *c+d*), 1.35 (12H, m, *e+f+g*), 0.93 (6H, t, J = 6.7 Hz, *h*);

<sup>13</sup>C NMR: δ<sub>C</sub> (126 MHz, CD<sub>3</sub>CN, 25°C, TMS): 158.3 (**A**<sup>2</sup>/**B**<sup>2</sup>), 156.7 (**A**<sup>2</sup>/**B**<sup>2</sup>), 153.8 (**A**<sup>6</sup>), 155.6 (**C**<sup>4</sup>), 146.2 (**C**<sup>2</sup>), 142.0 (**B**<sup>4</sup>), 139.5 (**A**<sup>4</sup>), 128.9 (**A**<sup>5</sup>), 127.5 (**C**<sup>3</sup>), 126.0 (**A**<sup>3</sup>), 123.3 (**B**<sup>3</sup>), 62.7 (*a*), 32.3 (*el/fl/g*), 31.7 (*b*), 29.5 (*el/fl/g*), 29.4 (*c/d*), 26.6 (*c/d*), 23.25 (*el/fl/g*), 14.4 (*h*);

Found: C, 42.28; H, 4.26; N, 7.24; C<sub>55</sub>H<sub>60</sub>F<sub>24</sub>N<sub>8</sub>P<sub>4</sub>Ru.3H<sub>2</sub>O

requires C, 42.15; H, 4.33; N, 7.08;

MALDI-TOF (MeCN): *m/z* 1384.1 [M-PF<sub>6</sub>]<sup>+</sup> (calc. 1383.3), 1239.6 [M-2PF<sub>6</sub>]<sup>+</sup> (calc. 1238.3), 1094.5 [M-3PF<sub>6</sub>]<sup>+</sup> (calc. 1093.4)

## Computational Methods

Complexes [RuL<sub>2</sub>]<sup>4+</sup> with L<sup>+</sup> = **1-7** and [Ru(pytpy)<sub>2</sub>]<sup>2+</sup> were modelled using TD-DFT implemented in the Gaussian 09<sup>36</sup>. Each complex was initially geometry-optimized using the RHF method with a 3-21G basis set applied to non-metal atoms, and the Los Alamos National Laboratory 2 double ζ (LANL2DZ) effective core potential (ECP) used to describe the Ru<sup>2+</sup> centre<sup>37</sup>. A double-zeta Ru basis set associated with the LANL2DZ ECP was taken from the Basis Set Exchange<sup>38</sup>. The ECP and basis set were defined explicitly in Gaussian 09 using the 'GEN' and 'Pseudo=Read' keywords. Frequency calculations were performed at this level of theory for each complex to confirm the identification of a local minimum energy structure. Further refinement of complex geometries followed using the B3LYP hybrid density functional<sup>39</sup> and a larger 6-31G(d) basis set for non-metal atoms, with the same Ru<sup>2+</sup> ECP/basis set combination as before. The Integral Equation Formalism

polarisable continuum model (PCM) was used during geometry optimization and for subsequent TD-DFT calculations to describe solvation of each complex in MeCN to more closely match the experimental conditions<sup>40-43</sup>. A similar level of calculation has been applied to a series of  $[\text{Ru}(\text{tpy})_2]^{2+}$  complexes<sup>20</sup>, and the general reliability of the LANL2DZ ECP combined with the B3LYP hybrid density functional for transition metal complexes has been highlighted<sup>44</sup>. Predicted TD-DFT UV-VIS transitions were calculated at the B3LYP level, and simulated spectra were generated from the Gaussian 09 output using the GaussSum program<sup>45</sup>. Grids containing orbital densities were written as 'cube' files by Gaussian 09, and were used to generate isodensity surfaces for selected MOs using the Molekel<sup>35</sup>.

## 2.7 References

1. S. Campagna, F. Puntoriero, F. Nastasi, G. Bergamini, V. Balzani, V. Balzani and S. Campagna, Springer Berlin / Heidelberg, 2007, vol. 280, pp. 117-214.
2. A. J. Bard and M. A. Fox, *Accounts Chem. Res.*, 1995, **28**, 141-145.
3. A. Juris, V. Balzani, F. Barigelletti, S. Campagna, P. Belser and A. von Zelewsky, *Coord. Chem. Rev.*, 1988, **84**, 85-277.
4. K. Zeitler, *Angew. Chem. Int. Ed.*, 2009, **48**, 9785-9789.
5. J. P. Sauvage, J. P. Collin, J. C. Chambron, S. Guillerez, C. Coudret, V. Balzani, F. Barigelletti, L. De Cola and L. Flamigni, *Chem. Rev.*, 1994, **94**, 993-1019.
6. J. Wang and G. S. Hanan, *Synlett*, 2005, **2005**, 1251,1254.
7. A. Amini, A. Harriman and A. Mayeux, *Phys. Chem. Chem. Phys.*, 2004, **6**, 1157-1164.
8. J. R. Winkler, T. L. Netzel, C. Creutz and N. Sutin, *J. Am. Chem. Soc.*, 1987, **109**, 2381-2392.
9. V. Balzani, S. Campagna, G. Denti, A. Juris, S. Serroni and M. Venturi, *Accounts Chem. Res.*, 1998, **31**, 26-34.
10. E. A. Medlycott and G. S. Hanan, *Coord. Chem. Rev.*, 2006, **250**, 1763-1782.
11. J. A. Treadway, B. Loeb, R. Lopez, P. A. Anderson, F. R. Keene and T. J. Meyer, *Inorg. Chem.*, 1996, **35**, 2242-2246.
12. E. A. Medlycott and G. S. Hanan, *Chem. Soc. Rev.*, 2005, **34**, 133-142.
13. M. Maestri, N. Armaroli, V. Balzani, E. C. Constable and A. M. W. C. Thompson, *Inorg. Chem.*, 1995, **34**, 2759-2767.
14. J. E. Beves, E. L. Dunphy, E. C. Constable, C. E. Housecroft, C. J. Kepert, M. Neuburger, D. J. Price and S. Schaffner, *Dalton Trans.*, 2008, 386-396.
15. S. Fantacci, F. De Angelis and A. Selloni, *J. Am. Chem. Soc.*, 2003, **125**, 4381-4387.
16. M. K. Nazeeruddin, F. De Angelis, S. Fantacci, A. Selloni, G. Viscardi, P. Liska, S. Ito, B. Takeru and M. Grätzel, *J. Am. Chem. Soc.*, 2005, **127**, 16835-16847.
17. M. K. Nazeeruddin, T. Bessho, L. Cevey, S. Ito, C. Klein, F. De Angelis, S. Fantacci, P. Comte, P. Liska, H. Imai and M. Graetzel, *J. Photoch. Photobio. A*, 2007, **185**, 331-337.
18. Kohjiro Hara and H. Arakawa, in *Handbook of Photovoltaic Science and Engineering*, John Wiley & Sons, Ltd, 2003, pp. 663-700.
19. E. Jakubikova, W. Chen, D. M. Dattelbaum, F. N. Rein, R. C. Rocha, R. L. Martin and E. R. Batista, *Inorg. Chem.*, 2009, **48**, 10720-10725.
20. K. C. D. Robson, B. D. Koivisto, T. J. Gordon, T. Baumgartner and C. P. Berlinguette, *Inorg. Chem.*, 2010, **49**, 5335-5337.
21. R. Siebert, C. Hunger, J. Guthmüller, F. Schlütter, A. Winter, U. S. Schubert, L. González, B. Dietzek and J. Popp, *J. Phys. Chem. C*, 2011, **115**, 12677-12688.
22. S. Kupfer, J. Guthmüller, M. Wächtler, S. Losse, S. Rau, B. Dietzek, J. Popp and L. González, *Phys. Chem. Chem. Phys.*, 2011, **13**, 15580-15588.
23. M. G. Lobello, S. Fantacci, A. Credi and F. De Angelis, *Eur. J. Inorg. Chem.*, 2011, **2011**, 1605-1613.
24. E. C. Constable and A. M. W. C. Thompson, *J. Chem. Soc. Dalton Trans.*, 1994, 1409-1418.

25. E. L. Dunphy, PhD Thesis, University of Basel, 2009.
26. E. C. Constable, C. E. Housecroft, M. Neuburger, S. Schaffner and F. Schaper, *Inorg. Chem. Commun.*, 2006, **9**, 616-619.
27. J. E. Beves, D. J. Bray, J. K. Clegg, E. C. Constable, C. E. Housecroft, K. A. Jolliffe, C. J. Kepert, L. F. Lindoy, M. Neuburger, D. J. Price, S. Schaffner and F. Schaper, *Inorg. Chim. Acta*, 2008, **361**, 2582-2590.
28. M. L. Scudder, H. A. Goodwin and I. G. Dance, *New J. Chem.*, 1999, **23**, 695-705.
29. J. McMurtrie and I. Dance, *CrystEngComm*, 2009, **11**, 1141-1149.
30. J. McMurtrie and I. Dance, *CrystEngComm*, 2005, **7**, 216-229.
31. J. McMurtrie and I. Dance, *CrystEngComm*, 2005, **7**, 230-236.
32. I. Dance and M. Scudder, *CrystEngComm*, 2009, **11**, 2233-2247.
33. A. L. Spek, *Acta Crystallogr. D*, 2009, **65**, 148-155.
34. C. Janiak, *J. Chem. Soc. Dalton Trans.*, 2000, 3885-3896.
35. U. Varetto, in *Swiss National Computing Centre*, Lugano, Switzerland, 2009.
36. M. J. Frisch, G. W. Trucks, H. B. Schlegel, G. E. Scuseria, M. A. Robb, J. R. Cheeseman, G. Scalmani, V. Barone, B. Mennucci, G. A. Petersson, H. Nakatsuji, M. Caricato, X. Li, H. P. Hratchian, A. F. Izmaylov, J. Bloino, G. Zheng, J. L. Sonnenberg, M. Hada, M. Ehara, K. Toyota, R. Fukuda, J. Hasegawa, M. Ishida, T. Nakajima, Y. Honda, O. Kitao, H. Nakai, T. Vreven, J. J. A. Montgomery, J. E. Peralta, F. Ogliaro, M. Bearpark, J. J. Heyd, E. Brothers, K. N. Kudin, V. N. Staroverov, R. Kobayashi, J. Normand, K. Raghavachari, A. Rendell, J. C. Burant, S. S. Iyengar, J. Tomasi, M. Cossi, N. Rega, J. M. Millam, M. Klene, J. E. Knox, J. B. Cross, V. Bakken, C. Adamo, J. Jaramillo, R. Gomperts, R. E. Stratmann, O. Yazyev, A. J. Austin, R. Cammi, C. Pomelli, J. W. Ochterski, R. L. Martin, K. Morokuma, V. G. Zakrzewski, G. A. Voth, P. Salvador, J. J. Dannenberg, S. Dapprich, A. D. Daniels, Ö. Farkas, J. B. Foresman, J. V. Ortiz, J. Cioslowski and D. J. Fox, Gaussian Inc., Wallingford CT, 2009.
37. P. J. Hay and R. W. Willard, *J. Chem. Phys.*, 1985, **82**, 270-283.
38. K. L. Schuchardt, B. T. Didier, T. Elsethagen, L. Sun, V. Gurumoorthi, J. Chase, J. Li and T. L. Windus, *J. Chem. Inf. Comp. Sci.*, 2007, **47**, 1045-1052.
39. C. Lee, W. Yang and R. G. Parr, *Phys. Rev. B*, 1988, **37**, 785-789.
40. M. Benedetta and T. Jacopo, *J. Chem. Phys.*, 1997, **106**, 5151-5158.
41. E. Cancés, B. Mennucci and J. Tomasi, *J. Chem. Phys.*, 1997, **107**, 3032-3041.
42. B. Mennucci, E. Cancés and J. Tomasi, *J. Phys. Chem. B*, 1997, **101**, 10506-10517.
43. J. Tomasi, B. Mennucci and E. Cancés, *J. Mol. Struct. Theochem*, 1999, **464**, 211-226.
44. Y. Yang, M. N. Weaver and K. M. Merz, *J. Phys. Chem. A*, 2009, **113**, 9843-9851.
45. N. M. O'Boyle, A. L. Tenderholt and K. M. Langner, *J. Comp. Chem.*, 2008, **29**, 839-845.

## Chapter 3

### Water soluble alkylated bis{4'-(4-pyridyl)-2,2':6',2''}-terpyridine}ruthenium(II) complexes for application as water oxidation catalysts.

#### 3.1 Introduction

In the search for new efficient fuel sources, scientists have looked to nature for inspiration. Plants are capable of using the sun's energy to convert CO<sub>2</sub> into carbohydrates and to split water into protons and oxygen via photosynthesis. The oxidation of water to produce oxygen (Eqn. 3.1) is challenging as it is a four electron process.



In plants, this process is carried out by photosystem II (Fig. 3.1). A manganese-oxygen cluster [MnCa] oxidises water and passes electrons on to the amino acid tyrosine, which in turn delivers them to P680<sup>1</sup>. P680 is a chlorophyll cluster that absorbs light at 680 nm and acts as a photosensitiser<sup>2</sup>. These cascade reactions are a vital part of photosynthesis and the structure of the oxygen evolving unit was found to be a cubane-like Mn<sub>3</sub>CaO<sub>4</sub> cluster<sup>3,4</sup>.

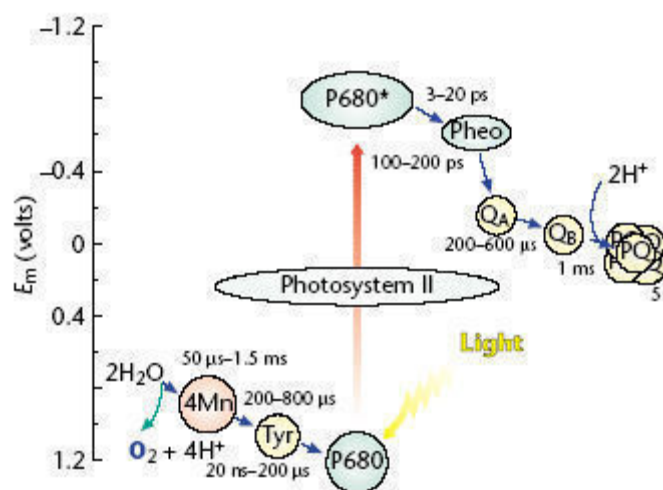


Fig. 3.1 A representation of the processes involved in photosystem II in plants<sup>1</sup>.

To further understand this [MnCa] cluster, research has been carried out towards the synthesis of mononuclear and polynuclear Mn clusters for testing as water oxidation catalysts (WOCs)<sup>5-7</sup>. In 1985 Tames *et al.* reported the first dinuclear Mn complex that



was active as a water oxidation catalyst<sup>5</sup> and in 1999 Brudvig *et al.* reported the first functional model for photosystem II<sup>8</sup>. This model was a dinuclear Mn complex with two 2,2':6',2''-terpyridine ligands, two coordinated water molecules and two bridging- $\mu$ -oxido ligands (Fig. 3.2).

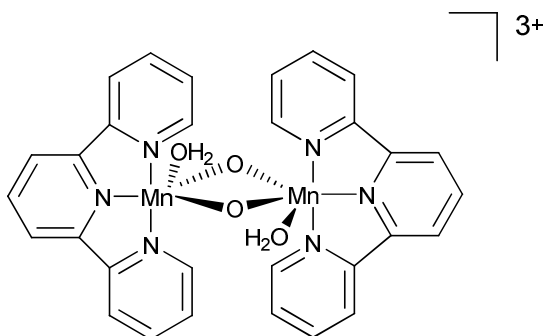


Fig. 3.2 The cation in  $[H_2O(tpy)Mn^{III}(O)_2Mn^{IV}(tpy)OH_2][NO_3]_3$ , the first functional model for photosystem II<sup>8</sup>.

Polypyridine ligands have also been used in ruthenium complexes which demonstrate catalytic water oxidation ability. Whitten *et al.*, in 1976, described the use of ruthenium complexes with surfactant-functionalised bipyridine ligands (Fig. 3.3), which were prepared as chloroform films, to oxidise water<sup>9</sup>.

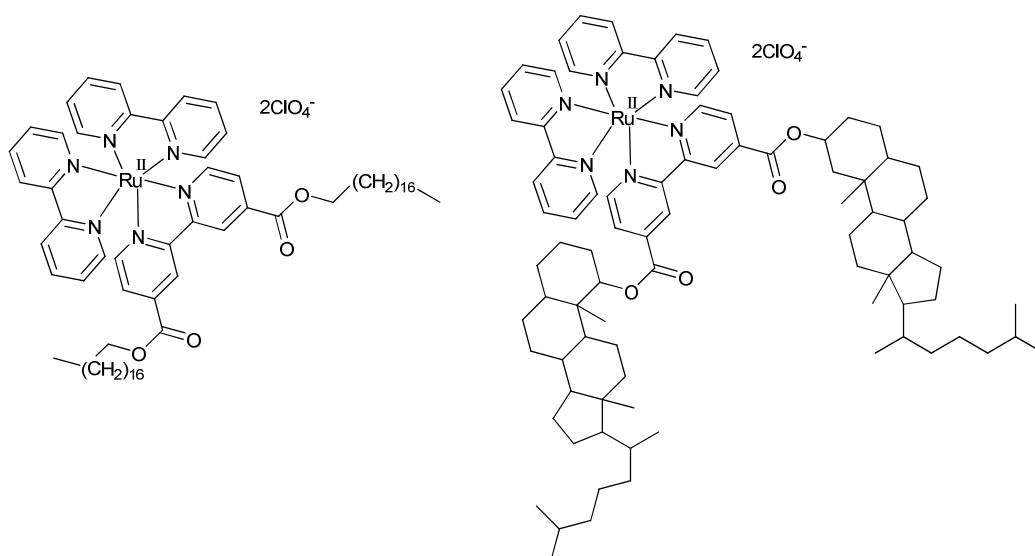


Fig. 3.3 First reported water-splitting ruthenium complexes<sup>9</sup>.

Thereafter, little progress was made in the field until 2005 when Thummel *et al.* reported three novel mononuclear ruthenium complexes which showed WOC activity<sup>10</sup>. These complexes contained polypyridyl ligands and a coordinated water molecule, and could produce O<sub>2</sub> with a turnover number (TON) of 260. TON is the number of moles of substrate (in this case water) that one mole of catalyst can convert before becoming inactive<sup>11</sup>. Following this, many ruthenium-pyridyl complexes were reported and have been the subject of recent reviews<sup>6, 7, 12, 13</sup>.

In general, ruthenium complexes which are active as water oxidation catalysts consist of the following: a polydentate (bis- to tetra-dentate) polypyridyl ligand, one or more pyridine ligands and either a coordinated water molecule or a coordinated halide (Fig. 3.4)<sup>13</sup>.

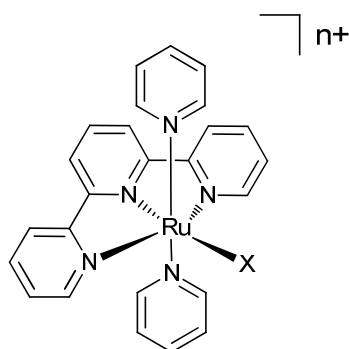


Fig. 3.4. A representative structure of a ruthenium-based water oxidation catalyst,  $X = H_2O$ ,  $n = 2$ ,  $X = Cl, Br, I$ ,  $n = 1$ .

Many possible types of complexes are summarised in a recent paper by Thummel *et al.*<sup>14</sup> where a family of 28 mononuclear Ru(II) complexes were synthesised and tested as catalysts for water splitting. In this family of complexes the highest TON achieved was 1170, in 24 hours.

The reaction mechanism of water oxidation by ruthenium complexes of the aforementioned type has been studied in detail by Meyer *et al.*<sup>15</sup>. The mechanism has been shown to be dependent on the ruthenium atom being able to coordinate a water molecule and then achieve oxidation states of +4 and +5 by forming a Ru=O double bond (Fig. 3.5).

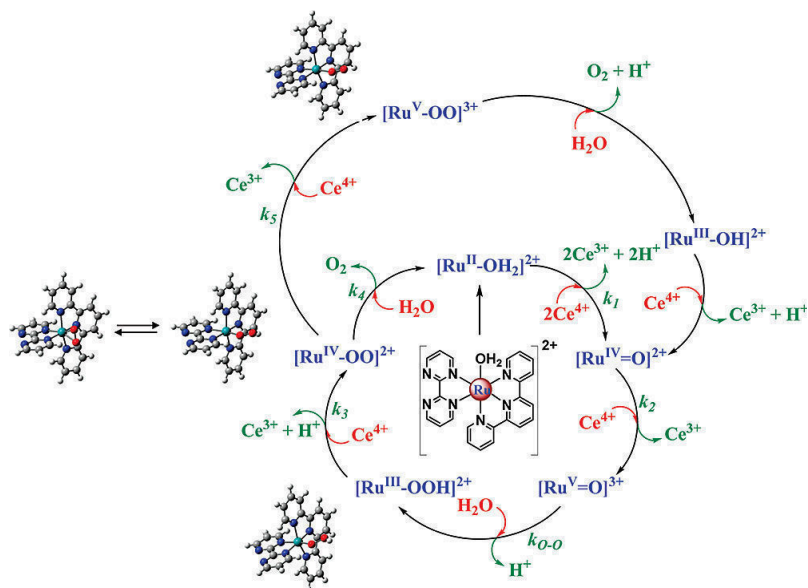


Fig. 3.5 Proposed single site water oxidation mechanism for ruthenium polypyridyl complexes with one coordinated water molecule<sup>15</sup>.

The most active ruthenium complex reported to date, prepared by Sun *et al.*, has a turnover frequency (TOF) of 300 s<sup>-1</sup>, which is comparable to the rate of oxygen production by photosystem II (Fig. 3.6)<sup>16</sup>. TOF is the turnover per unit time<sup>11</sup>.

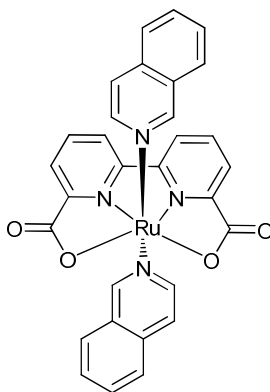


Fig. 3.6 [Ru(bda)(isoq)<sub>2</sub>] (H<sub>2</sub>bda = 2,2'-bipyridine-6,6'-dicarboxylic acid; isoq = isoquinoline). The most active water oxidation catalyst reported to date<sup>16</sup>.

Reported in this chapter are homoleptic ruthenium complexes which have neither a coordinated water molecule nor a coordinated halide. Therefore, water oxidation by the

aforementioned mechanism is not possible. However, they can be used in conjunction with another emerging class of compounds for water oxidation catalysis, the polyoxometallates (POMs)<sup>6, 12, 17-22</sup>.

POMs are metal oxido clusters that can include heteroanions, such as  $\text{SO}_4^{2-}$  or  $\text{PO}_4^{3-}$ <sup>17, 23</sup>.

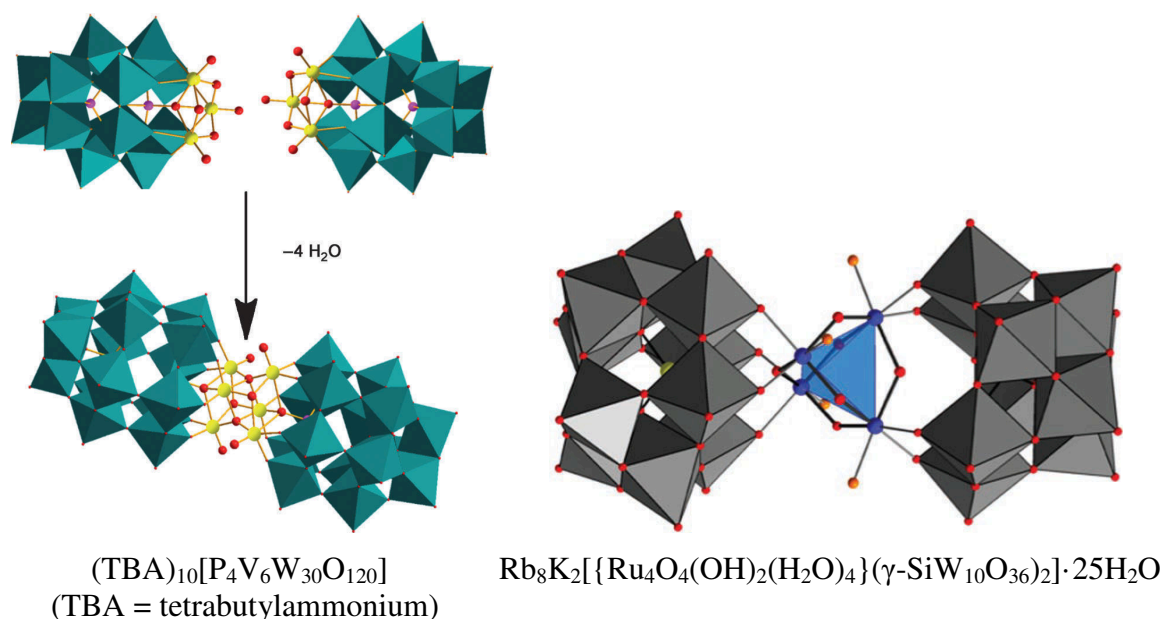


Fig. 3.7 General examples of POMS prepared by (left) Cronin *et al.*<sup>24</sup> and (right) Hill *et al.*<sup>21</sup>.

POMs have a number of advantages over the aforementioned ruthenium-based complexes<sup>13, 17, 23</sup>. A lack of organic ligands means that they are highly stable, even under harsh conditions<sup>25</sup>. The POM can undergo at least four sequential reductions without the structural integrity of the cluster shell being damaged and can, therefore, be thought of as an electron sink<sup>17</sup>. POMs have very strong LMCT absorptions in the UV ( $\epsilon > 1 \times 10^4 \text{ dm}^3 \text{ mol}^{-1} \text{ cm}^{-1}$ ) which tail into the visible region of the spectrum. The band is a result of promotion of an electron from an oxygen bonding orbital into an anti-bonding orbital and is formally an  $\text{O} \rightarrow \text{M}$  ( $\text{M} = \text{metal}$ ) LMCT<sup>17</sup>. To aid the absorption of visible light a photosensitiser (often  $[\text{Ru}(\text{bpy})_3]^{2+}$ <sup>6, 17-21</sup>) is used in cooperation with the POM (Fig. 3.8).

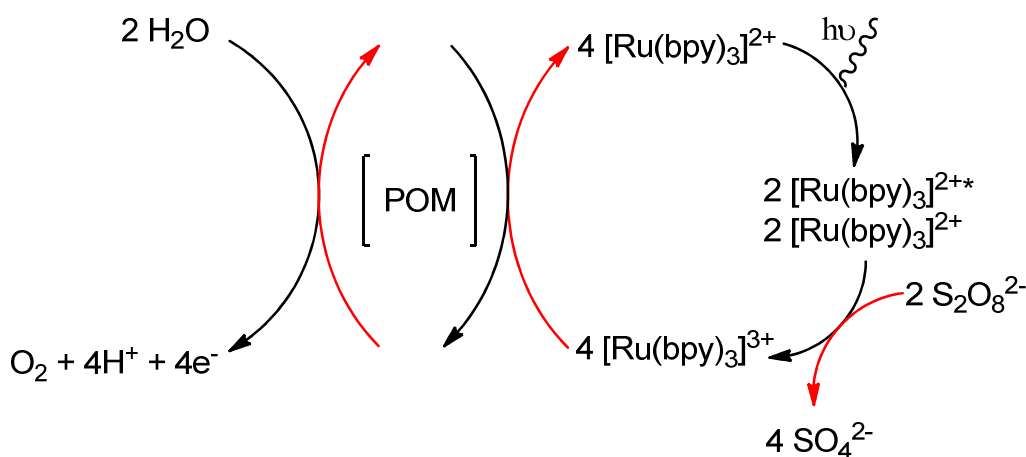


Fig. 3.8 The use of  $[\text{Ru}(\text{bpy})_3]^{2+}$  as a photosensitiser for a POM, figure redrawn from reference <sup>18</sup>.

The  $[\text{Ru}(\text{bpy})_3]^{2+}$  is excited on absorption of light to  $[\text{Ru}(\text{bpy})_3]^{2+*}$ . This excited state is a better reducing agent than its ground state and it reduces the  $\text{S}_2\text{O}_8^{2-}$  to  $\text{SO}_4^{2-}$  whilst itself being oxidised to  $[\text{Ru}(\text{bpy})_3]^{3+}$  (the same process occurs for a  $[\text{Ru}(\text{bpy})_3]^{2+}$  complex in the ground state). The ruthenium complex then returns to the ground state,  $[\text{Ru}(\text{bpy})_3]^{2+}$ , by gaining an electron from the POM. This cycle is repeated four times, at which point the POM has enough energy to break the O-H bond and oxidise the water to  $\text{O}_2$  and  $4\text{H}^+$ . The system is photocatalytic and, therefore, repeats itself, with only the consumption of  $\text{S}_2\text{O}_8^{2-}$  <sup>18</sup>.

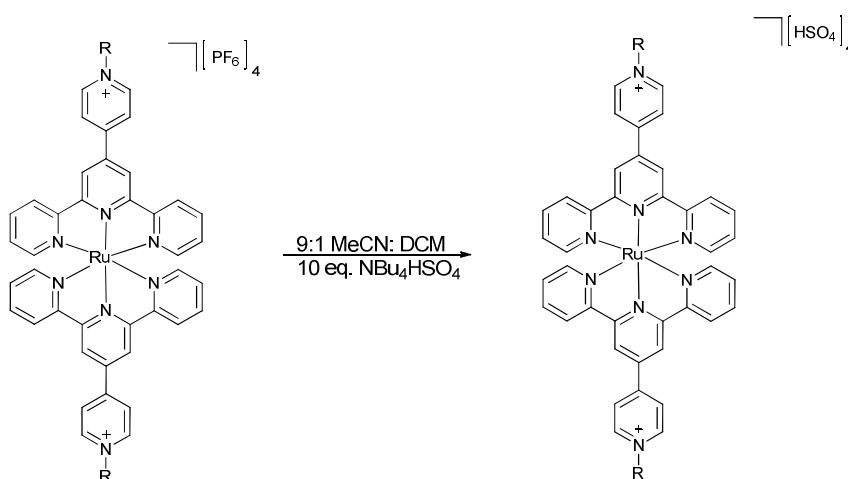
The *exact* mechanism of water oxidation by the POM system is a current subject of debate. Some reports suggest that the POM is a pre-catalyst that decomposes over time or on oxidation to a metal oxide species which is the active catalyst <sup>26-28</sup>. There are also studies on aggregates which arise from ion-pairing of the negatively charged POM and the positively charged dye sensitiser <sup>29-32</sup>. Further mechanistic studies have been carried out specifically investigating water exchange at the metal core of the POM <sup>33</sup>.

The POM with the highest water oxidation activity reported to date is based on cobalt and has the formula  $\text{Na}_{10}[\text{Co}_4(\text{H}_2\text{O})_2(\text{PW}_9\text{O}_{34})_2]$  <sup>20, 34</sup>. When used in conjunction with  $[\text{Ru}(\text{bpy})_3]^{2+}$ , the turnover number can reach  $>220$  and the quantum yield can be as high as 30 % <sup>20</sup>. To further improve the system, it is possible to optimise two components: the

POM itself and the photosensitiser. The work in this chapter describes the synthesis of homoleptic ruthenium complexes as photosensitiser alternatives to  $[\text{Ru}(\text{bpy})_3]^{2+}$ .

### 3.2 Synthesis of $[\text{Ru}(\text{R-pytpy})_2][\text{HSO}_4]_4$ Complexes

The complexes described in Chapter 2 were designed for application as water oxidation co-catalysts. In order for this application to be realised, the complexes needed to be water soluble. This was effected through anion exchange of the  $[\text{Ru}(\text{pytpy})_2][\text{PF}_6]_2$  and  $[\text{Ru}(\text{L})_2][\text{PF}_6]_4$  ( $\text{L}^+ = \mathbf{1-7}$ ) complexes with  $[\text{Bu}_4\text{N}][\text{HSO}_4]$  (Scheme 1) to give  $[\text{Ru}(\text{pytpy})_2][\text{HSO}_4]_2$  and  $[\text{Ru}(\text{L})_2][\text{HSO}_4]_4$  ( $\text{L}^+ = \mathbf{1-7}$ ) respectively.



*Scheme 3.1* A general synthesis for  $[\text{Ru}(\text{L})_2][\text{HSO}_4]_4$  complexes ( $\text{L}^+ = \mathbf{1-7}$ ).

Ten equivalents of tetra-*n*-butylammonium hydrogensulfate were added to a stirred solution of the relevant complex in a mixture of 9:1 acetonitrile:dichloromethane. A red precipitate formed immediately and was isolated as a red powder, which was soluble in water but insoluble in common organic solvents. The red powder was then stirred in boiling acetonitrile for *ca.* 20 minutes to remove both excess  $[\text{Bu}_4\text{N}][\text{HSO}_4]$  and the tetrabutylammonium hexafluoridophosphate ( $[\text{Bu}_4\text{N}][\text{PF}_6]$ ), which forms during the reaction. The reaction yields are summarised in Table 3.1

Complex	Yield (%)
[Ru(pytpy) <sub>2</sub> ][HSO <sub>4</sub> ] <sub>2</sub>	79
[Ru( <b>1</b> ) <sub>2</sub> ][HSO <sub>4</sub> ] <sub>4</sub>	99
[Ru( <b>2</b> ) <sub>2</sub> ][HSO <sub>4</sub> ] <sub>4</sub>	60
[Ru( <b>3</b> ) <sub>2</sub> ][HSO <sub>4</sub> ] <sub>4</sub>	98
[Ru( <b>4</b> ) <sub>2</sub> ][HSO <sub>4</sub> ] <sub>4</sub>	99
[Ru( <b>5</b> ) <sub>2</sub> ][HSO <sub>4</sub> ] <sub>4</sub>	66
[Ru( <b>6</b> ) <sub>2</sub> ][HSO <sub>4</sub> ] <sub>4</sub>	82
[Ru( <b>7</b> ) <sub>2</sub> ][HSO <sub>4</sub> ] <sub>4</sub>	68

Table 3.1 Summary of yields of [Ru(pytpy)<sub>2</sub>][HSO<sub>4</sub>]<sub>2</sub> and the Ru(II) complexes of ligands 1-7 with HSO<sub>4</sub><sup>-</sup> counter-anions.

### 3.3 Results and Discussion

#### 3.3.1 <sup>1</sup>H NMR Spectroscopy

Proton NMR spectroscopy was used to confirm that the [Ru(L)<sub>2</sub>]<sup>4+</sup> cation had been unaffected by the anion exchange.

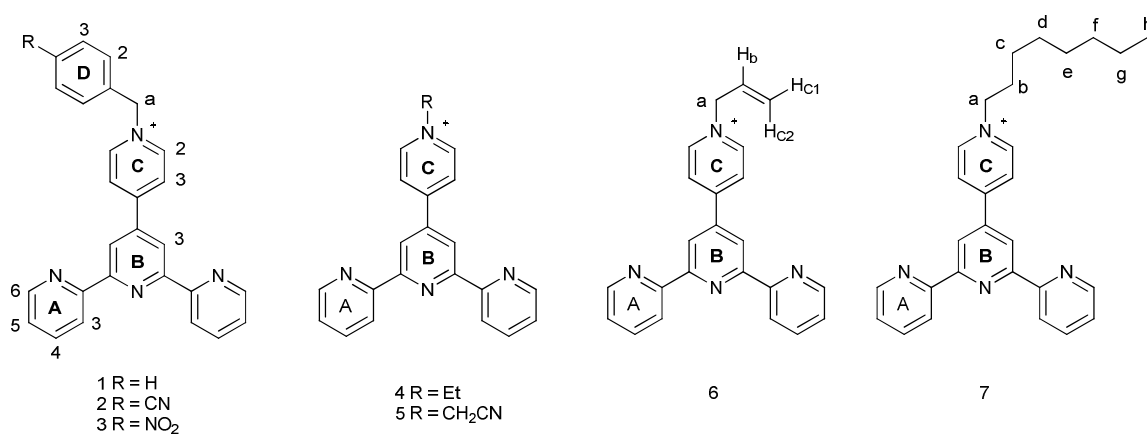


Fig. 3.9 Ligands 1-7 with labelling for <sup>1</sup>H NMR spectroscopic assignments.

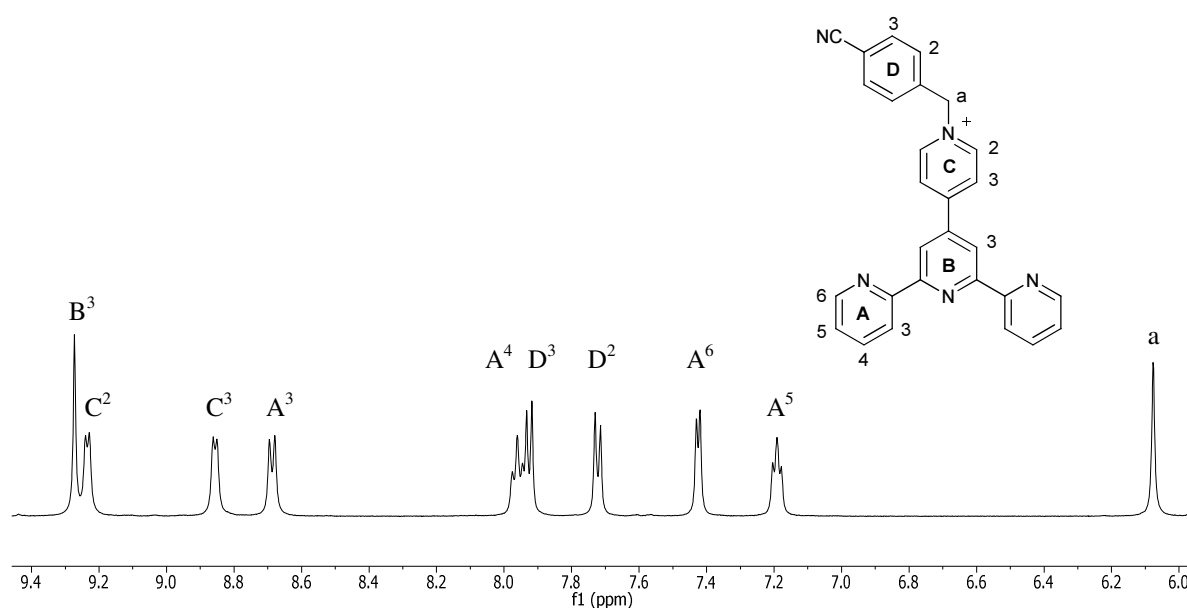


Fig. 3.10 <sup>1</sup>H NMR spectrum of [Ru(2)<sub>2</sub>][HSO<sub>4</sub>]<sub>4</sub> in D<sub>2</sub>O; 500 MHz, 25°C, TMS.

As previously described (§Ch. 2) for the [Ru(L)<sub>2</sub>][PF<sub>6</sub>]<sub>4</sub> complexes, the signals were assigned using the 1D <sup>1</sup>H NMR spectrum in conjunction with 2D COSY and NOESY spectra. The appearance of both one set and the correct number of signals (Fig. 3.10) confirms that the [Ru(L)<sub>2</sub>]<sup>4+</sup> core of the complex has been unaffected by the anion exchange. The singlet, for [Ru(2)<sub>2</sub>][HSO<sub>4</sub>]<sub>4</sub> at δ 6.08 ppm (Fig. 3.10) is assigned to the H<sup>a</sup> proton and is characteristic of this set of complexes. The signal shifts, depending on the electron-donating or -withdrawing properties of the substituent, between δ 4.78 and 6.14 ppm (L<sup>+</sup> = 7 and 3, respectively). When L<sup>+</sup> = 4 (ethyl-substituted) or L<sup>+</sup> = 7 (octyl-substituted), this signal is coincident with the peak due to residual HOD. This is confirmed by a cross-peak present in the HMQC spectrum (Fig. 3.11)



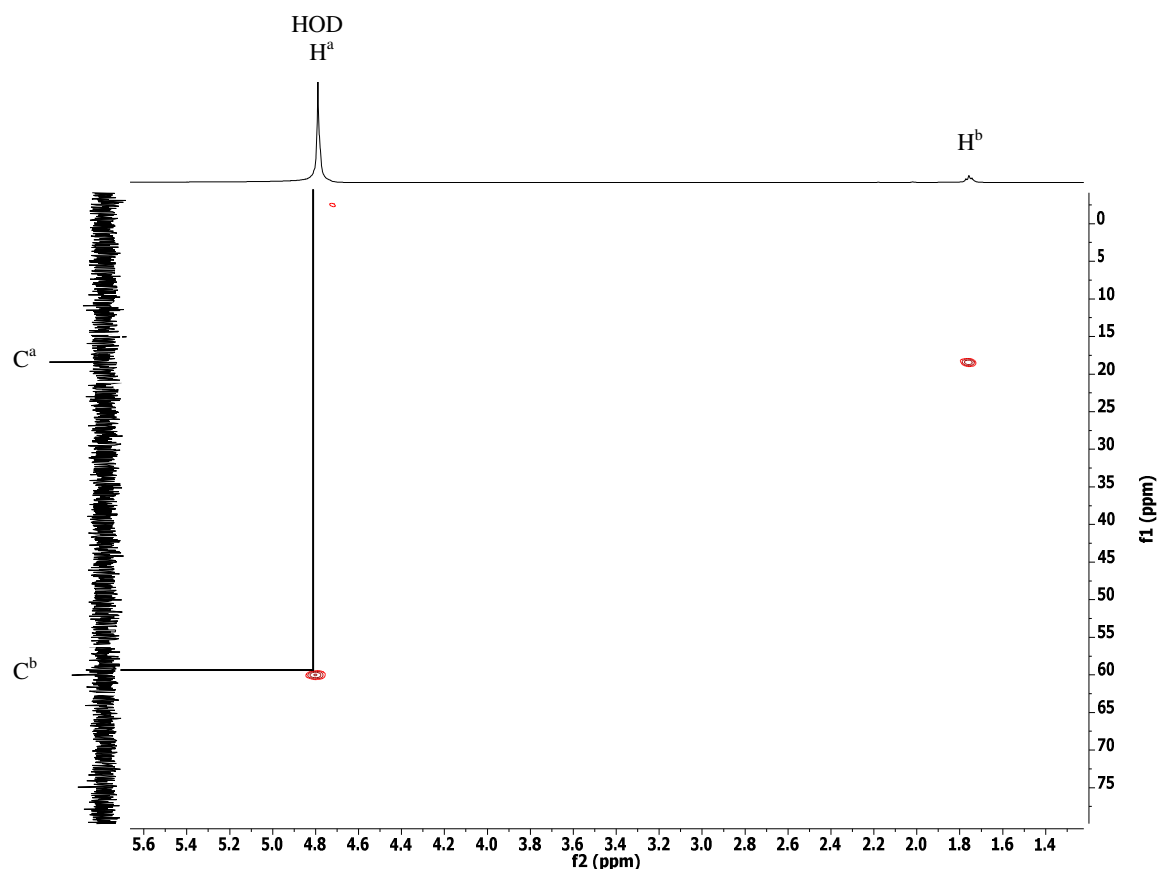


Fig. 3.11 Partial HMQC spectrum of  $[\text{Ru}(\mathbf{4})_2][\text{HSO}_4]_4$  showing that the  $\text{CH}_2$  (a) peak lies under the residual HOD peak of the solvent, 500 MHz,  $\text{D}_2\text{O}$ , 25°C, TMS.

### 3.3.2 $^{13}\text{C}\{^1\text{H}\}$ NMR Spectroscopy

All  $^{13}\text{C}$  NMR measurements were referenced with respect to  $\text{Na}[\text{Me}_3\text{Si}(\text{CH}_2)_3\text{SO}_3]$  (DSS) with the methyl signal set to  $\delta$  0.0 ppm. The signals were assigned using DEPT, HMQC and HMBC techniques, however, it was not possible to unambiguously ascribe all signals. The  $^{13}\text{C}\{^1\text{H}\}$  spectrum of  $[\text{Ru}(\mathbf{6})_2][\text{HSO}_4]_4$  with added DSS is depicted in Fig. 3.12.

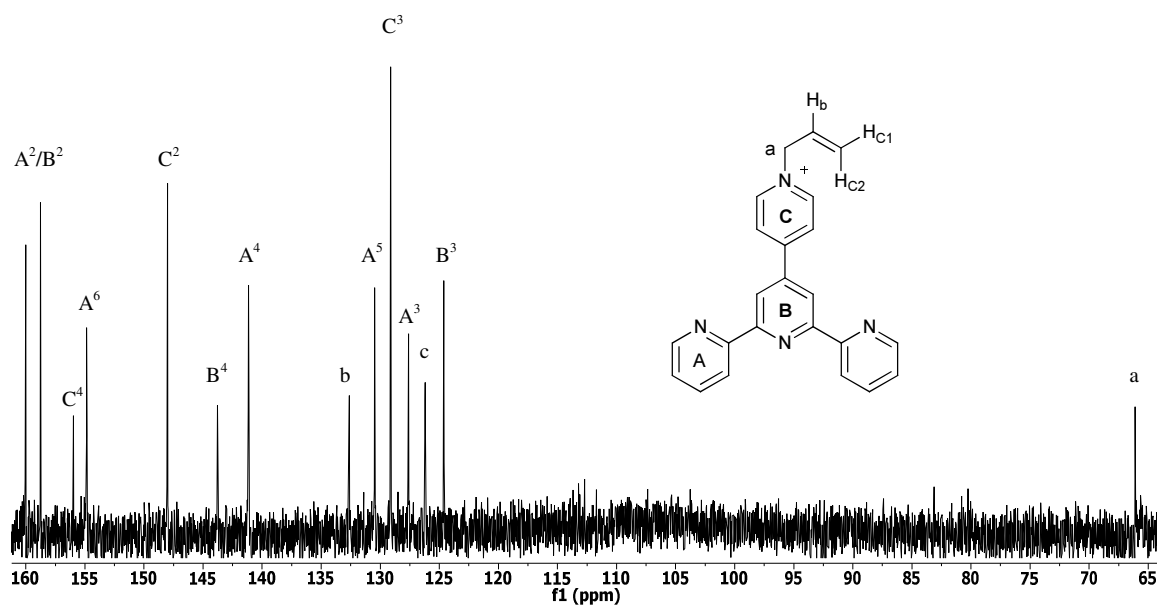


Fig. 3.12  $^{13}\text{C}\{^1\text{H}\}$  NMR spectrum of  $[\text{Ru}(\mathbf{6})_2][\text{HSO}_4]_4$  in  $\text{D}_2\text{O}$ ; 126 MHz,  $25^\circ\text{C}$ , DSS.

### 3.3.3 Mass Spectrometry

Electrospray ionisation mass spectrometry (ESI-MS) was used to characterise the  $[\text{Ru}(\text{pytpy})_2][\text{HSO}_4]_2$  complex. A peak corresponding to the cation was observed at  $m/z$  361.0, which corresponded to the loss of both anions;  $[\text{M}-2\text{HSO}_4]^{2+}$ .

The  $[\text{Ru}(\text{L})_2][\text{HSO}_4]_4$  complexes were characterised using MALDI-TOF mass spectrometry. The fragmentation patterns confirmed successful anion exchange as fragmentation peaks corresponding to  $[\text{M}-n\text{HSO}_4]^+$  ( $n=1-3$ ) were observed. Peaks corresponding to the loss of one substituent were also present for most complexes. The base peaks, assigned to  $[\text{Ru}(\text{Hpytpy})_2]^+$ ,  $[\text{Ru}(\text{Hpytpy})(\text{pytpy})]^+$  and  $[\text{Ru}(\text{pytpy})_2]^+$  at  $m/z$  724, 723 and 722, respectively, were also present in the spectra.

### 3.3.4 Elemental Analysis and Thermogravimetric Analysis

Elemental analysis of  $[\text{Ru}(\mathbf{2})_2][\text{HSO}_4]_4$  and  $[\text{Ru}(\mathbf{3})_2][\text{HSO}_4]_4$  pointed to the formation of hydrates. This was unsurprising given the ability of  $\text{HSO}_4^-$  anions to form hydrogen bonds. It was not possible to obtain elemental analysis of the anhydrous complexes, due to their hygroscopic nature. Therefore, TGA was used to quantify the theory that the elemental analyses were consistent with the formation of hydrates. TGA-MS analysis of a sample of  $[\text{Ru}(\mathbf{3})_2][\text{HSO}_4]_4$  showed an initial 2.3% weight loss ( $\leq 200^\circ\text{C}$ ) followed by two

further steps of water loss (2.4 and 4.7% weight loss between 200 and 400°C). Sample decomposition occurred at higher temperatures. The initial degradation steps correspond to loss of 2H<sub>2</sub>O, 2H<sub>2</sub>O and 4H<sub>2</sub>O, consistent with the elemental analytical data of the complex: Found: C 42.42, H 3.64, N 9.32; C<sub>54</sub>H<sub>44</sub>N<sub>10</sub>O<sub>20</sub>RuS<sub>4</sub>·8H<sub>2</sub>O requires C 42.49, H 3.96, N 9.18.

### 3.3.5 Absorption Spectroscopy

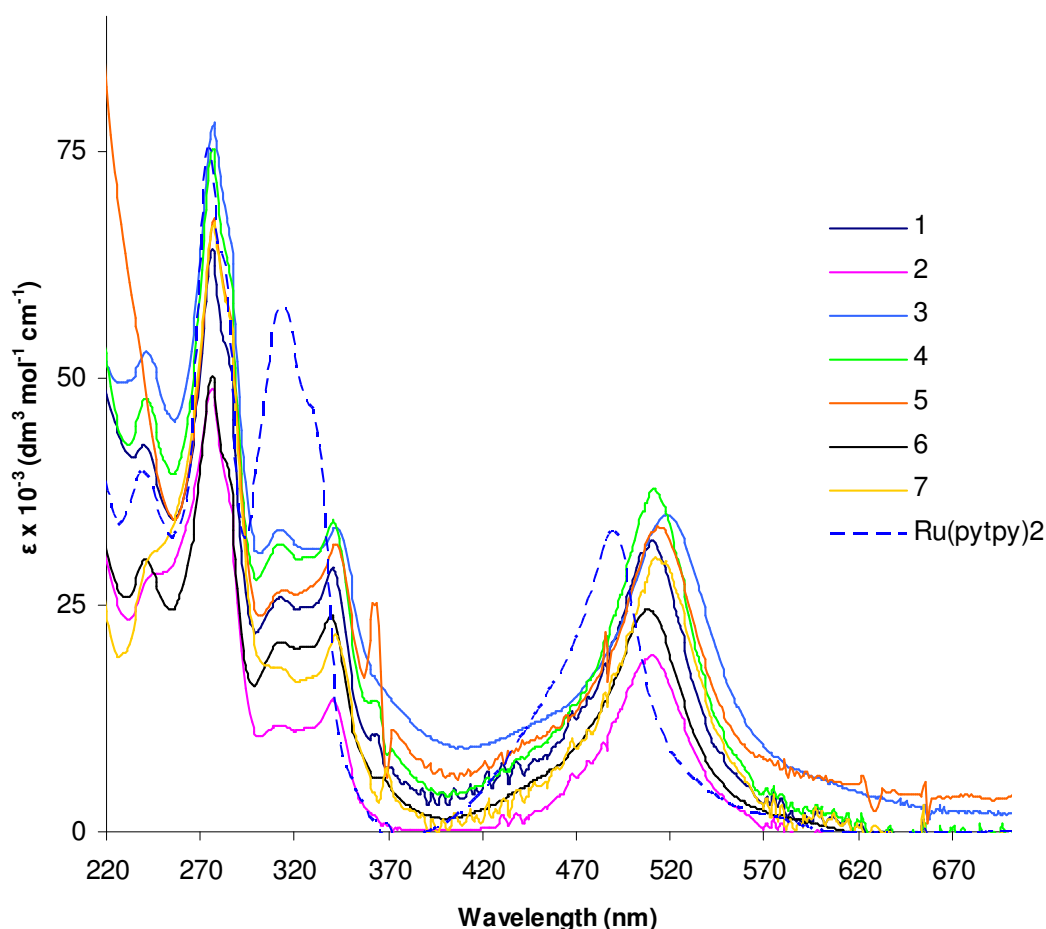


Fig. 3.13 Absorption spectra for  $[Ru(pytpy)_2][HSO_4]_2$  and  $[Ru(L)_2][HSO_4]_4$  ( $L^+ = 1-7$ ), measured in water at concentrations of  $10^{-6} \text{ mol dm}^{-3}$ .

To be effective as photosensitisers for the POM (§ Introduction), the ruthenium complexes should ideally absorb over the entire visible spectrum. The broad MLCT absorptions (390-560 nm for  $[Ru(pytpy)_2][HSO_4]_2$  and 390-580 nm for all other complexes) cover a large proportion of the visible spectrum.

As observed for the  $[\text{Ru}(\text{L})_2][\text{PF}_6]_4$  complexes (§ Chapter 2) the MLCT band is red-shifted on alkylation of the pendant pyridyl moiety. The energy of the MLCT band is the same for  $[\text{Ru}(\text{pytpy})_2][\text{PF}_6]_2$  and  $[\text{Ru}(\text{pytpy})_2][\text{HSO}_4]_2$  ( $\lambda_{\text{max}} = 490 \text{ nm}$ ) and this is also true for each  $[\text{Ru}(\text{L})_2][\text{HSO}_4]_4$  complex, except for  $[\text{Ru}(\mathbf{3})_2][\text{HSO}_4]_4$  and  $[\text{Ru}(\mathbf{5})_2][\text{HSO}_4]_4$  (Fig. 3.13), which are slightly red-shifted (518 nm), compared to 513 nm for their  $\text{PF}_6^-$  precursors.

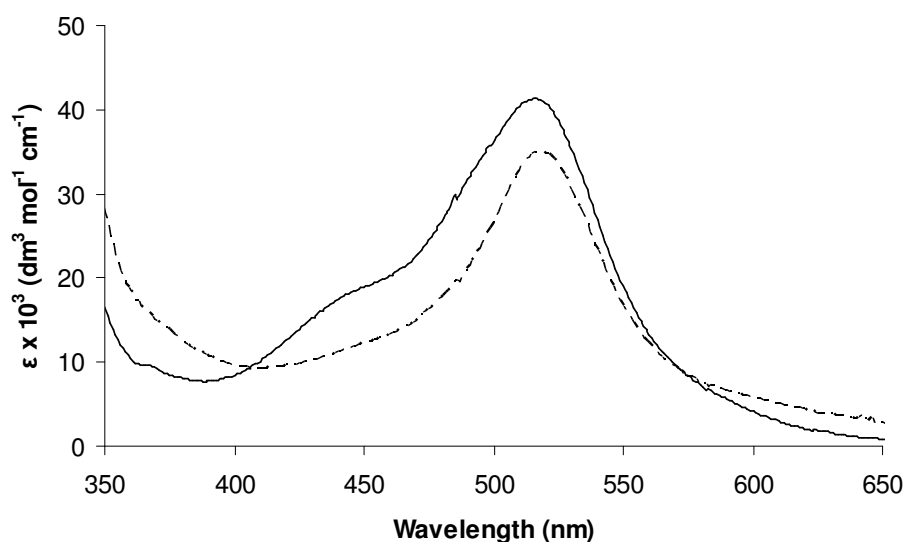


Fig. 3.14 A comparison of the absorption properties of  $[\text{Ru}(\mathbf{5})_2][\text{PF}_6]_4$  (solid black line) and  $[\text{Ru}(\mathbf{5})_2][\text{HSO}_4]_4$  (dashed black line). Concentration =  $10^{-6} \text{ mol dm}^{-3}$ .

The change in anion and solvent, from  $\text{PF}_6^-$  in MeCN to  $\text{HSO}_4^-$  in water, affects the ability of the complexes to absorb light. The molar absorption coefficients for the MLCT band ranges from  $19.6 \times 10^3$  ( $L^+ = \mathbf{7}$ )  $\text{dm}^3 \text{ mol}^{-1} \text{ cm}^{-1}$  to  $37.8 \times 10^3$  ( $L^+ = \mathbf{1}$ ) for the  $\text{HSO}_4^-$  salts, compared to  $29.7 \times 10^3$  ( $L^+ = \mathbf{3}$ ) to  $48.7 \times 10^3$  ( $L^+ = \mathbf{7}$ ) for the  $\text{PF}_6^-$  salts. In general the  $\text{HSO}_4^-$  water-soluble salts are weaker absorbers than their  $\text{PF}_6^-$  precursors but the  $\epsilon$  values are in the same order of magnitude. However,  $\epsilon$  values of  $10^4 \text{ mol dm}^{-3} \text{ cm}^{-1}$  means the complexes are still good absorbers and, therefore, reasonable catalyst candidates<sup>35</sup>.

In the UV region of the spectrum the most intense band for the majority of complexes was around 276 nm. This band arises from a  $\pi \rightarrow \pi^*$  transition on the pytpy ligand<sup>36</sup>. The data for all complexes are summarised in Table 3.2.

Complex	MLCT					
	( $\epsilon$ , $10^{-3}$ dm <sup>3</sup> mol <sup>-1</sup> cm <sup>-1</sup> )	( $\epsilon$ , $10^{-3}$ dm <sup>3</sup> mol <sup>-1</sup> cm <sup>-1</sup> ) $\lambda_{\max}$				
[Ru(pytpy) <sub>2</sub> ][HSO <sub>4</sub> ] <sub>2</sub>	490 (33.1)		313 (58.1)		274 (75.5)	239 (39.6)
[Ru( <b>1</b> ) <sub>2</sub> ][HSO <sub>4</sub> ] <sub>4</sub>	511 (37.8)	341 (34.4)	308 (30.8)	281 sh (62.2)	276 (75.4)	241 (48.2)
[Ru( <b>2</b> ) <sub>2</sub> ][HSO <sub>4</sub> ] <sub>4</sub>	513 (33.7)	342 (31.8)	310 (26.1)	284 sh (58.2)	277 (67.8)	
[Ru( <b>3</b> ) <sub>2</sub> ][HSO <sub>4</sub> ] <sub>4</sub>	518 (29.8)	342 (21.8)	307 (18.1)	285 sh (57.4)	277 (67.3)	
[Ru( <b>4</b> ) <sub>2</sub> ][HSO <sub>4</sub> ] <sub>4</sub>	508 (24.6)	340 (23.9)	308 (11.4)	287 sh (36.1)	276 (50.3)	
[Ru( <b>5</b> ) <sub>2</sub> ][HSO <sub>4</sub> ] <sub>4</sub>	518 (35.1)	342 (33.6)	307 (32.2)	283 sh (64.2)	277 (78.3)	238 (53.5)
[Ru( <b>6</b> ) <sub>2</sub> ][HSO <sub>4</sub> ] <sub>4</sub>	511 (32.1)	340 (29.2)	309 (25.9)	288 sh (51.1)	276 (64.2)	237 (41.9)
[Ru( <b>7</b> ) <sub>2</sub> ][HSO <sub>4</sub> ] <sub>4</sub>	510 (19.6)	340 (14.6)	308 (20.2)	282 sh (41.7)	276 (49.0)	

Table 3.2 A summary of the electronic absorption data, recorded in water at concentrations of  $10^{-6}$  mol dm<sup>-3</sup>, for the Ru(II) complexes of ligands 1-7.

### 3.3.6 Emission Spectroscopy

If an excited state is energetically accessible it can often be observed by the presence of phosphorescent decay<sup>37</sup>. This is important in the water splitting cycle as it is the excited state that is required to do the ‘work’. In solution all of the complexes were emissive. A water solution of the complex [Ru(pytpy)<sub>2</sub>][HSO<sub>4</sub>]<sub>2</sub> was excited at 490 nm, resulting in a broad emission centered on  $\lambda_{\text{em}} = 660$  nm.

Water solutions of complexes  $[\text{Ru}(\text{L})_2][\text{HSO}_4]_4$  were excited in the MLCT band,  $\lambda_{\text{ex}} = 510 \text{ nm}$ , which resulted in emission from the complexes between 600 and 850 nm, with  $\lambda_{\text{max}}$  generally centred around 724 nm. The spectra are depicted in Fig. 3.15.

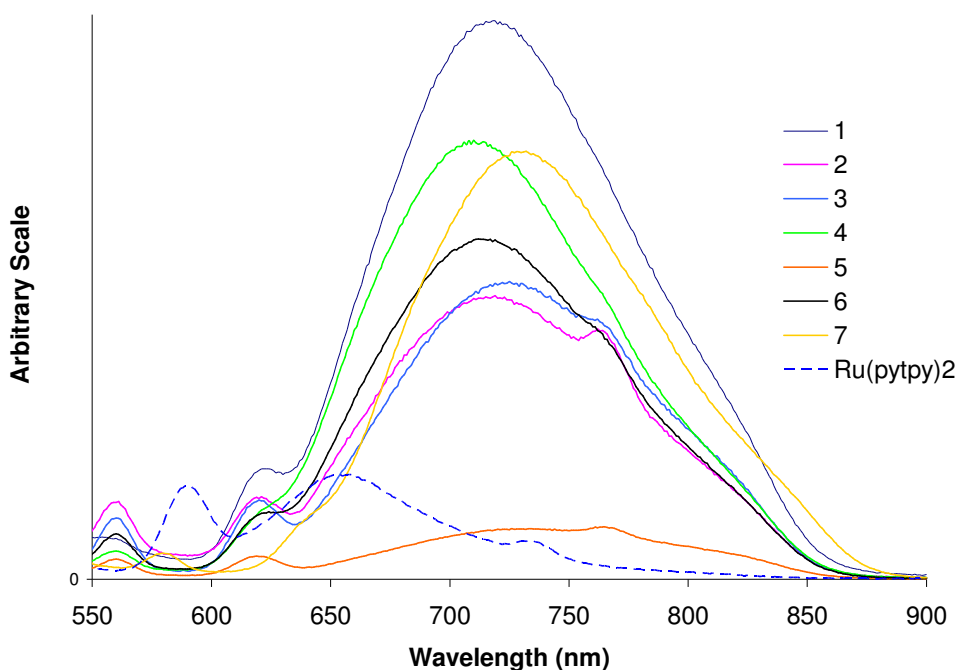


Fig. 3.15 Emission spectra for  $[\text{Ru}(\text{pytpy})_2][\text{HSO}_4]_2$  and  $[\text{Ru}(\text{L})_2][\text{HSO}_4]_4$  ( $\text{L}^+ = \mathbf{1-7}$ ), measured in water. All solutions are of  $10^{-6} \text{ mol dm}^{-3}$  concentration.

The complex  $[\text{Ru}(\mathbf{1})_2][\text{HSO}_4]_4$  emits with the highest intensity and complex  $[\text{Ru}(\mathbf{5})_2][\text{HSO}_4]_4$  emits with the lowest intensity, which follows the trend observed for the  $\text{PF}_6^-$  salts. The emission of the  $\text{HSO}_4^-$  salts overall was weaker than their precursor  $\text{PF}_6^-$  salts.

The phosphorescence lifetimes of the complexes were also measured. There is a slight decrease in lifetime for the  $\text{HSO}_4^-$  salts compared to the  $\text{PF}_6^-$  salts. The emission maxima and lifetimes are summarised in Table 3.3.

Complex	Excitation Wavelength (nm)	Emission Max (nm)	$\tau$ (ns) (+/- 15 ns)
[Ru(pytpy) <sub>2</sub> ][HSO <sub>4</sub> ] <sub>2</sub>	490	660	73
[Ru( <b>1</b> ) <sub>2</sub> ][HSO <sub>4</sub> ] <sub>4</sub>	510	719	135
[Ru( <b>2</b> ) <sub>2</sub> ][HSO <sub>4</sub> ] <sub>4</sub>	510	722	108
[Ru( <b>3</b> ) <sub>2</sub> ][HSO <sub>4</sub> ] <sub>4</sub>	510	724	103
[Ru( <b>4</b> ) <sub>2</sub> ][HSO <sub>4</sub> ] <sub>4</sub>	510	732	146
[Ru( <b>5</b> ) <sub>2</sub> ][HSO <sub>4</sub> ] <sub>4</sub>	510	734	98
[Ru( <b>6</b> ) <sub>2</sub> ][HSO <sub>4</sub> ] <sub>4</sub>	510	716	137
[Ru( <b>7</b> ) <sub>2</sub> ][HSO <sub>4</sub> ] <sub>4</sub>	510	722	142

Table 3.3 A summary of the emission properties of Ru(II) complexes with ligands **1-7**, recorded in water at concentrations of  $10^{-6}$  mol dm<sup>-3</sup>.

Although the lifetimes appear short for phosphorescence it is important to note that the measurements were carried out at room temperature in aerated solvent and both of these factors should decrease the lifetime. The measurement was also carried out in water and the <sup>3</sup>O<sub>2</sub> present quenches the <sup>3</sup>MLCT state, further decreasing the lifetime. The lifetime of the complex needs to be long enough for the electron transfer to the S<sub>2</sub>O<sub>8</sub><sup>2-</sup> (reducing it to SO<sub>4</sub><sup>2-</sup>) and  $\geq 70$  ns should be sufficient. The lifetimes are similar to that of an analogous complex reported by Kaledin *et al.*<sup>35</sup>.

### 3.3.7 Electrochemistry

Cyclic voltammetry was used to investigate the electrochemical properties of the complexes selected for testing as WOCs. The complexes selected were [Ru(pytpy)<sub>2</sub>][HSO<sub>4</sub>]<sub>2</sub> and [Ru(L)<sub>2</sub>][HSO<sub>4</sub>]<sub>4</sub> (L<sup>+</sup> = **1**, **2**, **4** and **6**).

To be used as a WOC the complex needs to have an oxidation potential above the half reaction of water oxidation ( $2\text{H}_2\text{O} \rightarrow \text{O}_2 + 4\text{H}^+ + 4\text{e}^-$ ) but within a value that allows for oxidation. The measurements were carried out in a water solution of the complex using 0.1M NaHSO<sub>4</sub> as the electrolyte, with a glassy carbon working electrode, Ag/AgCl

reference electrode and a Pt wire counter-electrode. The measurements were referenced to  $\text{Ag}/\text{Ag}^+$ . Fig. 3.16 depicts a representative cyclic voltammogram of  $[\text{Ru}(\mathbf{2})_2][\text{HSO}_4]_4$ , showing only the Ru(II)/Ru(III) oxidation; a meaningful reduction spectrum could not be obtained.

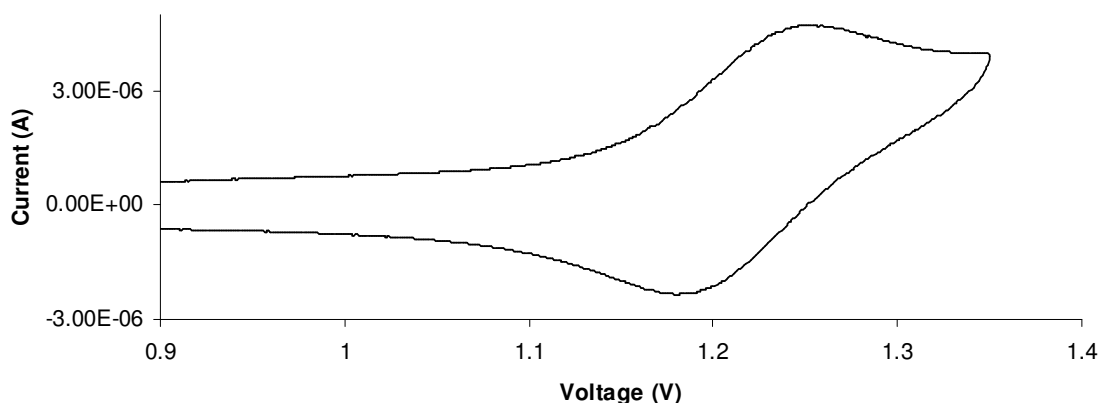


Fig. 3.16 Cyclic Voltammogram for  $[\text{Ru}(\mathbf{2})_2][\text{HSO}_4]_4$  ( $\text{H}_2\text{O}$ ,  $0.1\text{M NaHSO}_4$ , vs.  $\text{Ag}/\text{Ag}^+$ ). Only oxidation process shown.

A broad quasi-reversible oxidation wave was observed for all complexes. This was attributed to the oxidation of  $\text{Ru}^{\text{II}}$  to  $\text{Ru}^{\text{III}}$ . The  $[\text{Ru}(\text{pytpy})_2][\text{HSO}_4]_2$  complex is more easily oxidised than the  $[\text{Ru}(\text{L})_2][\text{HSO}_4]_4$  complexes. The data are summarised in Table 3.4.

Complex	Redox potential (V)	$E_{\text{ox}} - E_{\text{red}}$ (V)
$[\text{Ru}(\text{pytpy})_2][\text{HSO}_4]_2$	+1.21	1.25 – 1.16
$[\text{Ru}(\mathbf{1})_2][\text{HSO}_4]_4$	+1.24	1.25 – 1.17
$[\text{Ru}(\mathbf{2})_2][\text{HSO}_4]_4$	+1.22	1.26 – 1.18
$[\text{Ru}(\mathbf{4})_2][\text{HSO}_4]_4$	+1.22	1.26 – 1.17
$[\text{Ru}(\mathbf{6})_2][\text{HSO}_4]_4$	+1.22	1.32 - 1.12

Table 3.4 A summary of the redox potentials for Ru(II) complexes with ligands **1-7**. Measurements carried out in water using  $0.1\text{M NaHSO}_4$  as the electrolyte and referenced to  $\text{Ag}/\text{Ag}^+$ .

It is reported that  $[\text{Ru}(\text{bpy})_3]^{3+}$  can act as a water oxidation catalyst<sup>18, 19</sup> and so it is probable that these complexes can also oxidise water. Cyclic voltammetry only gives information on what is happening at the tip of the electrode and not of the bulk sample.



If the water is being oxidised then not all of the Ru(III) will be reduced by the tip of the electrode as it will have already been reduced by the water. Therefore, the Ru(II)/Ru(III) oxidations are quasi-reversible.

### 3.3.8 Water Oxidation Activity

This work was carried out in collaboration with members of the Hill research group at Emory University (Atlanta).

Figures 3.17 and 3.18 show the preliminary water oxidation results when using the afore-described dyes in the water splitting system (Fig. 3.8).

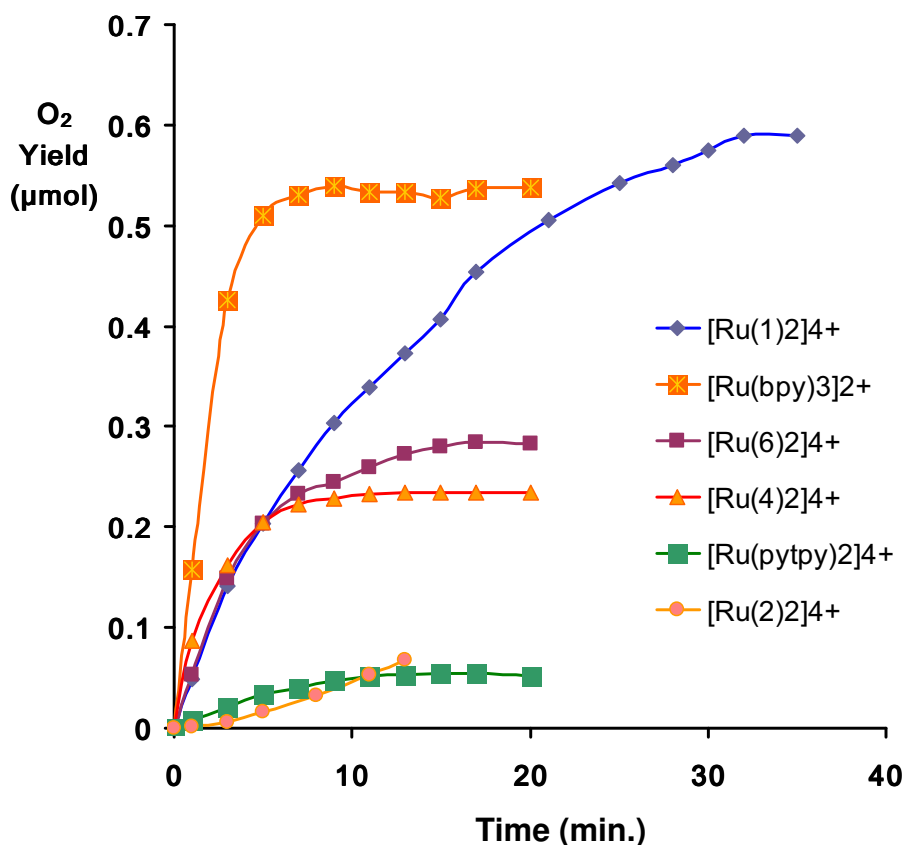


Fig. 3.17 Water oxidation activity of the  $[Ru(pytpy)_2][HSO_4]_2$  and  $[Ru(L)_2][HSO_4]_4$  complexes at pH 8. Measurements were carried out in the dark with 0.125 mM dye, 2.5 mM  $Na_2S_2O_8$  and 4  $\mu M$   $Co_4$ -POM (for full details see experimental section).

After ~20 minutes the reaction stops for all dyes except  $[Ru(1)_2]^{4+}$ . This is due to the consumption of the sacrificial electron donor, persulfate. The reaction involving  $[Ru(1)_2]^{4+}$  continues for a further ~ 15 minutes, at which point it also stops. However,

under these experimental conditions this dye is more effective at oxidising water than the standard  $[\text{Ru}(\text{bpy})_3]^{2+}$  dye.

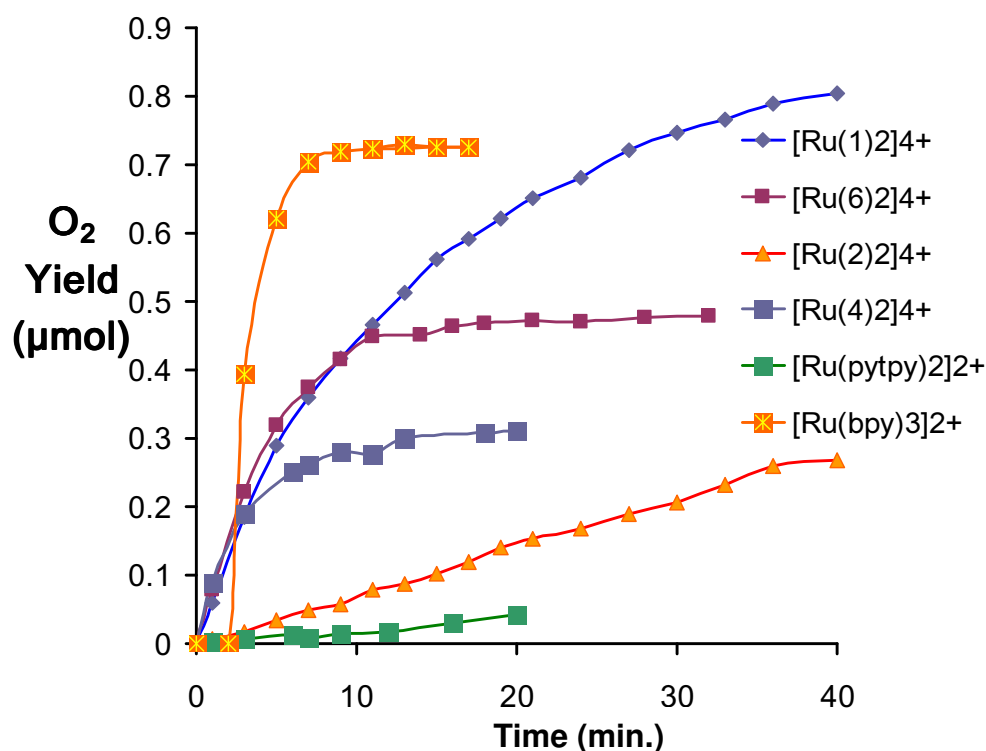


Fig. 3.18 Water oxidation activity of the  $[\text{Ru}(\text{pytpy})_2][\text{HSO}_4]_2$  and  $[\text{Ru}(\text{L})_2][\text{HSO}_4]_4$  complexes at pH 9. Measurements were carried out in the dark with 0.125 mM dye, 2.5 mM  $\text{Na}_2\text{S}_2\text{O}_8$  and 4  $\mu\text{M}$   $\text{Co}_4\text{-POM}$  (for full details see experimental section).

On increasing the pH from 8 to 9 the reactions involving all dyes yield a higher amount of  $\text{O}_2$ . After ~20 minutes the reaction stops for all dyes except  $[\text{Ru}(\text{L})_2]^{4+}$  (L = 1, 2, 6). This is due to the consumption of the sacrificial electron acceptor, persulfate. The reaction involving  $[\text{Ru}(\mathbf{6})_2]^{4+}$  continues for a further ~ 10 minutes, at which point it also stops. The reactions involving  $[\text{Ru}(\mathbf{1})_2]^{4+}$  and  $[\text{Ru}(\mathbf{2})_2]^{4+}$  continue for 40 minutes. Under these experimental conditions the  $[\text{Ru}(\mathbf{1})_2]^{4+}$  dye is again more effective at oxidising water than the standard  $[\text{Ru}(\text{bpy})_3]^{2+}$  dye.

The different activities of the complexes are explained as follows:

1. The activity of  $[\text{Ru}(\text{pytpy})_2]^{2+}$  is expected to be different to that of the other dyes as it has a +2 charge as opposed to a +4 charge.

- The initial rates of reaction of the +4 dyes are all the same, which follows the trend observed in the photophysical and electrochemical properties of the dyes.
- The change in the dyes' overall ability to oxidise water can be explained in terms of their susceptibility to basic attack at the C2 proton (Fig. 3.19).

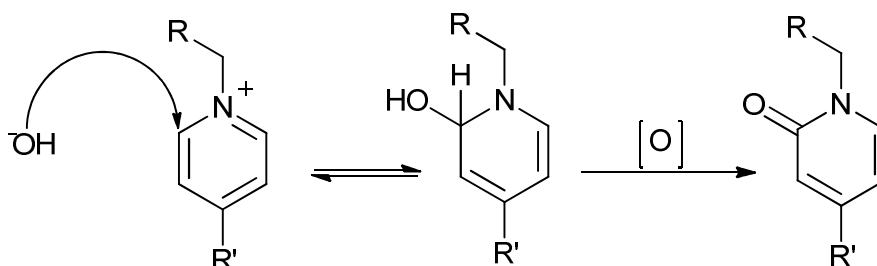


Fig. 3.19 Proposed mechanism of basic attack at the C2 proton on the terminal pyridyl rings of the  $[Ru(L)_2]^{4+}$  ( $L = 1, 2, 4, 6$ ) dyes.

Basic attack at C2 destroys the aromaticity of the pyridyl group to form a hydroxopyridyl species. This species can then be oxidised to form the pyridone, which will behave differently to the original pyridyl. Confirmation of the different susceptibilities to basic attack of the complexes can be obtained by looking at the Mulliken charges, using DFT (Table 3.5).

Complex	Stability (high to low)	Mulliken Charge on C2
$[Ru(\text{pytpy})_2]^{2+}$	1	0.146
$[Ru(\mathbf{2})_2]^{4+}$	2	0.138
$[Ru(\mathbf{4})_2]^{4+}$	3	0.128
$[Ru(\mathbf{6})_2]^{4+}$	4	0.131
$[Ru(\mathbf{1})_2]^{4+}$	5	0.142

Table 3.5 The relationship between the stability of the dye and the Mulliken Charge on C2. (DFT carried out using B3LYP/LANL2DZ/6-31G\*, see Chapter 2 for details)

As has already been stated, the  $[Ru(\text{pytpy})_2]^{2+}$  behaves differently as it has a +2 overall charge and can therefore be ignored. For complexes  $[Ru(L)_2]^{4+}$  ( $L = 1, 4, 6$ ) the trend in

Mulliken charge follows the trend in stability, ie. the more electropositive C2 is, the more susceptible the complex is to basic attack and, therefore, the less stable that complex is.

The  $[\text{Ru}(\mathbf{2})_2]^{4+}$  dye behaves differently and this is due to the potential for hydrolysis at the cyano group, which results in a zwitterion. The charge of the complex subsequently decreases from +4 to +2 and it would, therefore, be expected to behave in a similar manner to that of  $[\text{Ru}(\text{pytpy})_2]^{2+}$ , which is observed experimentally (Fig. 2.19).

### 3.4 Conclusion

In summary, the  $[\text{Ru}(\text{L})_2][\text{HSO}_4]_4$  complexes demonstrated very similar photophysical and photochemical properties to their  $[\text{Ru}(\text{L})_2][\text{PF}_6]_4$  parent complexes. Selected dyes showed water oxidation activity when used in conjunction with the  $\text{Co}_4$ -POM of the Hill group<sup>34</sup>. The different catalytic activities of the dyes could be rationalised in terms of the overall charge of the complex and their susceptibility to basic attack at the C2 position of the terminal pyridine moiety. Use of the dye  $[\text{Ru}(\mathbf{1})_2]^{4+}$  resulted in the highest  $\text{O}_2$  yield and longest running reaction. Under the experimental conditions used it performed more effectively than the standard  $[\text{Ru}(\text{bpy})_3]^{2+}$  dye. Further work in this area should be carried out into alternative sacrificial electron donors to enable a longer running water oxidation reaction.

### 3.5 Experimental

#### General Synthesis of $[\text{Ru}(\text{L})_2][\text{HSO}_4]_4$ :

The complex  $[\text{Ru}(\text{L})_2][\text{PF}_6]_4$  was stirred with ten equivalents of  $[\text{N}(\text{tBu})_4][\text{HSO}_4]$  in a mixture of 9:1 acetonitrile:dichloromethane for 30 min, during which time a precipitate formed. The precipitate was filtered over celite and washed with  $20 \text{ cm}^3$  acetonitrile, then re-dissolved in deionised water, which was subsequently removed under reduced pressure, yielding a red powder. The red powder was stirred in  $30 \text{ cm}^3$  boiling acetonitrile for 20 min, to remove any remaining  $[\text{N}(\text{tBu})_4][\text{PF}_6]$ , filtered over a sinter and washed with  $20 \text{ cm}^3$  EtOH and  $20 \text{ cm}^3$  Et<sub>2</sub>O. The product was isolated as a red powder.

#### $[\text{Ru}(\text{pytpy})_2][\text{HSO}_4]_2$

Yield: 107 mg, 78.7% (starting with 150 mg of  $[\text{Ru}(\text{pytpy})_2][\text{HSO}_4]_2$ )

<sup>1</sup>H NMR: (500 MHz, D<sub>2</sub>O, 25°C, TMS) δ/ppm: 9.30 (s, 4H, **B**<sup>3</sup>),

9.13 (d, J = 5 Hz, 4H, **C**<sup>2</sup>), 8.83 (d, J=10 Hz, 4H, **C**<sup>3</sup>), 8.72 (d, J=10 Hz, 4H, **A**<sup>3</sup>),

7.99 (t, J = 20 Hz, 10 Hz, 4H, **A**<sup>4</sup>), 7.46 (d, J = 5 Hz, 4H, **A**<sup>6</sup>),

7.22 (t, J = 10, 5 Hz, 4H **A**<sup>5</sup>);

<sup>13</sup>C NMR: (126 MHz, D<sub>2</sub>O, 25°C, TMS) δ/ppm: 160.1 (**A**<sup>2</sup>/**B**<sup>2</sup>), 158.8 (**A**<sup>2</sup>/**B**<sup>2</sup>), 156.9 (**C**<sup>4</sup>),

154.9 (**A**<sup>6</sup>), 145.2 (**C**<sup>2</sup>), 144.5 (**B**<sup>4</sup>), 141.2 (**A**<sup>4</sup>), 130.5 (**A**<sup>5</sup>), 128.4 (**C**<sup>3</sup>), 127.6 (**A**<sup>3</sup>),

124.7 (**B**<sup>3</sup>)

ESI-MS: m/z 361.0  $[\text{M}-2\text{HSO}_4]^{2+}$  (base peak, calc. 361.1);

Found: C 48.29, H 3.70, N 11.05; C<sub>40</sub>H<sub>30</sub>N<sub>8</sub>O<sub>8</sub>RuS<sub>2</sub>·4H<sub>2</sub>O requires: C 48.63, H 3.88,

N 11.34.

#### $[\text{Ru}(\mathbf{1})_2][\text{HSO}_4]_4$

Yield: 150 mg, 99.1% (starting with 174 mg of  $[\text{Ru}(\mathbf{1})_2][\text{HSO}_4]_4$ )

$^1\text{H}$  NMR: (500 MHz,  $\text{D}_2\text{O}$ ,  $25^\circ\text{C}$ , TMS)  $\delta/\text{ppm}$ : 9.25 (s, 4H,  $\mathbf{B}^3$ ),  
9.21 (d,  $J = 5.3$  Hz, 4H,  $\mathbf{C}^2$ ), 8.81 (d,  $J = 5.3$  Hz, 4H,  $\mathbf{C}^3$ ), 8.68 (d,  $J = 7.7$  Hz,  $\mathbf{A}^3$ ),  
7.95 (t,  $J = 7.3$  Hz, 4H,  $\mathbf{A}^4$ ), 7.59 (m, 4H,  $\mathbf{D}^2$ ), 7.56 (m, 6H,  $\mathbf{D}^3 + \mathbf{D}^4$ ),  
7.42 (d,  $J = 5.2$  Hz, 4H,  $\mathbf{A}^6$ ), 7.18 (m, 4H,  $\mathbf{A}^5$ ), 5.97 (s, 4H, *a*).  
 $^{13}\text{C}$  NMR: (126 MHz,  $\text{D}_2\text{O}$ ,  $25^\circ\text{C}$ , TMS)  $\delta/\text{ppm}$ : 160.0 ( $\mathbf{A}^2/\mathbf{B}^2$ ), 158.8 ( $\mathbf{A}^2/\mathbf{B}^2$ ),  
156.0 ( $\mathbf{C}^4$ ), 154.9 ( $\mathbf{A}^6$ ), 148.0 ( $\mathbf{C}^2$ ), 143.7 ( $\mathbf{B}^4$ ), 141.2 ( $\mathbf{A}^4$ ), 135.4 ( $\mathbf{D}^1$ ), 132.9 ( $\mathbf{D}^4$ ),  
132.5 ( $\mathbf{D}^3$ ), 132.1 ( $\mathbf{D}^2$ ), 130.5 ( $\mathbf{A}^5$ ), 129.2 ( $\mathbf{C}^3$ ), 127.6 ( $\mathbf{A}^3$ ), 124.6 ( $\mathbf{B}^3$ ), 67.3 (*a*).  
MALDI-TOF:  $m/z$  1193.1 [ $\text{M} - \text{HSO}_4$ ] $^+$  (calc. 1195.1).

### [Ru(2)<sub>2</sub>][HSO<sub>4</sub>]<sub>4</sub>

Yield: 41.7 mg, 59.6% (starting with 80 mg of [Ru(2)<sub>2</sub>][HSO<sub>4</sub>]<sub>4</sub>)

$^1\text{H}$  NMR: (500 MHz,  $\text{D}_2\text{O}$ ,  $25^\circ\text{C}$ , TMS)  $\delta/\text{ppm}$ : 9.28 (s, 4H,  $\mathbf{B}^3$ ),  
9.25 (d,  $J = 5.6$  Hz, 4H,  $\mathbf{C}^2$ ), 8.87 (d,  $J = 5.6$  Hz, 4H,  $\mathbf{C}^3$ ), 8.70 (d,  $J = 7.9$  Hz,  $\mathbf{A}^3$ ),  
7.97 (t,  $J = 7.6$  Hz, 4H,  $\mathbf{A}^4$ ), 7.94 (d,  $J = 8.1$  Hz, 4H,  $\mathbf{D}^3$ ), 7.73 (d,  $J = 8.0$  Hz, 4H,  $\mathbf{D}^2$ ),  
7.44 (d,  $J = 5.2$  Hz, 4H,  $\mathbf{A}^6$ ), 7.20 (m, 4H,  $\mathbf{A}^5$ ), 6.09 (s, 4H, *a*).  
 $^{13}\text{C}$  NMR: (126 MHz,  $\text{D}_2\text{O}$ ,  $25^\circ\text{C}$ , TMS)  $\delta/\text{ppm}$ : 160.1 ( $\mathbf{A}^2/\mathbf{B}^2$ ), 158.8 ( $\mathbf{A}^2/\mathbf{B}^2$ ), 155.0 ( $\mathbf{A}^6$ ),  
148.4 ( $\mathbf{C}^2$ ), 131.2 ( $\mathbf{A}^4$ ), 140.7 ( $\mathbf{D}^1$ ), 136.4 ( $\mathbf{D}^3$ ), 132.4 ( $\mathbf{D}^2$ ), 130.6 ( $\mathbf{A}^5$ ), 129.4 ( $\mathbf{C}^3$ ),  
127.7 ( $\mathbf{A}^3$ ), 124.7 ( $\mathbf{B}^3$ ), 122.7 ( $\mathbf{D}-\text{C}\equiv\text{N}$ ), 115.4 ( $\mathbf{D}^4$ ), 66.5 (*a*), ( $\text{C}^{\text{B}4}$  and  $\text{C}^{\text{C}4}$  not resolved).  
MALDI-TOF:  $m/z$  839.0 [Ru(2)(Hpytpy)] $^+$  (calc. 839.2), 723.9 [Ru(pytpy)(Hpytpy)] $^+$   
(calc. 723.2). Found: C 46.42, H 3.60, N 10.00;  $\text{C}_{56}\text{H}_{44}\text{N}_{10}\text{O}_{16}\text{RuS}_4 \cdot 6\text{H}_2\text{O}$  requires  
C 46.37, H 3.89, N 9.66 (see text).

### [Ru(3)<sub>2</sub>][HSO<sub>4</sub>]<sub>4</sub>

Yield: 230 mg, 97.9% (starting with 267 mg of [Ru(3)<sub>2</sub>][HSO<sub>4</sub>]<sub>4</sub>)

$^1\text{H}$  NMR: (500 MHz,  $\text{D}_2\text{O}$ ,  $25^\circ\text{C}$ , TMS)  $\delta/\text{ppm}$ : 9.29 (s, 4H,  $\mathbf{B}^3$ ),  
9.27 (d,  $J = 6.4$  Hz, 4H,  $\mathbf{C}^2$ ), 8.88 (d,  $J = 5.5$  Hz, 4H,  $\mathbf{C}^3$ ), 8.70 (d,  $J = 7.8$  Hz,  $\mathbf{A}^3$ ),  
8.39 (d,  $J = 20.8.2$  Hz, 4H,  $\mathbf{D}^3$ ), 7.97 (t,  $J = 7.6$  Hz, 4H,  $\mathbf{A}^4$ ), 7.80 (d,  $J = 8.2$  Hz, 4H,  $\mathbf{D}^2$ ),  
7.44 (d,  $J = 4.7$  Hz, 4H,  $\mathbf{A}^6$ ), 7.20 (m, 4H,  $\mathbf{A}^5$ ), 6.14 (s, 4H, *a*).  
 $^{13}\text{C}$  NMR: (126 MHz,  $\text{D}_2\text{O}$ ,  $25^\circ\text{C}$ , TMS)  $\delta/\text{ppm}$ : 160.0 ( $\mathbf{A}^2/\mathbf{B}^2$ ), 158.8 ( $\mathbf{A}^2/\mathbf{B}^2$ ), 154.9 ( $\mathbf{A}^6$ ),

151.4 (**D**<sup>4</sup>), 148.5 (**C**<sup>2</sup>), 143.5 (**D**<sup>1</sup>), 141.2 (**A**<sup>4</sup>), 132.9 (**D**<sup>2</sup>), 130.5 (**A**<sup>5</sup>), 129.5 (**C**<sup>3</sup>), 127.7 (**A**<sup>3</sup>), 127.4 (**D**<sup>3</sup>), 124.7 (**B**<sup>3</sup>), 66.1 (*a*), (**B**<sup>4</sup> and **C**<sup>4</sup> not resolved).

MALDI-TOF: 1001.6 [**M** – 3H<sub>2</sub>SO<sub>4</sub>]<sup>+</sup>

(calc. 1001.1), 724.0 [Ru(Hpytpy)<sub>2</sub>]<sup>+</sup> (calc. 724.2)

Found: C 42.42, H 3.64, N 9.32; C<sub>54</sub>H<sub>44</sub>N<sub>10</sub>O<sub>20</sub>RuS<sub>4</sub>·8H<sub>2</sub>O requires C 42.49, H 3.96, N 9.18 (see text).

### [Ru(**4**)<sub>2</sub>][HSO<sub>4</sub>]<sub>4</sub>

Yield: 257 mg, 98.7% (starting with 304 mg of [Ru(**4**)<sub>2</sub>][HSO<sub>4</sub>]<sub>4</sub>)

<sup>1</sup>H NMR: (500 MHz, D<sub>2</sub>O, 25°C, TMS) δ/ppm: 9.27 (s, 4H, **B**<sup>3</sup>), 9.18 (d, *J* = 6.3 Hz, 4H, **C**<sup>2</sup>), 8.81 (d, *J* = 6.4 Hz, 4H, **C**<sup>3</sup>), 8.69 (d, *J* = 7.9 Hz, **A**<sup>3</sup>), 7.96 (t, *J* = 7.8 Hz, 4H, **A**<sup>4</sup>), 7.44 (d, *J* = 5.1 Hz, 4H, **A**<sup>6</sup>), 7.20 (m, 4H, **A**<sup>5</sup>), 4.80 (coincident with solvent, *a*), 1.75 (t, *J* = 7.3 Hz, 6H, *b*).

<sup>13</sup>C NMR: (126 MHz, D<sub>2</sub>O, 25°C, TMS) δ/ppm 160.0 (**A**<sup>2</sup>/**B**<sup>2</sup>), 158.8 (**A**<sup>2</sup>/**B**<sup>2</sup>), 155.5 (**C**<sup>4</sup>), 154.9 (**A**<sup>6</sup>), 147.7 (**C**<sup>2</sup>), 143.9 (**B**<sup>4</sup>), 141.1 (**A**<sup>4</sup>), 130.5 (**A**<sup>5</sup>), 129.1 (**C**<sup>3</sup>), 127.6 (**A**<sup>3</sup>), 124.6 (**B**<sup>3</sup>), 60.0 (*a*), 18.4 (*b*).

MALDI-TOF: *m/z* 850.4 [Ru(**4**)(Hpytpy)(HSO<sub>4</sub>)]<sup>+</sup> (calc. 849.2),

821.4 [Ru(Hpytpy)<sub>2</sub>(HSO<sub>4</sub>)]<sup>+</sup> (calc. 821.1), 751.3 [Ru(**4**)(Hpytpy)(HSO<sub>4</sub>)]<sup>+</sup> (calc. 752.2), 723.3 [Ru(pytpy)(Hpytpy)]<sup>+</sup> (calc. 723.2).

### [Ru(**5**)<sub>2</sub>][HSO<sub>4</sub>]<sub>4</sub>

Yield: 95.5 mg, 65.9% (starting with 163 mg of [Ru(**5**)<sub>2</sub>][HSO<sub>4</sub>]<sub>4</sub>)

<sup>1</sup>H NMR: (500 MHz, D<sub>2</sub>O, 25°C, TMS) δ/ppm 9.36 (d, *J* = 6.5 Hz, 4H, **C**<sup>2</sup>), 9.33 (s, 4H, **B**<sup>3</sup>), 8.98 (d, *J* = 6.6 Hz, 4H, **C**<sup>3</sup>), 8.72 (d, *J* = 8.1 Hz, **A**<sup>3</sup>), 7.98 (t, *J* = 7.5 Hz, 4H, **A**<sup>4</sup>), 7.45 (d, *J* = 5.3 Hz, 4H, **A**<sup>6</sup>), 7.21 (m, 4H, **A**<sup>5</sup>), 6.09 (s, 4H, *a*).

$^{13}\text{C}$  NMR: (126 MHz,  $\text{D}_2\text{O}$ , 25°C, TMS)  $\delta/\text{ppm}$  159.9 ( $\text{A}^2/\text{B}^2$ ), 158.8 ( $\text{A}^2/\text{B}^2$ ), 157.7 ( $\text{C}^4$ ), 154.9 ( $\text{A}^6$ ), 148.6 ( $\text{C}^2$ ), 143.1 ( $\text{B}^4$ ), 141.2 ( $\text{A}^4$ ), 130.5 ( $\text{A}^5$ ), 129.6 ( $\text{C}^3$ ), 127.7 ( $\text{A}^3$ ), 124.7 ( $\text{B}^3$ ), 116.6 (b), 50.5 (a).

MALDI-TOF  $m/z$  859.8  $[\text{Ru}(\mathbf{5})(\text{pytpy})(\text{HSO}_4)]^+$  (calc. 859.1),

761.6  $[\text{Ru}(\mathbf{5})(\text{pytpy})]^+$  (calc. 762.2), 722.3  $[\text{Ru}(\text{pytpy})_2]^+$  (calc. 722.2).

### $[\text{Ru}(\mathbf{6})_2][\text{HSO}_4]_4$

Yield: 148 mg, 81.6% (starting with 210 mg of  $[\text{Ru}(\mathbf{6})_2][\text{HSO}_4]_4$ )

$^1\text{H}$  NMR: (500 MHz,  $\text{D}_2\text{O}$ , 25°C, TMS)  $\delta/\text{ppm}$ : 9.28 (s, 4H,  $\text{B}^3$ ), 9.16 (d,  $J = 5.9$  Hz, 4H,  $\text{C}^2$ ), 8.84 (d,  $J = 5.8$  Hz, 4H,  $\text{C}^3$ ), 8.70 (d,  $J = 7.9$  Hz, 4H,  $\text{A}^3$ ), 7.97 (t,  $J = 7.6$  Hz, 4H,  $\text{A}^4$ ), 7.45 (d,  $J = 5.3$  Hz, 4H,  $\text{A}^6$ ), 7.21 (m, 4H,  $\text{A}^5$ ), 6.27 (m, 2H, b), 5.66 (d,  $J = 10.3$  Hz, 2H,  $c_1$ ), 5.63 (d,  $J = 17.2$  Hz, 2H,  $c_2$ ), 5.39 (d,  $J = 6.1$  Hz, 4H, a).

$^{13}\text{C}$  NMR: (126 MHz,  $\text{D}_2\text{O}$ , 25°C, TMS)  $\delta/\text{ppm}$ : 160.0 ( $\text{A}^2/\text{B}^2$ ), 158.8 ( $\text{A}^2/\text{B}^2$ ), 156.0 ( $\text{C}^4$ ), 154.9 ( $\text{A}^6$ ), 148.0 ( $\text{C}^2$ ), 143.8 ( $\text{B}^4$ ), 141.2 ( $\text{A}^4$ ), 132.6 (b), 130.5 ( $\text{A}^5$ ), 129.1 ( $\text{C}^3$ ), 127.7 ( $\text{A}^3$ ), 126.2 (c), 124.6 ( $\text{B}^3$ ), 66.1 (a).

MALDI-TOF:  $m/z$  803.2  $[\text{Ru}(\mathbf{6})_2]^+$  (calc. 804.2), 763.2  $[\text{Ru}(\mathbf{6})(\text{pytpy})]^+$  (calc. 763.2), 724.0  $[\text{Ru}(\text{Hpytpy})_2]^+$  (calc. 724.2).

Found: C 42.84, H 3.65, N 8.99;  $\text{C}_{46}\text{H}_{42}\text{N}_8\text{O}_{16}\text{RuS}_4 \cdot 5\text{H}_2\text{O}$  requires C 43.09, H 4.09, N 8.74 (see text).

### $[\text{Ru}(\mathbf{7})_2][\text{HSO}_4]_4$

Yield: 35 mg, 68% (starting with 58 mg of  $[\text{Ru}(\mathbf{7})_2][\text{HSO}_4]_4$ )

$^1\text{H}$  NMR: (500 MHz,  $\text{D}_2\text{O}$ , 25°C, TMS)  $\delta/\text{ppm}$ : 9.29 (s, 4H,  $\text{B}^3$ ), 9.17 (d,  $J = 6.4$  Hz, 4H,  $\text{C}^2$ ), 8.83 (d,  $J = 6.4$  Hz, 4H,  $\text{C}^3$ ), 8.71 (d,  $J = 8.1$  Hz, 4H,  $\text{A}^3$ ), 7.98 (t,  $J = 7.8$  Hz, 4H,  $\text{A}^4$ ), 7.45 (d,  $J = 5.4$  Hz, 4H,  $\text{A}^6$ ), 7.21 (m, 4H,  $\text{A}^5$ ), 4.78 (t, overlapping solvent, a), 2.13 (m, 4H, b), 1.44 (m, 8H, c+d), 1.34-1.30 (overlapping m, 12H, e+f+g), 0.87 (t,  $J = 6.8$  Hz, 6H, h).



$^{13}\text{C}$  NMR: (126 MHz,  $\text{D}_2\text{O}$ ,  $25^\circ\text{C}$ , TMS)  $\delta/\text{ppm}$ : 160.0 ( $\text{A}^2/\text{B}^2$ ), 158.8 ( $\text{A}^2/\text{B}^2$ ), 155.5 ( $\text{C}^4$ ), 154.8 ( $\text{A}^6$ ), 147.9 ( $\text{C}^2$ ), 143.8 ( $\text{B}^4$ ), 141.1 ( $\text{A}^4$ ), 130.4 ( $\text{A}^5$ ), 129.0 ( $\text{C}^3$ ), 127.6 ( $\text{A}^3$ ), 124.6 ( $\text{B}^3$ ), 64.7 (*a*), 33.7 (*eff/g*), 33.4 (*b*), 30.9 (*c/d*), 30.8 (*eff/g*), 28.1 (*c/d*), 24.7 (*eff/g*), 16.2 (*h*).

MALDI-TOF:  $m/z$  1237.8 [ $\text{M} - \text{HSO}_4$ ] $^+$  (calc. 1239.3), 949.6 [ $\text{M} - 4\text{HSO}_4$ ] $^+$  (calc. 948.4), 723.3 [ $\text{Ru}(\text{pytpy})(\text{Hpytpy})$ ] $_3^+$  (calc. 723.2).

## Light-driven Catalytic Experiments

Measurements were carried out by Dr. Yurii Geletii and Hongjin Lv at Emory University in Atlanta.

The light-driven water oxidation was performed in a cylindrical cuvette (NSG, 32UV10) with a total volume of  $\sim 2.5$  ml. The cell was filled with 2.0 ml of reaction solution with 0.125 mM dye, 2.5 mM  $\text{Na}_2\text{S}_2\text{O}_8$ , 4  $\mu\text{M}$   $\text{Co}_4\text{P}_2\text{-POM}$  catalyst (in 80 mM sodium borate buffer (initial pH 8.0/ 9.0)). The reaction cell was sealed with a rubber septum, carefully deaired and filled with Ar. All procedures were performed with a minimum exposure to ambient light. The reaction was initiated by turning on the LED-light source ( $\lambda = 490$  nm; light intensity 7 mW, beam diameter  $\sim 0.4$  cm).

A magnetically-coupled stirring system (SYS 114, SPECTROCELL) was used to mix reaction solutions ( $4 \times 10^3$  RPM). The  $\text{O}_2$  concentration in the headspace was quantified by GC. The solution pH was measured after the reaction.

Analysis of dioxygen in the reaction headspace was performed using a computer controlled Agilent 6850 model gas chromatograph equipped with a thermal conductivity detector and a HP-MOLESIEVE capillary GC column (30 m x 0.535 mm x 25.00  $\mu\text{m}$ ) Argon was used as a carrier gas. Typically, the  $\text{O}_2$  yield was quantified by withdrawing a gas sample from the headspace without stopping the reaction. Contamination of the headspace with air was corrected by quantification of  $\text{N}_2$  present in the head-space (from the  $\text{N}_2$  peak in the GC traces).

### 3.6 References

1. G. J. Whitmarch, *Encyclopedia of Life Sciences*, Macmillan Publ., 2002.
2. J. Barber and M. D. Archer, *J. Photochem. Photobiol. A*, 2001, **142**, 97-106.
3. T. M. I. K.N. Ferreira, K. Maghlaoui, J. Barber, S. Iwata, *Science*, 2004, **303**, 1831-1838.
4. A. Mishra, W. Wernsdorfer, K. A. Abboud and G. Christou, *Chem. Commun.*, 2005, 54-56.
5. F. M. Ashmawy, C. A. McAuliffe, R. V. Parish and J. Tames, *J. Chem. Soc. Dalton Trans.*, 1985, 1391-1397.
6. X. Liu and F. Wang, *Coord. Chem. Rev.*, 2012, **256**, 1115-1136.
7. H. Yamazaki, A. Shouji, M. Kajita and M. Yagi, *Coord. Chem. Rev.*, 2010, **254**, 2483-2491.
8. J. S. V. J. Limburg, L.M. Liable-Sands, A.L. Rheingold, R.H. Crabtree, G.W. Brudvig, *Science*, 1999, **283**, 1524-1527.
9. G. Sprintschnik, H. W. Sprintschnik, P. P. Kirsch and D. G. Whitten, *J. Am. Chem. Soc.*, 1976, **98**, 2337-2338.
10. R. Zong and R. P. Thummel, *J. Am. Chem. Soc.*, 2005, **127**, 12802-12803.
11. J. Hagen, *Industrial Catalysis: A Practical Approach*, Wiley-VCH, Weinheim, Germany, 2006.
12. F. Puntoriero, A. Sartorel, M. Orlandi, G. La Ganga, S. Serroni, M. Bonchio, F. Scandola and S. Campagna, *Coord. Chem. Rev.*, 2011, **255**, 2594-2601.
13. B. Limburg, E. Bouwman and S. Bonnet, *Coord. Chem. Rev.*, 2012, **256**, 1451-1467.
14. N. Kaveevivitchai, R. Zong, H.-W. Tseng, R. Chitta and R. P. Thummel, *Inorg. Chem.*, 2012, **51**, 2930-2939.
15. J. J. Concepcion, M.-K. Tsai, J. T. Muckerman and T. J. Meyer, *J. Am. Chem. Soc.*, 2010, **132**, 1545-1557.
16. L. Duan, F. Bozoglian, S. Mandal, B. Stewart, T. Privalov, A. Llobet and L. Sun, *Nature Chem.*, 2012, **4**, 418-423.
17. C. Streb, *Dalton Trans.*, 2012, **41**, 1651-1659.
18. Y. V. Geletii, Z. Huang, Y. Hou, D. G. Musaev, T. Lian and C. L. Hill, *J. Am. Chem. Soc.*, 2009, **131**, 7522-7523.
19. Y. V. Geletii, C. Besson, Y. Hou, Q. Yin, D. G. Musaev, D. Quiñonero, R. Cao, K. I. Hardcastle, A. Proust, P. Kögerler and C. L. Hill, *J. Am. Chem. Soc.*, 2009, **131**, 17360-17370.
20. Z. Huang, Z. Luo, Y. V. Geletii, J. W. Vickers, Q. Yin, D. Wu, Y. Hou, Y. Ding, J. Song, D. G. Musaev, C. L. Hill and T. Lian, *J. Am. Chem. Soc.*, 2011, **133**, 2068-2071.
21. Y. V. Geletii, B. Botar, P. Kögerler, D. A. Hillesheim, D. G. Musaev and C. L. Hill, *Angew. Chem. Int. Ed.*, 2008, **47**, 3896-3899.
22. S. Tanaka, M. Annaka and K. Sakai, *Chem. Commun.*, 2012, **48**, 1653-1655.
23. D.-L. Long, E. Burkholder and L. Cronin, *Chem. Soc. Rev.*, 2007, **36**, 105-121.
24. C. Lydon, C. Busche, H. N. Miras, A. Delf, D.-L. Long, L. Yellowlees and L. Cronin, *Angew. Chem. Int. Ed.*, 2012, **51**, 2115-2118.
25. P. Putaj and F. Lefebvre, *Coord. Chem. Rev.*, 2011, **255**, 1642-1685.
26. J. J. Stracke and R. G. Finke, *J. Am. Chem. Soc.*, 2011, **133**, 14872-14875.

27. J. B. Gerken, J. G. McAlpin, J. Y. C. Chen, M. L. Rigsby, W. H. Casey, R. D. Britt and S. S. Stahl, *J. Am. Chem. Soc.*, 2011, **133**, 14431-14442.
28. M. Natali, S. Berardi, A. Sartorel, M. Bonchio, S. Campagna and F. Scandola, *Chem. Commun.*, 2012, **48**, 8808-8810.
29. K. Heussner, K. Peuntinger, N. Rockstroh, L. C. Nye, I. Ivanović-Burmazović, S. Rau and C. Streb, *Chem. Commun.*, 2011, **47**, 6852-6854.
30. P.-E. Car, M. Guttentag, K. K. Baldrige, R. Alberto and G. R. Patzke, *Green Chem.*, 2012, **14**, 1680-1688.
31. J. J. Walsh, J. Zhu, Q. Zeng, R. J. Forster and T. E. Keyes, *Dalton Trans.*, 2012, **41**, 9928-9937.
32. J. J. Walsh, C. T. Mallon, A. M. Bond, T. E. Keyes and R. J. Forster, *Chem. Commun.*, 2012, **48**, 3593-3595.
33. D. Lieb, A. Zahl, E. F. Wilson, C. Streb, L. C. Nye, K. Meyer and I. Ivanović-Burmazović, *Inorg. Chem.*, 2011, **50**, 9053-9058.
34. Q. Yin, J. M. Tan, C. Besson, Y. V. Geletii, D. G. Musaev, A. E. Kuznetsov, Z. Luo, K. I. Hardcastle and C. L. Hill, *Science*, 2010, **328**, 342-345.
35. A. L. Kaledin, Z. Huang, Q. Yin, E. L. Dunphy, E. C. Constable, C. E. Housecroft, Y. V. Geletii, T. Lian, C. L. Hill and D. G. Musaev, *J. Phys. Chem. A*, 2010, **114**, 6284-6297.
36. J. E. Beves, E. L. Dunphy, E. C. Constable, C. E. Housecroft, C. J. Kepert, M. Neuburger, D. J. Price and S. Schaffner, *Dalton Trans.*, 2008, 386-396.
37. A. Amini, A. Harriman and A. Mayeux, *Phys. Chem. Chem. Phys.*, 2004, **6**, 1157-1164.

## Chapter 4

### Copper(I) Polypyridyl Complexes for Application in DSSCs.

#### 4.1 Introduction

Nearly a decade after the Kyoto treaty<sup>1</sup> entered into force there is an increasing usage of energy sources which offer an alternative to the consumption of fossil fuels. One of these alternative energy sources is solar energy. There are a number of different types of solar cell available (§Introduction) and the focus of this project has been on dye-sensitised solar cells (DSSCs)<sup>2</sup>.

Dye sensitised solar cells consist of the following components (Fig. 4.1)<sup>2-6</sup>:

- **Counter electrode** – This is a transparent conducting oxide and the most commonly chosen type is fluorine doped tin oxide (FTO).
- **Semiconductor** – This is the main component of a DSSC. Titanium dioxide (TiO<sub>2</sub>) is the most frequently used in DSSCs. It was found that sheets of TiO<sub>2</sub> were not efficient enough so nanoparticles are now used<sup>7</sup>. This results in a larger surface area, which means that more dye particles can bind per unit area of the TiO<sub>2</sub>. There are three polymorphs of TiO<sub>2</sub> but anatase is used as it has the largest energy gap between the valence and the conductance bands (bandgap = 3.2 eV).
- **Dye** –A dye, which is capable of absorbing visible light and binding to TiO<sub>2</sub>, is used as a sensitizer because the band gap of TiO<sub>2</sub> is so large it is poor at absorbing visible light. Research into many organic and inorganic dyes has been carried out over the years and the most efficient sensitisers to date are based on ruthenium polypyridyl complexes.
- **Redox couple** – The most common redox couple is iodide (I<sup>-</sup>)/triiodide (I<sub>3</sub><sup>-</sup>) but alternatives include cobalt(II)/cobalt(III), thiocyanate/trithiocyanate and organic systems such as TEMPO<sup>8</sup>.

The working principles of a DSSC are depicted in Fig. 4.1.

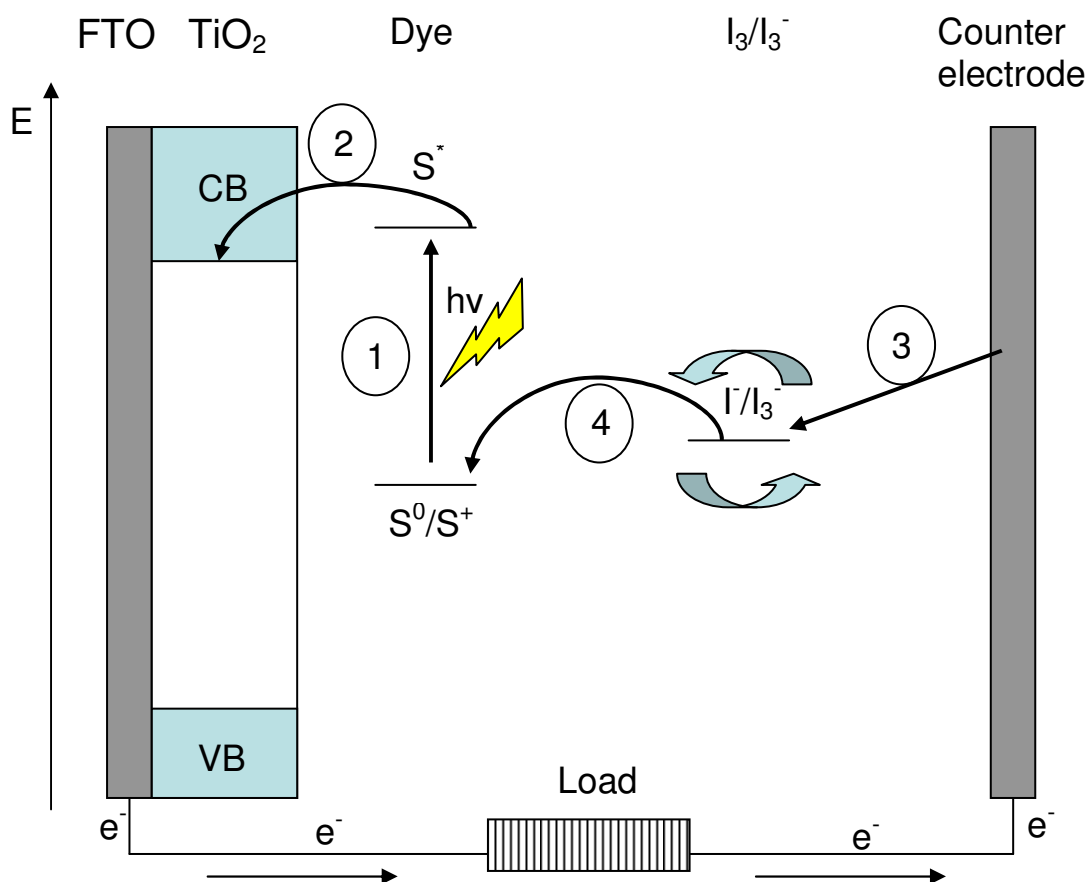
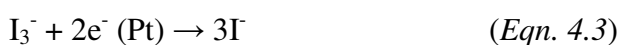


Fig. 4.1 The principles of a dye-sensitised solar cell.

On absorption of light, the dye (S) is promoted to an excited state ( $S^*$ ) as an electron is transferred from the highest-occupied molecular orbital (HOMO) of the complex, to the lowest unoccupied molecular orbital (LUMO) (step 1, eqn. 4.1). (This is a simplified model because there are multiple molecular orbitals close in energy around both the HOMO and the LUMO.) The electron is then injected into the  $\text{TiO}_2$  leaving the dye in an oxidised state ( $S^+$ ) (step 2, Eqn 4.2).



The counter-electrode donates two electrons to  $\text{I}_3^-$ , generating  $\text{I}^-$  (step 3, Eqn. 4.3).



The I<sup>-</sup> then reduces the oxidised dye back to its original state (step 4, Eqn. 4.4) and the whole cycle can start again.



Ideally, to be an efficient sensitiser, a dye needs to have the following characteristics<sup>2-6, 9</sup>:

- It must be able to absorb light over the entire visible spectrum and into the near infra-red.
- It must have anchoring groups, such as -COOH, -H<sub>2</sub>PO<sub>3</sub>, -CN, to enable binding to the TiO<sub>2</sub> nanoparticles.
- In its excited state, the dye must be higher in energy than the conductance band of the TiO<sub>2</sub> so that injection of an electron is faster than excited state decay.
- In its oxidised state, the dye needs to be more positive in energy than the redox couple, to enable reduction of the dye.

To compare solar cells and determine the efficiency four parameters are used<sup>2-6, 9-11</sup>.

1. **IPCE** – Incident monochromatic photon-to-electron conversion, also known as the external quantum efficiency. The IPCE is defined as the number of electrons, generated by light, in the external circuit, divided by the number of incident photons as a function of excitation wavelength.
2. **V<sub>oc</sub>** – Open circuit photovoltage. This is determined by the gap between the electrolyte (ie. redox couple) redox potential and the quasi Fermi level of TiO<sub>2</sub> under illumination.
3. **J<sub>sc</sub>** – Short circuit current density. This is the number of electrons being injected into the TiO<sub>2</sub> by the dye and it is limited by the absorption properties of said dye. For example, a dye with an absorption onset of 800 nm has a theoretical maximum J<sub>sc</sub> of 26 mA cm<sup>-2</sup>, whereas a dye with an absorption onset of 550 nm only has a theoretical maximum J<sub>sc</sub> of 10 mA cm<sup>-2</sup>.
4. **ff** – Fill factor. This is a number between 0 and 1 which expresses the ratio of the theoretical maximum power to the actual power obtained and is calculated using Eqn 4.5.

$$ff = \frac{P_{\max}}{J_{sc} \times V_{oc}} \quad (\text{Eqn. 4.5})$$

The overall efficiency ( $\eta$ ) of a solar cell is calculated as follows (Eqn 4.6):

$$\eta = \frac{J_{sc} \times V_{oc} \times FF}{P_{in}} \quad (\text{Eqn. 4.6})$$

where  $P_{in}$  is the intensity of the incident light.

Since Graetzel's first DSSC publication in 1991<sup>7</sup>, ruthenium has been the transition metal of choice when synthesising dyes for dye-sensitised solar cells and to date the most efficient DSSCs have been fabricated using ruthenium polypyridyl complexes (Fig 4.2).

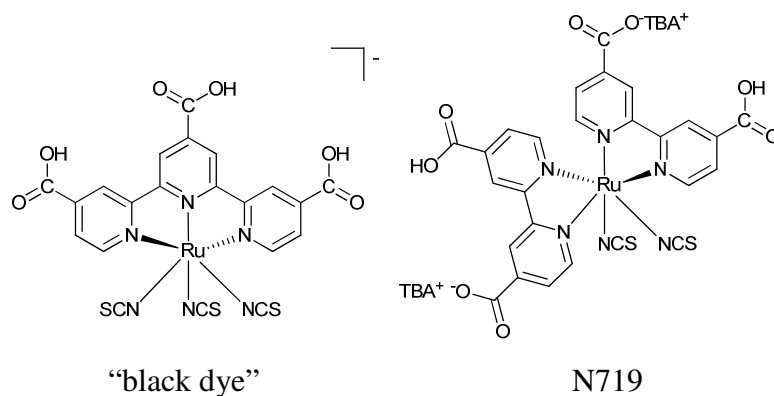


Fig. 4.2 Two of the best ruthenium polypyridyl complexes to date for application as sensitisers in DSSCs<sup>2, 12</sup>.

The dye N719 is often viewed as the research “standard”<sup>12</sup> and publications reporting efficiencies of solar cells using new dyes usually quote the efficiency values with respect to that of a cell made with N719, fabricated under the same conditions.

However, quoted efficiencies are dependent upon the construction of the cell, electrolyte etc. and comparisons across a range of measurements carried out in different laboratories can sometimes be meaningless.

Now, a new area of research is emerging utilising the transition metal, copper. There are two major advantages of copper over ruthenium. The advantage of copper is its availability; not only is it much more abundant in the Earth's crust than ruthenium but it can also be recovered from scrap metal, it is also easier to extract from its ore than

ruthenium. Due to its availability, copper is much cheaper than ruthenium. One gram of ruthenium powder from Sigma Aldrich costs 272 CHF, compared to one gram of copper powder for 0.20 CHF (prices correct August 2012). The first reported use of a Cu(I) complex as a photosensitiser was by Sauvage *et al* in 1994<sup>13</sup>. The complex consisted of two carboxyphenyl substituted phenanthroline ligands encapsulating a Cu(I) centre (Fig 4.3).

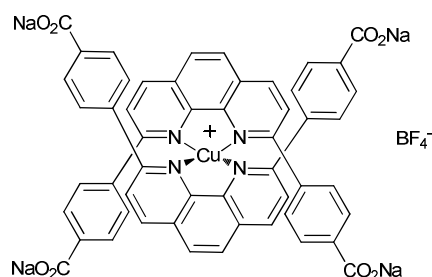


Fig. 4.3 Tetrasodium bis(2,9-(4-carboxylatophenyl)-1,10-phenanthroline)copper(I) tetrafluoroborate. The first Cu(I) complex used as a photosensitiser, reported by Sauvage *et al.*<sup>13</sup>.

In methanol solution the complex showed an MLCT band with  $\lambda_{\text{max}} = 440 \text{ nm}$  ( $\epsilon = 3000 \text{ dm}^3 \text{ mol}^{-1} \text{ cm}^{-1}$ ) and a shoulder at  $560 \text{ nm}$  ( $\epsilon = 1100 \text{ dm}^3 \text{ mol}^{-1} \text{ cm}^{-1}$ ). The dye was anchored to  $\text{TiO}_2$  by means of the carboxylate groups and the photocurrent was measured. The fill factor (ff) was found to be 0.6, the open circuit voltage ( $V_{\text{oc}}$ ) was 0.6 V and the photocurrent was measured at  $0.6 \text{ mA cm}^{-2}$ . The fill factor and the open circuit voltage were reasonable for a DSSC but the photocurrent was very poor.

The next publication describing the use of Cu(I) dyes as photosensitisers was not until 2002 when Hamada *et al.* reported a homoleptic Cu(I) complex with carboxy functionalised bipyridine ligands (Fig 4.4)<sup>14</sup>.



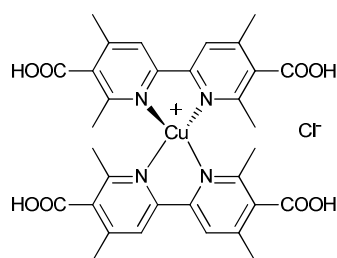


Fig. 4.4. Bis(4,4',6,6'-tetramethyl-2,2'-bipyridine-5,5'-dicarboxylic acid) copper(I) chloride reported by Hamada et al.<sup>14</sup>.

The complex exhibited an MLCT absorption with  $\lambda_{\max} = 450$  nm ( $\epsilon = 6400 \text{ dm}^3 \text{ mol}^{-1} \text{ cm}^{-1}$ ) and as such, was suitable for use as a sensitizer for a DSSC. The  $V_{\text{oc}}$  was slightly higher than that of Sauvage's complex (630 mV) as was the short circuit current ( $3.9 \text{ mA cm}^{-2}$ ). The IPCE was 30% at 460 nm.

Six years later the Constable group reported two complexes (Fig 4.5) which were very effective photosensitisers, resulting in DSSC devices with efficiencies of 1.9 and 2.3% (compared to N719 with an efficiency of 9.7%)<sup>15</sup>.

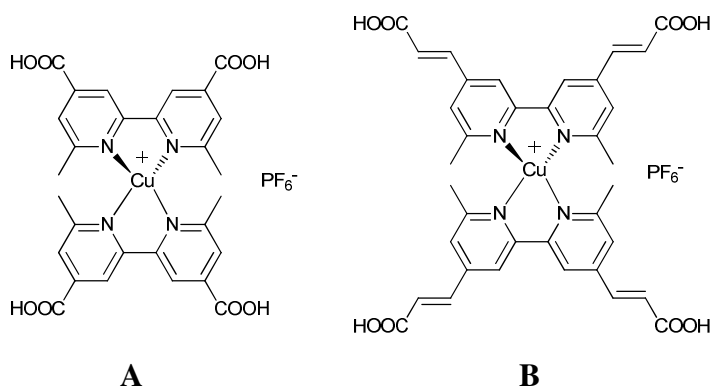


Fig. 4.5 The two Cu(I) complexes reported by Constable et al. in 2008<sup>15</sup>.

The MLCT band of complex **B** ( $\lambda_{\max} = 506$  nm) is red-shifted compared to that of complex **A** ( $\lambda_{\max} = 495$  nm). Complex **B** is also more efficient at absorbing light ( $\epsilon = 3650 \text{ dm}^3 \text{ mol}^{-1} \text{ cm}^{-1}$  compared to  $\epsilon = 450 \text{ dm}^3 \text{ mol}^{-1} \text{ cm}^{-1}$ ). Therefore, it is unsurprising that complex **B** results in a device with a higher efficiency than that of complex **A**. (The  $J_{\text{sc}}$ , and IPCE values are all higher for the device using complex **B** than for the device using complex **A**.)

A further paper detailed similar homoleptic Cu(I) complexes with various substituents (Fig 4.6)<sup>16</sup>.

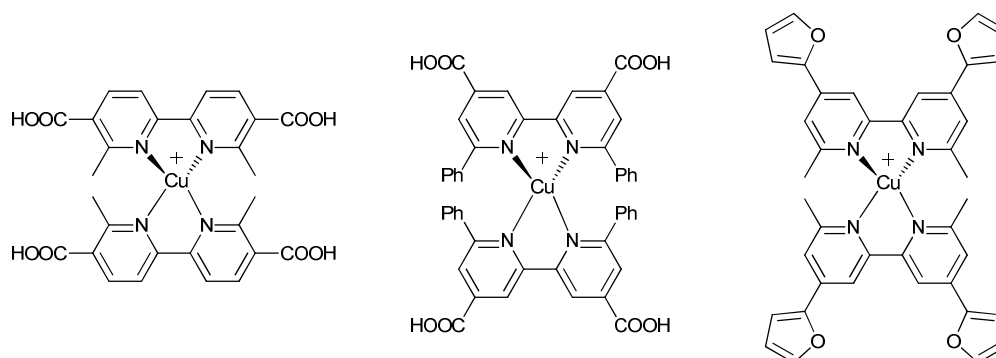


Fig. 4.6 The set of Cu(I) complexes reported by Constable *et al.* in 2009<sup>16</sup>.

The most efficient device used the copper complex with carboxylic acids in the 5 and 5' positions of the bipyridine ligands. The efficiency of the device (0.45%), was much poorer than those previously reported by the same group. However, the efficiency of the DSSC incorporating N719, prepared in same way, was only 5.0%.

In 2010 Robertson *et al.* reported the first heteroleptic Cu(I) complex for application in a DSSC<sup>17</sup>. To circumvent the challenging synthesis of 6,6'-substituted bipyridines a rigid POP (POP = bis{2-(diphenylphosphanyl)phenyl}ether) ligand was used to sterically hinder oxidation of the Cu(I) centre. A 4,4'-bis(carboxylic acid) substituted bipyridine ligand completed the complex (Fig. 4.7).

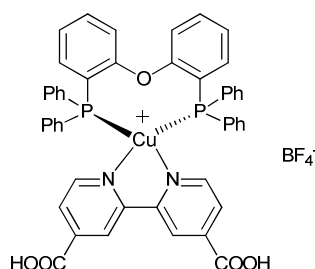


Fig. 4.7 The first heteroleptic Cu(I) complex tested in a DSSC<sup>17</sup>.

Assessing the efficacy of this dye is difficult as the efficiency of the device incorporating N719 was measured as being 3.05%. However, the low efficiency of the copper complex-containing device ( $\eta = 0.053\%$ ) is in part due to the irreversibility of the Cu(I)/Cu(II) oxidation<sup>17</sup>. If the Cu(II) cannot be reduced by the  $I/I_3^-$  redox couple, an electrical cycle

cannot be established and the device will quickly die. Another deficiency of the dye is that the MLCT band is only just into the visible region ( $\lambda_{\text{max}} = 394 \text{ nm}$ ).

In the same year copper(I) complexes based on N-phenylpyridin-2-methanamine ligands were reported by Constable *et al.* (Fig 4.8)<sup>18</sup>. Although the MLCT bands of these complexes were in the visible region of the spectrum with  $\lambda_{\text{max}} = 499\text{-}511 \text{ nm}$  the efficiencies of the complexes were very poor;  $\eta = 0.23$  and  $0.006\%$ , compared to N719,  $\eta = 4.60\%$ . The poor efficiencies were explained using low level DFT calculations. These calculations lead to the conclusion that the LUMO was not on the anchoring moieties of the complexes, which meant that injection of an electron into  $\text{TiO}_2$  would be poor.

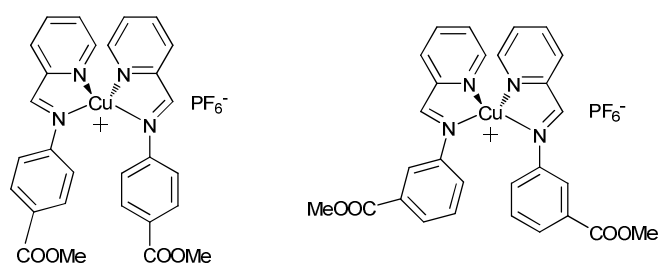


Fig. 4.8 The two Cu(I) dyes based on N-phenylpyridin-2-methanamine ligands<sup>18</sup>.

In 2011, a paper reporting DSSC devices using heteroleptic Cu(I) dyes was published<sup>19</sup>. In order to make the heteroleptic complexes, Constable *et al.* exploited the lability of Cu(I) complexes. By first attaching anchoring ligands (Fig 4.9), such as 6,6'-dimethyl-[2,2'-bipyridine]-4,4'-carboxylic acid, to  $\text{TiO}_2$  coated on FTO and then dipping this electrode into a solution of a homoleptic copper(I) complex, a ligand exchange could be carried out *in situ*. This method bypasses the challenge of synthesising and isolating heteroleptic copper(I) complexes.

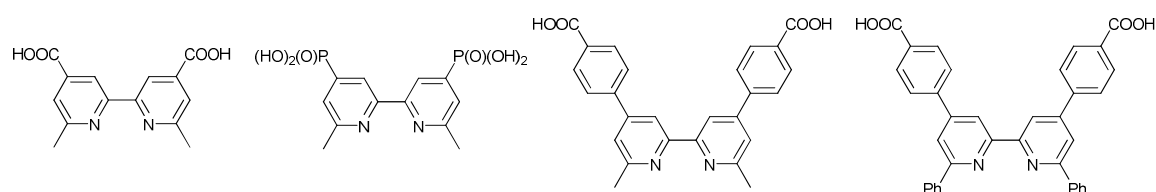


Fig. 4.9 Anchoring ligands used by the Constable group<sup>19</sup>.

The homoleptic complexes consisted of a copper(I) ion coordinated to two 6-aryl substituted bipyridine ligands. Aryl substituents were chosen because thiophene had previously been used to tune the properties of 2,2'-bipyridine<sup>19</sup>. The devices using the phosphonate-substituted anchoring ligand were the most efficient, regardless of the aryl substituent. The highest efficiency, 1.51%, was obtained after mixing the homoleptic furan-substituted copper(I) complex with the phosphonate-substituted anchoring ligand (N719 efficiency = 4.50% measured under the same conditions).

Heteroleptic complexes are desirable for use in DSSCs so that one of the ligands can be designed with groups that will anchor to the TiO<sub>2</sub> and the other ligand can be designed with groups to optimise the light absorption and redox properties of the complex. In this chapter one of the homoleptic complexes synthesised is [Cu(dmbpy)<sub>2</sub>][PF<sub>6</sub>] (dmbpy = 6,6'-dimethyl-2,2'-bipyridine), chosen due to its structural simplicity<sup>20-22</sup>. There are previous reports of the crystal structure of this complex with BF<sub>4</sub><sup>-</sup> counter anion<sup>23</sup> and ClO<sub>4</sub><sup>-</sup> counter anions<sup>24</sup> as well as the absorption spectrum of [Cu(dmbpy)<sub>2</sub>][ClO<sub>4</sub>] in ethanol and acetone<sup>25</sup> and [Cu(dmbpy)<sub>2</sub>][PF<sub>6</sub>] in dichloromethane<sup>26</sup>. To date there have been no reports of the full characterisation of [Cu(dmbpy)<sub>2</sub>][PF<sub>6</sub>] or its application in DSSCs. The second homoleptic complex utilises a ligand based on dmbpy which has extended  $\pi$ -conjugation using triphenylamine groups. Organic DSSCs sensitised with molecules containing triphenylamine groups have shown promising efficiencies<sup>27-29</sup>. In this chapter the same approach to heteroleptic complexes will be used as described in reference [19].

The ligands **8** and **9** depicted in Fig 4.10, and complexes thereof, are described in this chapter.

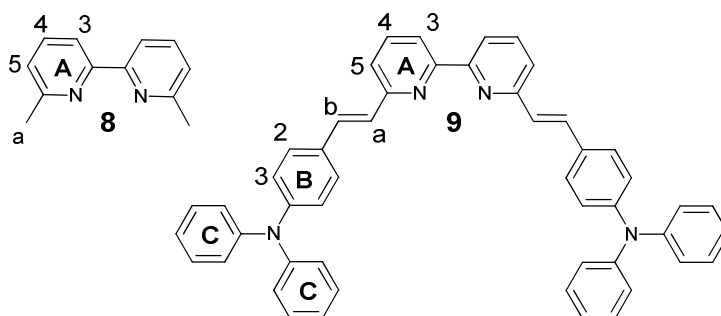
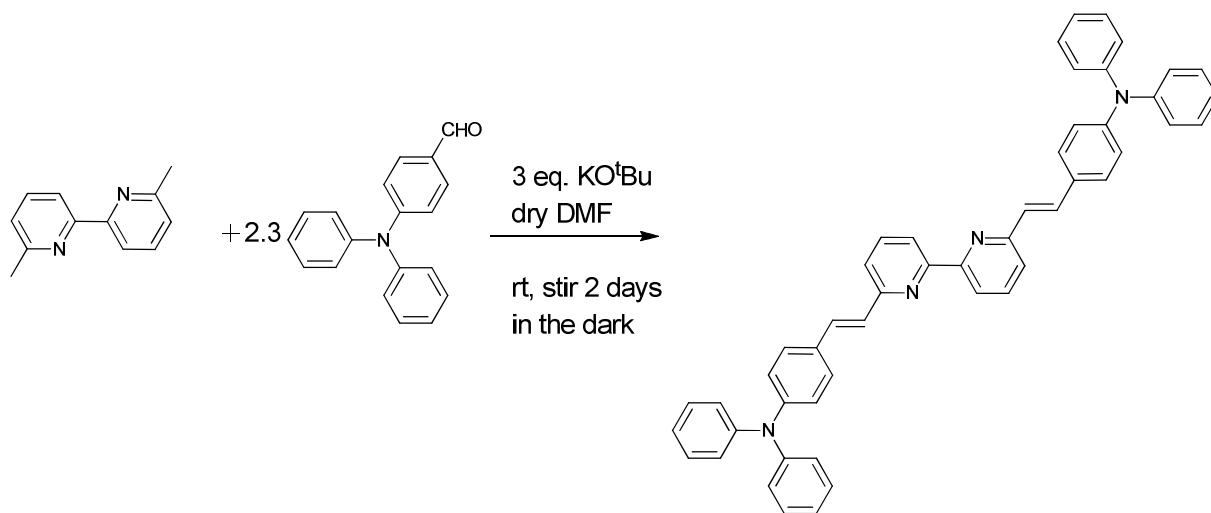


Fig. 4.10 Ligands **8** and **9** with labelling for spectroscopic assignments.

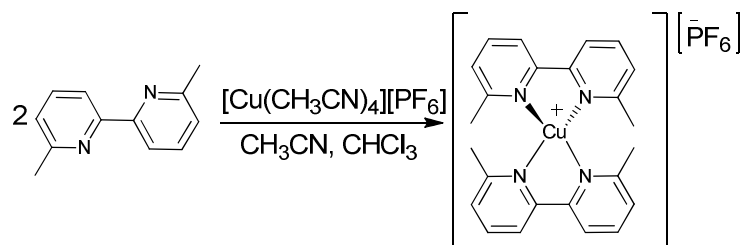
## 4.2 Synthesis of ligand **9** and corresponding Cu(I) complexes

The starting material for **9** was 6,6'-dimethyl-2,2'-bipyridine (**8**), which was commercially available. Compound **9** was synthesised by stirring one equivalent of **8** with 2.3 equivalents of 4-(diphenylamino)benzaldehyde in dry DMF for two days in the dark, using potassium *tert*-butoxide (KO<sup>t</sup>Bu) as the base (Scheme 4.1). The yield of the reaction was 55 %.

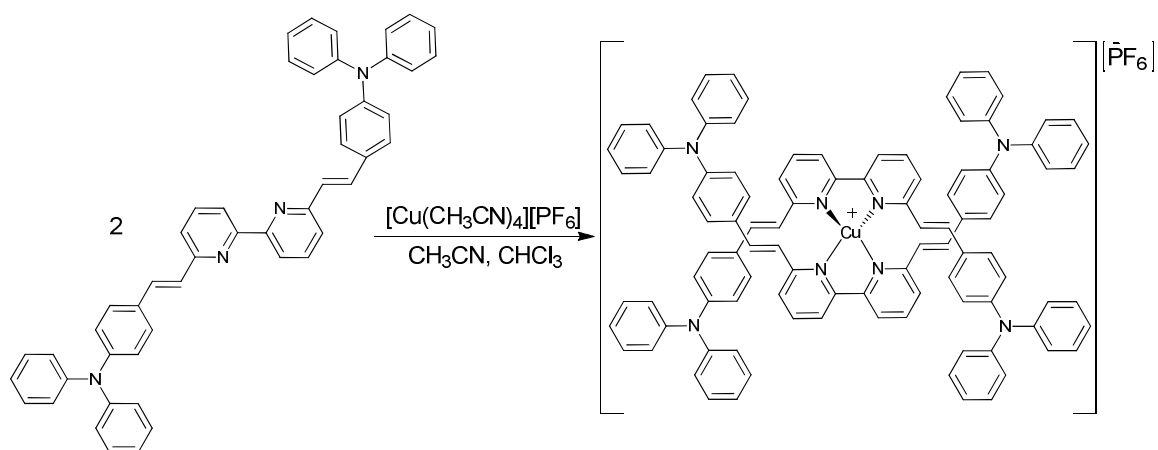


Scheme 4.1 The synthesis of compound **9**.

The synthesis of the copper(I) complexes was carried out by dissolving one equivalent of [Cu(MeCN)<sub>4</sub>][PF<sub>6</sub>] in acetonitrile and stirring (ultrasonicated for **9**) it with a chloroform solution of the relevant ligand for 30 minutes. The solution changed from colourless to red on addition of the ligand and the product was isolated as a red powder, after precipitation with diethyl ether (Schemes 4.2 and 4.3).



Scheme 4.2 The synthesis of [Cu(**8**)<sub>2</sub>][PF<sub>6</sub>], yield 77%.



Scheme 4.3 The synthesis of  $[\text{Cu}(\mathbf{9})_2][\text{PF}_6]$ , yield 81%.

### 4.3 Results and Discussion

#### 4.3.2 $^1\text{H}$ NMR Spectroscopy

$[\text{Cu}(\mathbf{8})_2][\text{PF}_6]$  was measured in  $\text{CD}_3\text{CN}$  and the spectrum is depicted (Fig 4.11).

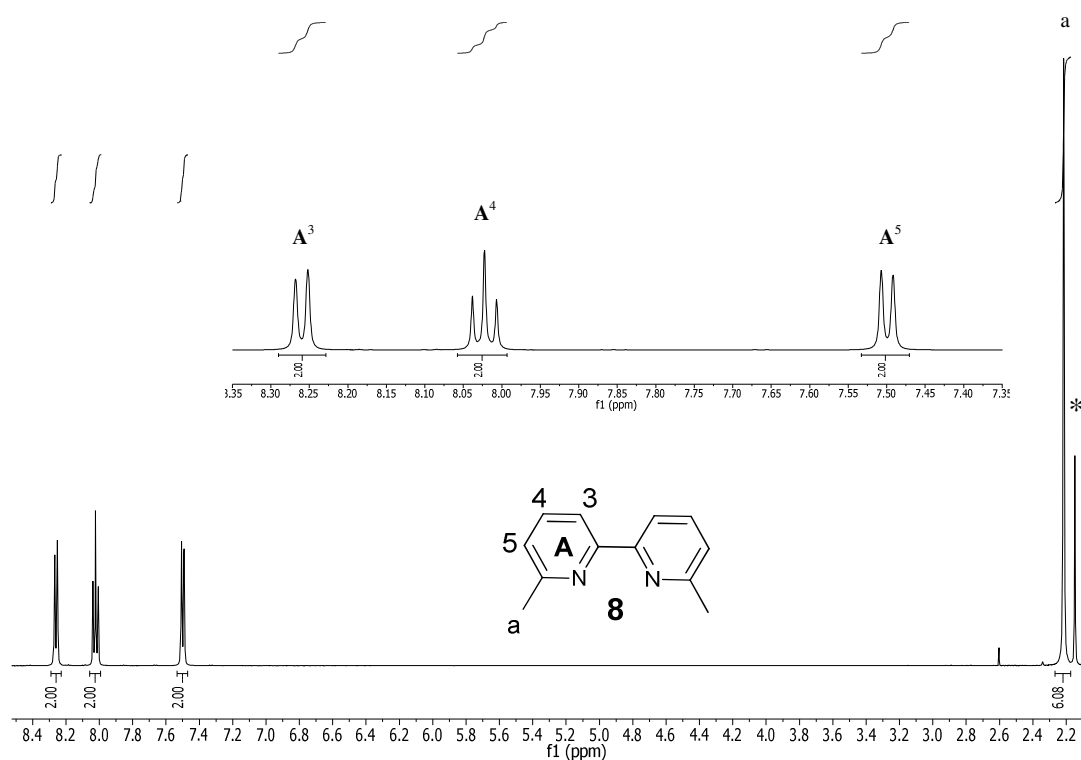


Fig. 4.11  $^1\text{H}$  NMR spectrum of  $[\text{Cu}(\mathbf{8})_2][\text{PF}_6]$  in  $\text{CD}_3\text{CN}$ ; 500 MHz, 25°C, TMS,  $\text{H}_2\text{O}(\ast)$ .

The appearance of one set of signals indicates that the complex is homoleptic. The singlet at  $\delta$  2.22 ppm was ascribed to the methyl substituent due to the chemical shift and the integral.

The triplet at  $\delta$  8.02 ppm was ascribed to proton  $A^4$  due to the splitting and protons  $A^3$  and  $A^5$  were assigned by their chemical shift. Proton  $A^5$  is much more shielded than proton  $A^3$  due to the +I effect of the methyl substituent, which means that the signal ascribed to  $A^5$  is further upfield compared to  $A^3$ .

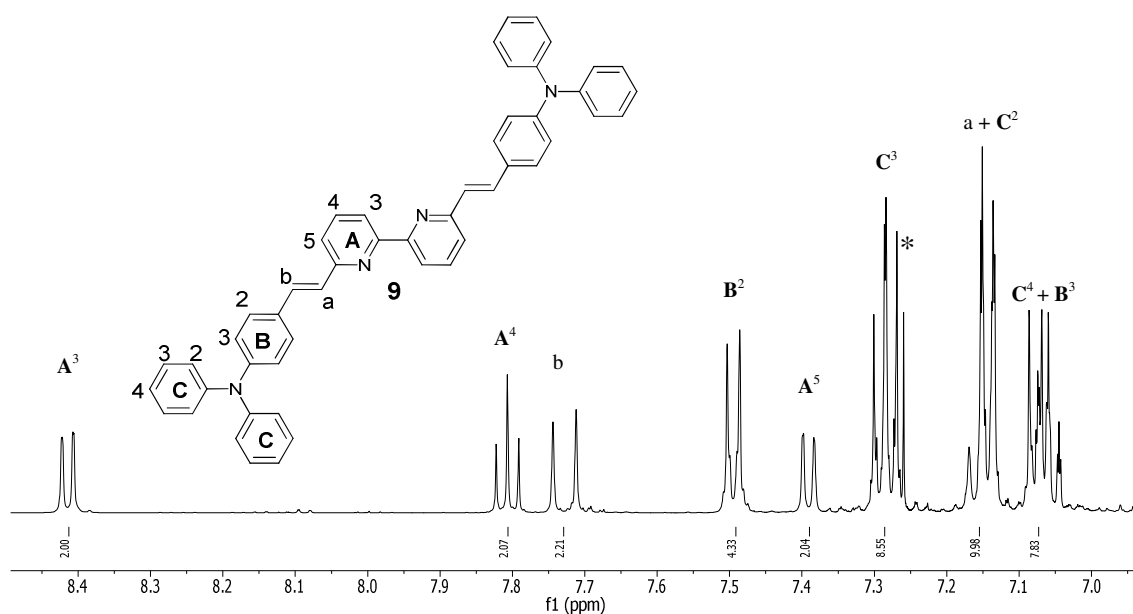


Fig. 4.12  $^1\text{H}$  NMR spectrum of **9** in  $\text{CDCl}_3$ ; 500 MHz, residual  $\text{CHCl}_3$  (\*),  $25^\circ\text{C}$ , TMS.

The  $^1\text{H}$  NMR spectrum of **9** (Fig. 4.12) was assigned using both COSY and NOESY techniques. The starting point for assignment was the triplet at  $\delta$  7.81 ppm which, due to the splitting, had to be ascribed to proton  $A^4$ . From the COSY spectrum it was then possible to ascribe the two doublets at  $\delta$  8.41 and 7.39 ppm to  $A^3$  and  $A^5$  by looking for COSY cross-peaks (Fig. 4.13) from the triplet at  $\delta$  7.81 ppm. The specific assignment of  $A^3$  and  $A^5$  was done by comparison with a spectrum of 6,6'-dimethyl-2,2'-bipyridine.

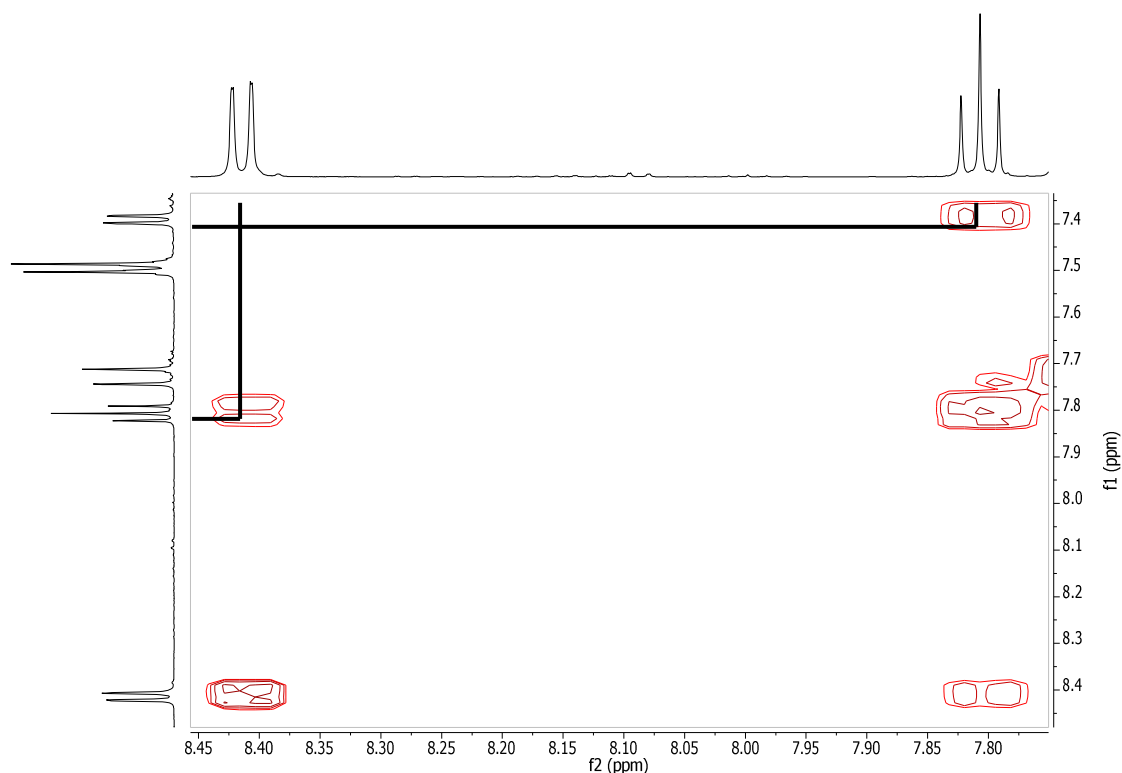


Fig. 4.13 Partial COSY spectrum of **9** (500 MHz,  $\text{CDCl}_3$ , 25°C, TMS) to show cross peaks between  $\mathbf{A}^3$ ,  $\mathbf{A}^4$  and  $\mathbf{A}^5$ .

Assignment was continued from the broad doublet at  $\delta$  7.73 ppm, which had a  $J$  coupling of 16.0 Hz. The large coupling constant indicated that this signal was due to a proton on a trans-alkene bond. The COSY spectrum (Fig 4.14) enabled location of the other broad trans-doublet (Fig 4.14) in the overlapping signals at  $\delta$  7.15 ppm, highlighted by a red circle. A NOESY interaction between the peak at  $\delta$  7.73 ppm and a doublet at  $\delta$  7.15 ppm (Fig 4.15) meant that the former peak could be ascribed to proton  $b$  and the latter peak ascribed to proton  $\mathbf{B}^2$ . This meant that the broad doublet in the multiplet at  $\delta$  7.15 ppm could be ascribed to proton  $a$ . A COSY cross peak between the doublet at  $\delta$  7.15 ppm and the multiplet at  $\delta$  7.07 ppm enabled the assignment of the peak at  $\delta$  7.07 ppm as  $\mathbf{B}^3$ . A NOESY correlation is observed between the peak ascribed to  $\mathbf{B}^3$  and a multiplet at  $\delta$  7.15 ppm, which means that the multiplet can be assigned as  $\mathbf{C}^2$ . Protons  $\mathbf{C}^3$  and  $\mathbf{C}^4$  are subsequently ascribed to the multiplets at  $\delta$  7.28 and  $\delta$  7.07 ppm, respectively, by observation of COSY cross peaks with  $\mathbf{C}^2$ .



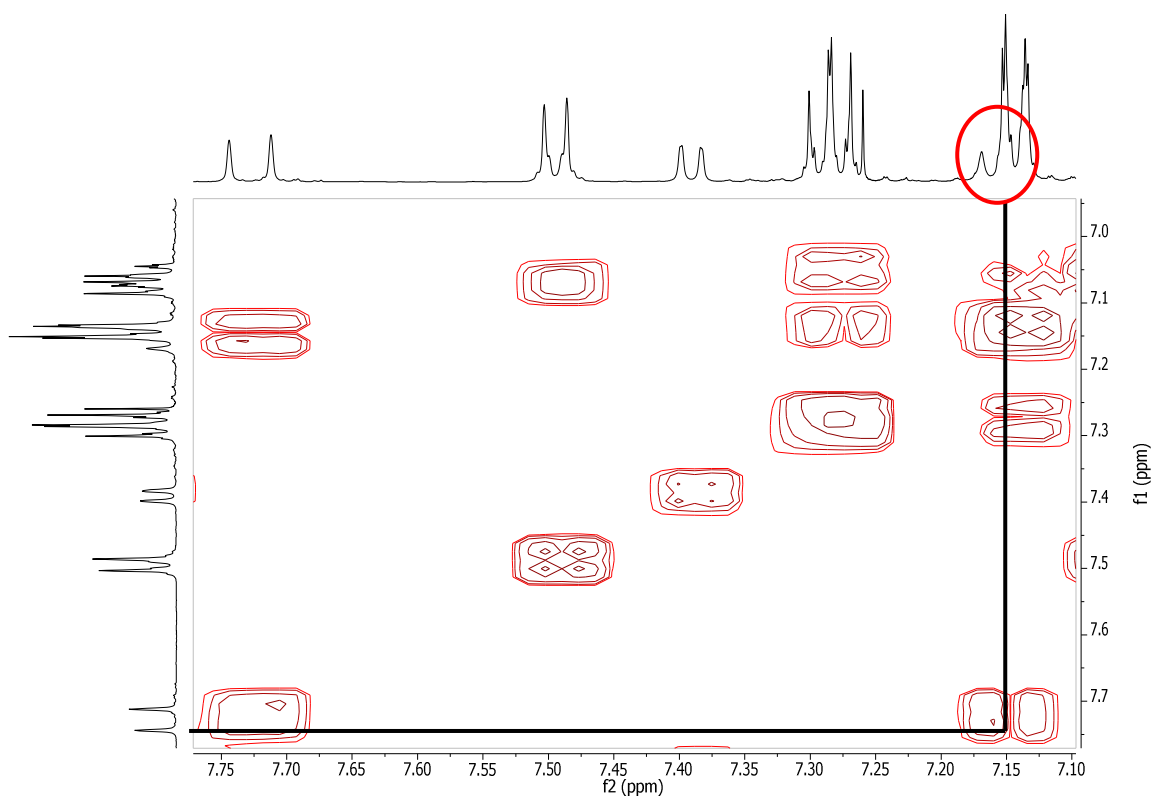


Fig. 4.14 Partial COSY spectrum of **9** (500 MHz,  $\text{CDCl}_3$ , 25°C, TMS) to show cross peak between protons *a* and *b*. Red circle highlights broad doublet.

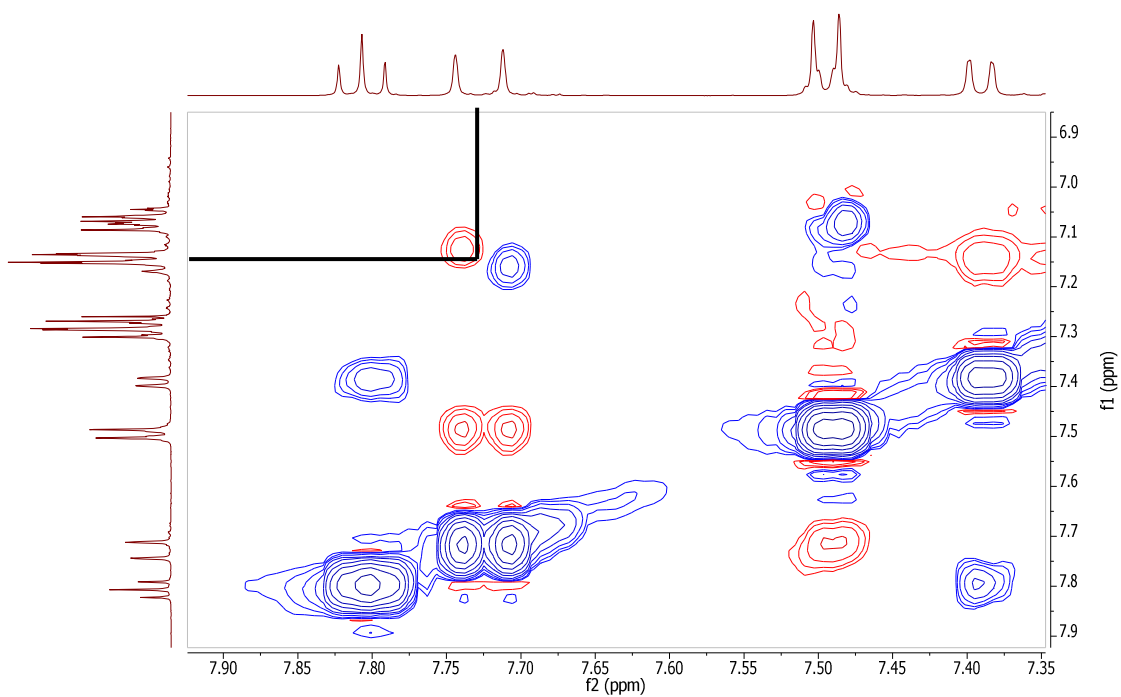


Fig. 4.15 Partial NOESY spectrum of **9** (500 MHz,  $\text{CDCl}_3$ , 25°C, TMS) to show NOE interaction between the protons ascribed to *b* and  $B^2$ .

The  $^1\text{H}$  NMR spectrum of  $[\text{Cu}(\mathbf{9})_2][\text{PF}_6]$  was measured in  $\text{CDCl}_3$  and was assigned using COSY and NOESY techniques (Fig. 4.16).

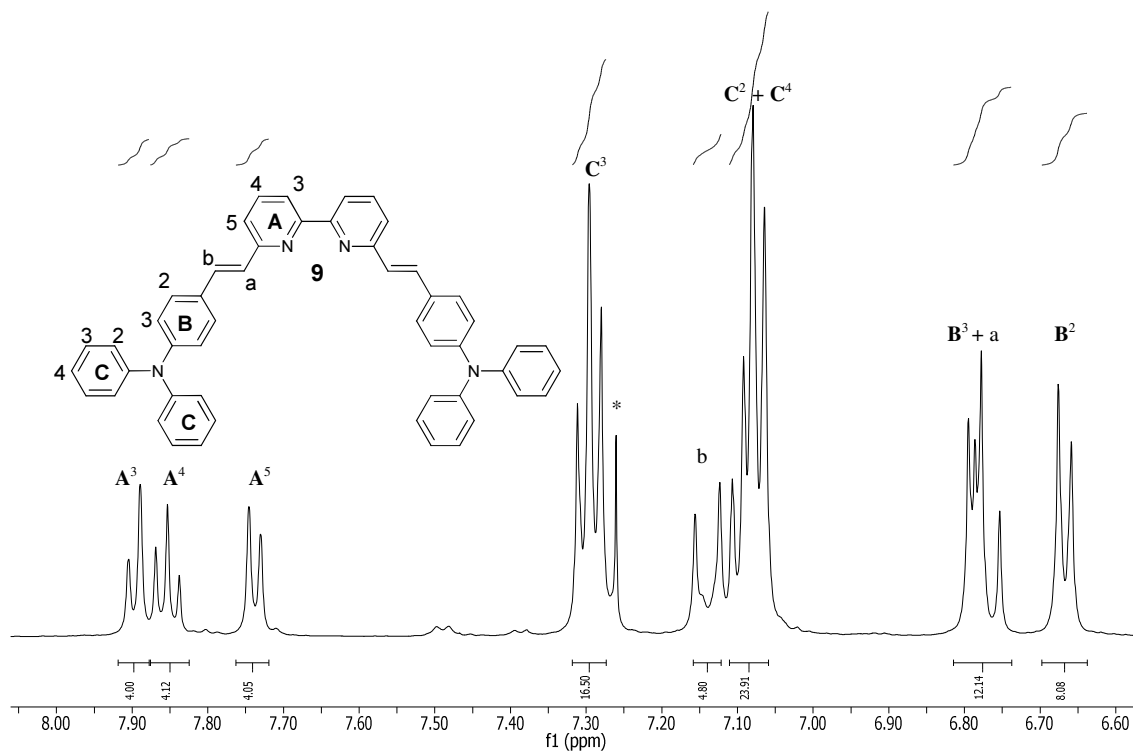


Fig. 4.16  $^1\text{H}$  NMR spectrum of  $[\text{Cu}(\mathbf{9})_2][\text{PF}_6]$  in  $\text{CDCl}_3$ ; 500 MHz, residual  $\text{CHCl}_3$  (\*),  $25^\circ\text{C}$ , TMS.

As for compound **9**, assignment of the  $^1\text{H}$  NMR spectrum of  $[\text{Cu}(\mathbf{9})_2][\text{PF}_6]$  started with the triplet peak at  $\delta$  7.85 ppm, which was ascribed to proton **A**<sup>4</sup>. Compared to the ligand **A**<sup>4</sup> proton, this signal was shifted slightly downfield. COSY correlations identified the doublets at  $\delta$  7.90 and  $\delta$  7.74 ppm as **A**<sup>3</sup> and **A**<sup>5</sup>. By comparison with the ligand spectrum the doublet at  $\delta$  7.90 ppm could be ascribed to **A**<sup>3</sup> and the doublet at  $\delta$  7.74 ppm could be ascribed to **A**<sup>5</sup>.

The signals corresponding to the protons on the **A** ring of the complex have significantly different shifts to those of the ligand (Table 4.1), the signal for proton **A**<sup>3</sup> is shifted upfield and the signal for proton **A**<sup>5</sup> is shifted downfield on complexation. This is due to the nitrogen atom becoming deshielded by donating electron density to the copper, which subsequently affects the **A** ring protons.

An NOE interaction between  $\mathbf{A}^5$  and the broad doublet at  $\delta$  7.12 ppm ascribes the broad doublet to proton  $b$  (Fig 4.18). Due to their proximity in space an NOE interaction can be observed between  $\mathbf{A}^5$  and  $b$ , this interaction is not observed between  $\mathbf{A}^5$  and  $a$  as  $a$  is not conformationally aligned in such a way to allow an NOE interaction to occur. A COSY correlation between the peak ascribed to  $b$  and a broad doublet at  $\delta$  6.77 ppm assigns the broad doublet at  $\delta$  6.77 ppm as proton  $a$  (Fig 4.17). A NOE interaction between  $b$  and the doublet at  $\delta$  6.67 ppm ascribes that doublet to proton  $\mathbf{B}^2$  (Fig 4.18).

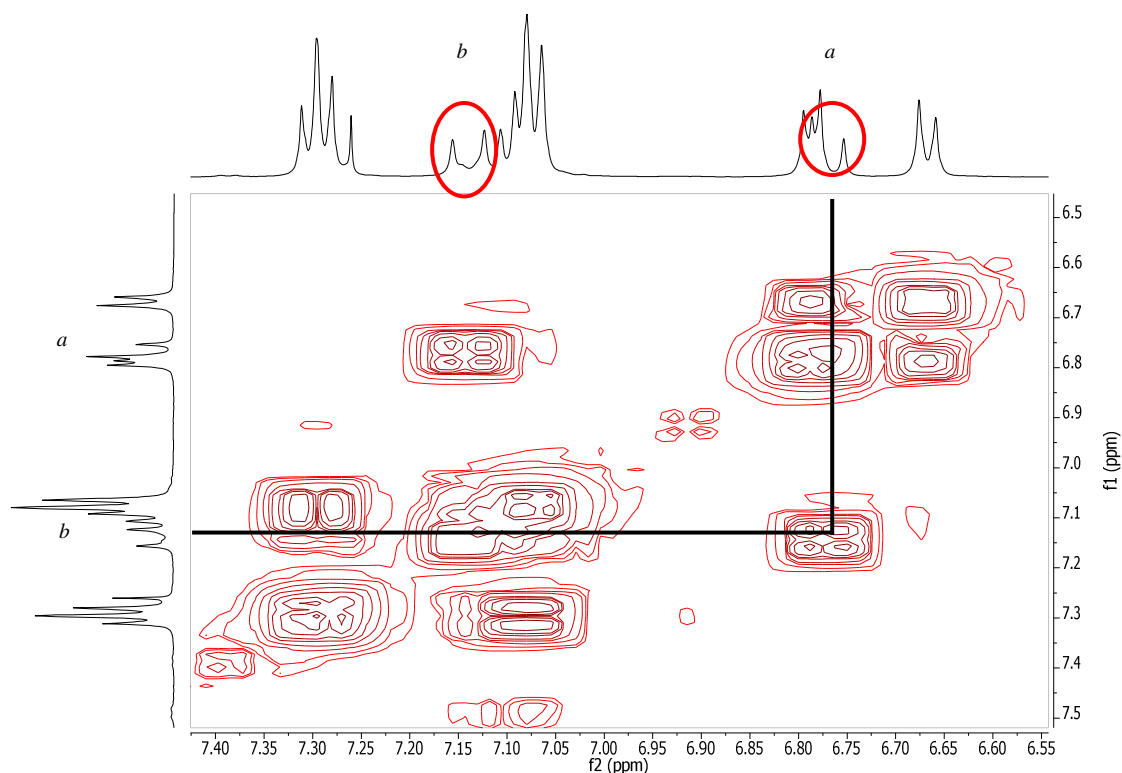


Fig. 4.17 Partial COSY spectrum of  $[\text{Cu}(\mathbf{9})_2][\text{PF}_6]$  (500 MHz,  $\text{CDCl}_3$ , 25°C, TMS) to show cross peak between protons  $a$  and  $b$ . Red circles highlight broad doublets.

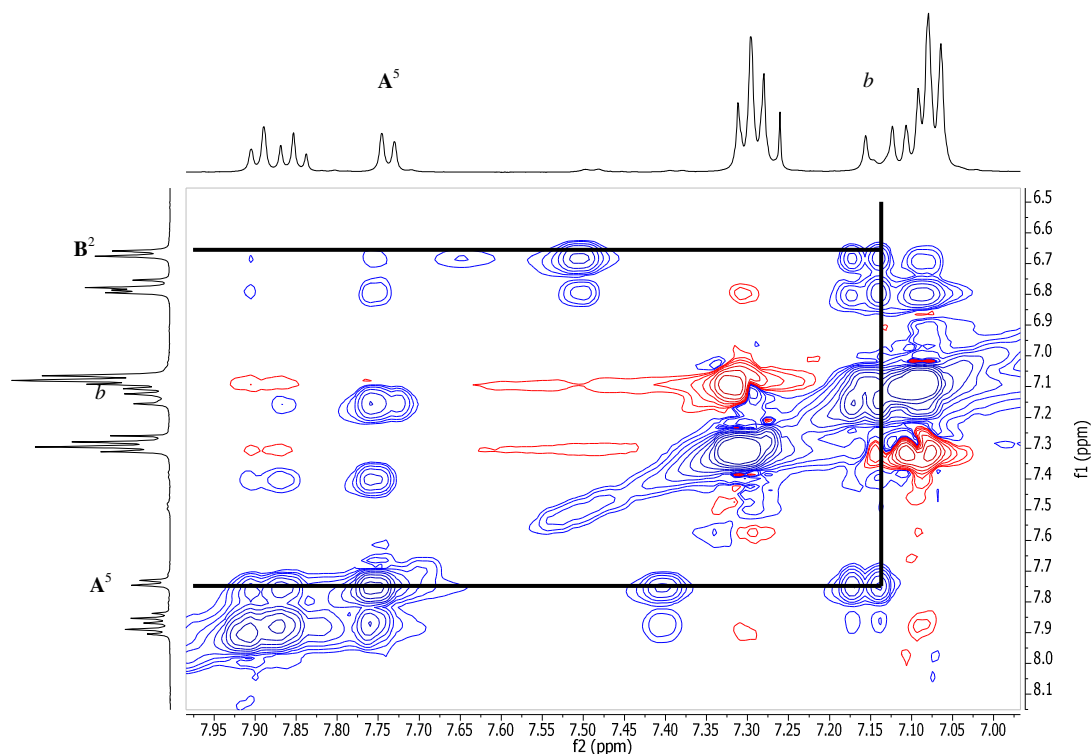


Fig. 4.18 Partial NOESY spectrum of  $[\text{Cu}(\mathbf{9})_2][\text{PF}_6]$  (500 MHz,  $\text{CDCl}_3$ ,  $25^\circ\text{C}$ , TMS) to show NOE interaction between the protons ascribed to  $b$  and  $\mathbf{A}^5$  (lower line) and  $b$  and  $\mathbf{B}^2$  (upper line).

From  $\mathbf{B}^2$  a COSY correlation to the doublet at  $\delta$  6.79, which overlaps with the signal for proton  $a$ , enables assignment of said doublet as  $\mathbf{B}^3$ . A weak NOE interaction between  $\mathbf{B}^3$  and the triplet at  $\delta$  7.30 ppm means that the triplet can be ascribed to proton  $\mathbf{C}^3$ . (There is also a strong NOE interaction between  $\mathbf{B}^3$  and  $\mathbf{C}^2$ .) Finally COSY correlations between  $\mathbf{C}^3$  and the multiplet at  $\delta$  7.08 ppm means that the multiplet can be assigned to protons  $\mathbf{C}^2$  and  $\mathbf{C}^4$ , which is confirmed by the integrals.

On complexation the bipyridine unit of the ligand undergoes a conformational shift from transoid to cisoid (Fig 4.19), which has a significant effect on the shift of the  $a$ ,  $b$  and  $\mathbf{B}^2$  peaks in the  $^1\text{H}$  NMR spectrum (Table 4.1).

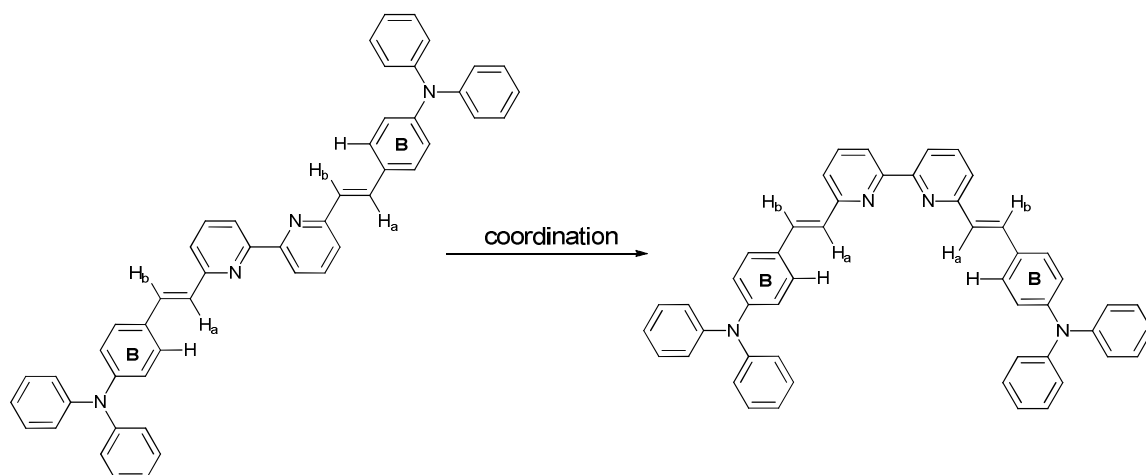


Fig 4.19 Conformational changes of ligand **9** on binding to copper.

Compound	<i>a</i>	<i>b</i>	<b>B</b> <sup>2</sup>
<b>9</b>	7.15	7.74	7.49
[Cu( <b>9</b> ) <sub>2</sub> ][PF <sub>6</sub> ]	6.77	7.12	6.67

Table 4.1 Comparison of shifts ( $\delta/\text{ppm}$ ) on complexation of compound **9**. Spectra measured in CDCl<sub>3</sub> at room temperature.

Compared to the ligand, the signals for protons *a* and *b* are shifted upfield. This is because i) the alkene protons are forced into close proximity with the copper atom and ii) the effect of the nitrogen atoms on the alkene protons is lessened as the nitrogen atoms are complexed to copper. The signal for **B**<sup>2</sup> is most affected on complexation of the ligand and this is due to the close proximity of the protons to the copper ion.

#### 4.3.2 <sup>13</sup>C NMR Spectroscopy

The <sup>13</sup>C{<sup>1</sup>H} NMR spectrum of [Cu(**8**)<sub>2</sub>][PF<sub>6</sub>] was measured in CD<sub>3</sub>CN and assigned using HMQC and HMBC techniques. The chemical shifts and peak assignments can be found in the experimental section at the end of this chapter.

The <sup>13</sup>C{<sup>1</sup>H} NMR spectrum of **9** was measured in CDCl<sub>3</sub> and is depicted in Fig 4.20.

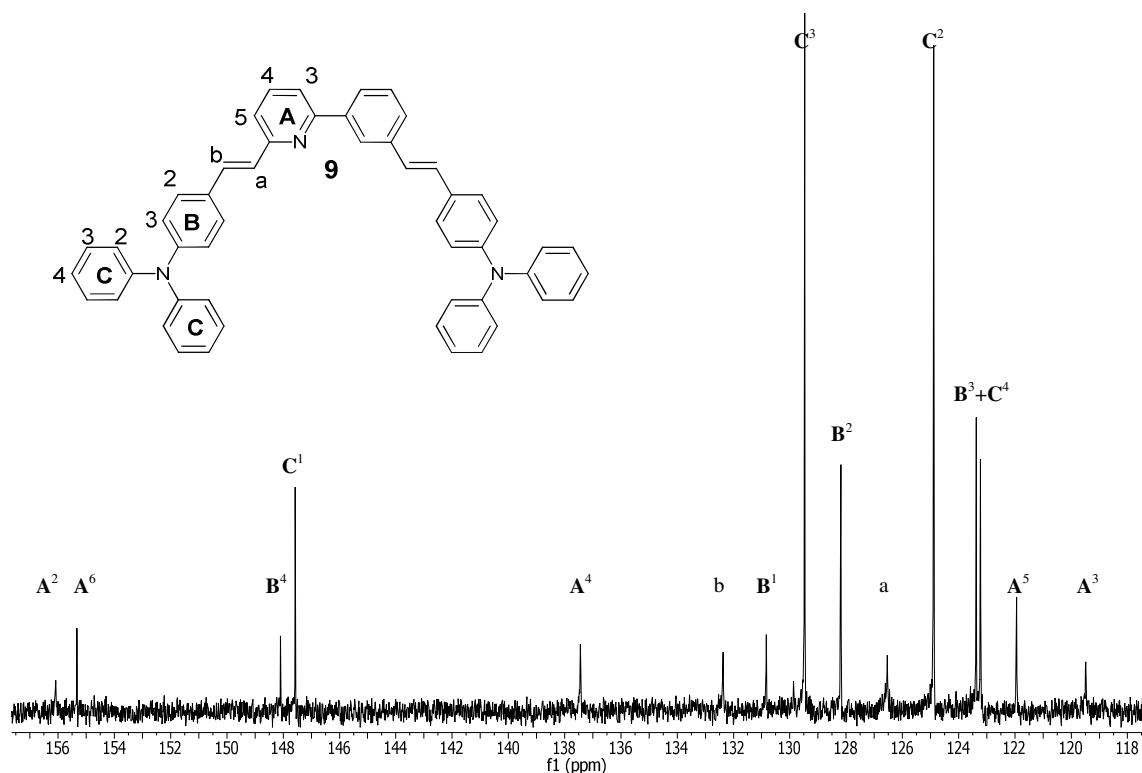


Fig. 4.20  $^{13}\text{C}\{^1\text{H}\}$  NMR spectrum of **9** in  $\text{CDCl}_3$ ; 126 MHz, 25°C, TMS.

The peaks arising from  $^{13}\text{C}\text{-H}$  carbons were assigned using the HMQC spectrum. The cross-peaks involving the alkene protons and their respective carbon signals were very distinct (Fig 4.21). The quaternary carbon signals were assigned using the HMBC spectrum. Proton **C**<sup>3</sup> had an HMBC interaction with a signal at  $\delta$  147.5 ppm, which was assigned to **C**<sup>1</sup>. Proton **B**<sup>2</sup> had a HMBC interaction with a signal at  $\delta$  148.5 ppm, which was assigned to **B**<sup>4</sup>. Proton **B**<sup>3</sup> had a HMBC interaction with a signal at  $\delta$  130.8 ppm, which was assigned to **B**<sup>1</sup>. Proton **A**<sup>4</sup> had HMBC interactions with signals at  $\delta$  156.1 and  $\delta$  155.3 ppm, which were assigned to the **A** ring (Fig 4.22). Proton *b* had an HMBC interaction with the signal at  $\delta$  155.3 ppm, which was assigned to **A**<sup>6</sup> (Fig 4.22). By deduction, the signal at  $\delta$  156.1 ppm was then assigned to **A**<sup>2</sup>.

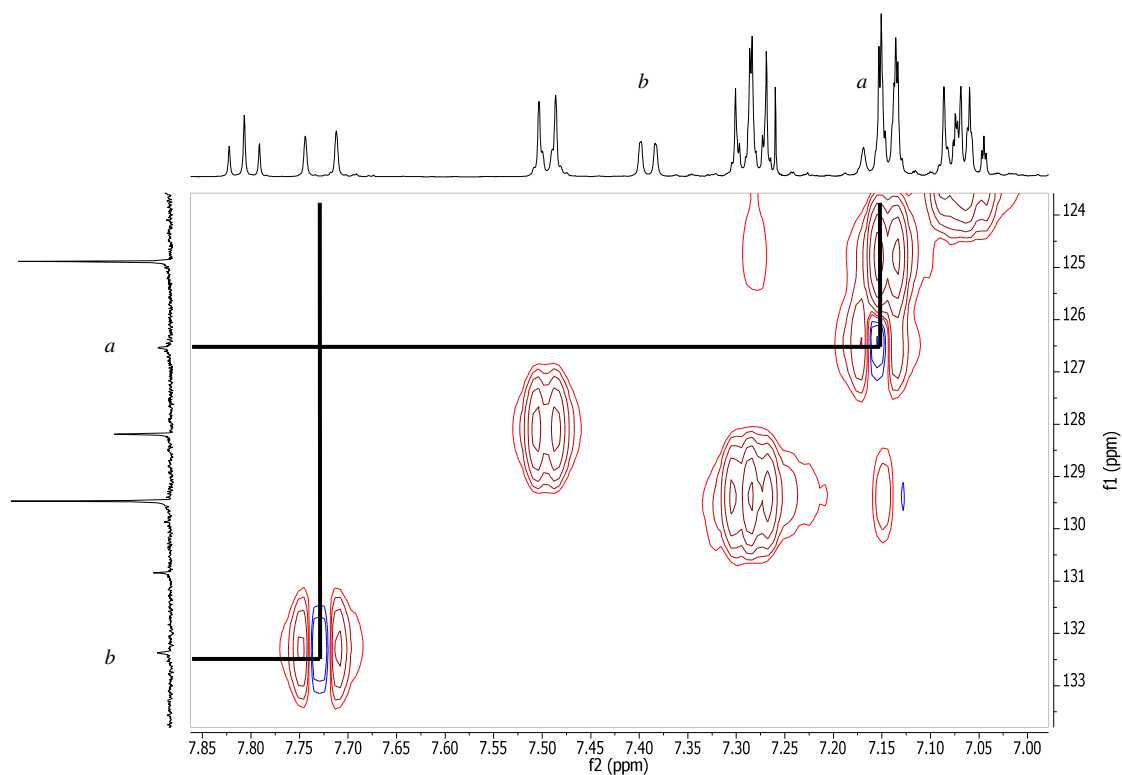


Fig 4.21 Partial HMQC spectrum of compound **9**, measured in  $CDCl_3$  at  $25^\circ C$ .

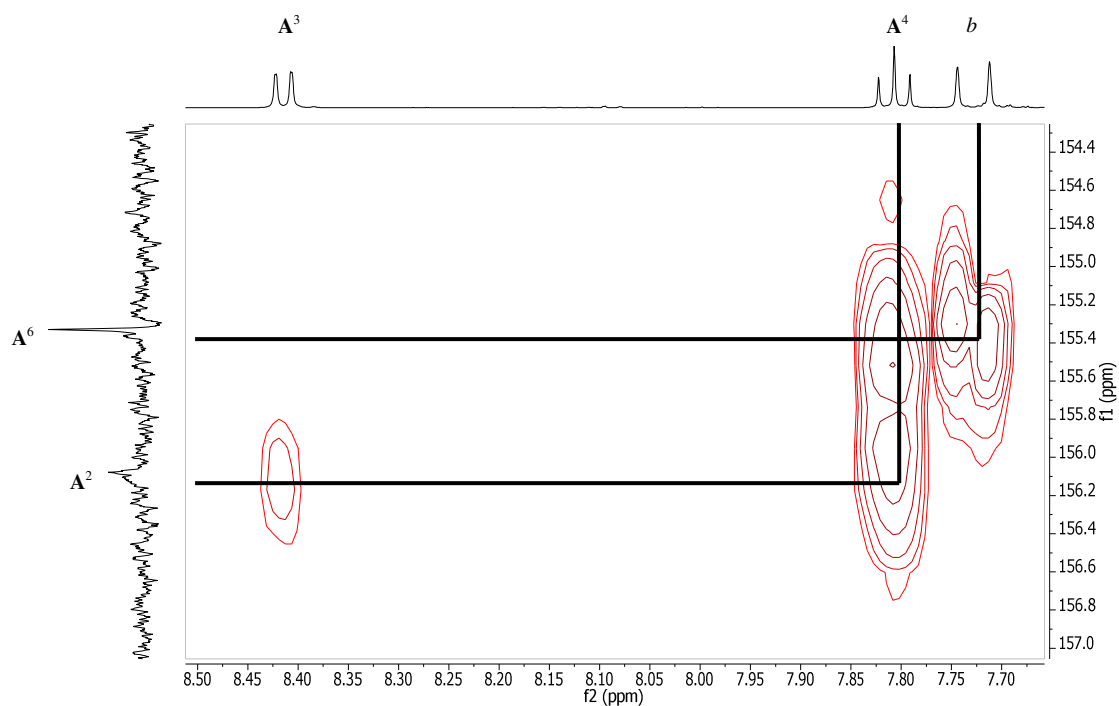


Fig 4.22 HMBC spectrum of compound **9**, measured in  $CDCl_3$  at  $25^\circ C$ , depicting the interactions between  $H(A^4)$  and  $C(A^2)$ ,  $C(A^6)$  and  $H(b)$  and  $C(A^6)$  specifically.

The  $^{13}\text{C}$  NMR spectrum of  $[\text{Cu}(\mathbf{9})_2][\text{PF}_6]$  was measured in  $\text{CDCl}_3$  and is depicted in Fig. 4.23.

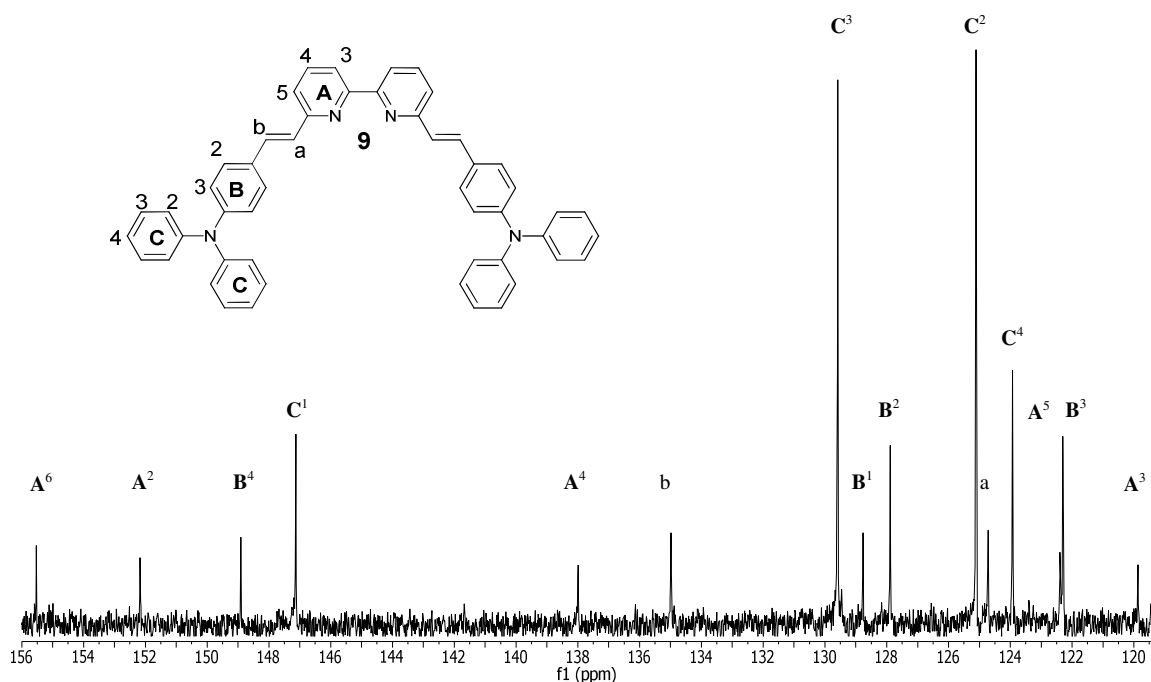


Fig 4.23  $^{13}\text{C}\{^1\text{H}\}$  NMR spectrum of  $[\text{Cu}(\mathbf{9})_2][\text{PF}_6]$  in  $\text{CDCl}_3$ ; 126 MHz, 25°C, TMS.

The  $^{13}\text{C}\{^1\text{H}\}$  NMR spectrum was assigned using HMQC and HMBC techniques. In the HMQC spectrum the alkene signals were easily identified as observed in the HMQC spectrum of compound **9** (Fig. 4.21). All carbons except the quaternary carbons were assigned using the HMQC spectrum. The quaternary carbons were assigned by use of the HMBC spectrum in the same way that has previously been described for compound **9**.

### 3.3.3 Mass Spectrometry

$[\text{Cu}(\mathbf{8})_2][\text{PF}_6]$  was characterised using MALDI-TOF mass spectrometry. The fragmentation patterns confirmed complexation as fragmentation peaks corresponding to  $[\text{M}-\text{PF}_6]^+$  ( $m/z$  431.0) and  $[\text{M}-\mathbf{8}-\text{PF}_6]^+$  (247.0) were observed.

Compound **9** was characterised using ESI mass spectrometry and a peak corresponding to  $[\text{M}+\text{H}]^+$  ( $m/z$  695.3) was observed, confirming that the synthesis of the compound had been successful.



[Cu(**9**)<sub>2</sub>][PF<sub>6</sub>] was also characterised using ESI mass spectrometry. Successful complexation was confirmed by the observation of a peak corresponding to [M-PF<sub>6</sub>]<sup>+</sup> (*m/z* =1453.7) in the spectrum. The base peak, assigned to [**9**+H]<sup>+</sup> (*m/z* 695.3), was also present in the spectrum.

#### 4.3.4 Absorption Spectroscopy

As discussed in the introduction to this chapter, to be truly efficient as photosensitisers for DSSCs the copper complexes should ideally absorb over the entire visible spectrum. There are currently many examples of ruthenium complexes which have this property, the most famous being “the black dye”<sup>30</sup>, but no copper complexes yet meet this criterion. Whilst copper complexes are not at this stage of development, they do give rise to an MLCT band in the red-orange region of the spectrum, thus absorbing some visible light. UV-vis spectroscopy was used to ascertain how much light from the visible spectrum was absorbed by the compounds described in this chapter.

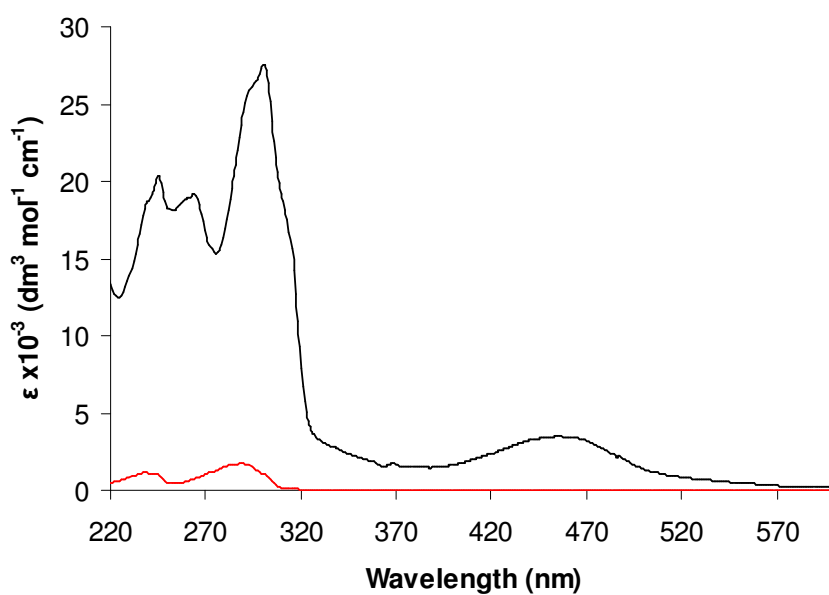


Fig. 4.24 Absorption spectra for **8** (red line) and [Cu(**8**)<sub>2</sub>][PF<sub>6</sub>](black line) measured in MeCN with a concentration of 10<sup>-5</sup> mol dm<sup>-3</sup>.

Compared to the ligand (**8**), the complex is much more strongly absorbing (Fig. 4.24). A new band with  $\lambda_{\text{max}} = 452$  nm is observed for the complex, which gives rise to its red

colour and means that the complex absorbs visible light. This band is due to an MLCT transition; promotion of an electron from an occupied copper d-orbital to an empty ligand  $\pi^*$  orbital. The UV region of the spectrum is dominated by ligand-based  $\pi \rightarrow \pi^*$  transitions. The data are summarised in Table 4.2.

Compound	MLCT		$\lambda_{\max}$			
	$(\epsilon, 10^3 \text{ dm}^3 \text{ mol}^{-1} \text{ cm}^{-1})$		$(\epsilon, 10^3 \text{ dm}^3 \text{ mol}^{-1} \text{ cm}^{-1})$			
<b>8</b>			300	289	245	239
			(1.07)	(1.70)	(1.05)	(1.13)
$[\text{Cu}(\mathbf{8})_2][\text{PF}_6]$	457	311 sh	302	266	246	241 sh
	(3.47)	(18.68)	(27.19)	(18.66)	(20.3)	(18.90)

Table 4.2 A summary of the absorbance data, recorded in acetonitrile, for **8** and  $[\text{Cu}(\mathbf{8})_2][\text{PF}_6]$  with concentrations of  $10^{-5} \text{ mol dm}^{-3}$ .

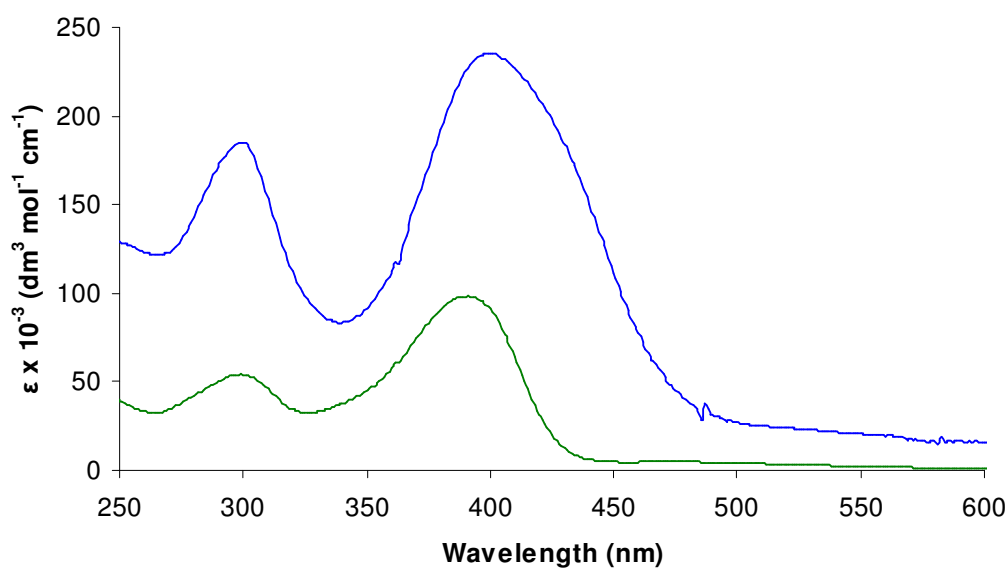


Fig. 4.25 Absorption spectra of **9** (green line) and  $[\text{Cu}(\mathbf{9})_2][\text{PF}_6]$  (blue line) measured in  $\text{CH}_2\text{Cl}_2$  with concentrations of  $10^{-6} \text{ mol dm}^{-3}$ .

The absorptions of compound **9** and its copper(I) complex (Fig. 4.25) are much more intense than those of the  $[\text{Cu}(\mathbf{8})_2][\text{PF}_6]$  complex. This is due to the extended  $\pi$ -system of ligand **9**, compared to ligand **8**. The spectrum of **9** contains two peaks with  $\lambda_{\max} = 296$  and 389 nm. The latter absorption gives rise to the yellow-orange colour of the compound.

In the case of the complex  $[\text{Cu}(\mathbf{9})_2][\text{PF}_6]$  these peaks are slightly red-shifted to 299 and 400 nm. The peak with  $\lambda_{\text{max}} = 400$  nm tails further into the visible region, giving rise to the orange colour of the complex. Contrary to the case of  $[\text{Cu}(\mathbf{8})_2][\text{PF}_6]$ , no MLCT peak is observed in the UV-vis spectrum of  $[\text{Cu}(\mathbf{9})_2][\text{PF}_6]$  and this is explored later using DFT and TD-DFT (§ Chapter 5). The data for both compounds are summarised in Table 4.3.

Compound	$\lambda_{\text{max}}$ ( $\epsilon$ , $10^3 \text{ dm}^3 \text{ mol}^{-1} \text{ cm}^{-1}$ )	
<b>9</b>	296 (53.6)	389 (97.3)
$[\text{Cu}(\mathbf{9})_2][\text{PF}_6]$	299 (185.4)	400 (235.5)

*Table 4.3 A summary of the absorption data, recorded in dichloromethane, for **9** and  $[\text{Cu}(\mathbf{9})_2][\text{PF}_6]$*

#### 4.3.5 Excitation and Emission Spectroscopy

In the cycle of a DSSC it is the excited state of the copper complex that does the ‘work’, which in this case is the donation of an electron to the titanium dioxide. If an excited state is energetically accessible it can be observed by the presence of luminescent decay, provided that the lifetime is sufficiently long and the non-radiative processes are not too efficient. Emission spectroscopy was used to identify luminescent decay and, in the case of **9** and  $[\text{Cu}(\mathbf{9})_2][\text{PF}_6]$ , excitation spectroscopy was used to confirm the origin of the emission.

The excitation and emission spectra of  $[\text{Cu}(\mathbf{8})_2][\text{PF}_6]$  were measured in acetonitrile and the spectra are depicted in Fig. 4.26.

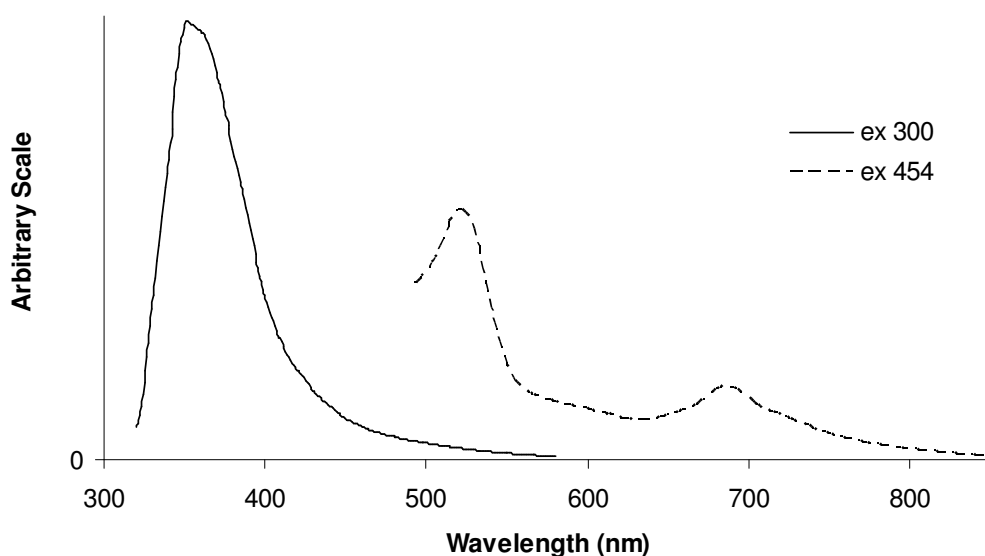
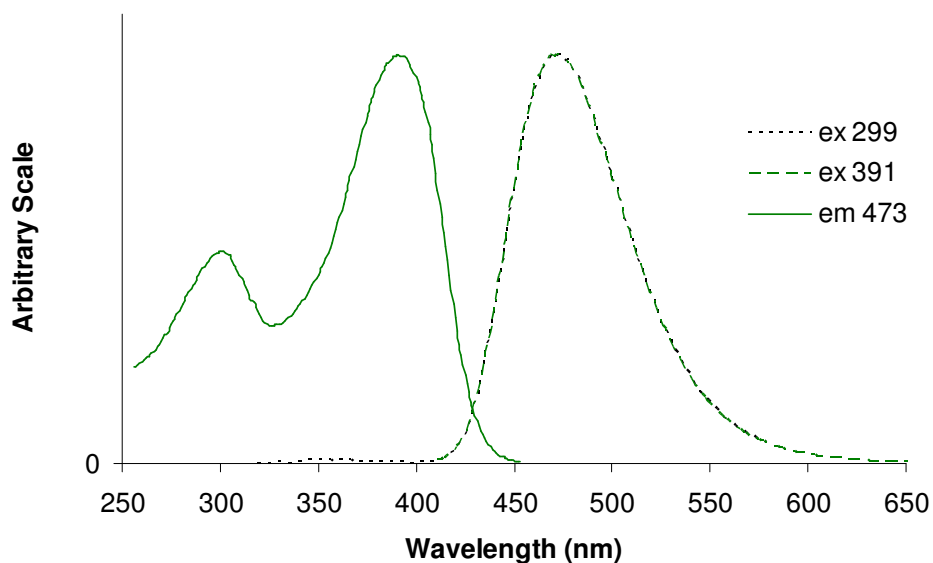


Fig. 4.26 Emission spectra of  $[\text{Cu}(\mathbf{8})_2][\text{PF}_6]$  measured in acetonitrile after exciting into a ligand-based absorption at 300 nm and the MLCT band at 454 nm.

Excitation into the ligand-based absorption band at 300 nm gives rise to a ligand-based emission in the UV region of the spectrum with  $\lambda_{\text{em}} = 351$  nm, which tails into the visible region of the spectrum. Excitation into the MLCT band results in two emissions. The first in the blue-green region of the spectrum, with  $\lambda_{\text{em}} = 525$  nm and the second in the orange-red region, with  $\lambda_{\text{em}} = 690$  nm, which also tails into the red region.

The lifetime of the emission with  $\lambda_{\text{em}} = 525$  nm was 4 ns and the lifetime of the emission with  $\lambda_{\text{em}} = 690$  nm was 2 ns. For application in DSSCs the lifetime of the complex needs to be longer than the timescale of electron injection from the complex in its excited state into  $\text{TiO}_2$ . Electron injection happens on the picosecond timescale<sup>2</sup> and as such this complex fulfils said criterion. An attempt was made to measure the quantum yield of the complex using the Quantaaurus instrument but the quantum yield was below the detectable limit of the machine ( $< 0.1\%$ ).



*Fig. 4.27 Emission and excitation spectra of **9** measured in dichloromethane depicting emission spectra from excitation into the absorption bands at 299 and 391 nm and an excitation spectrum recorded after scanning the excitation holding the emission at 473 nm.*

Excitation into the absorption bands at 291 and 391 nm of compound **9**, gave rise to the same emission spectrum, which has  $\lambda_{\text{em}} = 473$  nm (Fig. 4.27). By holding the emission at 473 nm and scanning the excitation wavelengths, the excitation spectrum of the complex is obtained, which consists of two peaks with  $\lambda_{\text{ex}} = 291$  and 391 nm. This confirms the origin of the emission with  $\lambda_{\text{em}} = 473$  nm.

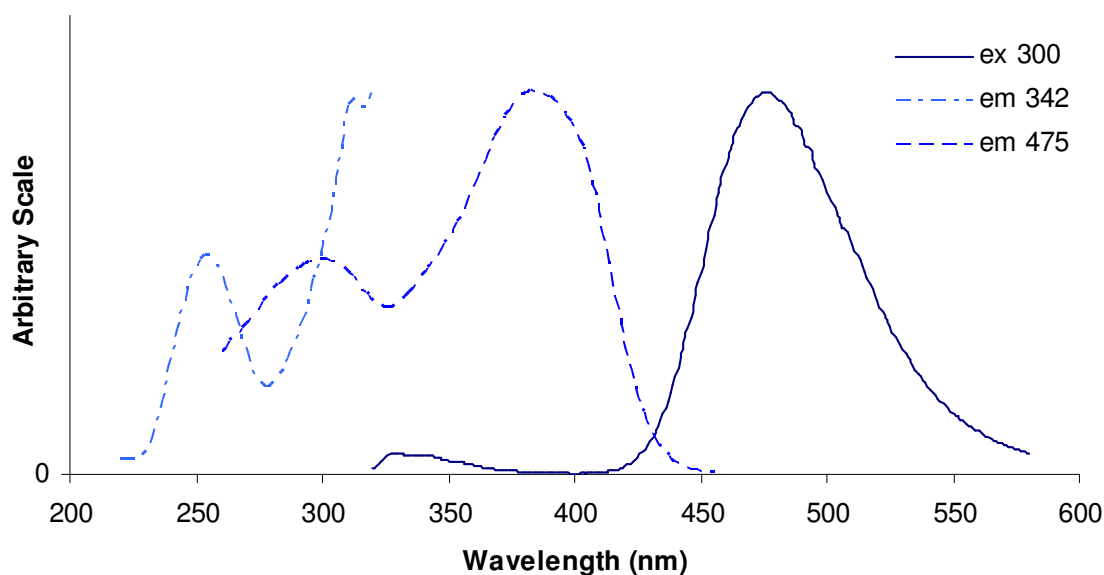


Fig. 4.28 Emission and excitation spectra of  $[\text{Cu}(\mathbf{9})_2][\text{PF}_6]$  measured in dichloromethane depicting an emission spectrum (-) from excitation into the absorption band at 300 nm and an excitation spectra after scanning the excitation holding the emission at 342 (- -) and then 475(- · -) nm.

Excitation into the absorption band at 300 nm of complex  $[\text{Cu}(\mathbf{9})_2][\text{PF}_6]$  (Fig. 4.28) gives rise to two emissions. One emission is very weak and has  $\lambda_{\text{em}} = 342$  nm, the other emission is stronger and has  $\lambda_{\text{em}} = 475$  nm. The latter emission is the same as that observed for the ligand (compound **9**). From the excitation spectrum it can be determined that the emission also has the same origin as that of the ligand, namely the absorption around 391 nm. This is unsurprising given the similarity of the absorption spectra of the ligand and its corresponding copper complex. Measuring the excitation spectrum whilst holding the emission at 342 nm gives rise to a peak with  $\lambda_{\text{ex}} = 257$  nm. The emission at 342 nm is, therefore, ligand-based.

The data for ligand **9** and its copper complex are summarised in Table 4.4.

Compound	$\lambda_{\text{ex}}$	$\lambda_{\text{em}}$	$\lambda_{\text{em}}$	$\lambda_{\text{ex}}$	$\lambda_{\text{em}}$
<b>9</b>	291	473	473	391	473
$[\text{Cu}(\mathbf{9})_2][\text{PF}_6]$	300	342	475		

Table 4.4 A summary of the emission data, recorded in dichloromethane, for **9** and  $[\text{Cu}(\mathbf{9})_2][\text{PF}_6]$

The lifetime of the  $[\text{Cu}(\mathbf{9})_2][\text{PF}_6]$  complex was 2 ns, which is longer than the rate of electron injection. The quantum yield of the complex was reasonable; 37 % in aerated dichloromethane solution at room temperature.

#### 4.3.6 Electrochemistry

A desirable property of a dye for DSSC application is that it is able to donate an electron to  $\text{TiO}_2$ . A further desirable property is that the oxidised dye can be reduced back to the ground state by the  $\text{I}^-/\text{I}_3^-$  redox couple. The oxidation potential of a dye can be explored using cyclic voltammetry.

All measurements were carried out using a solution of the complex in an organic solvent (see figure captions for details), using 0.1M  $\text{TBAPF}_6$  as the electrolyte, a glassy carbon working electrode, Pt wire as the counter-electrode and silver wire as a pseudo-reference electrode, measurements were referenced to  $\text{Fc}/\text{Fc}^+$ .

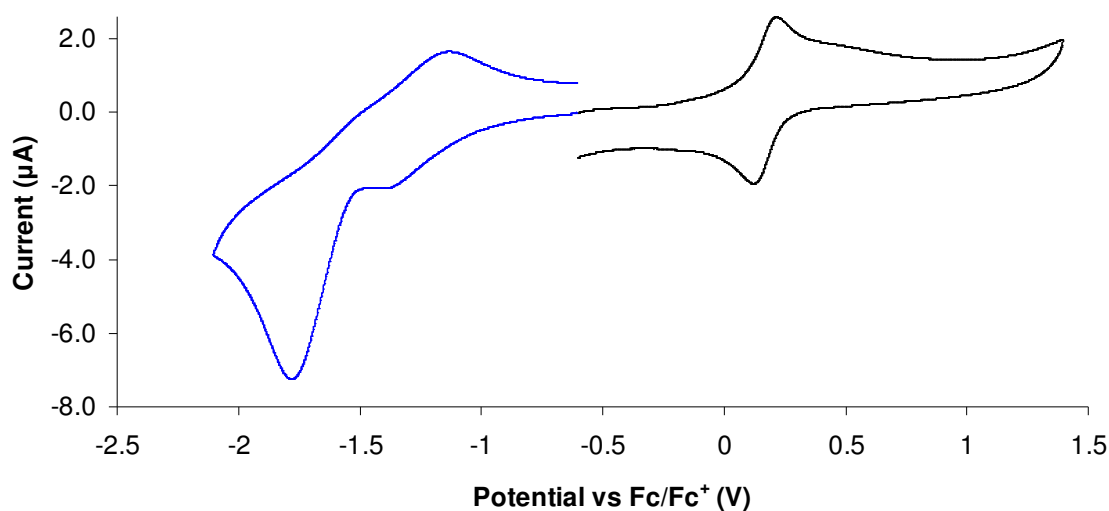


*Fig. 4.29 Cyclic Voltammogram for  $[\text{Cu}(\mathbf{8})_2][\text{PF}_6]$  ( $\text{MeCN}$ , 0.1M  $\text{TBAPF}_6$ , internal reference; ferrocene), oxidative (black) and reductive (blue) scans shown.*

In the oxidative cycle of  $[\text{Cu}(\mathbf{8})_2][\text{PF}_6]$  (Fig. 4.29), a reversible, one-electron oxidation wave is observed at  $E_{1/2} = + 0.17$  V. This is attributed to a  $\text{Cu}(\text{I})/\text{Cu}(\text{II})$  oxidation. The low oxidation potential and reversibility mean that this dye is a potential candidate for application in DSSCs.

Two reductions are observed in the reductive cycle (Fig. 4.29); a small peak at -1.37 V and a large peak at -1.79 V. The peak at -1.13 V could either correspond to the reduction at -1.37 V, rendering said peak quasi-reversible, or it could be due to deposition of by-products from decomposition of the complex.

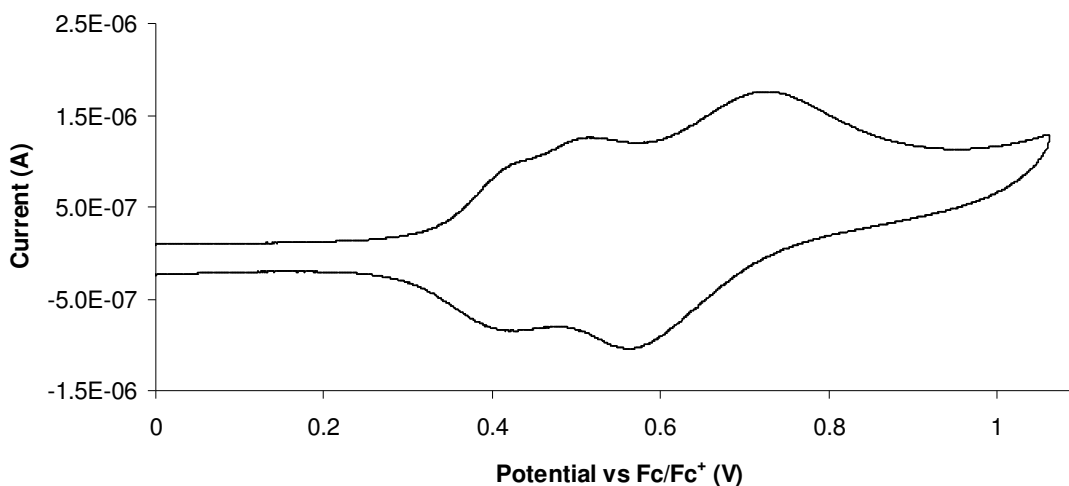


Fig. 4.30 Cyclic Voltammogram for **9** measured (dichloromethane, 0.1M TBAPF<sub>6</sub>, internal reference; ferrocene).

Three oxidation waves are observed in the cyclic voltammogram of **9** (Fig 4.30). The first, with  $E_{1/2} = 0.43$  V, and second, with  $E_{1/2} = 0.47$  V, are largely reversible. The third, at 0.66 V, is very broad and could be due to a slow electron transfer or two overlapping one electron processes. The extensive overlapping means that it is difficult to ascertain reversibility. It is postulated that the oxidation of the compound leads to the sequential formation of radical cations centered on the triphenylamine groups. In order to obtain more information spectroelectrochemistry was employed (Fig. 4.31).



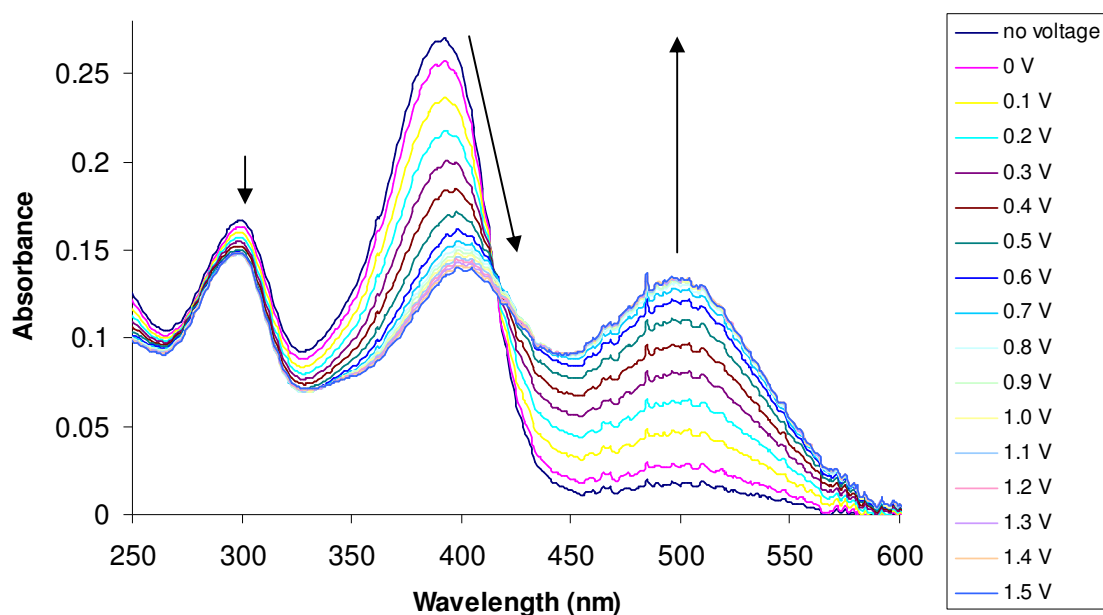
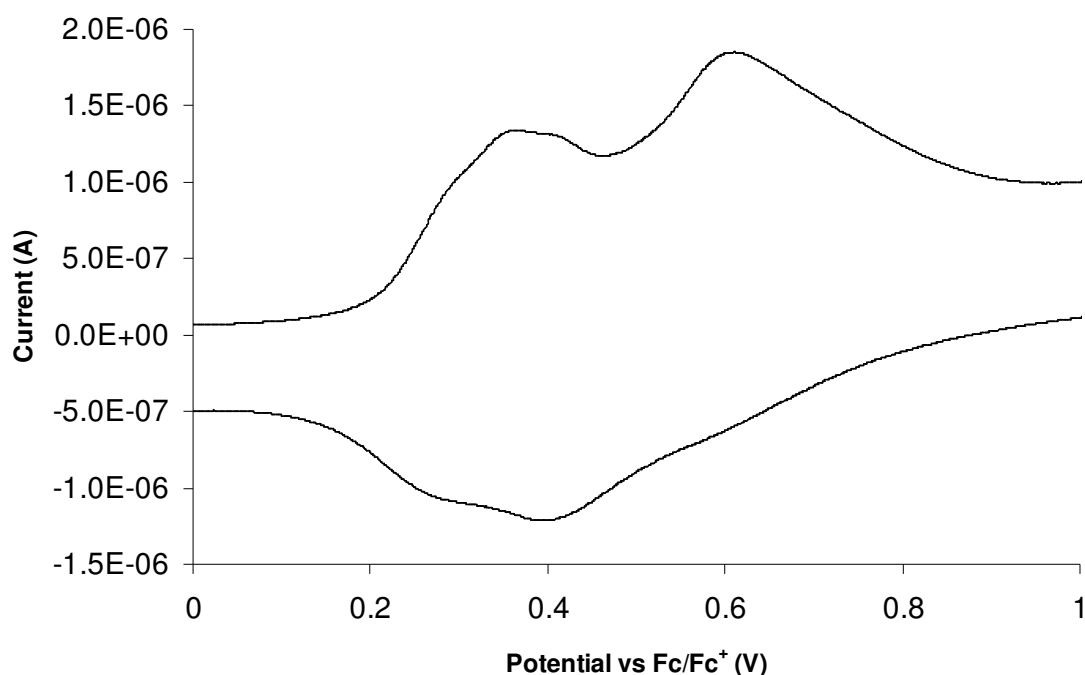


Fig. 4.31. Spectroelectrochemistry of ligand **9**, measured in dichloromethane.

Using spectroelectrochemistry it is possible to observe changes in the UV-vis spectrum of the compound as a result of changing the voltage. The peak at  $\lambda_{\text{max}} = 302$  nm is due to the bipyridine unit<sup>31</sup> and is only slightly affected by increasing the voltage. The peak at  $\lambda_{\text{max}} = 399$  nm is greatly affected on increasing the voltage, which indicates that the triphenylamine group is being oxidised. The growth of the peak with  $\lambda_{\text{max}} = 505$  nm is indicative of the formation of a radical cation as removal of an electron from the HOMO raises the level of the SHOMO (second highest occupied molecular orbital), decreasing the HOMO-LUMO gap and, therefore, giving rise to a peak at a longer wavelength than the original<sup>32</sup>. This also puts forward the postulation that although many processes are observed in the cyclic voltammogram, they are similar processes occurring over the triphenylamine moieties at opposite sides of the molecule as there is only one overall change in the UV-vis spectrum on oxidation, confirmed by the isosbestic point in the spectroelectrochemistry.



*Fig. 4.32 Cyclic Voltammogram for [Cu(9)<sub>2</sub>][PF<sub>6</sub>] measured (dichloromethane, 0.1M TBAPF<sub>6</sub>, internal reference; ferrocene), depicting the oxidations of the complex only.*

The cyclic voltammogram of [Cu(9)<sub>2</sub>][PF<sub>6</sub>] (Fig. 4.32) differs slightly from that of the corresponding ligand. Two broad oxidation waves are observed; the first, centered at 0.33 V, is made up of at least three overlapping quasi-reversible oxidations, the second, centered at 0.60 V is also quasi-reversible. The first broad oxidation wave is coincidental with the expected oxidation of Cu(I)/Cu(II). Spectroelectrochemical studies of the complex gave very similar results to that of the ligand. As will be discussed in Chapter 5 calculations at the B3LYP level indicate that the HOMO of the complex is centered on the triphenylamine groups, which supports the postulation in regard to the oxidation of these groups. Overall the complex is more easily oxidised than the ligand and as it has a quasi-reversible oxidation at low potential it is a plausible candidate for application in DSSCs.

### 4.3.7 Crystal Structures

Red blocks of  $[\text{Cu}(\mathbf{8})_2][\text{PF}_6]$  were grown by diffusing diethyl ether into an acetonitrile solution of the complex. The structure solved in the monoclinic  $P2_1/c$  space group with a very good R factor of 2.93 %. The asymmetric unit contains one cation and one  $\text{PF}_6^-$  anion. The structure of the cation is depicted in Fig. 4.33.

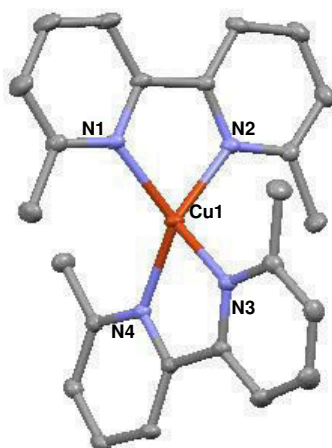


*Fig. 4.33 Structure of  $[\text{Cu}(\mathbf{8})_2][\text{PF}_6]$  with ellipsoids plotted at 50% probability and the hydrogens removed for clarity. Selected bond parameters:  $\text{Cu1-N1} = 2.0249(9)$ ,  $\text{Cu1-N2} = 2.0471(9)$ ,  $\text{Cu1-N3} = 2.0446(9)$ ,  $\text{Cu1-N4} = 2.0335(9)$  Å;  $\text{N1-Cu1-N2} = 81.13(4)$ ,  $\text{N1-Cu1-N3} = 127.51(4)$ ,  $\text{N3-Cu1-N4} = 81.59(4)$ ,  $\text{N2-Cu1-N4} = 132.08(4)^\circ$ .*

The structures of  $[\text{Cu}(\mathbf{8})_2][\text{BF}_4]^{23}$  and  $[\text{Cu}(\mathbf{8})_2][\text{ClO}_4]^{24}$  have previously been reported. By comparison, the Cu-N1 and Cu-N4 bond lengths in the structure of  $[\text{Cu}(\mathbf{8})_2][\text{PF}_6]$  are slightly shorter and the Cu-N2 and Cu-N3 bond lengths are slightly longer than those of previously reported structures (Table 4.5). The N1-Cu-N2 and N3-Cu-N4 bond angles are smaller than those reported for  $[\text{Cu}(\mathbf{8})_2][\text{BF}_4]$  and the same as those reported for  $[\text{Cu}(\mathbf{8})_2][\text{ClO}_4]$  (Table 4.5). The N1-Cu-N3 bond angle is smaller and the N2-Cu-N4 bond angle is larger than those reported for both  $[\text{Cu}(\mathbf{8})_2][\text{BF}_4]$  and  $[\text{Cu}(\mathbf{8})_2][\text{ClO}_4]$  (Table 4.5)

Bond (Å)/ Angle (°)	[Cu(8) <sub>2</sub> ][BF <sub>4</sub> ]	[Cu(8) <sub>2</sub> ][ClO <sub>4</sub> ]	[Cu(8) <sub>2</sub> ][PF <sub>6</sub> ]
Cu-N1	2.052(1)	2.047(2)	2.0249(9)
Cu-N2	2.018(1)	2.029(2)	2.0471(9)
Cu-N3	2.024(1)	2.021(2)	2.0446(9)
Cu-N4	2.040(1)	2.045(2)	2.0335(9)
N1-Cu-N2	81.66(6)	81.13(9)	81.13(4)
N3-Cu-N4	82.22(6)	81.72(10)	81.59(4)
N1-Cu-N3	128.46(4)	130.42(9)	127.51(4)
N2-Cu-N4	130.33(7)	128.48(9)	132.08(4)

Table 4.5 Comparison of selected bond parameters for [Cu(8)<sub>2</sub>][BF<sub>4</sub>], [Cu(8)<sub>2</sub>][ClO<sub>4</sub>] and [Cu(8)<sub>2</sub>][PF<sub>6</sub>].

The angle between the two bipyridine planes is 76.37°, which is considerably smaller than that observed in the structures of [Cu(8)<sub>2</sub>][BF<sub>4</sub>] (80.9°) and [Cu(8)<sub>2</sub>][ClO<sub>4</sub>] (80.7°). As in the case of [Cu(8)<sub>2</sub>][BF<sub>4</sub>] and [Cu(8)<sub>2</sub>][ClO<sub>4</sub>], the bipyridine ligands are not planar and twists of 10.56° around the N3-N4 bipyridine and 0.61° around the N1-N2 bipyridine C-C bonds are present in the structure.

The [Cu(8)<sub>2</sub>]<sup>+</sup> cations pack in chains (Fig. 4.34). There is one crystallographically independent CH-π interaction between H141 and the py ring containing N2 (x, y, -1+z) which leads to propagation of chains that follow the crystallographic c axis (Fig 4.35). There are also extensive CH...F interactions throughout the lattice.

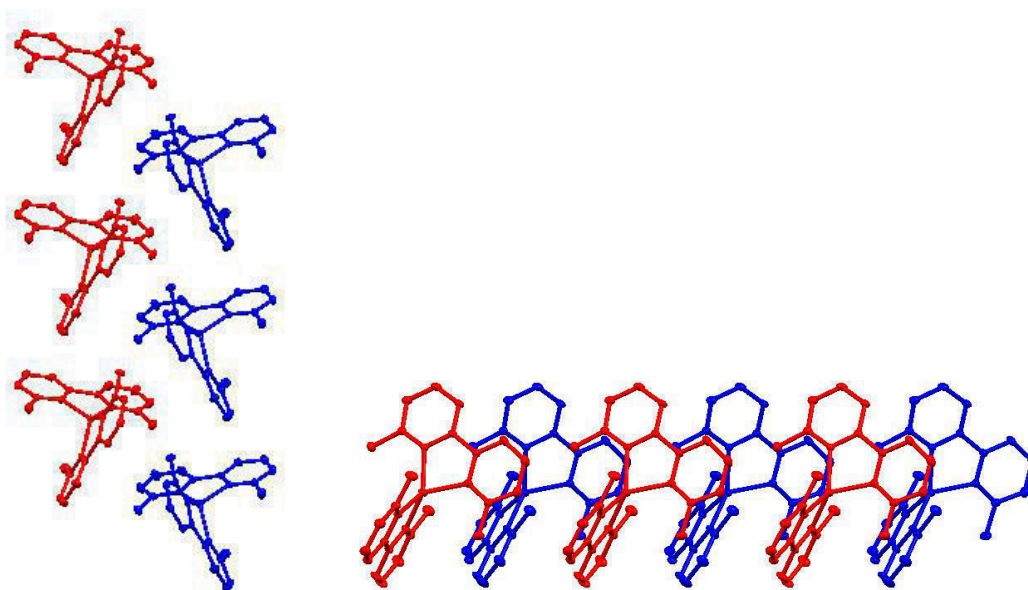


Fig. 4.34 Packing of the [Cu(8)<sub>2</sub>]<sup>+</sup> cations viewed along the (left) a axis and (right) b axis.

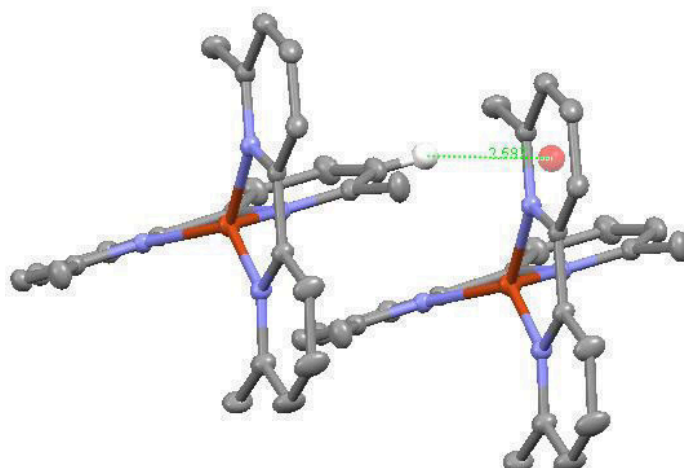


Fig. 4.35 Face to edge interaction between H141 and the ring including N2 (H141-centroid distance = 2.587 Å).

Yellow plates of **9** were grown by slowly diffusing hexanes into a dichloromethane solution of the compound. The structure solved in the orthorhombic *Pbca* space group with an R factor of 3.84 %. The asymmetric unit contains half a molecule. The second half of the molecule is generated by symmetry and is related to the first half by an inversion centre.

The structure of the molecule is depicted in Fig. 4.36 and selected bond lengths and angles are listed in the caption.

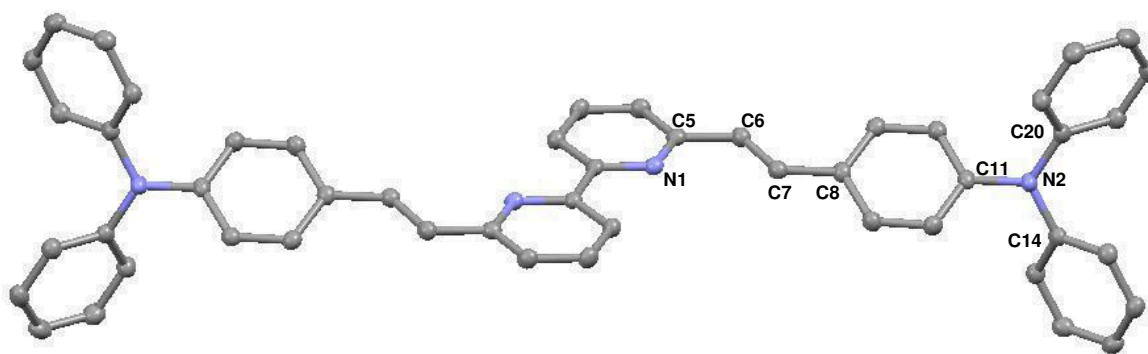
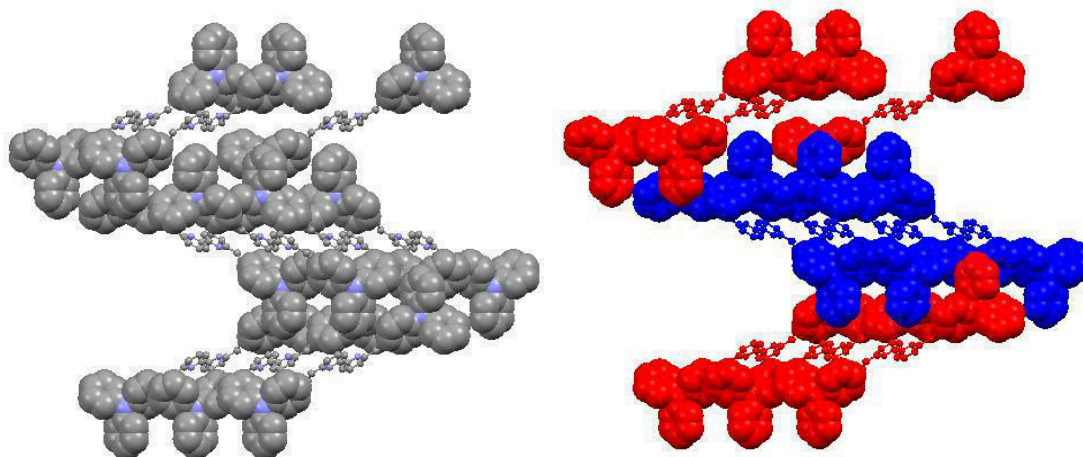


Fig. 4.36 Structure of **9** with ellipsoids plotted at 50% probability and hydrogens omitted for clarity. Selected bond parameters:  $N1-C5 = 1.352(2)$ ,  $C5-C6 = 1.467(2)$ ,  $C6-C7 = 1.337(2)$ ,  $C7-C8 = 1.461(2)$ ,  $C11-N2 = 1.425(2)$ ,  $N2-C14 = 1.418(2)$ ,  $N2-C20 = 1.417(2)$  Å;  $N1-C5-C6 = 117.6(1)$ ,  $C5-C6-C7 = 123.7(1)$ ,  $C6-C7-C8 = 127.2(1)$ ,  $C11-N2-C14 = 119.3(1)$ ,  $C11-N2-C20 = 119.3(1)$ ,  $C14-N2-C20 = 120.3(1)^\circ$ .

As expected the bipyrindine unit is in the *trans*-conformation. This is to minimise electron repulsion between the two nitrogen lone pairs. Due to half of the molecule being generated by symmetry the bipyrindine unit is planar. The bond lengths around the bipyrindine ring and triphenylamine unit are unexceptional. The C5-C6 and C7-C8 bond lengths are consistent with single bonds. In comparison, the C6-C7 bond is contracted and has a smaller bond length, which is consistent with a double bond. The C8-C13 ring is twisted slightly, relative to the bipyrindine, and the angle between the planes is  $30.11^\circ$  (Plane 1 = ring containing N1, plane 2 = ring containing C8).

The molecules pack with intermeshing triphenylamine moieties (Figs. 4.37 and 4.38). There are no interactions between the bipyrindine moieties.



*Fig. 4.37 Packing of the molecules, (left) atoms coloured by element, (right) red and blue colours highlight the intermeshing of the triphenylamine units. Both viewed along the *a* axis.*

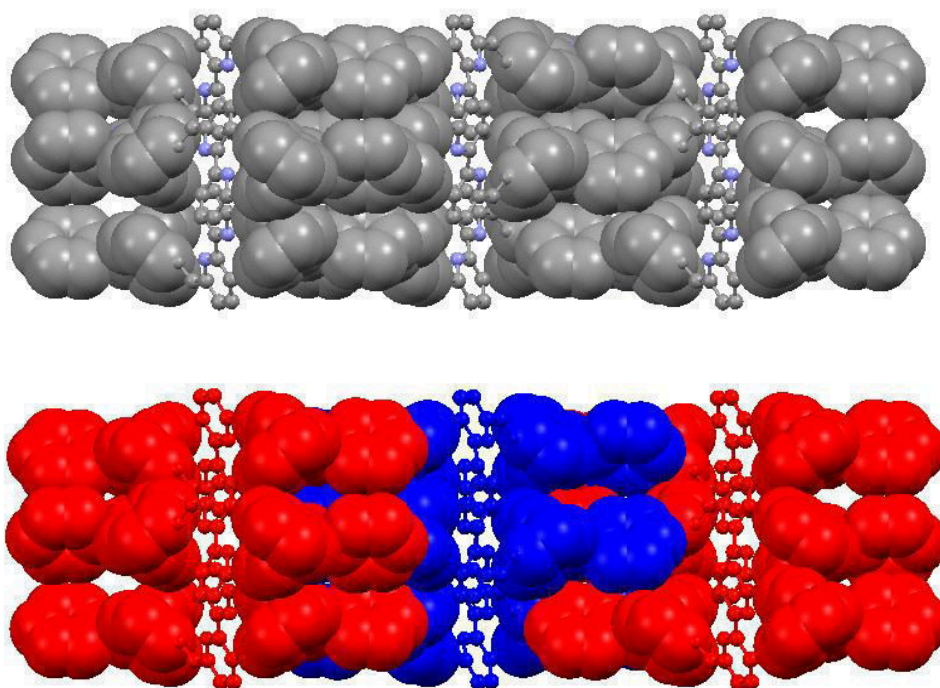


*Fig. 4.38 Packing of the molecules, (top) atoms coloured by element, (bottom) red and blue colours highlight the intermeshing of the triphenylamine units. Both viewed along the *b* axis.*

Orange plates of  $[\text{Cu}(\mathbf{9})_2][\text{PF}_6]$  were grown by slowly diffusing hexanes into a dichloromethane solution of the complex. The crystal solved in the tetragonal  $P4/n$  space group with an R factor of 4.72 %. Unidentifiable electron density within the lattice voids was removed using the program SQUEEZE<sup>33</sup> which slightly improved the R factor to 4.65 %. The asymmetric unit contains one quarter of the complex and a quarter of a disordered  $\text{PF}_6^-$  anion. The structure of the  $[\text{Cu}(\mathbf{9})_2]^+$  cation is depicted in Fig. 4.39 and selected bond lengths and angles are listed in the caption.

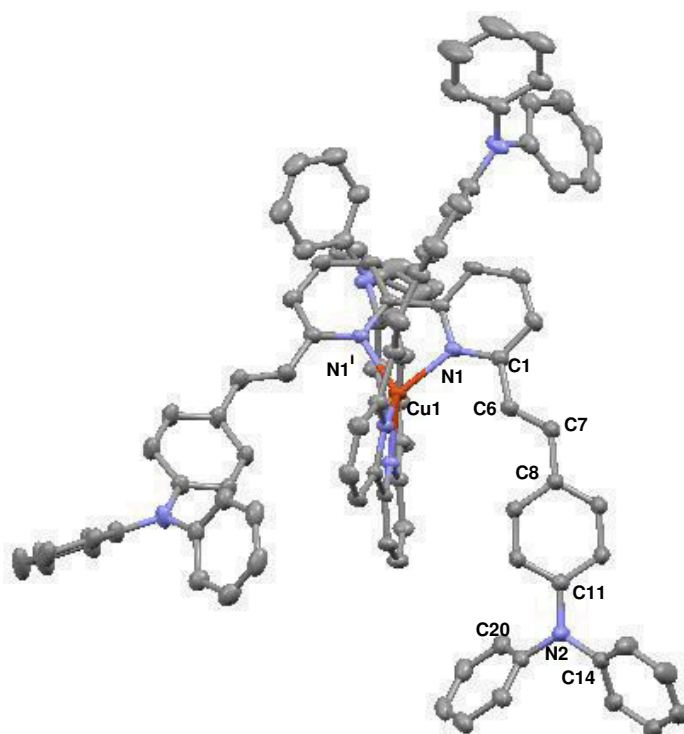


Fig. 4.39 Cation in  $[\text{Cu}(\mathbf{9})_2][\text{PF}_6]$  with ellipsoids plotted at 50% probability and hydrogens omitted for clarity. Selected bond parameters:  $\text{Cu1-N1} = 2.038(2)$ ,  $\text{N1-C1} = 1.353(2)$ ,  $\text{C5-C6} = 1.481(3)$ ,  $\text{C6-C7} = 1.320(3)$ ,  $\text{C7-C8} = 1.465(3)$ ,  $\text{C11-N2} = 1.418(3)$ ,  $\text{N2-C14} = 1.411(3)$ ,  $\text{N2-C20} = 1.426(3)$  Å;  $\text{N1}^i\text{-Cu1-N1} = 80.48(6)$ ,  $\text{N1-C1-C6} = 113.9(2)$ ,  $\text{C1-C6-C7} = 125.9(2)$ ,  $\text{C6-C7-C8} = 122.5(2)$ ,  $\text{C11-N2-C14} = 122.1(2)$ ,  $\text{C11-N2-C20} = 119.0(2)$ ,  $\text{C14-N2-C20} = 118.8(2)$  °.

Upon coordination, the geometry of the bipyridine domain has changed from *trans* to *cis* and the two ligands coordinate orthogonally (angle between the planes is  $89.7^\circ$ ) to the copper atom, causing a tetragonal geometry of the cation. The bond lengths of the ligand



are virtually unchanged on coordination. Of note are the C1-C6 and N2-C20 bonds, which are slightly elongated upon complexation. As in the case of the ligand the short C6-C7 bond lengths are confirmation of a double bond.

The ligands wrap tightly around the  $\text{Cu}^+$  ion (Fig 4.40) which probably causes the twist in the bipyridine (angle between pyridine planes is  $16.6^\circ$ ).

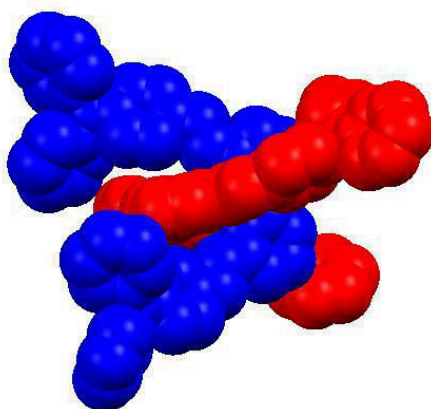


Fig. 4.40 Space-filling diagram of the  $[\text{Cu}(\mathbf{9})_2]^+$  cation in  $[\text{Cu}(\mathbf{9})_2][\text{PF}_6]$  with the two ligands shown in red and blue.

The complexes pack with intermeshing triphenylamine groups (Fig 4.41). Similarly to the packing of compound **9**, there are no interactions between the bipyridine groups. The numerous  $\text{CH}\dots\text{F}$  interactions throughout the lattice play an important role in the crystal packing.

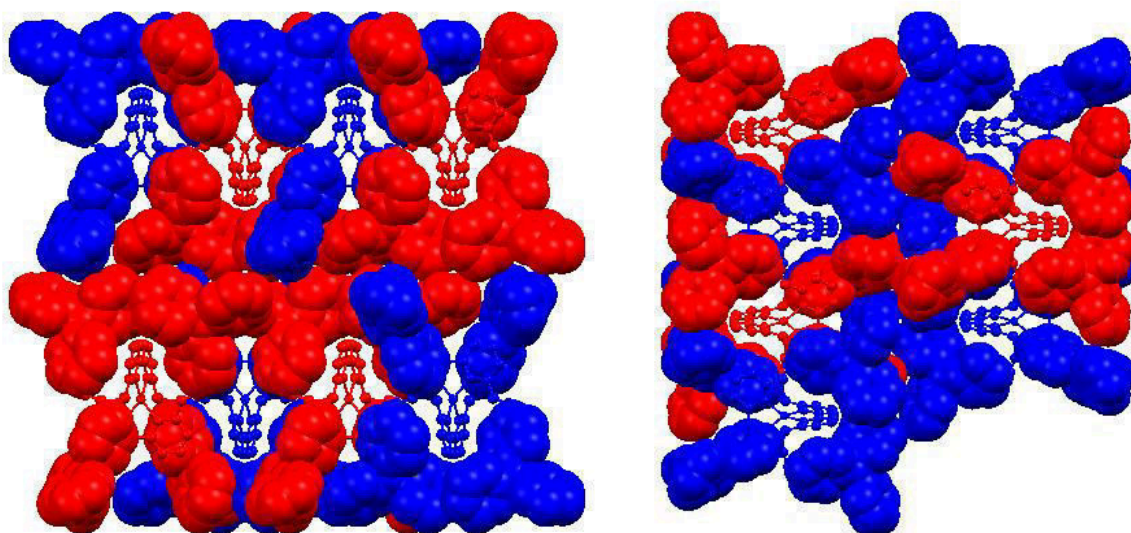


Fig. 4.41 Packing of the cations with red and blue colours highlighting the intermeshing of the triphenylamine units, (right) viewed along the  $a$  axis, (bottom) viewed along the  $b$  axis.

#### 4.3.8 DSSCs Incorporating the Cu(I) Complexes

The following discussion is based on data obtained by Liselotte Siegfried and Dr. Biljana Bozic-Weber in the in-house solar cell laboratory.

The lability of Cu(I) has been exploited to form heteroleptic complexes bound to titanium dioxide, starting from a homoleptic complex in the following step-wise manner:

First, the anodes for the solar cells (see experimental section) were dipped into DMSO solutions of ligands **10**, **11**, **12** or **13** (Fig. 4.42). After washing and drying, the electrodes were immersed in EtOH solutions of  $[\text{Cu}(\mathbf{8})_2][\text{PF}_6]$  or  $\text{CH}_2\text{Cl}_2$  solutions of  $[\text{Cu}(\mathbf{9})_2][\text{PF}_6]$  for 64 hours. During this period, the  $\text{TiO}_2$  changed from colourless to orange. When the slides were washed with EtOH, the orange colour was retained, indicating that ligand exchange at copper(I) had occurred with formation of a surface-bound heteroleptic complex. It is unlikely that the bound species is the homoleptic complex  $[\text{Cu}(\text{L})_2]^+$  ( $\text{L} = \mathbf{8}$ ,  $\mathbf{9}$ ) since ligands **8** and **9** have no substituents capable of binding the complex to the surface.

The anchoring ligands that were used are depicted in Fig 4.42.

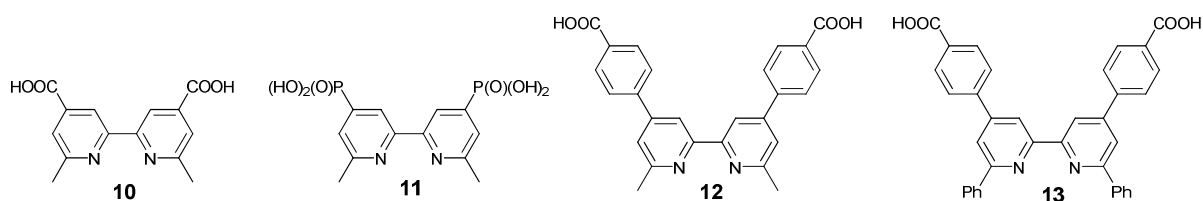


*Fig. 4.42 Structures of the anchoring ligands, 10-13. The anchoring groups are the carboxylic or phosphonic acids or their conjugate bases.*

The cells were measured two days after sealing and the efficiencies are given in Table 4.6. Cells made using complex  $[\text{Cu}(\mathbf{9})_2][\text{PF}_6]$  were generally more efficient than those made with  $[\text{Cu}(\mathbf{8})_2][\text{PF}_6]$ . The greater efficiency is attributed in part to the greater light-harvesting ability of  $[\text{Cu}(\mathbf{9})_2][\text{PF}_6]$  due to the extended  $\pi$ -conjugation of the ligand. It is also thought that the bulky triphenylamine groups may help to minimise back migration of an electron from the semiconductor to the dye (§ Chapter 5).

For both starting complexes, ligand exchange with **11** or **12** resulted in DSSCs with the highest efficiency and this is consistent with previously reported DSSCs made in the

Constable group<sup>19</sup>. Combination with ligand **13** resulted in DSSCs with the poorest overall efficiencies and this may be due to steric crowding at the copper(I) centre, particularly in the case of [Cu(**9**)(**13**)]PF<sub>6</sub>.

[Cu(L) <sub>2</sub> ] <sup>+</sup>	L'	J <sub>sc</sub> / A cm <sup>-2</sup>	V <sub>oc</sub> / mV	ff	η / %
[Cu( <b>8</b> ) <sub>2</sub> ] <sup>+</sup>	<b>10</b>	0.003	518	0.58	1.03
[Cu( <b>8</b> ) <sub>2</sub> ] <sup>+</sup>	<b>11</b>	0.004	618	0.46	1.18
[Cu( <b>8</b> ) <sub>2</sub> ] <sup>+</sup>	<b>12</b>	0.006	563	0.45	1.63
[Cu( <b>8</b> ) <sub>2</sub> ] <sup>+</sup>	<b>13</b>	0.001	536	0.64	0.49
[Cu( <b>9</b> ) <sub>2</sub> ] <sup>+</sup>	<b>10</b>	0.001	482	0.65	0.47
[Cu( <b>9</b> ) <sub>2</sub> ] <sup>+</sup>	<b>11</b>	0.005	609	0.60	1.95
[Cu( <b>9</b> ) <sub>2</sub> ] <sup>+</sup>	<b>12</b>	0.005	555	0.60	1.70
[Cu( <b>9</b> ) <sub>2</sub> ] <sup>+</sup>	<b>13</b>	0.001	555	0.63	0.51
N719		0.018	718	0.58	7.29

Table 4.6 DSSC efficiency data two days after the sealing of the cell, compared to N719 prepared under the same conditions.

The DSSCs were measured again, seven days after sealing (Table 4.7). The efficiencies of the cells with [Cu(**9**)<sub>2</sub>]<sup>+</sup>/**11** and [Cu(**9**)<sub>2</sub>]<sup>+</sup>/**12** were much improved and as such show comparable efficiency to those reported by Bessho *et al.* in 2009<sup>15</sup>. Although it is unclear why the efficiency has increased so much, it could be due to the rearrangement of aggregates on the surface of the TiO<sub>2</sub><sup>34-36</sup>. From in-house observations this appears to be a general phenomenon for Cu(I) containing dyes in sealed cells.

$[\text{Cu}(\text{L})_2]^+$	L'	$J_{\text{sc}} / \text{A cm}^{-2}$	$V_{\text{oc}} / \text{mV}$	ff	$\eta / \%$
$[\text{Cu}(\mathbf{8})_2]^+$	<b>10</b>	0.004	530	0.58	1.17
$[\text{Cu}(\mathbf{8})_2]^+$	<b>11</b>	0.005	643	0.44	1.30
$[\text{Cu}(\mathbf{8})_2]^+$	<b>12</b>	0.006	595	0.46	1.69
$[\text{Cu}(\mathbf{8})_2]^+$	<b>13</b>	0.001	563	0.63	0.45
$[\text{Cu}(\mathbf{9})_2]^+$	<b>10</b>	0.002	522	0.66	0.64
$[\text{Cu}(\mathbf{9})_2]^+$	<b>11</b>	0.006	627	0.61	2.35
$[\text{Cu}(\mathbf{9})_2]^+$	<b>12</b>	0.007	579	0.60	2.33
$[\text{Cu}(\mathbf{9})_2]^+$	<b>13</b>	0.002	562	0.63	0.57
N719	-	0.018	718	0.58	7.29

Table 4.7 DSSC efficiency data seven days after the sealing of the cell, compared to N719 prepared under the same conditions.

#### 4.4 Conclusions

Two homoleptic copper(I) complexes were synthesised for application in dye sensitised solar cells. One complex  $[\text{Cu}(\mathbf{8})_2][\text{PF}_6]$  was very simple, utilising the 6,6'-dimethyl-2,2'-bipyridine ligand and the other  $[\text{Cu}(\mathbf{9})_2][\text{PF}_6]$ , based on the same ligand, had extended  $\pi$ -conjugation. The absorption properties of  $[\text{Cu}(\mathbf{9})_2][\text{PF}_6]$  were consistent with extended  $\pi$ -conjugation, in that the complex absorbed more light than the simpler  $[\text{Cu}(\mathbf{8})_2][\text{PF}_6]$  complex. Both complexes were capable of being oxidised to their corresponding copper(II) complexes and being reduced back to the copper(I) complex, which meant that they were suitable for use in a DSSC. Finally heteroleptic complexes were made *in situ* and their efficiencies measured. It was found that DSSCs made with  $[\text{Cu}(\mathbf{9})_2]^+/\mathbf{11}$  and  $[\text{Cu}(\mathbf{9})_2]^+/\mathbf{12}$  had the highest efficiencies; 2.35 and 2.33 % respectively seven days after sealing the cells, compared to an efficiency of 7.29% with N719.

## 4.5 Experimental

### 9

Synthesis:

Compound **8** (550 mg, 2.98 mmol) and 4-(diphenylamino)benzaldehyde (1.87 g, 6.87 mmol) were stirred in dry DMF (70 cm<sup>3</sup>) in a reaction flask and KO<sup>t</sup>Bu (1.005g, 8.96 mmol) was added. The vessel was flushed with N<sub>2</sub> for 10 min and the reaction mixture was stirred for 56 h in the dark after which time a dark yellow solid precipitated. This was filtered and dried in air. The crude product was dissolved in the minimum amount of CH<sub>2</sub>Cl<sub>2</sub> and purified by column chromatography (SiO<sub>2</sub>, CH<sub>2</sub>Cl<sub>2</sub>). The first (orange) fraction was collected and solvent was removed *in vacuo*. Compound **9** was isolated as a yellow powder

Yield: 1.13 g, 54.7%

<sup>1</sup>H NMR: (500 MHz, CDCl<sub>3</sub>, 25 °C, TMS) δ/ppm: 8.41 (dd, *J* = 7.8, 0.6 Hz, 2H, **A**<sup>3</sup>), 7.81 (t, *J* = 7.8 Hz, 2H, **A**<sup>4</sup>), 7.73 (d, *J* = 16.0 Hz, 2H, *b*), 7.49 (d<sub>AB</sub>, *J* = 8.6 Hz, 2H, **B**<sup>2</sup>), 7.39 (dd, *J* = 7.7, 0.6 Hz, 2H, **A**<sup>5</sup>), 7.28 (m, 4H, **C**<sup>3</sup>), 7.15 (m, 10H, **C**<sup>2+a</sup>), 7.07 (m, 8H, **C**<sup>4+B<sup>3</sup>).</sup>

<sup>13</sup>C NMR (126 MHz, CDCl<sub>3</sub>, 25 °C, TMS) δ/ppm: 156.1 (**A**<sup>2</sup>), 155.3 (**A**<sup>6</sup>), 148.1 (**B**<sup>4</sup>), 147.6 (**C**<sup>1</sup>), 137.4 (**A**<sup>4</sup>), 132.4 (*b*), 130.8 (**B**<sup>1</sup>), 129.5 (**C**<sup>3</sup>), 128.2 (**B**<sup>2</sup>), 126.5 (*a*), 124.9 (**C**<sup>3</sup>), 123.4 (**B**<sup>3/C<sup>4</sup>), 123.3 (**B**<sup>3/C<sup>4</sup>), 121.9 (**A**<sup>5</sup>), 119.5 (**A**<sup>3</sup>).</sup></sup>

ESI: *m/z* 695.3 [M + H]<sup>+</sup> (calc. 695.3)

Found: C 85.49, H 5.64, N 7.96; C<sub>50</sub>H<sub>38</sub>N<sub>4</sub>·0.5H<sub>2</sub>O requires C 85.32, H 5.58, N 7.96.

Melting point: 241.4 °C

[Cu(**8**)<sub>2</sub>][PF<sub>6</sub>]

Synthesis:

[Cu(MeCN)<sub>4</sub>][PF<sub>6</sub>] (37.3 mg, 0.100 mmol) was dissolved in MeCN (2 cm<sup>3</sup>) and the solution was added to a solution of compound **8** (36.8 mg, 0.200 mmol) in CHCl<sub>3</sub> (5 cm<sup>3</sup>). The solution immediately became red in colour and was stirred for 30 min. Addition of Et<sub>2</sub>O (10 cm<sup>3</sup>) afforded a red precipitate, which was collected by filtration

over Celite. The product was washed with H<sub>2</sub>O and Et<sub>2</sub>O and removed from the Celite by dissolution in MeCN. Solvent was removed *in vacuo* and [Cu(**8**)<sub>2</sub>][PF<sub>6</sub>] was isolated as red crystals.

Yield: 44.6 mg, 77.3%

<sup>1</sup>H NMR: (500 MHz, CD<sub>3</sub>CN, 25 °C, TMS) δ/ppm: 8.26 (d, *J* = 8.0 Hz, 2H, **A**<sup>3</sup>),

8.02 (t, *J* = 7.9 Hz, 2H, **A**<sup>4</sup>), 7.50 (d, *J* = 7.7 Hz, 2H, **A**<sup>5</sup>), 2.22 (s, 6H, *a*)

<sup>13</sup>C NMR: δ<sub>C</sub> (126 MHz, CD<sub>3</sub>CN, 25 °C, TMS): 158.4 (**A**<sup>6</sup>), 152.6 (**A**<sup>2</sup>), 139.2 (**A**<sup>4</sup>), 126.7 (**A**<sup>5</sup>), 120.4 (**A**<sup>3</sup>), 25.2 (*a*).

MALDI-TOF: *m/z* 431.0 [M – PF<sub>6</sub>]<sup>+</sup> (calc. 431.1), 246.5 [M – **8** – PF<sub>6</sub>]<sup>+</sup> (calc. 247.0).

Found: C 49.38, H4.18, N 9.63; C<sub>24</sub>H<sub>24</sub>N<sub>4</sub>CuPF<sub>6</sub>•0.5H<sub>2</sub>O requires

C 49.19, H15 4.30, N 9.56.

[Cu(**9**)<sub>2</sub>][PF<sub>6</sub>]

Synthesis: [Cu(MeCN)<sub>4</sub>][PF<sub>6</sub>] (26.8 mg, 0.0719 mmol) was dissolved in MeCN (2 cm<sup>3</sup>) and the solution was added to a solution of **2** (100 mg, 0.14 mmol) in CHCl<sub>3</sub> (10 cm<sup>3</sup>). The solution immediately changed from yellow to orange and was ultrasonicated for 60 min. The solvents were then removed *in vacuo* and [Cu(**9**)<sub>2</sub>][PF<sub>6</sub>] was isolated as an orange powder.

Yield: 92.5 mg, 80.4 %

<sup>1</sup>H NMR: (500 MHz, CDCl<sub>3</sub>, 25 °C, TMS) δ/ppm: 7.90 (d, *J* = 7.6, 4H, **A**<sup>3</sup>),

7.85 (t, *J* = 7.8 Hz, 4H, **A**<sup>4</sup>), 7.74 (d, *J* = 7.7 Hz, 4H, **A**<sup>5</sup>), 7.30 (t, *J* = 7.9 Hz, 16H, **C**<sup>3</sup>),

7.12 (d, *J* = 16.3 Hz, 4H, *b*), 7.08 (m, 24H, **C**<sup>2</sup>+**C**<sup>4</sup>), 6.79 (d, *J* = 8.6 Hz, 8H, **B**<sup>3</sup>)

overlapping with 6.77 (d, *J* = 16.3 Hz, 4H, *a*), 6.67 (d, *J* = 8.6 Hz, 8H, **B**<sup>2</sup>).

<sup>13</sup>C NMR: (126 MHz, CDCl<sub>3</sub>, 25 °C, TMS) δ/ppm: 155.5 (**A**<sup>6</sup>), 152.2 (**A**<sup>2</sup>), 148.9 (**B**<sup>4</sup>),

147.1 (**C**<sup>1</sup>), 138.0 (**A**<sup>4</sup>), 135.0 (*b*), 129.6 (**C**<sup>3</sup>), 128.8 (**B**<sup>1</sup>), 127.9 (**B**<sup>2</sup>) 125.1 (**C**<sup>2</sup>),

124.7 (*a*), 123.9 (**C**<sup>4</sup>), 122.4 (**A**<sup>5</sup>), 122.3 (**B**<sup>3</sup>), 119.9 (**A**<sup>3</sup>).

ESI: *m/z* 1453.7 [M – PF<sub>6</sub>]<sup>+</sup> (calc. 1452.6), 695.5 [**2** + H]<sup>+</sup> (calc. 695.3).

Found: C 73.98, H 4.76, N 7.71; C<sub>100</sub>H<sub>76</sub>CuF<sub>6</sub>N<sub>8</sub>P•MeCN•H<sub>2</sub>O requires

C73.92, H 4.93, N 7.61.

## Preparation of Solar Cells:

TiO<sub>2</sub> paste was prepared adapting the procedure of Grätzel and coworkers<sup>37</sup>; changes to the published procedure were the use of a porcelain (in place of alumina) mortar, sonicator bath in place of an ultrasonic horn, terpineol (CAS: 8000-41-7) rather than  $\alpha$ -terpineol, and the omission of the three roller mill treatment. The FTO glass (Solaronix TCO22-7, 2.2 mm thickness, sheet resistance  $\approx 7 \Omega \text{ square}^{-1}$ ) was cleaned by sonicating in acetone, EtOH, Hellmanex® surfactant (2% in water), water and EtOH baths sequentially for 10 min. After treatment in a UV-O<sub>3</sub> system (Model 256-220, Jelight Company Inc), the FTO plates were immersed in aqueous TiCl<sub>4</sub> solution (40 mmol dm<sup>-3</sup>) at 70°C for 30 min, and washed with H<sub>2</sub>O and EtOH. Nanocrystalline TiO<sub>2</sub> electrodes were made by doctor blading the TiO<sub>2</sub> paste onto a conducting glass slide and keeping them at room temperature for 10 min to allow the paste to mature to minimize surface irregularities. The electrode was then gradually heated under an air flow at 70°C for 30 min, 135°C for 5 min, 325°C for 5 min, 375°C for 90 min, 450°C for 15 min, and 500°C for 15 min. After annealing, the TiO<sub>2</sub> film was treated with 40 mM TiCl<sub>4</sub> solution as described above, rinsed with H<sub>2</sub>O and EtOH and sintered at 500°C for 30 min. After cooling to  $\approx 80^\circ\text{C}$ , each electrode was immersed in a DMSO solution of anchoring ligand **10**, **11**, **12** or **13** (1 mmol dm<sup>-3</sup>) for 24 h. The colourless slide was removed from the solution, washed with DMSO and EtOH, and dried. The electrode with adsorbed anchoring ligand was immersed in an EtOH solution of [Cu(**8**)<sub>2</sub>][PF<sub>6</sub>] or a CH<sub>2</sub>Cl<sub>2</sub> solution of [Cu(**9**)<sub>2</sub>][PF<sub>6</sub>] (0.4 mmol dm<sup>-3</sup>) and this was left to stand for 64 h during which time the slide turned orange. The electrode was removed from the solution and was washed with EtOH. To prepare the counter electrode, a hole was drilled in an FTO glass plate (cleaned and pre-treated as above). The perforated sheet was heated in air for 15 min at 450°C to remove organic residues and was then washed as described for the working electrode. The Pt catalyst was deposited on the FTO glass by coating with a drop of H<sub>2</sub>PtCl<sub>6</sub>, 5 mmol dm<sup>-3</sup> in propan-2-ol and heated to 400°C for 15 min. The dye-covered TiO<sub>2</sub> electrode and Pt counter-electrode were assembled using thermoplast hot-melt sealing foil (Solaronix, Meltonix 1170-25 Series, 25 microns thick) by heating while pressing them together. The electrolyte comprised LiI (0.1 mol dm<sup>-3</sup>), I<sub>2</sub> (0.05 mol dm<sup>-3</sup>), 1-methylbenzimidazole (0.5 mol dm<sup>-3</sup>) and 1-butyl-3-methylimidazolium iodide (0.6 mol dm<sup>-3</sup>) in methoxypropionitrile, and was introduced into the cell by vacuum

backfilling. The hole on the counter electrode was finally sealed using the hot-melt sealing foil and a cover glass. Measurements were made by irradiating from behind using a light source SolarSim 150 ( $100 \text{ mW cm}^{-2} = 1 \text{ sun}$ ). The power of the simulated light was calibrated by using a reference Si photodiode. The standard dye N719 was purchased from Solaronix. The active area of the cell was  $0.288 \text{ cm}^2$  and the cell was not masked during the measurements.



## 4.6 References

1. *Kyoto Treaty*, [http://unfccc.int/kyoto\\_protocol/items/3145.php](http://unfccc.int/kyoto_protocol/items/3145.php), Accessed 4th December, 2012.
2. A. Hagfeldt, G. Boschloo, L. Sun, L. Kloo and H. Pettersson, *Chem. Rev.*, 2010, **110**, 6595-6663.
3. M. Grätzel, *J. Photochem. Photobiol. C*, 2003, **4**, 145-153.
4. S. Ardo and G. J. Meyer, *Chem. Soc. Rev.*, 2009, **38**, 115-164.
5. G. J. Meyer, *ACS Nano*, 2010, **4**, 4337-4343.
6. M. K. Nazeeruddin, E. Baranoff and M. Grätzel, *Sol. Energy*, 2011, **85**, 1172-1178.
7. B. O'Regan and M. Gratzel, *Nature*, 1991, **353**, 737-740.
8. Z. Yu, N. Vlachopoulos, M. Gorlov and L. Kloo, *Dalton Trans.*, 2011, **40**, 10289-10303.
9. M. Grätzel, *J. Photochem. Photobiol. C*, 2003, 145-153.
10. M. K. Nazeeruddin, C. Klein, P. Liska and M. Grätzel, *Coord. Chem. Rev.*, 2005, **249**, 1460-1467.
11. M. K. Nazeeruddin, S. M. Zakeeruddin, J. J. Lagref, P. Liska, P. Comte, C. Barolo, G. Viscardi, K. Schenk and M. Graetzel, *Coord. Chem. Rev.*, 2004, **248**, 1317-1328.
12. M. A. Green, K. Emery, Y. Hishikawa and W. Warta, *Prog. Photovoltaics*, 2008, **16**, 435-440.
13. N. Alonso-Vante, J.-F. Nierengarten and J.-P. Sauvage, *J. Chem. Soc. Dalton Trans.*, 1994, 1649-1654.
14. S. Sakaki, T. Kuroki and T. Hamada, *J. Chem. Soc. Dalton Trans.*, 2002, 840-842.
15. T. Bessho, E. C. Constable, M. Graetzel, A. Hernandez Redondo, C. E. Housecroft, W. Kylberg, M. K. Nazeeruddin, M. Neuburger and S. Schaffner, *Chem. Commun.*, 2008, 3717-3719.
16. E. C. Constable, A. H. Redondo, C. E. Housecroft, M. Neuburger and S. Schaffner, *Dalton Trans.*, 2009, 6634-6644.
17. C. L. Linfoot, P. Richardson, T. E. Hewat, O. Moudam, M. M. Forde, A. Collins, F. White and N. Robertson, *Dalton Trans.*, 2010, **39**, 8945-8956.
18. B. Bozic-Weber, E. C. Constable, C. E. Housecroft, M. Neuburger and J. R. Price, *Dalton Trans.*, 2010, **39**, 3585-3594.
19. B. Bozic-Weber, E. C. Constable, C. E. Housecroft, P. Kopecky, M. Neuburger and J. A. Zampese, *Dalton Trans.*, 2011, **40**, 12584-12594.
20. W. L. Parker and G. A. Crosby, *J. Phys. Chem.*, 1989, **93**, 5692-5696.
21. T. Maruyama and T. Yamamoto, *Inorg. Chim. Acta*, 1995, **238**, 9-13.
22. L. Allouche, A. Marquis and J.-M. Lehn, *Chem. Eur. J.*, 2006, **12**, 7520-7525.
23. P. J. Burke, D. R. McMillin and W. R. Robinson, *Inorg. Chem.*, 1980, **19**, 1211-1214.
24. S. Itoh, N. Kishikawa, T. Suzuki and H. D. Takagi, *Dalton Trans.*, 2005, 1066-1078.
25. S. Kitagawa, M. Munakata and A. Higashie, *Inorg. Chim. Acta*, 1984, **84**, 79-84.
26. Z. A. Siddique, Y. Yamamoto, T. Ohno and K. Nozaki, *Inorg. Chem.*, 2003, **42**, 6366-6378.

27. V. Tamilavan, N. Cho, C. Kim, J. Ko and M. H. Hyun, *Tetrahedron*, 2012, **68**, 5890-5897.
28. J. Jia, K. Cao, P. Xue, Y. Zhang, H. Zhou and R. Lu, *Tetrahedron*, 2012, **68**, 3626-3632.
29. W. Fan, D. Tan and W.-Q. Deng, *ChemPhysChem*, 2012, **13**, 2051-2060.
30. P. Péchy, T. Renouard, S. M. Zakeeruddin, R. Humphry-Baker, P. Comte, P. Liska, L. Cevey, E. Costa, V. Shklover, L. Spiccia, G. B. Deacon, C. A. Bignozzi and M. Grätzel, *J. Am. Chem. Soc.*, 2001, **123**, 1613-1624.
31. M. Yamada, K. Araki and S. Shiraishi, *B. Chem. Soc. Jpn.*, 1988, **61**, 2208-2210.
32. U. B. Cappel, E. A. Gibson, A. Hagfeldt and G. Boschloo, *J. Phys. Chem. C*, 2009, **113**, 6275-6281.
33. A. L. Spek, *Acta Crystallogr. D*, 2009, **65**, 148-155.
34. B. Wenger, M. Grätzel and J.-E. Moser, *Chimia*, 2005, **59**, 123-125.
35. V. K. Thorsmølle, B. Wenger, J. Teuscher, C. Bauer and J.-E. Moser, *Chimia*, 2007, **61**, 631-634.
36. B. Wenger, M. Grätzel and J.-E. Moser, *J. Am. Chem. Soc.*, 2005, **127**, 12150-12151.
37. S. Ito, P. Chen, P. Comte, M. K. Nazeeruddin, P. Liska, P. Péchy and M. Grätzel, *Prog. Photovoltaics*, 2007, **15**, 603-612.

## Chapter 5

### A DFT and TD-DFT investigation of copper(I) polypyridyl complexes with application in DSSCs

#### 5.1 Introduction

Copper(I) complexes are a promising, cheap option to potentially use as sensitisers in dye sensitised solar cells (DSSCs)<sup>1, 2</sup>. Homoleptic complexes containing suitable anchoring ligands have shown reasonable efficiencies in DSSCs<sup>3-5</sup> but in order to incorporate both anchoring groups into the complex and allow the properties to be tuned, the use of heteroleptic complexes offers greater flexibility<sup>6, 7</sup>. Heteroleptic complexes can be made by attaching an anchoring ligand to nanoparticles of titanium dioxide (TiO<sub>2</sub>, anatase) and then placing the TiO<sub>2</sub> into a solution of a homoleptic copper(I) complex. This leads to the formation of a heteroleptic complex, attached to the surface of the TiO<sub>2</sub>. There is however a problem with this approach; due to the lability of Cu(I), a statistical mixture of heteroleptic and homoleptic complexes will be present in solution around the TiO<sub>2</sub>. It is not possible to isolate and characterise the heteroleptic complex. The only current means of characterising this heteroleptic complex is as the surface-bound species by means of solid state absorption spectroscopy and mass spectrometry<sup>6</sup>. Therefore, the properties of such a complex are currently not well understood.

DFT and TD-DFT have been used to investigate ruthenium-based sensitisers for DSSCs, examining both structural and electronic properties of the dye in question and probing the transitions making up its absorption spectrum.

The first notable study was carried out by Fantacci *et al.* in 2003 in a first principles investigation of the dye N3 (Fig. 5.1)<sup>8</sup>.

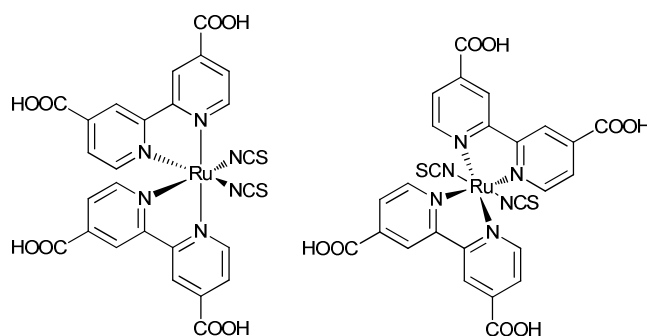


Fig. 5.1 The cis- and trans-structures of the N3 dye.

In order to validate the studies, the optimised geometries of the two stereoisomers of the complexes were compared to experimental crystallographic data. The agreement between the experimental and calculated data was good, verifying the choice of method and basis set. The highest occupied molecular orbital HOMO, (HOMO–1) and (HOMO–2) orbitals were found to be quasi-degenerate and predominantly localised on the thiocyanate (SCN<sup>-</sup>) ligands with minor contributions from the ruthenium *d*-orbitals. The (HOMO–4), (HOMO–5) and (HOMO–6) were localised on the metal atom whilst the LUMO to (LUMO+5) orbitals were based on the bipyridine ligands with substantial contributions from the carboxylic acid groups. This is favourable for injection of an electron into TiO<sub>2</sub> on excitation of the molecule. Using TD-DFT the predicted shape of the absorption bands and the separation of said bands was in reasonable agreement with experimental data, although the prediction of the specific positions of the bands was limited.

In 2006 Barolo *et al.* investigated a ruthenium complex with a tetradentate ligand, N886 (Fig 5.2)<sup>9</sup>. Although the complex was characterised experimentally with 4'-<sup>t</sup>butyl substituents, these were replaced by methyl substituents for computational convenience.

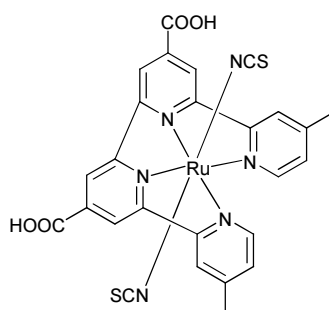


Fig. 5.2 The structure of the N886 dye, with <sup>t</sup>Bu substituents replaced with methyl groups

The calculations focussed on the effect of deprotonation of the carboxylic acid groups on the energy levels of the HOMO and LUMO of the complex and it was found that deprotonation of the –COOH groups led to greater destabilisation of the LUMO rather than the HOMO. The HOMO and nHOMOs (next HOMOs) possessed ruthenium *d*-orbital and thiocyanate character whereas the LUMO and nLUMOs (next LUMOs) were localised on the quaterpyridine (qpy) ligand, specifically the pyridine moieties with carboxylic acid substituents. Using TD-DFT to calculate the absorption spectrum of the di-protonated complex resulted in very good (within 15 nm) agreement with experimental

data, except in the case of the lowest-energy band. This band was predicted at 699 nm and observed experimentally at 637 nm. The transition is the result of electron promotion from a mixed ruthenium-thiocyanate orbital to an orbital based on the qpy ligand<sup>9</sup>. A higher energy band also involves promotion to an orbital based on the qpy ligand. The HOMO and LUMO of a  $\text{Ti}_{38}\text{O}_{72}$  cluster were also calculated and compared to the energy levels of the dye to explore how favourable the injection of an electron from the dye into the  $\text{TiO}_2$  was.

A similar study was carried out by Nazeeruddin *et al* in 2007 on the dye N945 (Fig. 5.3)<sup>10</sup>.

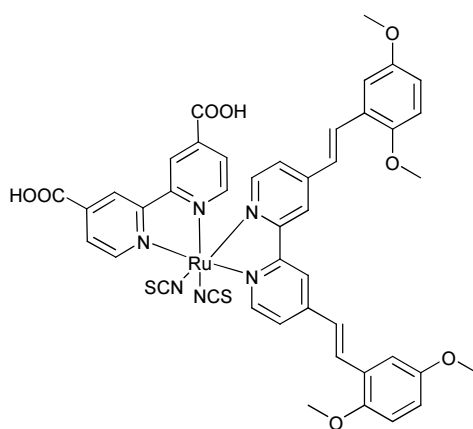


Fig. 5.3 The structure of the N945 dye.

It was found that the HOMO, (HOMO-1) and (HOMO-2) all had ruthenium *d*-orbital character, with significant contribution from the thiocyanate ligands. The LUMO and (LUMO+2) were localised on the carboxylic acid substituted bipyridine and the (LUMO+1) and (LUMO+3) were localised on the other bipyridine ligand. The energy levels of the orbitals were also calculated and compared to previous results for a model  $\text{TiO}_2$  nanoparticle. The results suggested that the LUMO and LUMO+1 were of a suitable energy match with the conductance band edge of  $\text{TiO}_2$  for favourable electron injection. This was corroborated experimentally as high photocurrents were measured.

DFT and TD-DFT studies have also been carried out on Cu(I) complexes. In 2010 Robertson and coworkers investigated the properties of four heteroleptic Cu(I) complexes (Fig. 5.4) of which one was then used in a DSSC<sup>7</sup>.

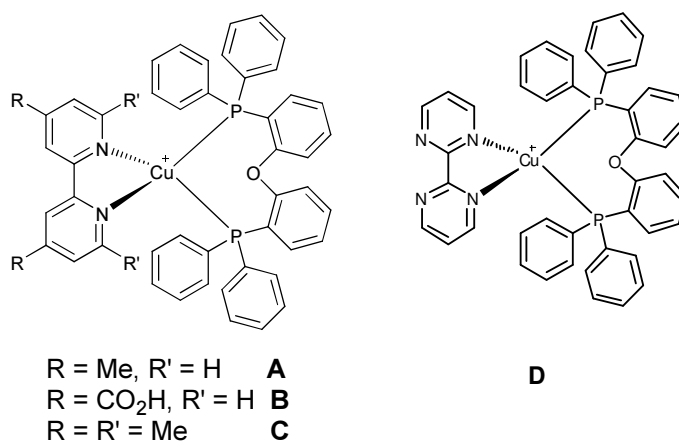


Fig. 5.4 Heteroleptic Cu(I) complexes investigated by Robertson *et al.*<sup>7</sup>

TD-DFT calculations carried out at the B3LYP/LANL2DZ level gave rise to two classes of transitions, MLCT and LLCT, in the low energy region of the spectrum. The spectrum of **A** contained one predicted MLCT transition at 416 nm. The spectrum of **B** contained an LLCT band at 509 nm and another at 420 nm. Calculations predicted one MLCT band at 402 nm for compound **C** and for **D** an MLCT band at 481 nm and a mixed MLCT, LLCT band at 383 nm. The MLCT and LLCT bands were consistently predicted at lower energy than those observed experimentally, although the red shift from **A** to **B** was well reproduced.

A similar problem was observed in TD-DFT calculations carried out by Lu *et al.*, which were reported in 2009 and 2011<sup>11,12</sup>. The DFT calculations were carried out at the B3LYP/6-31G\* and B3LYP/DZVP levels and the results were very similar. The anion was excluded from the calculations as, apart from minor geometry changes, it made little difference to the outputs of the calculations. It was found that geometry optimisation calculations at the B3LYP/DZVP level resulted in slightly longer bond lengths than when optimisations were calculated at the B3LYP/6-31G\* level. When carrying out the TD-DFT calculations (also at the B3LYP/6-31G\* level) the absorption spectra predicted contained MLCT bands at much lower energy than experimentally observed but trends were well reproduced.

The calculated dyes were based on copper(I) bis(6,6'-dimethyl-2,2'-bipyridine) with different substituents at the 4- and 4'-positions of the bipyridine units:

- Ethenyl groups to add conjugation
- Carboxylic acid or ester groups to look at protonation effects
- Heteroaromatic groups such as selenophene, furan and thiophene to adjust molecular orbital energies and compositions.

It was found the enhancing  $\pi$ -conjugation destabilises HOMOs and stabilises LUMOs and that the introduction of heteroaromatic groups stabilises HOMOs much more than LUMOs as the HOMO is based not only on the copper atom but also on the heteroaromatic-substituted ligand.

In order to minimise the synthesis of multiple dyes, which is both expensive and time-consuming, the aim of this chapter is to demonstrate that DFT and TD-DFT can be used to develop a method of screening multiple heteroleptic copper(I) complexes which could be used in DSSCs. In order to validate the method used theoretical data for the homoleptic complexes will be compared to experimental data. The heteroleptic complexes will then be calculated and the results rationalised in terms of efficiencies in DSSCs.

In this study, the following homoleptic complexes have been investigated (Fig. 5.5).

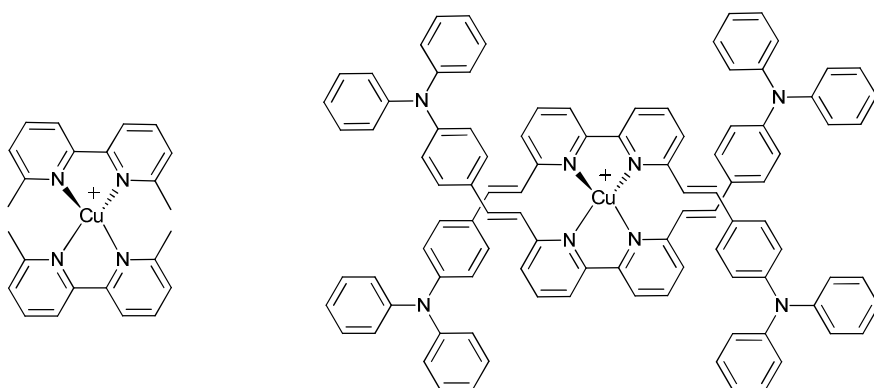


Fig. 5.5 The homoleptic complexes studied, (left)  $[\text{Cu}(\mathbf{8})_2]^+$ , (right)  $[\text{Cu}(\mathbf{9})_2]^+$ . The counter-anions were omitted from the calculations.

## 5.2 Calculation Details

The DFT calculations were carried out as follows: For  $[\text{CuL}_2]^+$  (L = **8** or **9**), the TD-DFT calculations were based upon known crystallographic data (this work). For  $[\text{CuLL}]^+$  (L =

**8** or **9**, L' = **10-12**) calculations were started from optimised structures of [Cu(**8**)<sub>2</sub>]<sup>+</sup> and [Cu(**9**)<sub>2</sub>]<sup>+</sup> and were computationally modified. Initial energy optimisation was carried out at the Hartree-Fock (HF) level with a 3-21G\* basis set, followed by HF/6-31G\*. Frequency calculations were carried out at this level to confirm that a minimum energy had been achieved. The structures were further relaxed with the hybrid 3-parameter Lee-Yang-Parr functional<sup>13, 14</sup> B3LYP/6-31G\*. To account for solvent effects, the conductor-like polarisable continuum model<sup>15, 16</sup> (CPCM) was used. The CPCM was used in geometry optimisation and for subsequent TD-DFT calculations.

As many of the calculations are computationally demanding, the influence of a considerably larger basis set (6-311++G\*\*) was assessed by alternatively using an extended basis set on either the metal atom or on all ligand atoms. For the smaller complexes the entire calculation was also carried out with the 6-311++G\*\* basis set throughout. Explorative calculations were also carried out with a LANL2DZ basis set on the Cu atom and 6-31G\* for the remaining system. Predicted electronic transitions were calculated at the B3LYP level and simulated spectra were generated from the Gaussian 09 output using the GaussSum program, version 2.2<sup>17</sup>.

The conversion factor from Hartree to eV is 1 Eh = 27.21128505 eV, taken from the NIST website 2010 values<sup>18</sup>. All calculations were carried out using the Gaussian 09 program package<sup>19</sup>.

### **5.3 Results and Discussion**

In order to validate the geometry optimisations, the calculated structures were compared to experimentally obtained crystallographic structures (this work) (Table 5.1).



Parameter	[Cu(8) <sub>2</sub> ] <sup>+</sup> (DFT)	[Cu(8) <sub>2</sub> ] <sup>+</sup> (expt)	[Cu(9) <sub>2</sub> ] <sup>+</sup> (DFT)	[Cu(9) <sub>2</sub> ] <sup>+</sup> (expt)
Cu1–N1 / Å	2.004	2.0248(9)	2.020	2.038(2)
Cu1–N2 / Å	2.004	2.0472(9)	2.020	2.038(2)
Cu1–N3 / Å	2.004	2.0447(9)	2.020	2.038(2)
Cu1–N4 / Å	2.004	2.0335(9)	2.020	2.038(2)
N1–Cu1–N2 / °	82.92	81.13(4)	83.06	80.48(6)
N1–Cu1–N3 / °	124.24	127.51(4)	131.56	125.64(6)
N2–Cu1–N3 / °	124.24	114.67(4)	131.56	125.64(6)
N1–Cu1–N4 / °	124.17	125.93(4)	131.56	125.64(6)
N2–Cu1–N4 / °	124.11	132.08(4)	131.56	125.64(6)
N3–Cu1–N4 / °	82.92	81.59(3)	83.06	80.48(6)

Table 5.1 Comparison of DFT and single crystal X-ray structural parameters for the coordination spheres in [Cu(8)<sub>2</sub>]<sup>+</sup> and [Cu(9)<sub>2</sub>]<sup>+</sup>. Atom numbering corresponds to Figs. 4.33 and 4.39, experimental data are from chapter 4.

Although the Cu1–N<sub>x</sub> (x = 1–4) bond lengths were slightly underestimated by the calculations, the geometries calculated using DFT were still realistic. The absorption spectra of the complexes were then calculated and the results compared with experimental data.

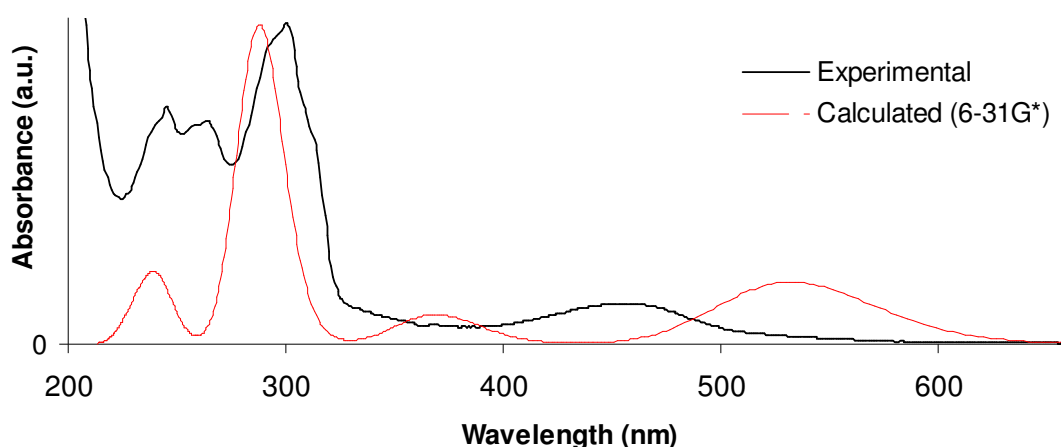


Fig. 5.6 Calculated (6-31G\* basis set) versus experimental electronic absorption spectra of [Cu(8)<sub>2</sub>]<sup>+</sup> in acetonitrile. The first fifty transitions were calculated. The figure was generated using the output of the GaussSum program<sup>17</sup>.

The agreement in the high energy region of the spectrum is good (Fig. 5.6). However, the TD calculations predict two MLCT bands in the visible region with  $\lambda_{\text{max}} = 378, 532 \text{ nm}$ , which are not observed experimentally. The band at 378 nm has two components, (HOMO-1)  $\rightarrow$  (LUMO+2) and HOMO  $\rightarrow$  (LUMO+3). The transition at 532 nm has two major components and these are depicted in Fig. 5.7.

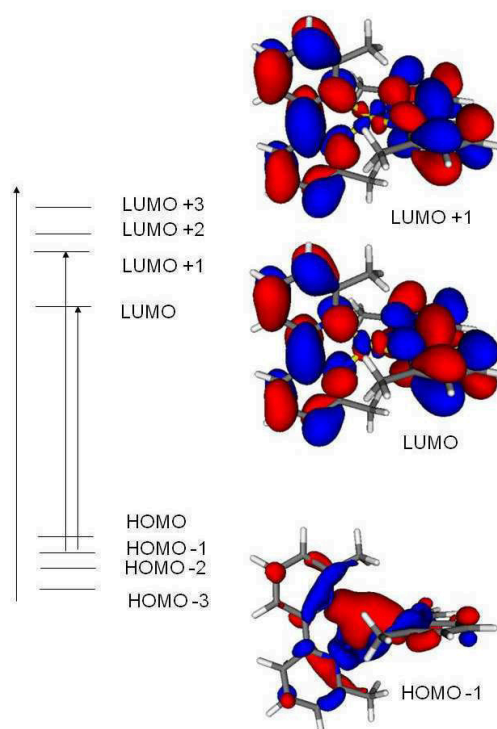


Fig. 5.7 The components of the MLCT band with  $\lambda_{\text{max}} = 532 \text{ nm}$  in  $[\text{Cu}(\mathbf{8})_2]^+$ .

The (HOMO-1) is predominantly metal based with some contribution from the pyridine rings. The LUMO and (LUMO+1) are predominantly ligand-based with some Cu *d*-orbital involvement. Whilst the band centered at 378 nm may be rationalised as corresponding to the tail of the experimentally observed band at 312 nm, the calculated band centered at 532 nm is 80 nm red-shifted with respect to the experimentally observed band with  $\lambda_{\text{max}} = 460 \text{ nm}$ . The over-estimation of the MLCT red-shift is also observed in reports by Lu *et al.*<sup>11, 12</sup>.

The absorption spectrum of  $[\text{Cu}(\mathbf{9})_2]^+$  was also calculated using TD-DFT (Fig. 5.8) and the agreement between the experimental and calculated spectra was better than that obtained for  $[\text{Cu}(\mathbf{8})_2]^+$ , the smallest basis set (6-31G\*) was used.

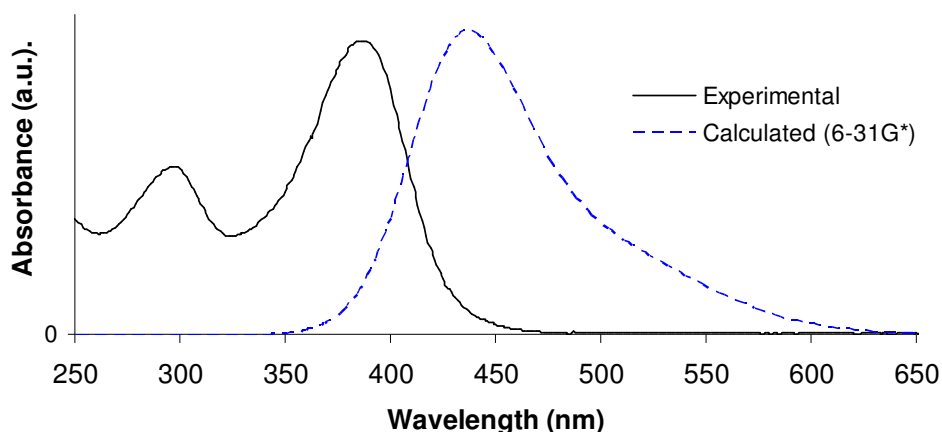


Fig. 5.8 Calculated (6-31G\* basis set) versus experimental electronic absorption spectra of  $[\text{Cu}(\mathbf{9})_2]^+$  in acetonitrile. The first fifty transitions were calculated. The figure was generated using the output of the GaussSum program<sup>17</sup>.

The lowest energy absorption in the experimental spectrum has  $\lambda_{\text{max}} = 390$  nm and the TD calculation predicts a spectrum with a band at  $\lambda_{\text{max}} = 435$  nm. The calculated and experimental spectra, therefore, are in tolerable agreement with one another, compared to some reports of ruthenium polypyridyl complexes where the predicted and calculated absorption spectra differ by up to 100 nm<sup>8, 10, 20, 21</sup>.

In order to obtain more accurately predicted UV-vis spectra a larger basis set was employed. Diffuse functionals were also added to the calculations as electron density is generally more spread out over molecules in the excited state. Starting from the geometry optimised structures using the 6-31G\* basis set the geometry was further optimised using the 6-311++G\*\* basis set in the presence of acetonitrile by means of the CPCM. The TD-DFT calculations were then also carried out using the 6-311++G\*\* basis set, also including the CPCM (Fig. 5.9).

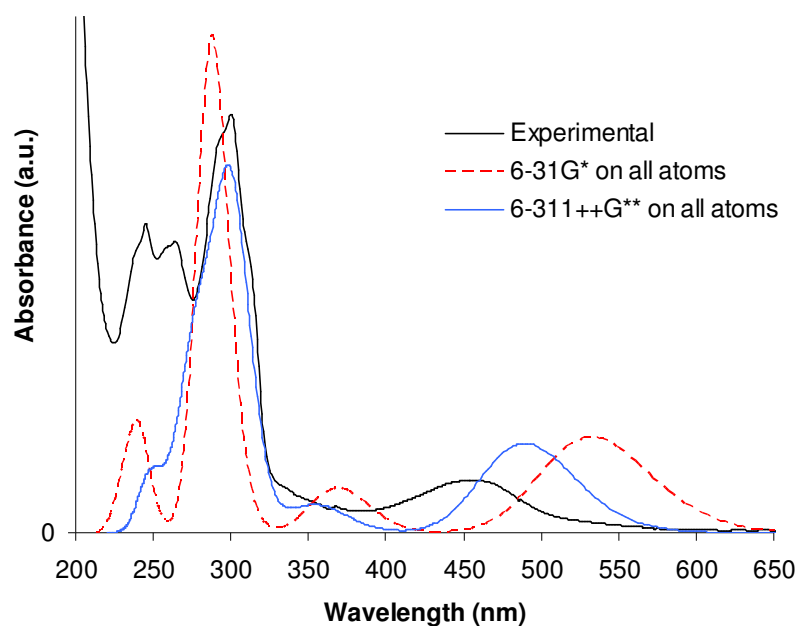


Fig. 5.9 Calculated versus experimental electronic absorption spectra of  $[\text{Cu}(\mathbf{8})_2]^+$  in acetonitrile. The first fifty transitions were calculated. The figure was generated using the output of the GaussSum program<sup>17</sup>.

As for the calculation with the 6-31G\* basis set, the agreement between the predicted and experimental spectra in the high energy region of the spectra is good. In the visible region the accuracy is much improved by using the 6-311G\*\* basis set; only one MLCT band is predicted and it is red-shifted by 29 nm ( $\lambda_{\text{max}} = 489 \text{ nm}$ ) with respect to the experimental peak ( $\lambda_{\text{max}} = 460 \text{ nm}$ ). However, using such a large basis set is computationally intensive and time-consuming. Whilst it is feasible for a small molecule such as  $[\text{Cu}(\mathbf{8})_2]^+$ , this is not the case for larger molecules. Therefore, a split basis set employing the 6-311++G\*\* basis set to describe the copper atom and the 6-31G\* basis set to describe the carbon, hydrogen and nitrogen atoms was used. Starting from the geometry optimised structures using the 6-31G\* basis set the geometry was further optimised using the split basis set (6-311++G\*\* on Cu and 6-31G\* on C, H, N) in the presence of acetonitrile by means of the CPCM. The TD-DFT calculations were also carried out using the split basis set and including the solvent model (Fig. 5.10).

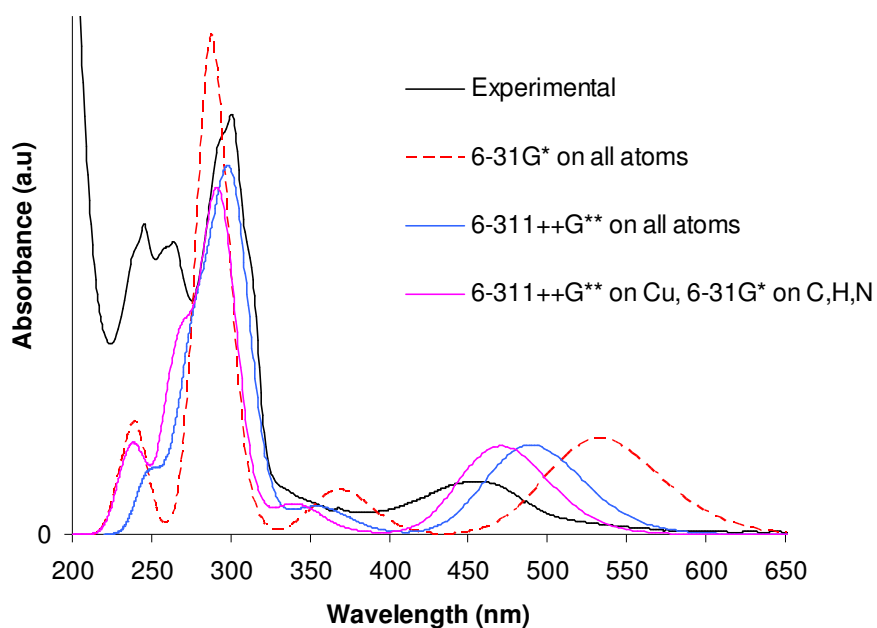


Fig. 5.10 Calculated versus experimental electronic absorption spectra of  $[\text{Cu}(\mathbf{8})_2]^+$  in acetonitrile. The first fifty transitions were calculated. The figure was generated using the output of the GaussSum program<sup>17</sup>.

The agreement between the calculated and experimental spectra improved again on employment of the split (6-311++G\*\*/6-31G\*) basis set. One MLCT transition centered at 470 nm is predicted, which is red-shifted by 10 nm compared to the experimental spectrum ( $\lambda_{\text{max}} = 460$  nm). The MLCT transition has four components which are depicted in Fig. 5.11, and involves the orbitals (HOMO-1), HOMO, LUMO and (LUMO+1).

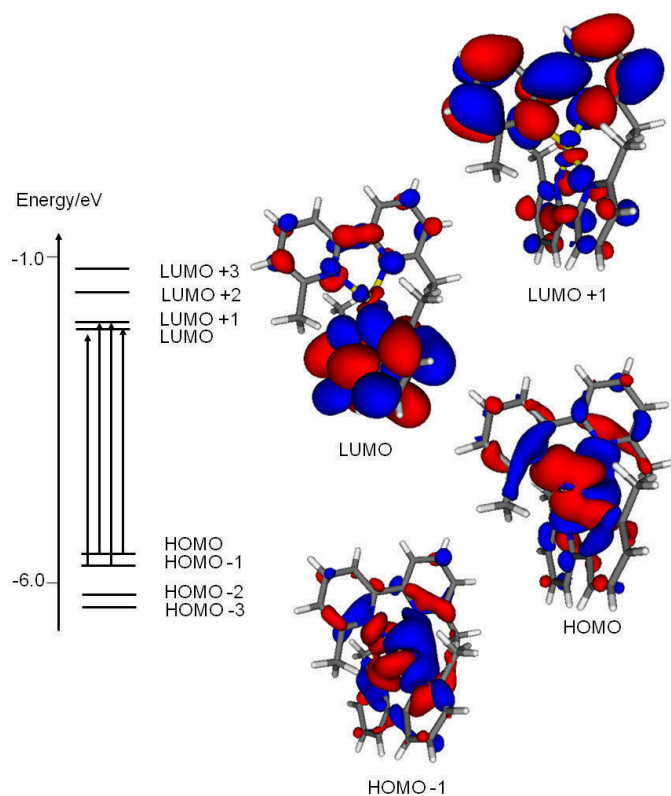


Fig. 5.11 The components of the calculated MLCT band at 470 nm for  $[\text{Cu}(\mathbf{8})_2]^+$  (basis set: 6-311++G\*\* on Cu and 6-31G\* on the ligand atoms). Isodensity surfaces for the MOs were generated from the Kohn-Sham orbitals using the MOLEKEL program<sup>22</sup>.

The character of the orbitals changes very little on altering the basis set. The HOMO and (HOMO–1) have predominantly Cu *d*-orbital character, with some contribution from the pyridine rings, particularly the nitrogen atoms. The LUMO and (LUMO+1) are essentially ligand based.

One further possibility for calculating the absorption spectra for these types of complexes is the use of the split basis set LANL2DZ<sup>23</sup>/6-31G\*. The spectrum of  $[\text{Cu}(\mathbf{8})_2]^+$  was calculated using this split basis set and the result was very similar to that obtained from using 6-311++G\*\*/6-31G\* (Fig. 5.12).

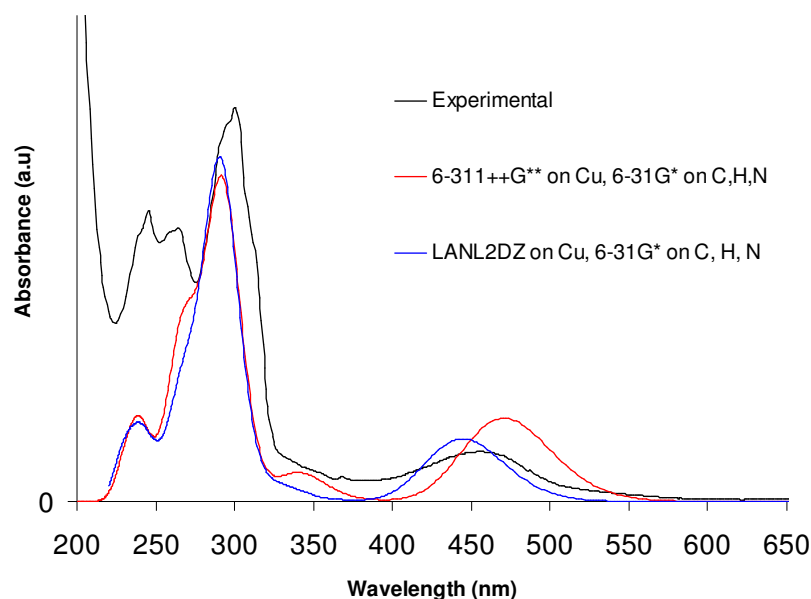


Figure 5.12. Predicted absorption spectra for  $[\text{Cu}(\mathbf{8})_2]^+$  showing that use of the LANL2DZ/6-31G\* basis set is as good as the use of the 6-311++G\*\*/6-31G\* basis set.

The LANL2DZ/6-31G\* calculation predicts an MLCT  $\lambda_{\text{max}}$  that is slightly blue-shifted, compared to experiment and the 6-311++G\*\*/6-31G\* calculation predicts an MLCT  $\lambda_{\text{max}}$  that is slightly red-shifted compared to experiment. Both calculations reproduce the high energy absorptions well.

It is concluded that the electronic absorption spectrum of  $[\text{Cu}(\mathbf{8})_2]^+$  can be realistically captured using either the LANL2DZ/6-31G\* or the 6-311++G\*\*/6-31G\* split basis set.

The absorption spectrum of  $[\text{Cu}(\mathbf{9})_2]^+$  was predicted using the split basis set (6-311++G\*\* on Cu, 6-31G\* on C, H and N) and the results are depicted in Fig. 5.13.

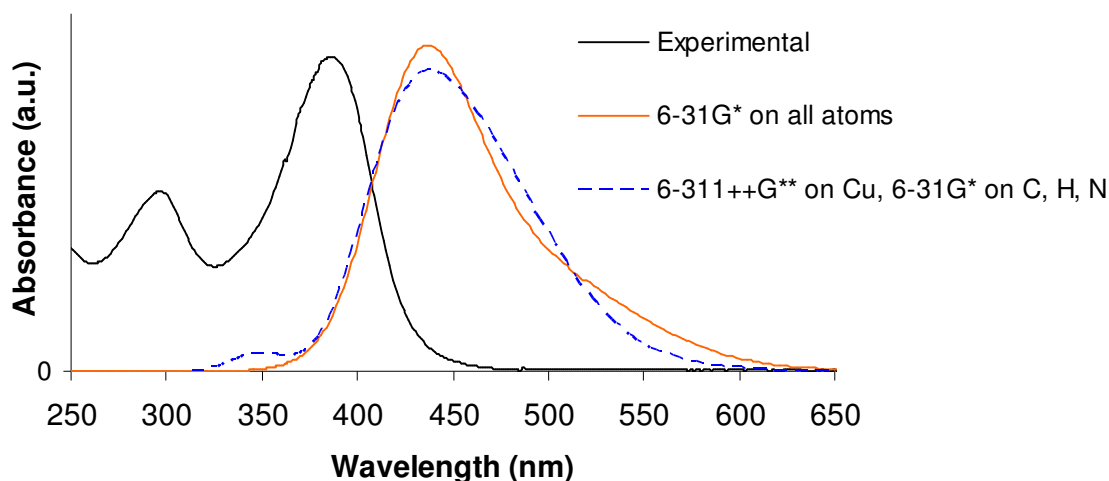


Fig. 5.13 Calculated versus experimental electronic absorption spectra of  $[\text{Cu}(\mathbf{9})_2]^+$  in acetonitrile. The first fifty transitions were calculated. The figure was generated using the output of the GaussSum program<sup>17</sup>.

The change in basis set has little effect on the predicted UV-vis spectrum. The transition centered at 438 nm comprises of both MLCT and ligand-based transitions, depicted in Fig. 5.14, and contributing orbitals are depicted in Fig. 5.15.

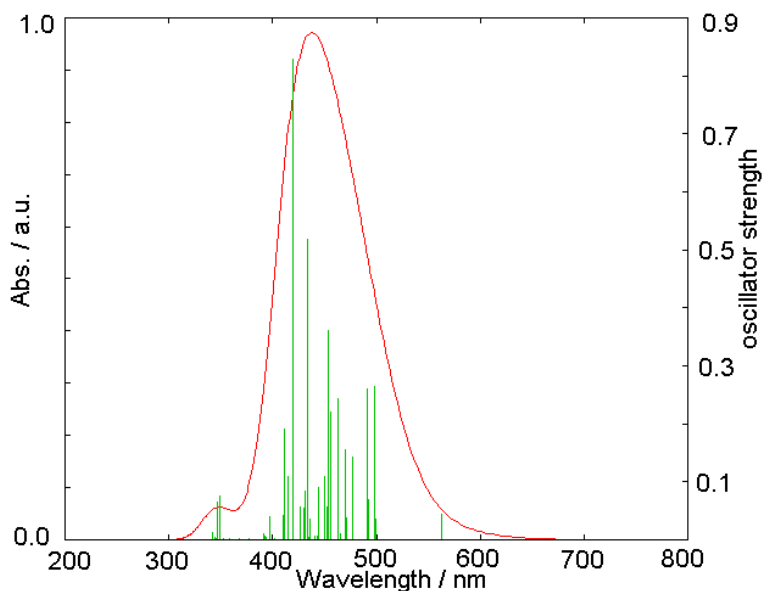


Fig. 5.14 Transitions making up the band at 438 nm in the calculated electronic absorption spectrum of  $[\text{Cu}(\mathbf{9})_2]^+$  using a 6-311++G\*\* basis set on Cu and 6-31G\* basis set on the ligand atoms.



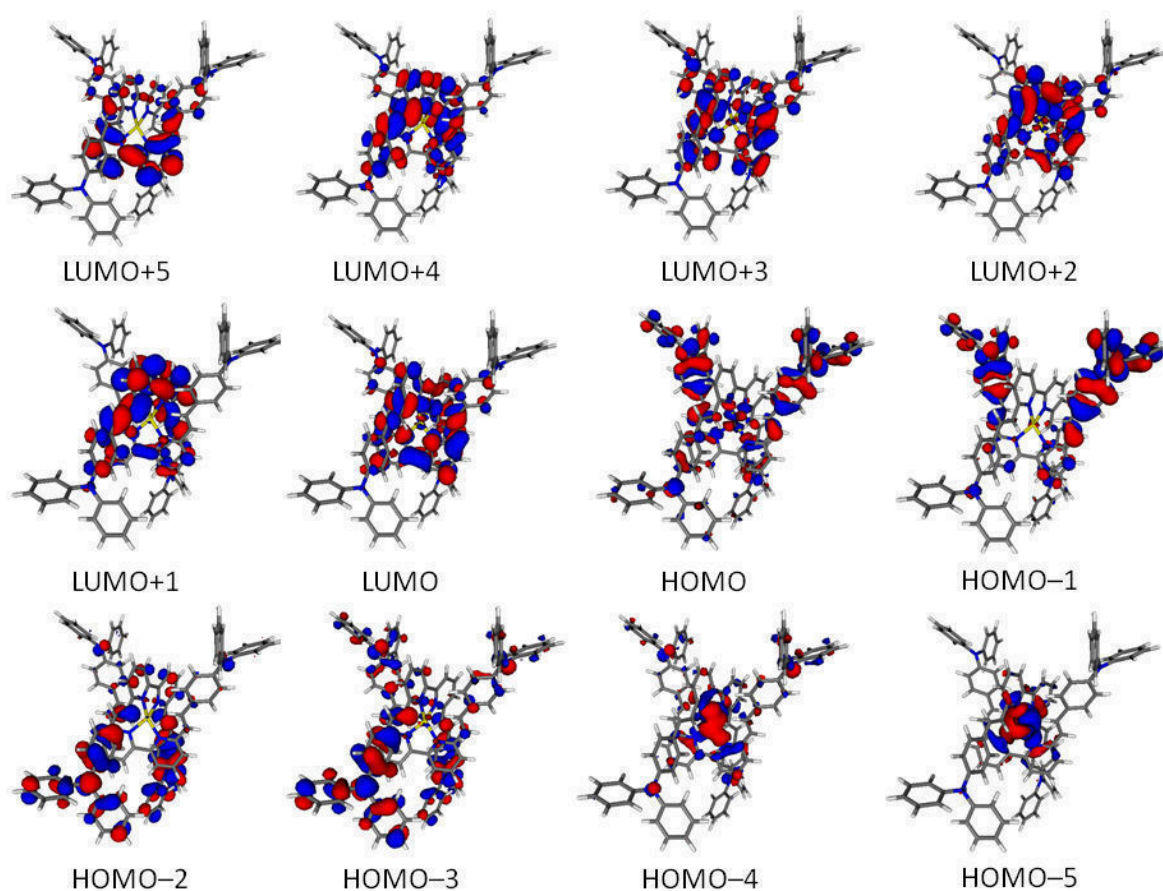


Fig. 5.15 Molecular orbitals (MOs) that contribute to the transitions that make up the calculated MLCT band at 438 nm for  $[\text{Cu}(\mathbf{9})_2]^+$  (basis set: 6-311++G\*\* on Cu and 6-31G\* on the ligand atoms). Isodensity surfaces for the MOs were generated from the Kohn-Sham orbitals using the MOLEKEL program<sup>22</sup>.

The majority of the molecular orbitals are predominantly ligand-based, accounting for the similarities in the photophysical and electrochemical properties of the ligand and the complex. Dominance of the triphenylamine moieties' contribution to the HOMO and (HOMO-1) supports the findings from the spectroelectrochemistry (§ 4.3.6).

As the level of agreement between the experimental and calculated data is satisfactory for both complexes  $[\text{Cu}(\text{L})_2]^+$  (L = **8**, **9**) TD-DFT calculations were carried out for heteroleptic complexes of the type  $[\text{Cu}(\text{L})(\text{L}')]^+$  where L = **8**, **9** and L' = **10-12** (see Fig 5.16 for structures of **10-12**), using the split 6-311++G\*\*/6-31G\* basis set.

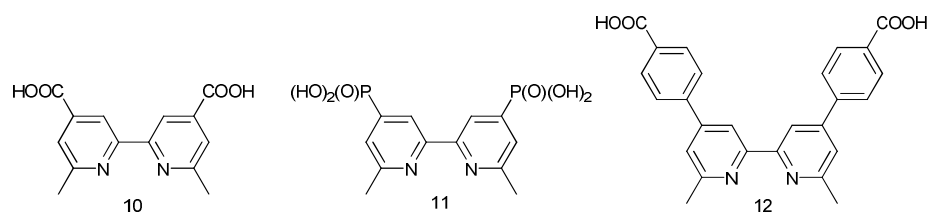


Fig 5.16 Structures of the anchoring ligands, **10-12**.

The UV-vis spectra of the complexes were calculated (Fig. 5.17)

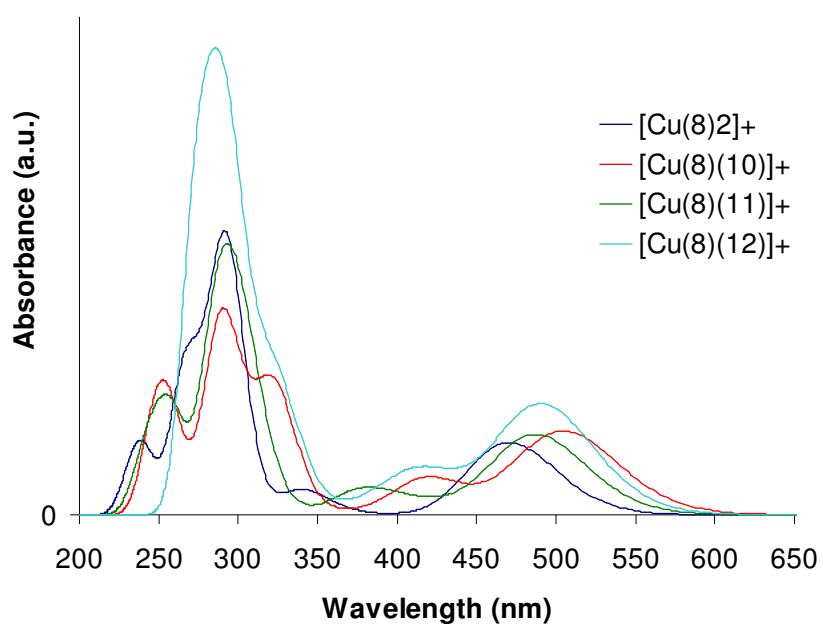


Fig. 5.17 Calculated (6-311++G\*\*/6-31G\*) electronic absorption spectra of  $[Cu(8)(L')]^+$  ( $L' = 8, 10-12$ ) in acetonitrile. The first fifty transitions were calculated. The figure was generated using the output of the GaussSum program<sup>17</sup>.

Complex	$\lambda_{\max}/\text{nm}$	Orbital Contributions
[Cu( <b>8</b> ) <sub>2</sub> ] <sup>+</sup>	470	45% LUMO←(HOMO-1)
		40% (LUMO+1)←HOMO
		7% (LUMO+1)←(HOMO-1)
		7% LUMO←HOMO
[Cu( <b>8</b> )( <b>10</b> )] <sup>+</sup>	504	86% LUMO←HOMO 12% (LUMO+1)←(HOMO-1)
	418	97% LUMO←HOMO
[Cu( <b>8</b> )( <b>11</b> )] <sup>+</sup>	486	81% LUMO←HOMO 15% (LUMO+1)←(HOMO-1)
	382	91% (LUMO+2)←HOMO 4% LUMO←(HOMO-3)
		[Cu( <b>8</b> )( <b>12</b> )] <sup>+</sup>
	414	77% (LUMO+2)←HOMO 19% (LUMO+2)←(HOMO-1)

Table 5.2 Orbital contributions to the electronic absorption transitions making up the MLCT band in the visible region for [Cu(**8**)<sub>2</sub>]<sup>+</sup> and [Cu(**8**)(L')]<sup>+</sup> (L' = **10-12**).

For all of the heteroleptic complexes [Cu(**8**)(L')]<sup>+</sup> the HOMOs have predominantly copper *d*-orbital character with some minor contribution from the pyridine rings (Figs. 5.18 and 5.19).

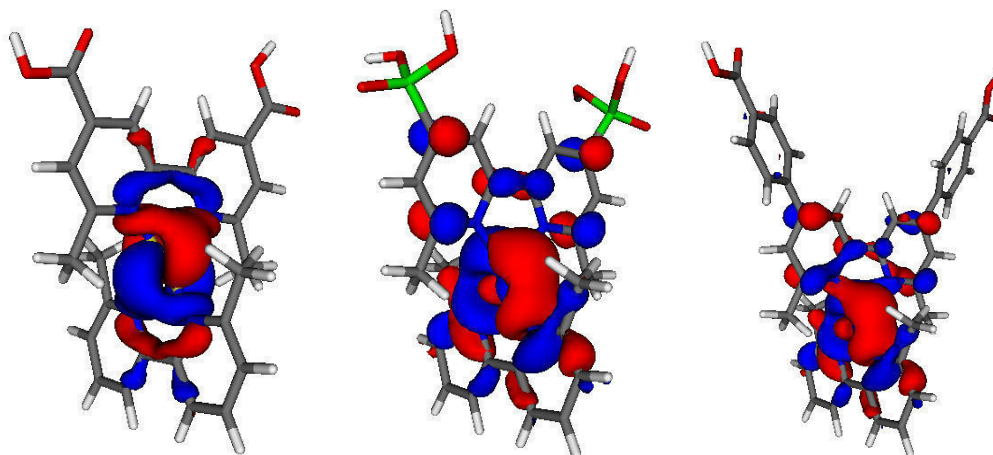


Fig. 5.18 Highest occupied MO involved in transitions contributing to the calculated absorption spectra of  $[\text{Cu}(\mathbf{8})(\mathbf{10})]^+$  (right),  $[\text{Cu}(\mathbf{8})(\mathbf{11})]^+$  (centre), and  $[\text{Cu}(\mathbf{8})(\mathbf{12})]^+$  (left).

The (HOMO–1) orbitals are also predominantly metal based, except in the case of  $[\text{Cu}(\mathbf{8})(\mathbf{10})]^+$  where there is significant contribution from ligand **8**. This is also the case for the (HOMO–3) orbital of  $[\text{Cu}(\mathbf{8})(\mathbf{11})]^+$ .

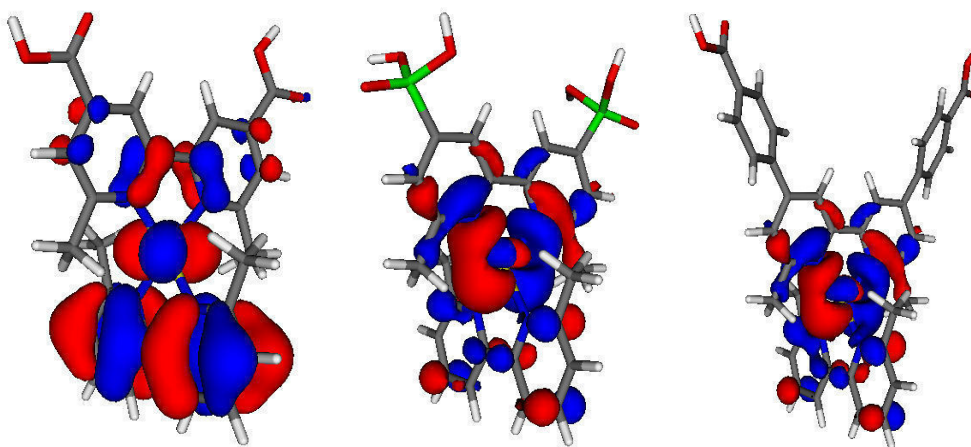


Fig. 5.19 Second highest occupied MO involved in transitions contributing to the calculated absorption spectra of  $[\text{Cu}(\mathbf{8})(\mathbf{10})]^+$  (right),  $[\text{Cu}(\mathbf{8})(\mathbf{11})]^+$  (centre), and  $[\text{Cu}(\mathbf{8})(\mathbf{12})]^+$  (left).

The LUMO and (LUMO+1) orbitals of the complex  $[\text{Cu}(\mathbf{8})(\mathbf{10})]^+$  are unexpectedly both metal- and ligand-based (Fig. 5.20). For favourable injection of an electron from the molecule in its excited state into the conduction band of  $\text{TiO}_2$ , the LUMO should lie on the anchoring ligand (ligand **10** for this complex). As this is not the case, a poorer

efficiency would be expected from a DSSC incorporating  $[\text{Cu}(\mathbf{8})(\mathbf{10})]^+$  as the sensitiser. This is validated by experiment (Table 5.3).

$[\text{CuL}_2]^+$	L'	$I_{\text{SC}} / \text{A cm}^{-2}$	$V_{\text{OC}} / \text{V}$	ff	$\eta / \%$
$[\text{Cu}(\mathbf{8})_2]^+$	<b>10</b>	0.004	0.530	0.58	1.17
$[\text{Cu}(\mathbf{8})_2]^+$	<b>11</b>	0.005	0.643	0.44	1.30
$[\text{Cu}(\mathbf{8})_2]^+$	<b>12</b>	0.006	0.595	0.46	1.69
N719	-	0.018	0.718	0.58	7.29

Table 5.3 DSSC efficiency data seven days after sealing. The  $[\text{Cu}(\mathbf{8})_2]^+$  complex is introduced for surface exchange as the  $[\text{PF}_6]^-$  salt.

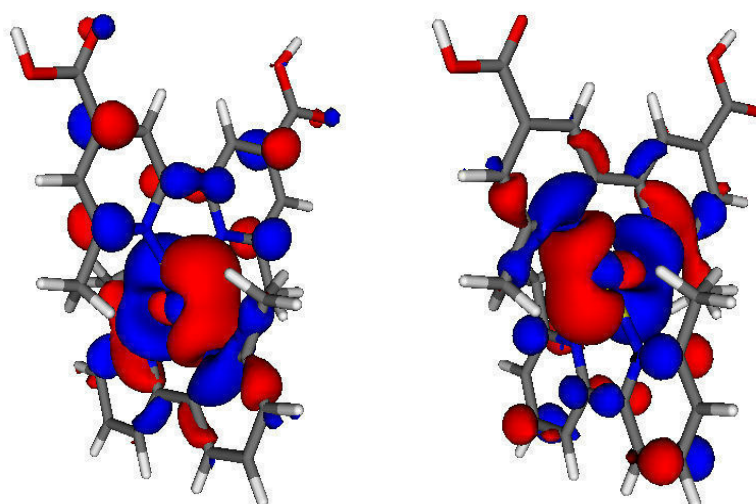


Fig 5.20 Lowest unoccupied MOs involved in transitions contributing to the calculated absorption spectrum of  $[\text{Cu}(\mathbf{8})(\mathbf{10})]^+$ , LUMO+1 (left), LUMO (right). The anchoring ligand **10** is at the top of each graphic.

In complex  $[\text{Cu}(\mathbf{8})(\mathbf{11})]^+$ , the LUMO and (LUMO+2) orbitals are localised on the anchoring ligand, **11** (Fig. 5.21). The (LUMO+1) is localised on ligand **8** but as contribution of the transition (HOMO-1) $\rightarrow$ (LUMO+1) is small this should not greatly affect the efficiency of a DSSC incorporating this dye.

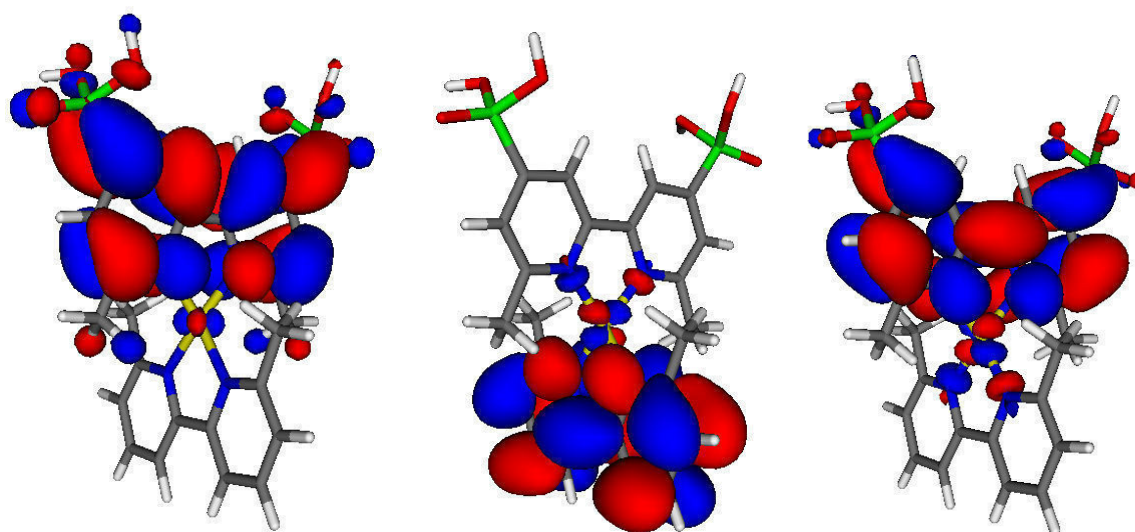


Fig 5.21 Lowest unoccupied MOs involved in transitions which contribute to the calculated absorption spectrum of  $[\text{Cu}(\mathbf{8})(\mathbf{11})]^+$ . The anchoring ligand **11** is at the top of each graphic. (LUMO+2) (left), (LUMO+1) (centre), and LUMO (right).

For complex  $[\text{Cu}(\mathbf{8})(\mathbf{12})]^+$  all of the unoccupied molecular orbitals involved in transitions contributing to the MLCT bands are localised on the anchoring ligand (Fig. 5.22). This indicates that the dye is a potential candidate for use as a sensitiser in DSSCs.

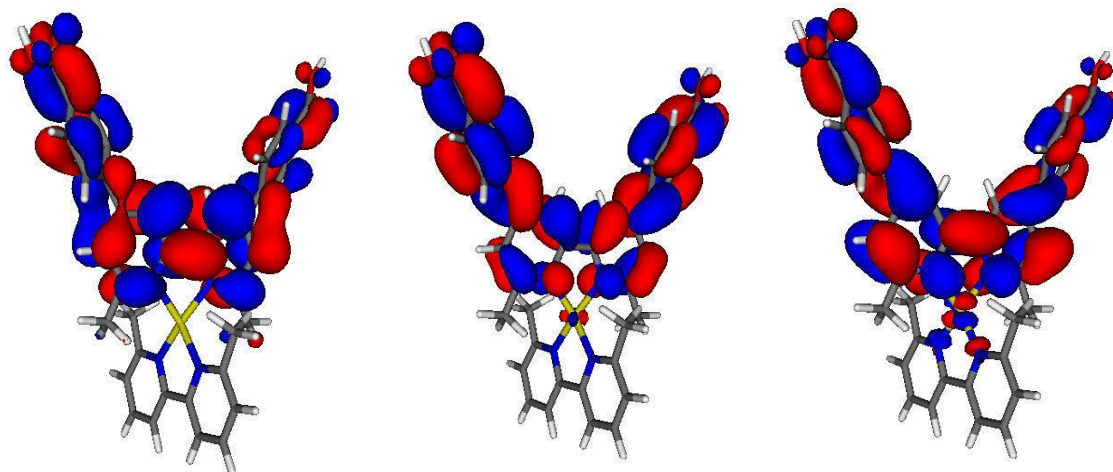


Fig 5.22 Lowest unoccupied MOs involved in transitions which contribute to the calculated absorption spectrum of  $[\text{Cu}(\mathbf{8})(\mathbf{12})]^+$ . The anchoring ligand **12** is at the top of each graphic. LUMO+2 (left), LUMO+1 (centre), and LUMO (right).

The efficiencies of the cells follow the same trend as the orbital contribution to the complexes. The higher the proportion of unoccupied molecular orbital localised on the

anchoring ligand, the greater the efficiency of the DSSC (Table 5.3). This gives a basis for screening complexes *in silico* before synthesis so that only dyes which have a large proportion of the unoccupied electron density on the anchoring ligands are made for use in DSSCs.

The UV-vis spectra of the heteroleptic complexes using **9** were also calculated (Fig. 5.23). The spectra are more complicated than those of complexes incorporating ligand **8** as the band in the visible region of the spectrum is made up of multiple transitions.

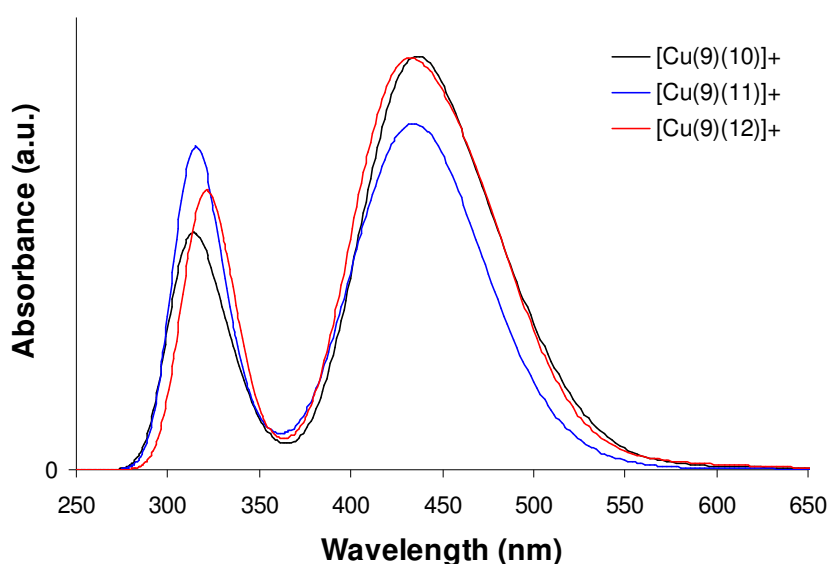


Fig. 5.23 Calculated (6-311++G\*\*/6-31G\*) electronic absorption spectra of  $[\text{Cu}(\mathbf{9})(L')]^+$  ( $L' = \mathbf{10-12}$ ) in acetonitrile. The first fifty transitions were calculated. The figure was generated using the output of the GaussSum program<sup>17</sup>.

All three spectra predict two absorption bands, the first in the UV region of the spectrum and the second in the visible region. For all complexes the band centred around 435 nm is the result of multiple MLCT and LLCT transitions. The orbitals involved in transitions for  $[\text{Cu}(\mathbf{9})(\mathbf{10})]^+$ ,  $[\text{Cu}(\mathbf{9})(\mathbf{11})]^+$  and  $[\text{Cu}(\mathbf{9})(\mathbf{12})]^+$  are depicted in Figs. 5.24, 5.25 and 5.26 respectively. (For transition tables see appendix)

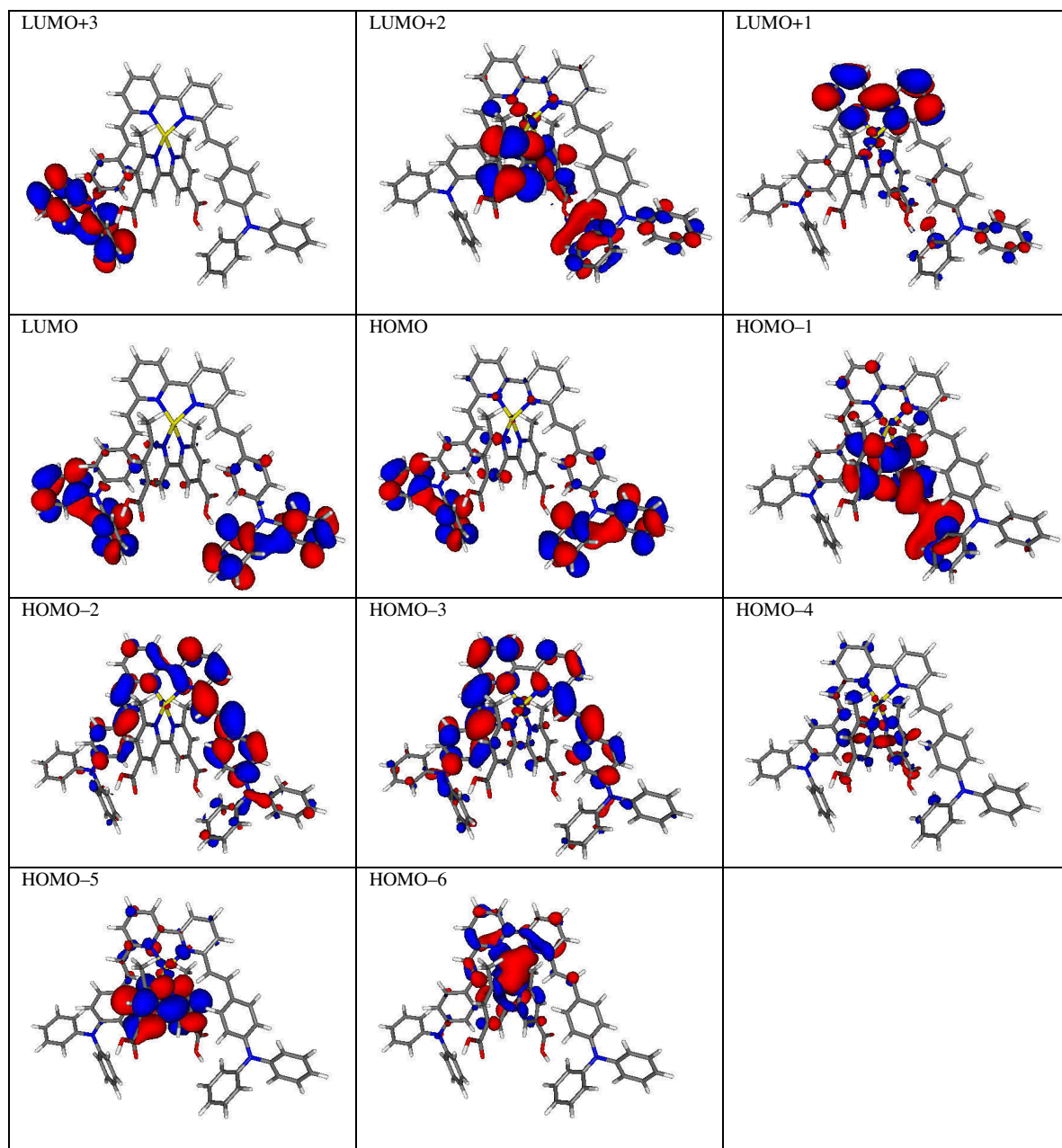


Fig 5.24 Highest occupied and lowest unoccupied MOs in  $[Cu(\mathbf{9})(\mathbf{10})]^+$ . The anchoring ligand  $\mathbf{10}$  is at the bottom of each graphic.

The (HOMO-6) orbital is the only occupied molecular orbital which participates in transitions and has predominantly metal character. The (HOMO-5), (HOMO-4) and (HOMO-1) orbitals are based on the anchoring ligand and the (HOMO-3) and (HOMO-2) orbitals are located on  $\mathbf{9}$ . Both the HOMO and the LUMO orbitals are centred on the triphenylamine unit of  $\mathbf{9}$ , as is the (LUMO+3). The (LUMO+1) resides mainly on the bipyridine moiety of  $\mathbf{9}$  and the only LUMO character residing on the anchoring ligand is that of (LUMO+2). This is not favourable for electron injection into



TiO<sub>2</sub> when the dye is used in DSSCs. Correspondingly; this complex shows a poor efficiency when used in a solar cell (Table 5.4).

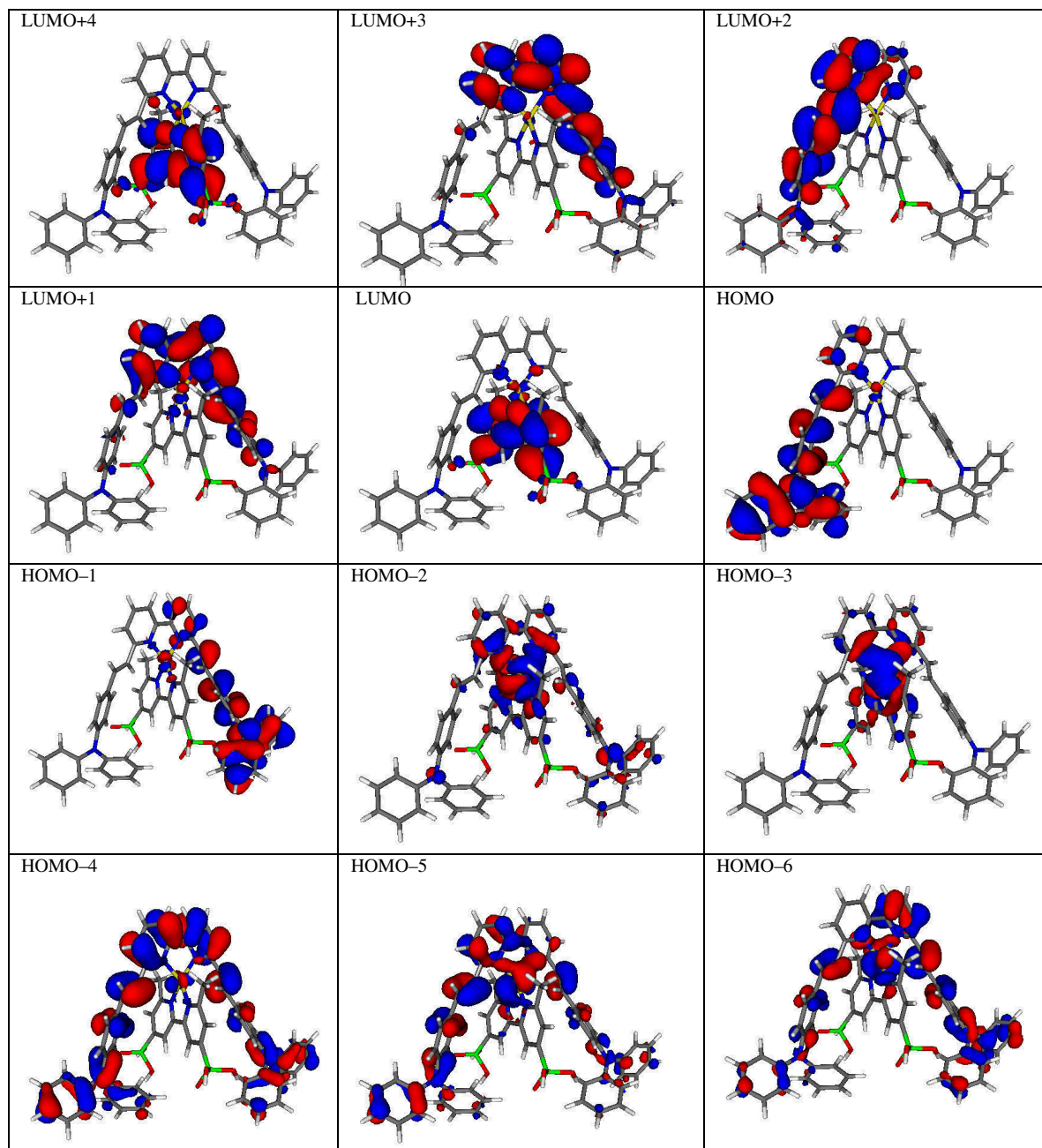


Fig 5.25 Highest occupied and lowest unoccupied MOs in  $[Cu(\mathbf{9})(\mathbf{11})]^+$ . The anchoring ligand  $\mathbf{11}$  is at the bottom of each graphic.

Both (HOMO-6) and (HOMO-5) have predominantly  $\mathbf{9}$  character with some contribution from the metal  $d$ -orbitals. The (HOMO-4) is predominantly based on  $\mathbf{9}$ , in contrast to the (HOMO-3) and (HOMO-2), which are predominantly metal based. Both (HOMO-1) and the HOMO are spread over half of ligand  $\mathbf{9}$ , in a similar manner to that

of (LUMO+2) and (LUMO+3). The LUMO and (LUMO+4) orbitals reside on the anchoring ligand, **11** and the (LUMO+1) orbital resides on the bipyridine unit of **9**. Use of this complex in a DSSC results in an efficiency of 2.35% (Table 5.4), which is the best efficiency of all the dyes described in this chapter.

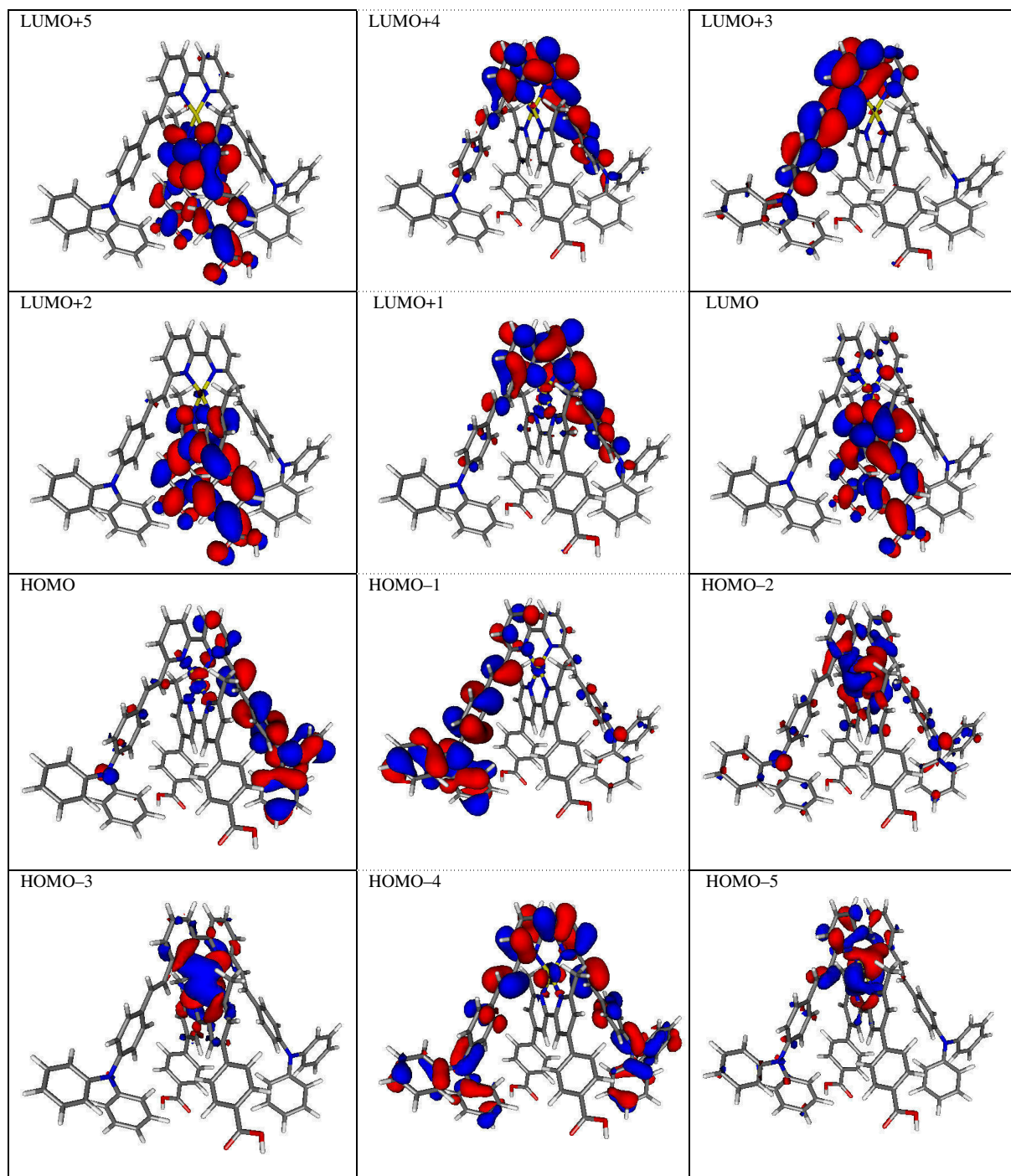


Fig 5.26 Highest occupied and lowest unoccupied MOs in  $[Cu(9)(12)]^+$ . The anchoring ligand **12** is at the bottom of each graphic.

The (HOMO-5), (HOMO-3) and (HOMO-2) orbitals have predominantly copper *d*-orbital character with minor contributions from the pyridine rings. The (HOMO-4), (HOMO-1) and HOMO are all ligand **9** based. The LUMO, (LUMO+2) and (LUMO+5) orbitals all reside on the anchoring ligand and, correspondingly, a good efficiency of 2.33% is observed when this complex is used in a DSSC. The (LUMO+1) and (LUMO+4) are based on the bipyridine unit of **9** and (LUMO+3) is delocalised over half of ligand **9**.

$[\text{CuL}_2]^+$	L'	$I_{\text{SC}} / \text{A cm}^{-2}$	$V_{\text{OC}} / \text{V}$	ff	$\eta / \%$
$[\text{Cu}(\mathbf{9})_2]^+$	<b>10</b>	0.002	0.522	0.66	0.64
$[\text{Cu}(\mathbf{9})_2]^+$	<b>11</b>	0.006	0.627	0.61	2.35
$[\text{Cu}(\mathbf{9})_2]^+$	<b>12</b>	0.007	0.579	0.60	2.33
N719	-	0.018	0.718	0.58	7.29

Table 5.4 DSC efficiency data 7 days after sealing, compared to standard dye N719 measured under the same conditions.  $[\text{Cu}(\mathbf{9})_2]^+$  is introduced for surface ligand exchange as the  $[\text{PF}_6]^-$  salt.

Complex	HOMO-LUMO gap / eV	Complex	HOMO-LUMO gap / eV
$[\text{Cu}(\mathbf{8})_2]^+$	3.42	$[\text{Cu}(\mathbf{9})_2]^+$	2.87
$[\text{Cu}(\mathbf{8})(\mathbf{10})]^+$	2.87	$[\text{Cu}(\mathbf{9})(\mathbf{10})]^+$	0.23
$[\text{Cu}(\mathbf{8})(\mathbf{11})]^+$	3.17	$[\text{Cu}(\mathbf{9})(\mathbf{11})]^+$	2.60
$[\text{Cu}(\mathbf{8})(\mathbf{12})]^+$	3.11	$[\text{Cu}(\mathbf{9})(\mathbf{12})]^+$	2.66

Table 5.5 Calculated HOMO-LUMO gaps for  $[\text{Cu}(\mathbf{8})(L')]^+$  ( $L' = \mathbf{8}, \mathbf{10}, \mathbf{11}, \mathbf{12}$ ) and  $[\text{Cu}(\mathbf{9})(L')]^+$  ( $L' = \mathbf{9}, \mathbf{10}, \mathbf{11}, \mathbf{12}$ ). The conversion factor from Hartrees to eV was  $1 \text{ Eh} = 27.21128505 \text{ eV}$ , taken from the NIST website 2010 values<sup>18</sup>.

The HOMO-LUMO gaps for the homoleptic and heteroleptic complexes are compared in Table 5.5. The energy gap is reduced on going from  $[\text{Cu}(\mathbf{8})_2]^+$  to  $[\text{Cu}(\mathbf{9})_2]^+$ , and the same trend is observed between pairs of compounds with a common anchoring ligand, e.g. HOMO-LUMO  $[\text{Cu}(\mathbf{8})(\mathbf{10})]^+ > [\text{Cu}(\mathbf{9})(\mathbf{10})]^+$ . The HOMO-LUMO gap for  $[\text{Cu}(\mathbf{8})(\mathbf{10})]^+$  is surprisingly small; however the character of these orbitals is very similar as both are

based on the triphenylamine units of **9**. The HOMO→LUMO transition does not contribute to the calculated band in the absorption spectrum and so the similarity of the orbital character appears to be an artefact of the calculation.

## 5.4 Conclusions

In summary, a number of basis sets have been screened to find a suitable basis set for predicting the absorption spectra of both homo- and heteroleptic Cu(I)-bipyridine complexes to an acceptable degree of accuracy. For the cation  $[\text{Cu}(\mathbf{8})_2]^+$  it was found that either the LANL2DZ/6-31G\* or the 6-311++G\*\*/6-31G\* basis set could be used. For the  $[\text{Cu}(\mathbf{8})(\text{L})]^+$  complexes an MLCT band involving transitions from orbitals localised on the copper atom to orbitals localised on bipyridine were predicted and the increasing localisation of the unoccupied molecular orbital on the anchoring ligand from L = **10** to L = **12** mirrors the increasing efficiencies of the dyes when used in DSSC devices.

For the  $[\text{Cu}(\mathbf{9})_2]^+$  complex, it was found that using the 6-311++G\*\* basis set resulted in an acceptable level of agreement with the experimental spectrum. For the  $[\text{Cu}(\mathbf{9})(\text{L})]^+$  complexes, a band in the visible region of the absorption spectrum is predicted, as a result of multiple transitions. The complex  $[\text{Cu}(\mathbf{9})(\mathbf{10})]^+$  shows little involvement of the anchoring ligand in these transitions and, correspondingly, a poor efficiency is observed when this complex is used in a DSSC. However, for complexes  $[\text{Cu}(\mathbf{9})(\mathbf{11})]^+$  and  $[\text{Cu}(\mathbf{9})(\mathbf{12})]^+$  the dominant unoccupied molecular orbitals were predicted over the anchoring ligand, which is necessary for efficient electron injection. The orbital character in the HOMOs of these dyes is dominated by the non-anchoring ligand, suggesting that ligand **9** enhances the performance of the sensitizer by minimizing back-migration of an electron from the semiconductor to the dye. The use of  $[\text{Cu}(\mathbf{9})(\mathbf{11})]^+$  and  $[\text{Cu}(\mathbf{9})(\mathbf{12})]^+$  in DSSCs results in the most efficient cells.

Further work includes the testing of this choice of basis set by calculation of the properties of more Cu(I) complexes and comparing them to experimental data. It may also be prudent to calculate the properties of heteroleptic complexes attached to TiO<sub>2</sub> nanoparticles to ascertain which properties change when the dye is *in situ*.

## 5.5 References

1. T. Bessho, E. C. Constable, M. Graetzel, A. Hernandez Redondo, C. E. Housecroft, W. Kylberg, M. K. Nazeeruddin, M. Neuburger and S. Schaffner, *Chem. Commun.*, 2008, 3717-3719.
2. A. Hernandez Rendondo, E. C. Constable and C. E. Housecroft, *Chimia*, 2009, **63**, 205-207.
3. B. Bozic-Weber, E. C. Constable, C. E. Housecroft, M. Neuburger and J. R. Price, *Dalton Trans.*, 2010, **39**, 3585-3594.
4. S. Sakaki, T. Kuroki and T. Hamada, *J. Chem. Soc. Dalton Trans.*, 2002, 840-842.
5. Y.-J. Yuan, Z.-T. Yu, J.-Y. Zhang and Z.-G. Zou, *Dalton Trans.*, 2012, **41**, 9594-9597.
6. B. Bozic-Weber, E. C. Constable, C. E. Housecroft, P. Kopecky, M. Neuburger and J. A. Zampese, *Dalton Trans.*, 2011, **40**, 12584-12594.
7. C. L. Linfoot, P. Richardson, T. E. Hewat, O. Moudam, M. M. Forde, A. Collins, F. White and N. Robertson, *Dalton Trans.*, 2010, **39**, 8945-8956.
8. S. Fantacci, F. De Angelis and A. Selloni, *J. Am. Chem. Soc.*, 2003, **125**, 4381-4387.
9. C. Barolo, M. K. Nazeeruddin, S. Fantacci, D. Di Censo, P. Comte, P. Liska, G. Viscardi, P. Quagliotto, F. De Angelis, S. Ito and M. Grätzel, *Inorg. Chem.*, 2006, **45**, 4642-4653.
10. M. K. Nazeeruddin, T. Bessho, L. Cevey, S. Ito, C. Klein, F. De Angelis, S. Fantacci, P. Comte, P. Liska, H. Imai and M. Graetzel, *J. Photochem. Photobiol. A*, 2007, **185**, 331-337.
11. X. Lu, C.-M. L. Wu, S. Wei and W. Guo, *J. Phys. Chem. A*, 2009, **114**, 1178-1184.
12. X. Lu, S. Wei, C.-M. L. Wu, S. Li and W. Guo, *J. Phys. Chem. C*, 2010, **115**, 3753-3761.
13. C. Lee, W. Yang and R. G. Parr, *Phys. Rev. B*, 1988, **37**, 785-789.
14. A. D. Becke, *J. Chem. Phys.*, 1993, **98**, 5648-5652.
15. S. Miertuš, E. Scrocco and J. Tomasi, *Chem. Phys.*, 1981, **55**, 117-129.
16. M. Cossi, V. Barone, R. Cammi and J. Tomasi, *Chem. Phys. Lett.*, 1996, **255**, 327-335.
17. N. M. O'Boyle, A. L. Tenderholt and K. M. Langner, *J. Comp. Chem.*, 2008, **29**, 839-845.
18. *NIST Website*, [http://physics.nist.gov/cgi-bin/cuu/Value?thre|search\\_for=hartree](http://physics.nist.gov/cgi-bin/cuu/Value?thre|search_for=hartree), Accessed July, 2011.
19. M. J. Frisch, G. W. Trucks, H. B. Schlegel, G. E. Scuseria, M. A. Robb, J. R. Cheeseman, G. Scalmani, V. Barone, B. Mennucci, G. A. Petersson, H. Nakatsuji, M. Caricato, X. Li, H. P. Hratchian, A. F. Izmaylov, J. Bloino, G. Zheng, J. L. Sonnenberg, M. Hada, M. Ehara, K. Toyota, R. Fukuda, J. Hasegawa, M. Ishida, T. Nakajima, Y. Honda, O. Kitao, H. Nakai, T. Vreven, J. J. A. Montgomery, J. E. Peralta, F. Ogliaro, M. Bearpark, J. J. Heyd, E. Brothers, K. N. Kudin, V. N. Staroverov, R. Kobayashi, J. Normand, K. Raghavachari, A. Rendell, J. C. Burant, S. S. Iyengar, J. Tomasi, M. Cossi, N. Rega, J. M. Millam, M. Klene, J. E. Knox, J. B. Cross, V. Bakken, C. Adamo, J. Jaramillo, R. Gomperts, R. E. Stratmann, O. Yazyev, A. J. Austin, R. Cammi, C. Pomelli, J. W. Ochterski, R. L. Martin, K. Morokuma, V. G. Zakrzewski, G. A. Voth, P. Salvador, J. J. Dannenberg, S.

- Dapprich, A. D. Daniels, Ö. Farkas, J. B. Foresman, J. V. Ortiz, J. Cioslowski and D. J. Fox, Gaussian Inc., Wallingford CT, 2009.
20. R. Siebert, C. Hunger, J. Guthmuller, F. Schlütter, A. Winter, U. S. Schubert, L. González, B. Dietzek and J. Popp, *J. Phys. Chem. C*, 2011, **115**, 12677-12688.
  21. M. K. Nazeeruddin, F. De Angelis, S. Fantacci, A. Selloni, G. Viscardi, P. Liska, S. Ito, B. Takeru and M. Grätzel, *J. Am. Chem. Soc.*, 2005, **127**, 16835-16847.
  22. U. Varetto, in *Swiss National Computing Centre*, Lugano, Switzerland, 2009.
  23. P. J. Hay and R. W. Willard, *J. Chem. Phys.*, 1985, **82**, 270-283.

## 5.6 Appendix

Orbital contributions to the electronic absorption transitions making up the band in the visible region of the absorption spectrum for  $[\text{Cu}(\mathbf{9})_2]^+$  and oscillator strengths.

Wavelength (nm)	$f$	Transition
562	0.043	62% LUMO←HOMO 28% LUMO←HOMO-4 2% LUMO+1←HOMO-4 2% LUMO+1←HOMO
499	0.035	16% LUMO←HOMO-5 21% LUMO←HOMO-3 20% LUMO+1←HOMO 17% LUMO+2←HOMO 5% LUMO+1←HOMO-4 7% LUMO+2←HOMO-4 2% LUMO+3←HOMO-4 5% LUMO+3←HOMO
498	0.2653	88% LUMO←HOMO-1 4% LUMO+3←HOMO
493	0.069	12% LUMO+1←HOMO-4 19% LUMO←HOMO-3 49% LUMO+1←HOMO 7% LUMO←HOMO-5 2% LUMO←HOMO-2 4% LUMO←HOMO
491	0.2597	89% LUMO←HOMO-2 2% LUMO←HOMO-1
477	0.1417	15% LUMO+3←HOMO-4 18% LUMO+2←HOMO 46% LUMO+3←HOMO 6% LUMO+2←HOMO-4 3% LUMO←HOMO-2 2% LUMO←HOMO-1 4% LUMO+4←HOMO
472	0.0385	14% LUMO←HOMO-5 45% LUMO←HOMO-3

		6% LUMO+2←HOMO-4 2% LUMO+4←HOMO-4 3% LUMO+1←HOMO 4% LUMO+2←HOMO 9% LUMO+4←HOMO
470	0.1556	13% LUMO+4←HOMO-4 60% LUMO+4←HOMO 3% LUMO←HOMO-5 7% LUMO←HOMO-3 2% LUMO+1←HOMO-2 5% LUMO+3←HOMO
463	0.2442	13% LUMO+2←HOMO-5 44% LUMO←HOMO-4 25% LUMO←HOMO 4% LUMO←HOMO-5 5% LUMO+3←HOMO-5 2% LUMO←HOMO-3
456	0.2201	14% LUMO+2←HOMO-5 12% LUMO←HOMO-4 24% LUMO+2←HOMO-3 4% LUMO←HOMO-5 6% LUMO+3←HOMO-5 8% LUMO+1←HOMO-3 9% LUMO+3←HOMO-3 2% LUMO+4←HOMO-2 3% LUMO+4←HOMO-1 4% LUMO←HOMO 3% LUMO+2←HOMO
454	0.36	47% LUMO+1←HOMO-2 13% LUMO+2←HOMO-1 8% LUMO+4←HOMO-3 4% LUMO+2←HOMO-2 3% LUMO+3←HOMO-2 8% LUMO+1←HOMO-1 5% LUMO+1←HOMO 3% LUMO+4←HOMO
453	0.0557	68% LUMO+1←HOMO-3 5% LUMO+1←HOMO-4 6% LUMO+2←HOMO-3 5% LUMO+1←HOMO-2 6% LUMO+2←HOMO-1 4% LUMO+5←HOMO
451	0.1084	10% LUMO+1←HOMO-2 41% LUMO+2←HOMO-1 16% LUMO+3←HOMO-1 5% LUMO+1←HOMO-3 7% LUMO+3←HOMO-3 7% LUMO+2←HOMO-2

		4% LUMO+3←HOMO-2 2% LUMO+1←HOMO-1
444	0.0905	18% LUMO+1←HOMO-2 51% LUMO+2←HOMO-2 13% LUMO+3←HOMO-2 5% LUMO+4←HOMO-3 2% LUMO+1←HOMO-1 3% LUMO+2←HOMO
436	0.0367	22% LUMO+2←HOMO-3 52% LUMO+3←HOMO-3 2% LUMO+3←HOMO-5 4% LUMO+1←HOMO-4 7% LUMO+4←HOMO-3 5% LUMO+3←HOMO-1
434	0.5181	39% LUMO+1←HOMO-4 10% LUMO+4←HOMO-1 15% LUMO+1←HOMO 7% LUMO←HOMO-5 4% LUMO←HOMO-4 3% LUMO+3←HOMO-2 5% LUMO+3←HOMO-1 4% LUMO+2←HOMO
432	0.0845	11% LUMO+2←HOMO-3 13% LUMO+4←HOMO-2 15% LUMO+2←HOMO-1 25% LUMO+3←HOMO-1 11% LUMO+4←HOMO-1 4% LUMO+1←HOMO-4 4% LUMO+2←HOMO 4% LUMO+3←HOMO
430	0.0555	63% LUMO+4←HOMO-3 4% LUMO+2←HOMO-3 2% LUMO+3←HOMO-3 2% LUMO+1←HOMO-2 8% LUMO+2←HOMO-2 4% LUMO+4←HOMO-2
427	0.0568	12% LUMO+2←HOMO-3 10% LUMO+3←HOMO-3 48% LUMO+4←HOMO-2 2% LUMO←HOMO-5 2% LUMO+2←HOMO-5 6% LUMO+4←HOMO-3 5% LUMO+3←HOMO-2 3% LUMO+4←HOMO-1
420	0.8285	23% LUMO+2←HOMO-5 14% LUMO+2←HOMO-3 12% LUMO+4←HOMO-2 8% LUMO+3←HOMO-5



		5% LUMO←HOMO-4 9% LUMO+1←HOMO-4 6% LUMO+3←HOMO-3 5% LUMO+3←HOMO-2 4% LUMO+4←HOMO-1
415	0.1099	24% LUMO+2←HOMO-4 44% LUMO+3←HOMO-4 13% LUMO+3←HOMO 5% LUMO+5←HOMO-1 6% LUMO+2←HOMO
411	0.1905	16% LUMO+4←HOMO-4 63% LUMO+5←HOMO-3 5% LUMO+1←HOMO-5 3% LUMO+5←HOMO-2 5% LUMO+5←HOMO
410	0.0429	25% LUMO+5←HOMO-2 50% LUMO+5←HOMO-1 7% LUMO+4←HOMO-4 7% LUMO+5←HOMO-3 3% LUMO+4←HOMO
397	0.0402	19% LUMO←HOMO-5 31% LUMO+2←HOMO-4 15% LUMO+3←HOMO-4 4% LUMO←HOMO-8 3% LUMO←HOMO-6 6% LUMO+2←HOMO-5 4% LUMO+3←HOMO-5 2% LUMO+1←HOMO-4 5% LUMO+5←HOMO-4

Orbital contributions to the electronic absorption transitions making up the band in the visible region of the absorption spectrum for [Cu(9)(10)]<sup>+</sup> and oscillator strengths.

Wavelength (nm)	<i>f</i>	Transition
484	0.0323	33% LUMO+1←HOMO-1 60% LUMO+1←HOMO 4% LUMO+2←HOMO-1
481	0.4163	71% LUMO+2←HOMO 3% LUMO←HOMO-3 3% LUMO←HOMO-2 8% LUMO+2←HOMO-1 6% LUMO+3←HOMO-1 2% LUMO+4←HOMO-1
456	0.113	20% LUMO+2←HOMO-3

		22% LUMO+2←HOMO-2 29% LUMO+2←HOMO-1 4% LUMO+1←HOMO-3 6% LUMO+1←HOMO-2 6% LUMO+1←HOMO-1 3% LUMO+3←HOMO-1 5% LUMO+2←HOMO
444	0.4481	10% LUMO+3←HOMO-2 62% LUMO+3←HOMO-1 2% LUMO+2←HOMO-1 6% LUMO+2←HOMO 6% LUMO+3←HOMO 5% LUMO+4←HOMO
440	0.044	13% LUMO←HOMO-6 37% LUMO+1←HOMO-2 12% LUMO+2←HOMO-2 13% LUMO+3←HOMO 2% LUMO+4←HOMO-2 2% LUMO+1←HOMO-1 6% LUMO+4←HOMO-1 6% LUMO+4←HOMO
439	0.0799	22% LUMO+1←HOMO-2 44% LUMO+3←HOMO 3% LUMO+3←HOMO-2 4% LUMO+4←HOMO-2 9% LUMO+4←HOMO-1 8% LUMO+4←HOMO
433	0.1185	36% LUMO←HOMO-6 15% LUMO+1←HOMO-2 15% LUMO+3←HOMO 10% LUMO+4←HOMO 7% LUMO←HOMO-4 2% LUMO+4←HOMO-2 5% LUMO+3←HOMO-1 5% LUMO+4←HOMO-1
431	0.2702	29% LUMO←HOMO-6 10% LUMO+3←HOMO-1 17% LUMO+4←HOMO-1 12% LUMO+3←HOMO 10% LUMO+4←HOMO 4% LUMO←HOMO-4 3% LUMO+2←HOMO-2 7% LUMO+4←HOMO-2
421	0.1904	40% LUMO+4←HOMO-1 39% LUMO+4←HOMO 2% LUMO+3←HOMO-2 8% LUMO+5←HOMO
417	0.1785	49% LUMO+5←HOMO-1

		26% LUMO+5←HOMO 3% LUMO+2←HOMO-3 8% LUMO+5←HOMO-2 2% LUMO+4←HOMO-1 8% LUMO+4←HOMO
409	0.0513	17% LUMO+1←HOMO-3 41% LUMO+3←HOMO-2 7% LUMO+2←HOMO-3 8% LUMO+2←HOMO-2 3% LUMO+2←HOMO-1 4% LUMO+5←HOMO-1 6% LUMO+3←HOMO 6% LUMO+4←HOMO
406	0.0991	43% LUMO+1←HOMO-3 28% LUMO+3←HOMO-2 9% LUMO+2←HOMO-2 5% LUMO+4←HOMO-2 3% LUMO+3←HOMO-1 3% LUMO+4←HOMO-1 2% LUMO+3←HOMO
403	0.041	24% LUMO+1←HOMO-3 21% LUMO+2←HOMO-3 18% LUMO+4←HOMO-2 7% LUMO←HOMO-7 5% LUMO←HOMO-4 4% LUMO+1←HOMO-2 4% LUMO+2←HOMO-2 6% LUMO+4←HOMO-1

Orbital contributions to the electronic absorption transitions making up the band in the visible region of the absorption spectrum for [Cu(9)(11)]<sup>+</sup> and oscillator strengths.

Wavelength (nm)	<i>f</i>	Transition
478	0.1443	21% LUMO+1←HOMO-3 10% LUMO←HOMO-2 14% LUMO+1←HOMO-2 30% LUMO+1←HOMO-1 9% LUMO←HOMO-3 3% LUMO+1←HOMO 7% LUMO+2←HOMO
464	0.2154	15% LUMO+1←HOMO-3 13% LUMO+1←HOMO-2 47% LUMO+1←HOMO-1 4% LUMO+2←HOMO
451	0.068	15% LUMO+1←HOMO-3

		10% LUMO+1←HOMO-1 39% LUMO+1←HOMO 10% LUMO+2←HOMO 3% LUMO←HOMO-3 6% LUMO+1←HOMO-2 4% LUMO+2←HOMO-2 7% LUMO+2←HOMO-1
442	0.4719	20% LUMO+1←HOMO-1 17% LUMO+2←HOMO-1 38% LUMO+2←HOMO 4% LUMO←HOMO-3 2% LUMO←HOMO-2 3% LUMO+1←HOMO-2 8% LUMO+2←HOMO-2
434	0.1323	51% LUMO+2←HOMO-1 27% LUMO+2←HOMO 9% LUMO+2←HOMO-2 4% LUMO+3←HOMO-1 2% LUMO+1←HOMO
428	0.1036	11% LUMO+1←HOMO-2 12% LUMO+3←HOMO-2 42% LUMO+3←HOMO-1 5% LUMO←HOMO-6 8% LUMO←HOMO-5 2% LUMO←HOMO-4 2% LUMO+1←HOMO-1 5% LUMO+2←HOMO 6% LUMO+3←HOMO
424	0.1707	24% LUMO←HOMO-6 34% LUMO←HOMO-5 10% LUMO←HOMO-4 10% LUMO+3←HOMO-1 5% LUMO+3←HOMO-2 3% LUMO+2←HOMO 5% LUMO+3←HOMO
411	0.0363	14% LUMO+4←HOMO-2 44% LUMO+4←HOMO-1 30% LUMO+4←HOMO
410	0.2965	18% LUMO+1←HOMO-3 15% LUMO+1←HOMO-2 21% LUMO+3←HOMO-1 23% LUMO+3←HOMO 7% LUMO+2←HOMO-2 3% LUMO+2←HOMO-1
405	0.0549	23% LUMO+2←HOMO-3 32% LUMO+2←HOMO-2 12% LUMO+4←HOMO 4% LUMO+1←HOMO-3

		4% LUMO+1←HOMO-2 2% LUMO+5←HOMO-2 7% LUMO+2←HOMO-1 6% LUMO+5←HOMO-1 3% LUMO+5←HOMO
396	0.0353	51% LUMO+2←HOMO-3 14% LUMO+2←HOMO-2 11% LUMO+3←HOMO-2 4% LUMO←HOMO-7 7% LUMO+3←HOMO-3 2% LUMO+2←HOMO-1 5% LUMO+2←HOMO-1 2% LUMO+3←HOMO

Orbital contributions to the electronic absorption transitions making up the band in the visible region of the absorption spectrum for [Cu(9)(12)]<sup>+</sup> and oscillator strengths.

Wavelength (nm)	<i>f</i>	Transition
473	0.3897	11% LUMO←HOMO-3 15% LUMO+1←HOMO-3 21% LUMO+1←HOMO-1 13% LUMO+3←HOMO-1 13% LUMO+1←HOMO 6% LUMO←HOMO-2 3% LUMO+1←HOMO-2 3% LUMO+3←HOMO-2 9% LUMO+3←HOMO
468	0.2013	39% LUMO+1←HOMO-3 16% LUMO+1←HOMO-2 16% LUMO+1←HOMO-1 14% LUMO+1←HOMO 3% LUMO←HOMO-2 3% LUMO+2←HOMO 2% LUMO+4←HOMO
450	0.1386	16% LUMO+4←HOMO-2 15% LUMO+1←HOMO-1 13% LUMO+1←HOMO 16% LUMO+3←HOMO 18% LUMO+4←HOMO 6% LUMO←HOMO-3 2% LUMO←HOMO-2 7% LUMO+3←HOMO-2 3% LUMO+4←HOMO-1
444	0.1268	11% LUMO+4←HOMO-2 22% LUMO+1←HOMO

		31% LUMO+4←HOMO 6% LUMO←HOMO-3 3% LUMO←HOMO-2 9% LUMO+1←HOMO-2 6% LUMO+1←HOMO-1 3% LUMO+4←HOMO-1
433	0.4728	73% LUMO+3←HOMO-1 10% LUMO+3←HOMO 2% LUMO←HOMO-3 3% LUMO+4←HOMO-2
422	0.0391	72% LUMO+2←HOMO-2 4% LUMO+3←HOMO-2 4% LUMO+2←HOMO 5% LUMO+3←HOMO 4% LUMO+5←HOMO
416	0.0912	34% LUMO+3←HOMO-2 13% LUMO+3←HOMO 23% LUMO+5←HOMO 2% LUMO+1←HOMO-3 8% LUMO+3←HOMO-3 3% LUMO+1←HOMO-2 4% LUMO+5←HOMO-2 4% LUMO+4←HOMO-1
415	0.5465	55% LUMO+4←HOMO-1 22% LUMO+4←HOMO 8% LUMO+1←HOMO-3 7% LUMO+1←HOMO-2
404	0.0641	29% LUMO+4←HOMO-2 13% LUMO+5←HOMO-1 10% LUMO+4←HOMO 12% LUMO+5←HOMO 7% LUMO←HOMO-5 3% LUMO←HOMO-4 2% LUMO+1←HOMO-3 8% LUMO+3←HOMO-3 5% LUMO+4←HOMO-3 2% LUMO+4←HOMO-1
391	0.0327	88% LUMO+2←HOMO-3 5% LUMO+3←HOMO-3 3% LUMO+7←HOMO-3

## Chapter 6

### Copper(I) complexes with pendant pyridyl functionalities for application in DSSCs

#### 6.1 Introduction

The necessary properties of copper(I) complexes for use in dye-sensitised solar cells have been described in chapter 4. One important requirement of the complex is that it absorbs over a large portion of the visible spectrum. Complexation of one or more quaterpyridine ligands, 4,4':2',2'':4'',4'''-quaterpyridine (Fig. 6.1) to ruthenium has been reported to red-shift the absorption spectrum of the complex compared to that of  $[\text{Ru}(\text{bpy})_3]^{2+}$ <sup>1-3</sup>.

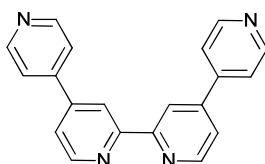


Fig. 6.1 4,4':2',2'':4'',4'''-Quaterpyridine.

As it is, this ligand is unsuitable for complexation to copper(I) atoms. To eliminate the possibility of auto-oxidation of the copper(I) atom it is necessary to incorporate blocking groups, typically methyl substituents, at the sites adjacent to the N,N' metal binding sites of the bipyridine unit. Synthesis of this 6,6'-dimethyl-4,4':2',2'':4'',4'''-quaterpyridine ligand has previously been attempted by members of the Constable group and has been unsuccessful. Consequently, another ligand with four pyridine groups and substitutions in the 6,6'-positions of the 2,2'-bipyridine unit was developed.

Coe *et al.* reported the use of a ligand with four pyridine groups and substitution in the 4- and 4'-positions of the 2,2'-bipyridine unit (Fig. 6.2)<sup>4</sup>. However, this ligand was still unsubstituted in the 6- and 6'-positions.

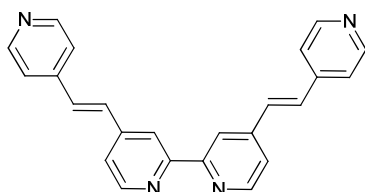


Fig. 6.2 4,4'-Bis((E)-2-(pyridin-4-yl)vinyl)-2,2'-bipyridine reported by Coe *et al* in 2010<sup>4</sup>.

Therefore, the initial aim of this chapter was to synthesise 6,6'-bis((E)-2-(pyridin-4-yl)vinyl)-2,2'-bipyridine. The use of this ligand has been previously reported by Shonfield *et al.* in 1999<sup>5</sup> but details of the synthesis were not published. For that reason, a number of synthetic routes to obtain this compound were attempted and are detailed in Fig. 6.3.

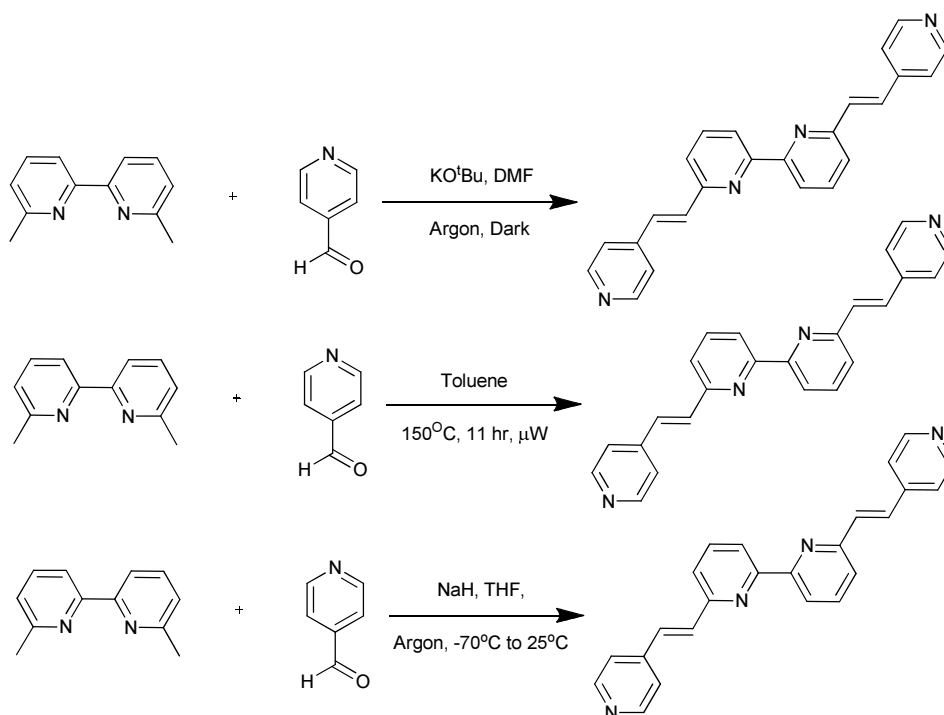
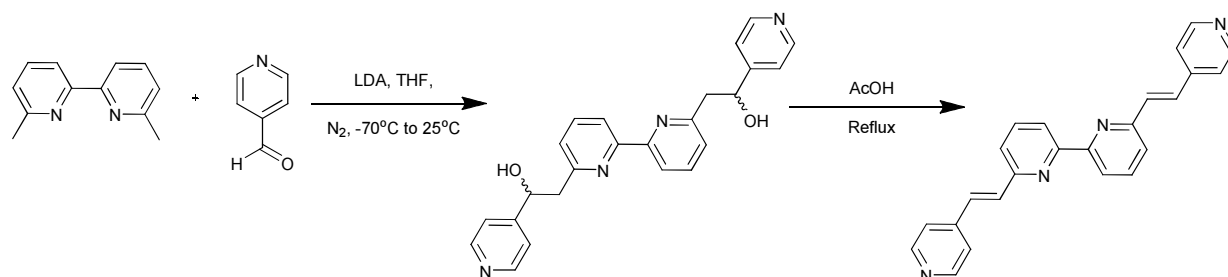


Fig. 6.3 Failed synthetic procedures to the quaterpyridine ligand.

All of the synthetic approaches detailed in Fig. 6.3 failed and so a stepwise procedure of first synthesising the 2,2'-([2,2'-bipyridine]-6,6'-diyl)bis(1-(pyridin-4-yl)ethanol) and then dehydrating it to form the alkene was adopted (Scheme 6.1).



Scheme 6.1 Proposed synthetic route to 6,6'-bis((E)-2-(pyridin-4-yl)vinyl)-2,2'-bipyridine.



The stepwise procedure failed; regardless of the number of equivalents of 4-pyridine carbaldehyde and lithium diisopropylamide (LDA) added to the reaction, it was only possible to form the mono-substituted compound, 2-(6'-methyl-[2,2'-bipyridin]-6-yl)-1-(pyridin-4-yl)ethanol (**14**). The product of this reaction was then dehydrated to form the mono-substituted compound (E)-6-methyl-6'-(2-(pyridine-4-yl)vinyl)-2,2'-bipyridine (**15**). The ligands depicted in Fig 6.4, and complexes thereof, are described in this chapter.

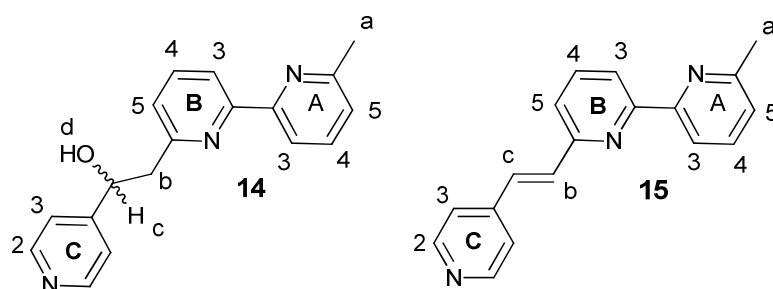
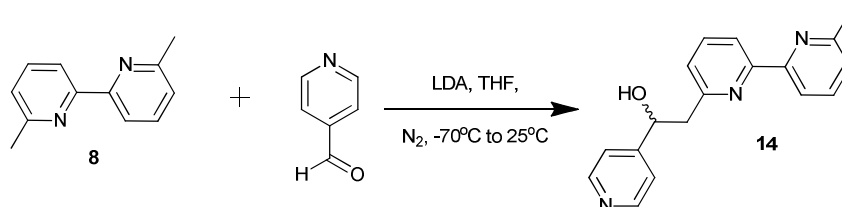


Fig. 6.4 Ligands **14** and **15** with labelling for spectroscopic assignments.

## 6.2 Synthesis - Ligands

The starting material for **14** was 6,6'-dimethyl-2,2'-bipyridine (**8**), which was commercially available. Compound **14** was synthesised in a stepwise manner (Scheme 6.2) by first deprotonating **8** using LDA in dry THF at  $-78^{\circ}\text{C}$ . Then 1.3 equivalents of pyridine-4-carbaldehyde were added and the reaction was left to warm to room temperature, whilst stirring, overnight. The compound was extracted into dichloromethane and purified using column chromatography. The yield of the reaction was 65%.



Scheme 6.2 The synthesis of compound **14**.

A by-product formed during the reaction and was identified, using  $^1\text{H}$  NMR spectroscopy and X-ray crystallography, as pyridin-4-yl isonicotinate (**16**), a compound related to the 4-pyridine carbaldehyde starting material (Fig. 6.5).

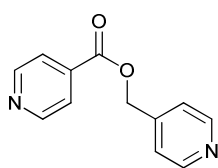
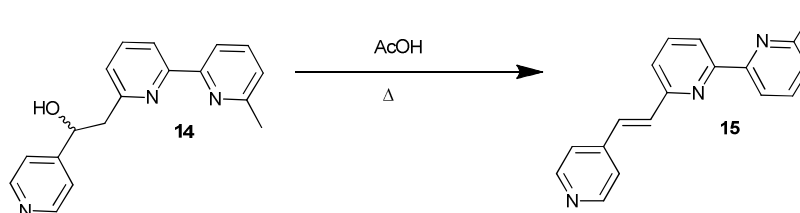


Fig. 6.5 Compound **16**, the by-product formed during the synthesis of **14**.

Compound **15** was synthesised by refluxing **14** in acetic acid overnight (Scheme 6.3).



Scheme 6.3 The synthesis of compound **15**.

The compound was then neutralised with sodium hydrogencarbonate ( $\text{NaHCO}_3$ ) and extracted with dichloromethane and purified by column chromatography. By carrying out a very slow column and collecting very small fractions it was possible to isolate a small amount of pure **15** from the early fractions. In the later fractions, **15** is contaminated by the related enol compound, **17** (Fig. 6.6), which is formed as a by-product in the reaction. This compound has almost the same  $R_f$  value as **15** regardless of the solvent system and the compounds **15** and **17** even co-crystallise.

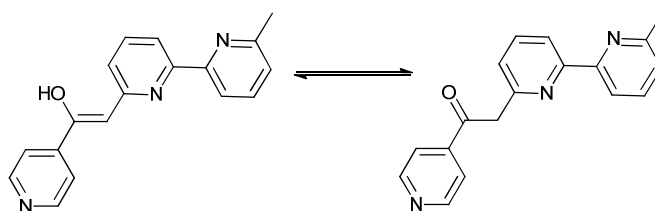


Fig. 6.6 Compound **17** in the keto- and enol-tautomeric forms.

Initially it was thought that the formation of the enol was due to the presence of oxygen in the reaction. However, repeating the reaction under Schlenk conditions gave the same products, **15** and **17**, in the same yield.

## 6.3 Results and Discussion (I)

### 6.3.1 $^1\text{H}$ NMR Spectroscopy - Ligands

The  $^1\text{H}$  NMR spectrum of compound **14** was measured in  $\text{CDCl}_3$  and the spectrum is depicted in Fig. 6.7.

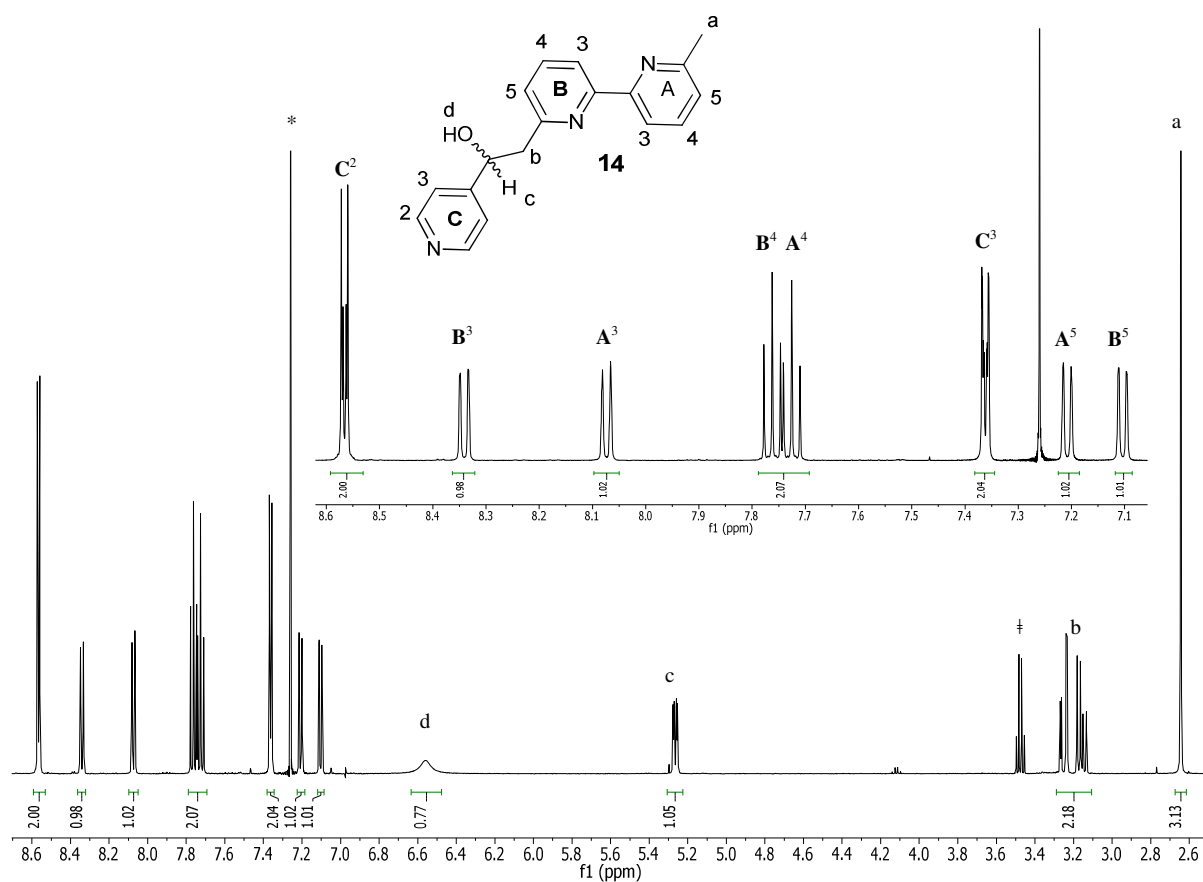


Fig. 6.7  $^1\text{H}$  NMR spectrum of **14** (500 MHz,  $\text{CDCl}_3$ , 25°C, TMS)  $\text{CHCl}_3$  (\*), Ethylacetate (‡).

The  $^1\text{H}$  NMR spectrum of **14** (Fig. 6.7) was assigned using both COSY and NOESY techniques. The singlet at  $\delta$  2.64 ppm was ascribed to the methyl substituent due to the chemical shift and the integral. The two signals with integrals of two were assigned to the C ring and the specific assignment of the peaks was done using a NOESY spectrum. The signal at  $\delta$  8.57 ppm showed no NOESY cross peaks and was therefore assigned as  $\text{C}^2$ . The signal at  $\delta$  7.36 ppm showed a NOESY cross peak to the doublet of doublets at

$\delta$  5.26 ppm and was assigned to proton  $\mathbf{C}^3$ . The broad singlet at  $\delta$  6.55 ppm was assigned to  $d$  as  $-\text{OH}$  signals are commonly broad and consequently the signal at  $\delta$  5.26 ppm could be ascribed to  $c$ . A COSY cross peak between  $c$  and the multiplet at  $\delta$  3.20 ppm assigned the multiplet as  $b$ . Protons  $b$  show a NOESY cross peak with a doublet at  $\delta$  7.10 ppm, which ascribes said doublet as proton  $\mathbf{B}^5$ . A COSY cross-peak to the triplet at  $\delta$  7.76 ppm leads to the assignment of the triplet as  $\mathbf{B}^4$ , which in turn assigns the doublet at  $\delta$  8.34 ppm as  $\mathbf{B}^3$ , due to a COSY cross peak between  $\mathbf{B}^4$  and said doublet. A NOESY peak between  $\mathbf{B}^3$  and the doublet at  $\delta$  8.07 ppm ascribes the doublet as  $\mathbf{A}^3$  and the  $\mathbf{A}$  ring is assigned in the same manner as the  $\mathbf{B}$  ring, which was just described.

The  $^1\text{H}$  NMR spectrum of **15** was measured in  $\text{CDCl}_3$  and was assigned using COSY and NOESY techniques (Fig. 6.8).

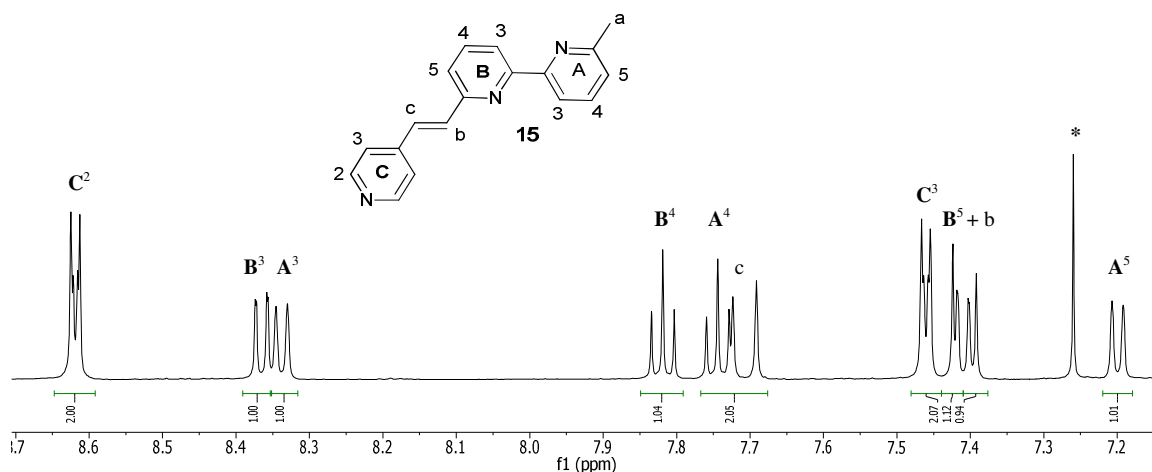


Fig. 6.8  $^1\text{H}$  NMR spectrum of **15** (500 MHz, residual  $\text{CHCl}_3$  (\*),  $\text{CDCl}_3$ , 25°C, TMS). Only aromatic region shown.

The appearance of two broad doublets at  $\delta$  7.71 and 7.42 ppm in the  $^1\text{H}$  NMR spectrum is confirmation that the dehydration reaction was successful. These broad doublets had  $J$  couplings of 16 Hz, indicating that they correspond to a double bond with *trans*-stereochemistry. The rest of the spectrum was assigned following the same procedure as described for **14**.

Compared to **14**, the signals ascribed to  $\mathbf{B}^4$ ,  $\mathbf{B}^5$ ,  $\mathbf{C}^2$  and  $\mathbf{C}^3$  are shifted downfield in the spectrum of **15** (Table 6.1). This is due to the extended  $\pi$ -conjugation in **15**.

Compound	B <sup>4</sup>	B <sup>5</sup>	C <sup>2</sup>	C <sup>3</sup>
<b>14</b>	7.76	7.10	8.57	7.36
<b>15</b>	7.83	7.42	8.62	7.47

Table 6.1 Comparison of shifts ( $\delta$ /ppm) for compounds **14** and **15**. Spectra measured in  $CDCl_3$  at room temperature.

### 6.3.2 $^{13}C\{^1H\}$ NMR Spectroscopy - Ligands

The  $^{13}C\{^1H\}$  NMR spectrum of **14** was measured in  $CDCl_3$  and is depicted in Fig 6.9.

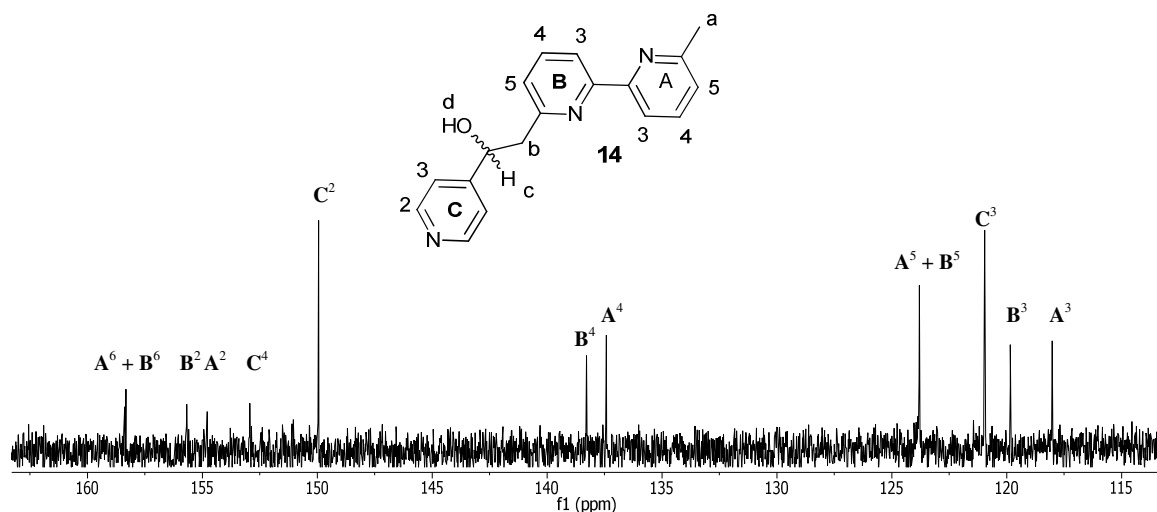


Fig. 6.9  $^{13}C\{^1H\}$  NMR spectrum of **14** (126 MHz,  $CDCl_3$ , 25°C, TMS).

The spectrum was ascribed using HMQC and HMBC techniques along with a DEPT 135 spectrum (Fig. 6.10). The assignment of *b* was facile as  $-CH_2-$  groups “point down” in DEPT 135 spectra.

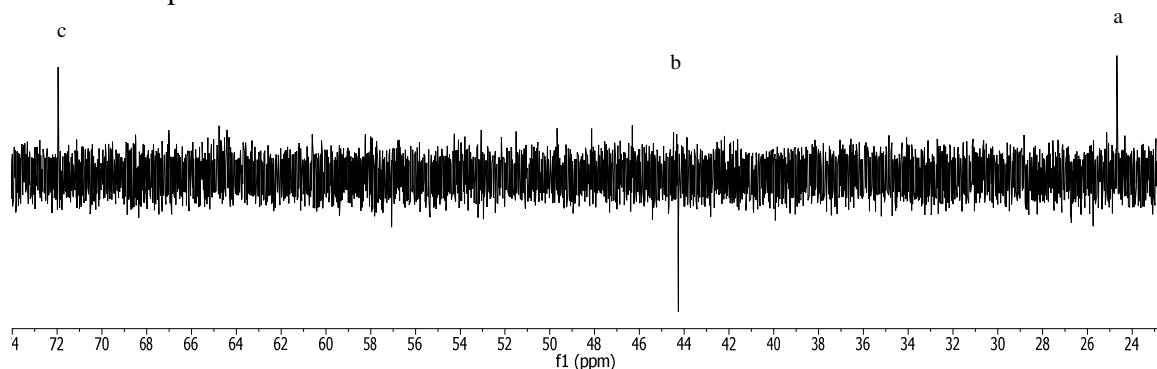


Fig. 6.10 DEPT135 spectrum of **14** specifically showing the signal ascribed to *b*.

The peaks arising from  $^{13}\text{C}$ -H carbons were assigned using the HMQC spectrum and the quaternary carbon signals were assigned using the HMBC spectrum. Proton  $\text{C}^2$  had an HMBC interaction with a signal at  $\delta$  152.9 ppm, which was assigned to  $\text{C}^4$  (Fig. 6.11). An HMBC interaction between proton  $c$  and a signal at  $\delta$  158.3 ppm meant that said signal could be ascribed to  $\text{B}^6$ . Proton  $\text{B}^4$  had two HMBC interactions; one to the peak at  $\delta$  158.3 ppm, already ascribed to  $\text{B}^6$ , and one to a peak at  $\delta$  155.7, ascribing the latter peak to  $\text{B}^2$ . The assignment of the peak at  $\delta$  155.7 ppm was confirmed on observation of a HMBC interaction between proton  $\text{A}^3$  and the signal ascribed to  $\text{B}^2$ . The carbon signal for  $\text{A}^2$  was assigned after observation of a HMBC interaction from  $\text{B}^3$  to a signal at  $\delta$  154.8 ppm. Proton  $\text{A}^4$  showed two HMBC interactions, the first to the signal at  $\delta$  154.8 ppm, confirming the assignment as  $\text{A}^2$  and the second to a signal at  $\delta$  158.4 ppm, assigning this latter signal to  $\text{A}^6$  (Fig. 6.11).

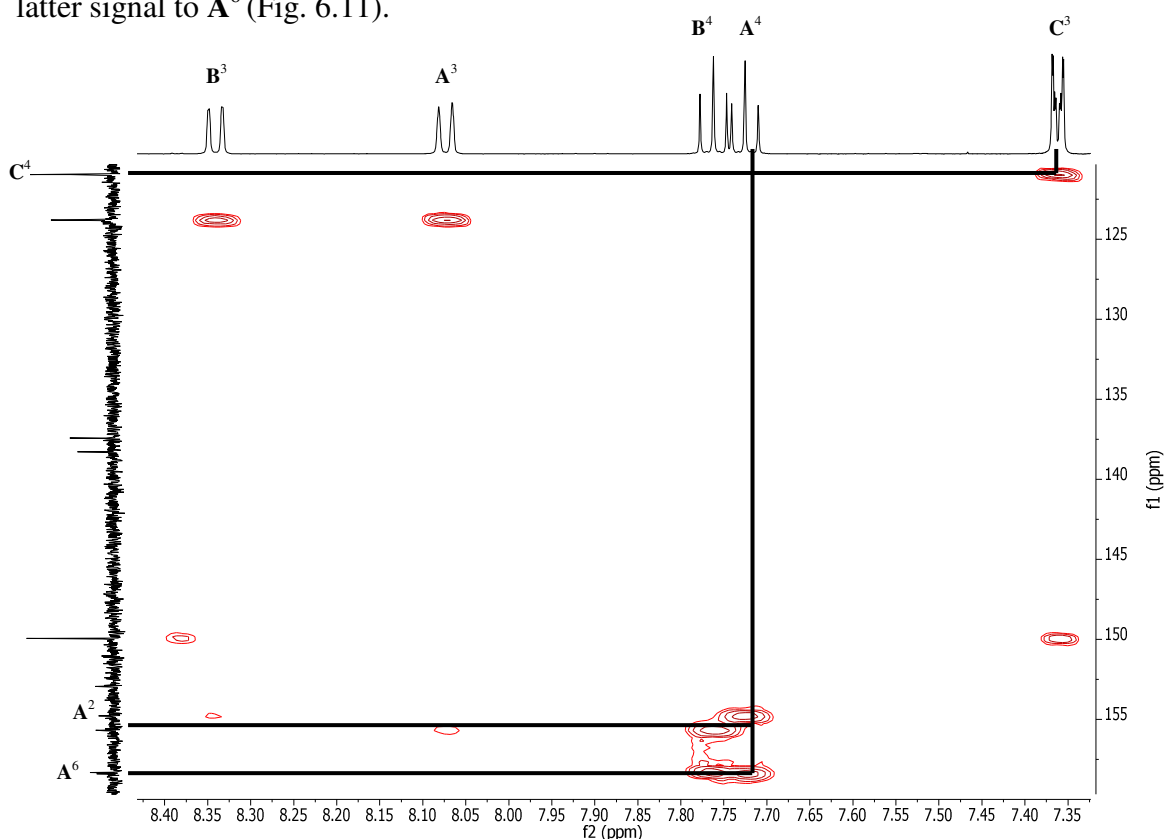


Fig 6.11 HMBC spectrum of compound **14**, measured in  $\text{CDCl}_3$  at  $25^\circ\text{C}$ , depicting the interactions between  $\text{H}(\text{A}^4)$  and  $\text{C}(\text{A}^2)$ ,  $\text{C}(\text{A}^6)$  and  $\text{H}(\text{C}^3)$  and  $\text{C}(\text{C}^4)$  specifically.

The  $^{13}\text{C}\{^1\text{H}\}$  spectrum of **15** was also measured in  $\text{CDCl}_3$  and the spectrum was assigned using HMQC and HMBC techniques. The cross peaks between the alkene protons and their respective carbon signals were very distinct (Fig. 6.12). All carbons except the

quaternary carbons were assigned using the HMQC spectrum. The quaternary carbons were assigned using the HMBC spectrum in the manner previously described for **14**.

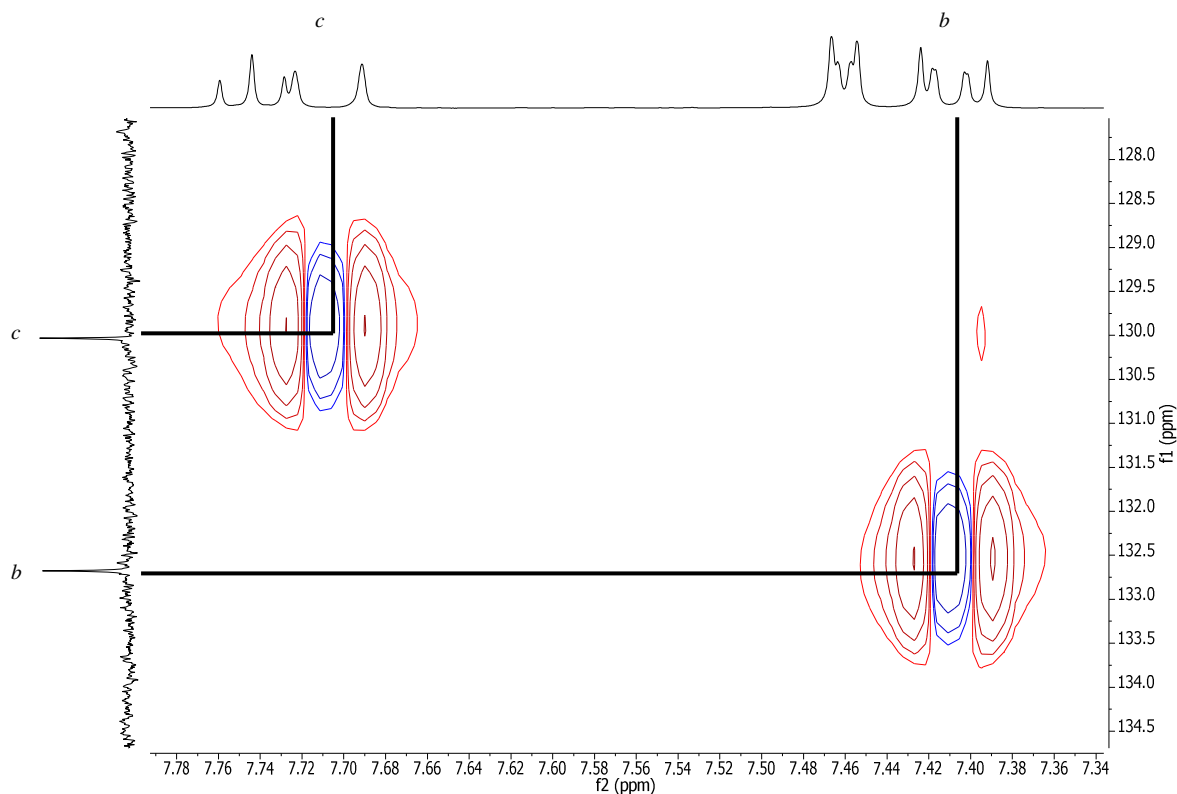


Fig. 6.12 Partial HMQC spectrum of **15**, measured in  $CDCl_3$  at  $25^\circ C$ .

### 6.3.3 Mass Spectrometry – Ligands

Compounds **14** and **15** were characterised using ESI mass spectrometry. For **14**, a peak corresponding to  $[M+Na]^+$  was observed at  $m/z$  314.2 which was in good agreement with the calculated peak (314.1) and therefore confirmed that the synthesis of the compound had been successful.

Two peaks were observed in the ESI mass spectrum of **15**. These peaks corresponded to  $[M+K]^+$  and  $[M+Na]^+$  at  $m/z$  312.1 and 296.2 respectively. Again the experimentally observed values were in good agreement with the calculated values and confirmed that the dehydration of the alcohol to form the alkene had been successful.

### 6.3.4 Absorption Spectroscopy - Ligands

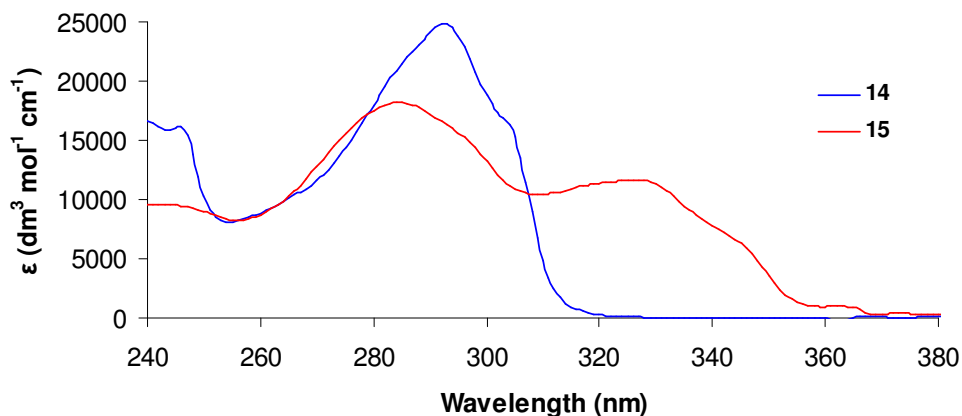


Fig. 6.13 Absorption spectra for **14** and **15** measured in dichloromethane ( $10^{-5}$  mol dm $^{-3}$ ).

The electronic absorption spectra are dominated by ligand-based  $\pi \rightarrow \pi^*$  transitions and the data are summarised in Table 6.2.

Compound	$\lambda_{\max}$ ( $\epsilon$ , dm $^3$ mol $^{-1}$ cm $^{-1}$ )			
<b>14</b>	303	293	283 sh	247
	(16262)	(24883)	(20261)	(15440)
<b>15</b>	342 sh	327	285	
	(7215)	(11612)	(18186)	

Table 6.2 A summary of the photophysical data, recorded in dichloromethane, for **14** and **15**.

The absorptions at 247, 283, 293 and 303 nm of compound **14** are all due to the bipyridine unit<sup>6</sup>. This is unsurprising as there is no conjugation between the bipyridine moiety and the pendant pyridyl unit. No absorption due to the pendant pyridyl unit is observed in the spectrum.

The absorption spectrum of **15** is very different. Contribution to the spectrum from the bipyridine unit is observed in the high energy region of the spectrum, namely the peak with  $\lambda_{\max} = 285$  nm. The lower energy peaks are a result of the conjugation between the pendant pyridyl ring and the bipyridine unit through the double bond.



### 6.3.5 Emission and Excitation Spectroscopy - Ligands

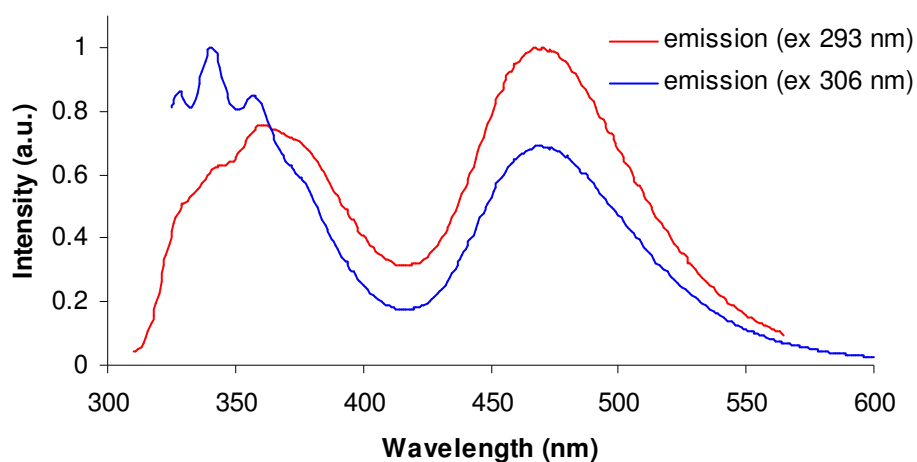


Fig. 6.14 Emission spectra of **14** measured in dichloromethane.

The origins of the emissions at 329, 342 and 359 nm were confirmed by measuring excitation spectra. The emission centred at 480 nm could be due to the formation of an exciplex. The excitation spectrum, when holding the emission at 480 nm, is dissimilar to the absorption spectrum (Fig. 6.15).

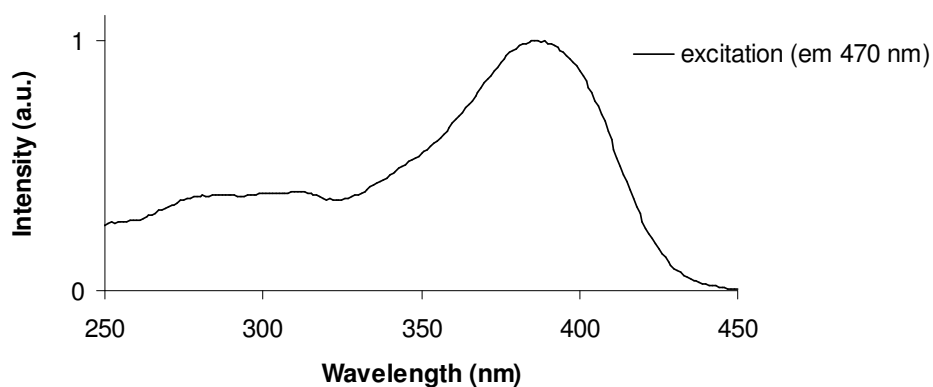


Fig. 6.15 Excitation spectrum of **14** measured in dichloromethane.

The dissimilarity between the absorption and excitation spectra indicates that the origin of the emission is through a non-luminescent absorption. Further investigation by testing the effect of a more polar solvent, such as methanol, on the exciplex needs to be carried out.

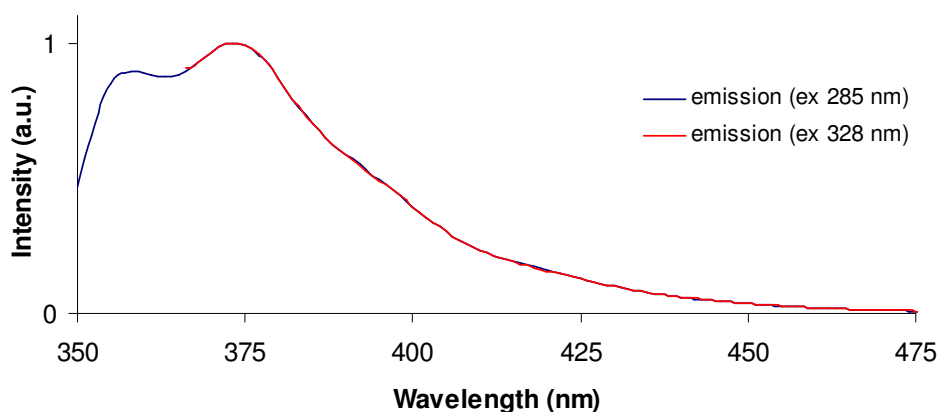


Fig. 6.16 Emission spectra of **15** measured in dichloromethane.

The emission spectrum of **15** is red-shifted compared to that of **14** due to the extended  $\pi$ -conjugation. The origins of the emissions at 358, 374 and 394 nm were confirmed by measuring excitation spectra.

### 6.3.6 Crystal Structures - Ligands

Single colourless needles of **14** were grown by diffusion of hexanes into a dichloromethane solution of the complex. The crystal solves in the monoclinic  $P2_1/c$  space group with a reasonable R factor of 7.8%. The asymmetric unit contains one molecule of **14**. The structure of the molecule is depicted in Fig. 6.17 and selected bond lengths and angles are listed in the caption.

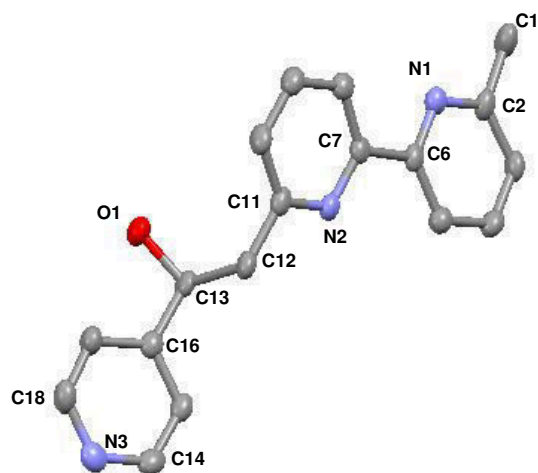


Fig. 6.17 Structure of **14** with ellipsoids plotted at 50% probability and hydrogen atoms omitted for clarity. Selected bond parameters: N1-C2 = 1.344(5), N1-C6 = 1.342(5), N2-C7 = 1.353(5), N2-C11 = 1.341(5), N3-C14 = 1.345(5), N3-C18 = 1.330(6), C11-C12 = 1.509(6), C12-C13 = 1.550(5), C13-O1 = 1.407(5), C13-C16 = 1.497(6) Å; N1-C2-C1 = 116.1(3), N2-C11-C12 = 118.0(3), C11-C12-C13 = 112.9(3), C12-C13-C16 = 109.2(3), C14-N3-C18 = 116.2(4)°.

As expected, the bipyrindine unit is in the *trans*-conformation. The bond lengths around the bipyrindine and pyridine units are unexceptional. The C11-C12 and C13-C16 bonds are the same length, within experimental error, and the lengths are consistent with single bonds. By comparison, the C12-C13 bond is elongated slightly but still consistent with a single bond. As expected the C13-O1 bond is longer than the single C-C bonds and shorter than the ring C-C bonds. The molecule is not planar and the rings containing atoms N1 and N2 are essentially coplanar. The molecules pack in chains due to hydrogen bonds between the -OH group (H1) on one molecule and the nitrogen atom (N3) of the pendant pyridyl ring on another molecule and both enantiomers can be observed in the packing (Fig. 6.18).

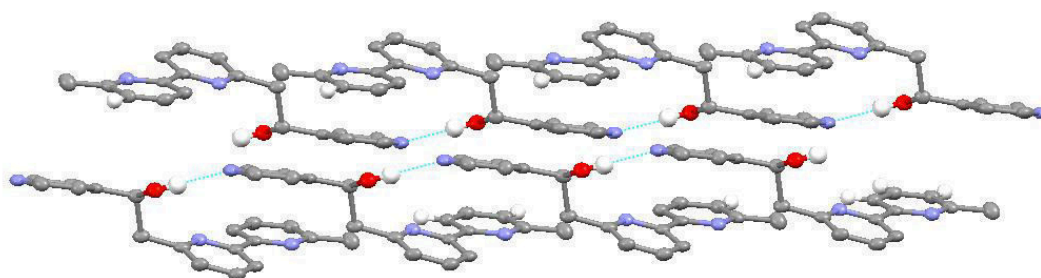


Fig. 6.18 Packing of **14** with the hydrogen bonds between the molecules denoted by dashed blue lines.

Colourless blocks of **15** were grown following the same procedure for **14**. The crystal solved in the monoclinic  $C2/c$  space group with a good R factor of 3.6%. The asymmetric unit contains one molecule of **15** and there is no solvent present in the crystal lattice. The structure of **15** is depicted in Fig. 6.19 and selected bond lengths and angles are listed in the caption.

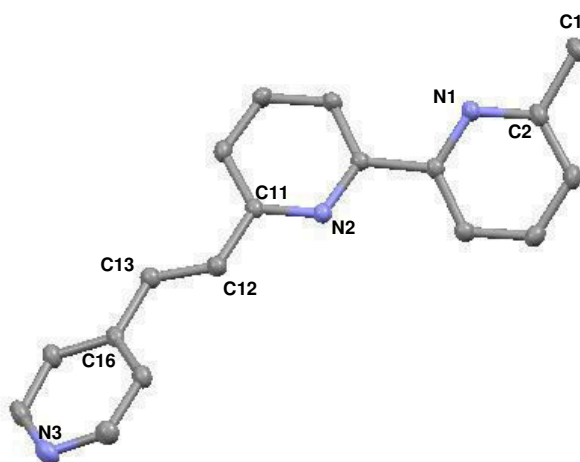
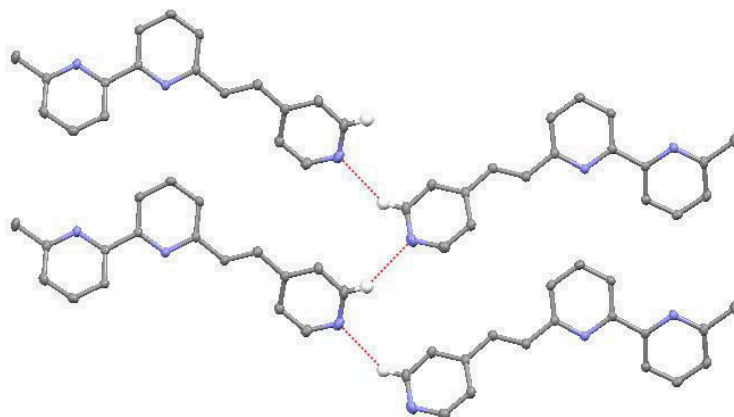


Fig. 6.19 Structure of **15** with ellipsoids plotted at 50% probability and hydrogen atoms omitted for clarity. Selected bond parameters:  $C11-C12 = 1.467(1)$ ,  $C12-C13 = 1.334(1)$ ,  $C13-C16 = 1.467(1)$  Å;  $N1-C2-C1 = 116.32(9)$ ,  $N2-C11-C12 = 114.89(9)$ ,  $C11-C12-C13 = 126.77(9)$ ,  $C12-C13-C16 = 124.17(9)^\circ$ .

As for **14** the bipyridine unit is in the *trans*-conformation. The main differences between the structures of **14** and **15** are the absence of the alcohol group in the structure of **15** and the shortening of the C12-C13 bond. Both of these differences are confirmation that the dehydration of the alcohol to form the alkene was successful. All other bond lengths are unremarkable.

The packing of the molecules is determined by hydrogen bonds between the proton on one pendant pyridyl moiety (H18) and the nitrogen atom of another pendant pyridyl moiety (N3). This is depicted in Fig. 6.20.



*Fig. 6.20 Packing of 15 with the hydrogen bonds between the molecules denoted by dashed red lines.*

As stated in Section 6.2, ligand **15** co-crystallises with the reaction by-product, compound **17**. This is depicted in Fig. 6.21. Yellow blocks were grown through slow evaporation of an ethylacetate and hexane solution. The crystal solves in the monoclinic  $P2_1/c$  space group with a good R factor of 3.8%. Ligand **15** is predominantly present in the crystal, with **17** present a third of the time. Compound **17** is present as the enol form of the keto-enol tautomer and there is an internal hydrogen bond between the bipyridine nitrogen and the proton of the enol moiety (denoted by the dashed blue line in Figs. 6.22)

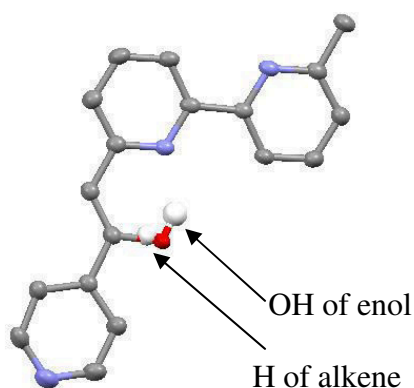


*Fig. 6.21 The structure in the asymmetric unit of the co-crystallised compounds 15 and 17. Ellipsoids plotted at 50% probability.*

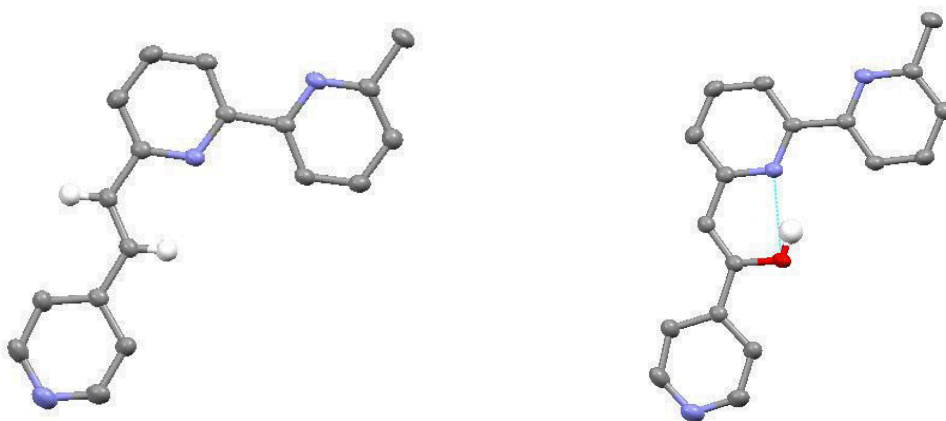


*Fig. 6.22 (Left) The desired compound, **15**. (Right) The reaction by-product, **17**. Ellipsoids plotted at 50% probability in both cases.*

The molecules pack with a mixture of face-to-face and edge-to-face interactions between the pyridine rings (Fig. 6.23). Contrary to the structures of **14** and **15** there is no hydrogen-bonding utilising the pendant pyridine nitrogen.

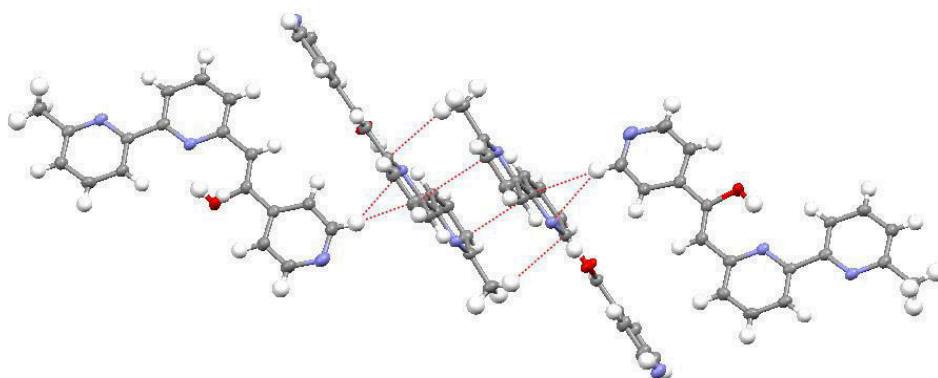


*Fig. 6.23 Packing of the structure of co-crystallised **15** and **17** with the short contacts denoting edge-to-face and face-to-face interactions with dashed red lines.*

Compound **16** was another by-product, formed during the reaction of **8** with 4-pyridine carbaldehyde. Colourless needles were grown by evaporation of ethyl acetate and hexane from a solution of the compound. The crystal solved in the monoclinic  $P2_1/c$  space group with a reasonable R factor of 6.26 %. The asymmetric unit contained one molecule of **16** and it is depicted in Fig. 6.24. As the compound was a reaction by-product there is no detailed discussion following the picture of the structure.

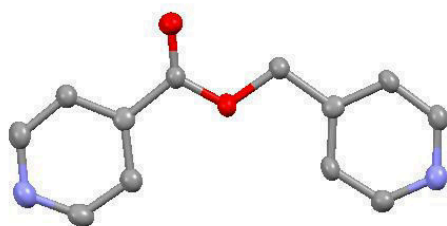
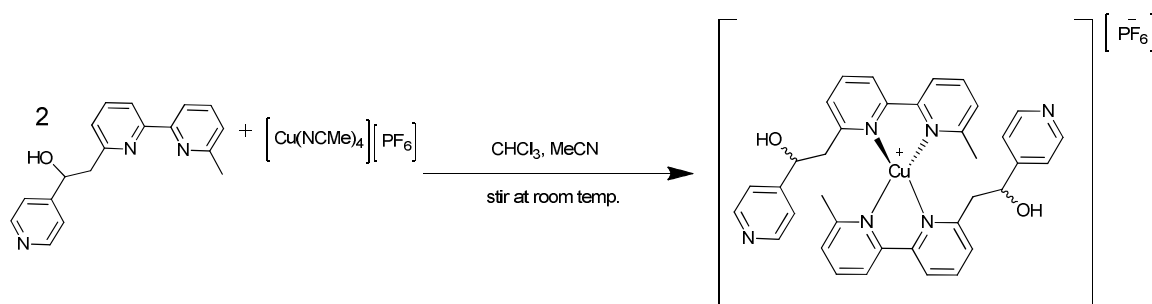


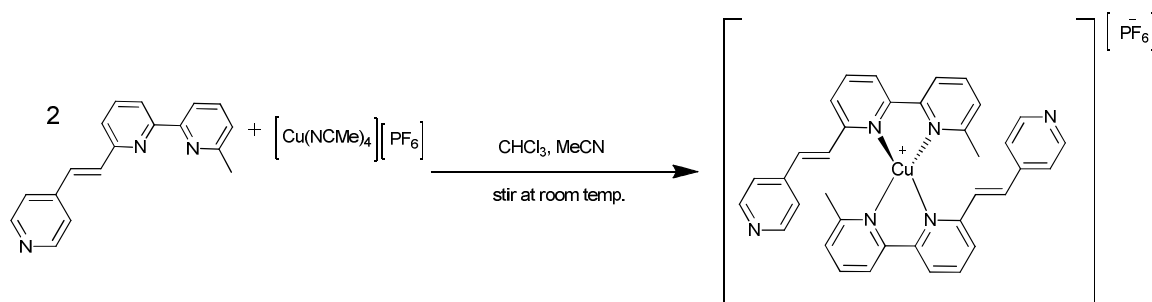
Fig. 6.24. Structure of **16** with ellipsoids plotted at 50% probability and hydrogens omitted for clarity.

## 6.4 Synthesis - Cu(I) Complexes

The Cu(I) complexes were synthesised by addition of two equivalents of the relevant ligand, in chloroform, to one equivalent of  $[\text{Cu}(\text{NCMe})_4][\text{PF}_6]$ , in acetonitrile. The complexes were isolated as red powders in good yield.



Scheme 6.3 Synthesis of  $[\text{Cu}(\mathbf{14})_2][\text{PF}_6]$ , yield = 70 %.



Scheme 6.4 Synthesis of  $[\text{Cu}(\mathbf{15})_2][\text{PF}_6]$ , yield = 85 %.

## 6.5 Results and Discussion (II)

### 6.5.1 Section Introduction

Chiral copper(I) complexes arise from the coordination of two asymmetric ligands to a copper(I) atom and were first reported by Thummel *et al.* in 2001<sup>7</sup>. As Cu(I) is labile, the

ligands exchange in solution and so variable temperature NMR was used to investigate the rates of ligand exchange in acetonitrile and chloroform. Sauvage *et al.* also reported chiral Cu(I) complexes in 2006<sup>8</sup>. Variable temperature NMR and introduction of an enantiopure chiral anion to the complexes were used to ascertain the stereoisomers present in solution and the stability of those isomers. The chirality of the copper(I) is denoted  $\Delta$  or  $\Lambda$ <sup>9</sup>.

### 6.5.2 <sup>1</sup>H NMR Spectroscopy – Cu(I) Complexes

The <sup>1</sup>H NMR spectrum of [Cu(**15**)<sub>2</sub>][PF<sub>6</sub>] was measured at room temperature and the signals were found to be broad, which lead to the hypothesis that the pendant pyridine group (ring **C**) was rotating in a hindered fashion on the NMR timescale. Therefore, variable temperature NMR spectroscopy was used to investigate the effect of temperature on the rotation of the **C** ring (Fig. 6.25).



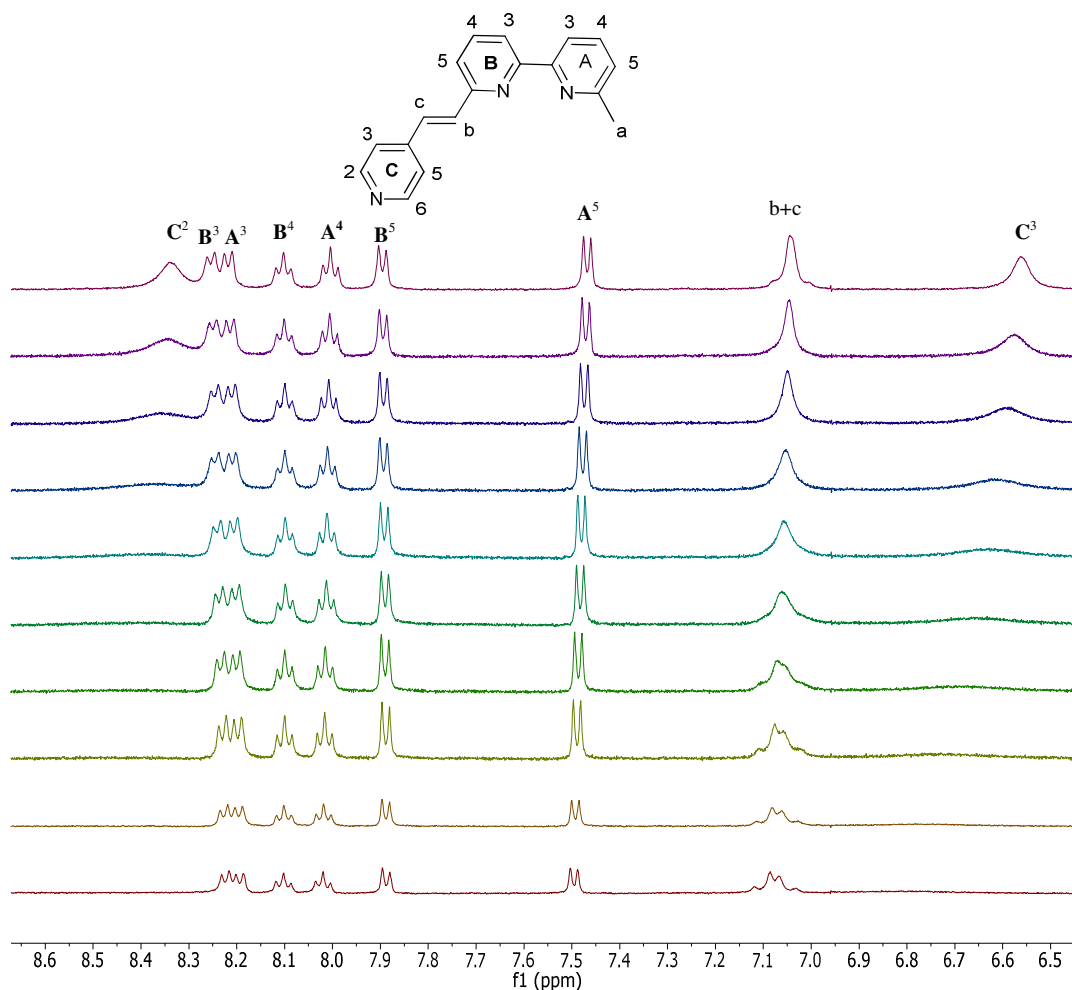


Fig. 6.25 Variable temperature  $^1\text{H}$  NMR (500 MHz,  $\text{CD}_2\text{Cl}_2$ , TMS) of  $[\text{Cu}(\mathbf{15})_2][\text{PF}_6]$ , (red) 295 K, (yellow) 285 K, (green) 275 K, (dark green) 265 K, (blue) 255 K, (royal blue) 245 K, (purple) 235 K. Only the aromatic region is shown.

At room temperature, the signal due to  $\text{C}^2$  is so broad that it is almost indistinguishable from the baseline. The signal for  $\text{C}^3$  is also very broad and only barely distinguishable from the baseline. In a static structure, two signals for protons  $\text{C}^2$  and  $\text{C}^6$  and two signals for protons  $\text{C}^3$  and  $\text{C}^5$  are expected as the environments of these pairs of protons are different. By cooling the NMR sample down, the C ring rotation slows and two two-site exchanges are expected to be frozen out. It is expected to observe the splitting of the broad signal for  $\text{C}^2$  into two signals and the broad signal for  $\text{C}^3$  also splitting into two signals. However, even after being cooled to 205 K, only two signals due to the C ring are observed and this suggests that another process is also occurring. This simultaneous

process is probably due to the interconversion of enantiomers<sup>10</sup>. The signal due to the methyl groups does not change throughout the cooling process.

The <sup>1</sup>H NMR spectrum was assigned by means of a COSY spectrum, which was measured at 205 K, and by comparison of the <sup>1</sup>H NMR spectrum of the ligand with the <sup>1</sup>H NMR spectrum of the complex.

The <sup>1</sup>H NMR spectrum of [Cu(**14**)<sub>2</sub>][PF<sub>6</sub>] was more complicated than that of [Cu(**15**)<sub>2</sub>][PF<sub>6</sub>] due to the presence of an asymmetric carbon atom in each ligand, resulting in diastereoisomers and enantiomers of the complex (Fig. 6.25). The asymmetric chiral carbon atoms in the following structures are assigned according to the rule set out by Cahn, Ingold and Prelog<sup>11</sup> and as such, are denoted R or S. Due to the asymmetric ligand and the chiral centres in [Cu(**14**)<sub>2</sub>][PF<sub>6</sub>], the product of the reaction consisted of six possible complexes; a mix of diastereoisomers and enantiomers (Fig. 6.26).

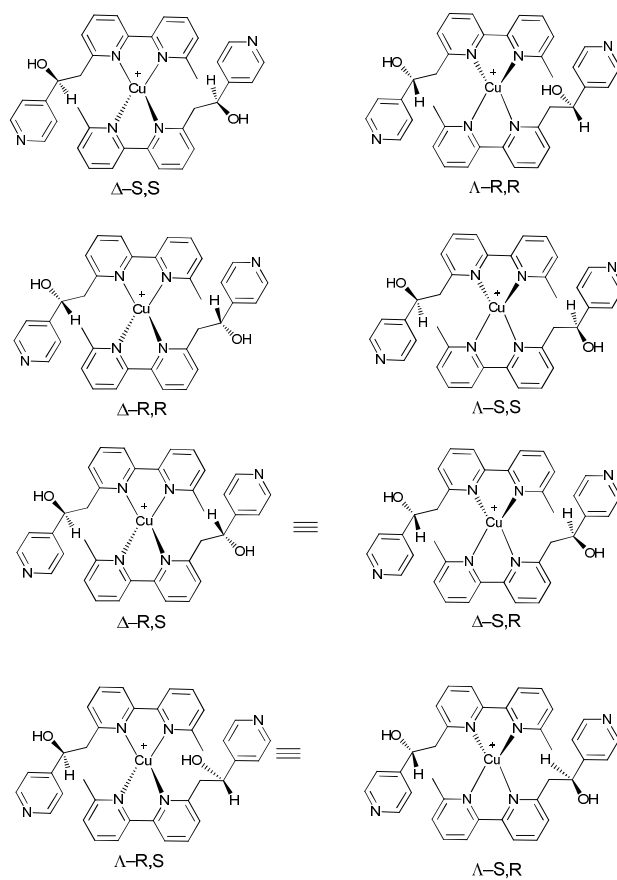


Fig. 6.26 The combinations of enantiomers and diastereoisomers possible for [Cu(**14**)<sub>2</sub>]<sup>+</sup>.

The compounds  $\Delta$ -R,R and  $\Lambda$ -S,S are enantiomers and so only one signal due to each proton environment for both of these compounds was expected in the NMR. The same is true for compounds  $\Delta$ -S,S and  $\Lambda$ -R,R.  $\Delta$ -R,S is an enantiomer of  $\Lambda$ -S,R and  $\Delta$ -S,R is an enantiomer  $\Lambda$ -R,S. The compounds  $\Delta$ -R,S and  $\Delta$ -S,R are chemically equivalent, as are  $\Lambda$ -S,R and  $\Lambda$ -R,S. The four pairs of enantiomers ( $\Delta$ -R,R+ $\Lambda$ -S,S and  $\Delta$ -S,S+ $\Lambda$ -R,R and  $\Delta$ -R,S+ $\Lambda$ -S,R and  $\Lambda$ -R,S+  $\Delta$ -S,R) are diastereoisomers of one another. Assuming that the signals for  $\Delta$ -R,S+ $\Lambda$ -S,R and  $\Lambda$ -R,S+  $\Delta$ -S,R are coincident, then three sets of signals should be observed in the  $^1\text{H}$  NMR spectrum of  $[\text{Cu}(\mathbf{14})_2][\text{PF}_6]$ .

At room temperature the spectrum of the complex is broad, consequently variable temperature NMR was used to try to observe the separation of diastereoisomers on cooling (Fig. 6.27).

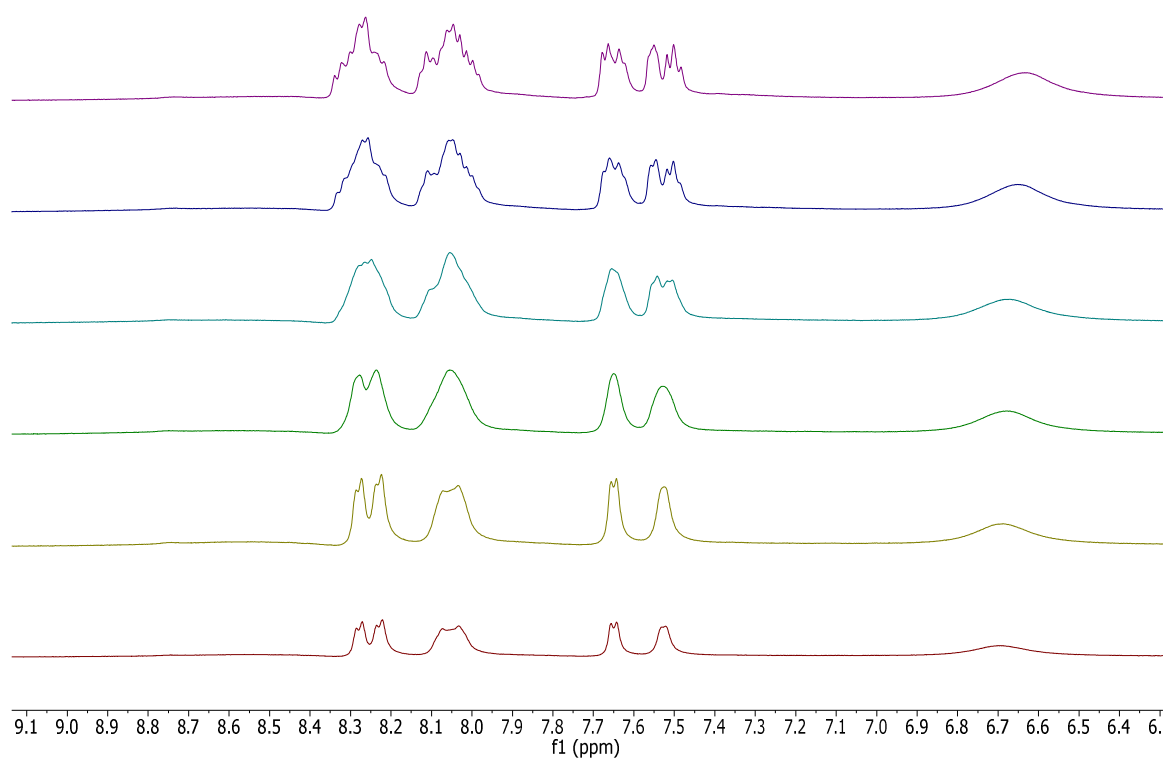


Fig. 6.27 Variable temperature  $^1\text{H}$  NMR (500 MHz,  $\text{CD}_3\text{CN}$ , TMS) of  $[\text{Cu}(\mathbf{15})_2][\text{PF}_6]$ , (red) 298 K, (yellow) 295 K, (green) 283 K, (light blue) 273 K, (royal blue) 263 K, (purple) 253 K. Only the aromatic region is shown.

On cooling, the broad peaks observed at room temperature begin to split and the very broad signal at  $\delta$  6.70 ppm becomes sharper.

The presence of diastereoisomers is more easily identifiable in the aliphatic region of the spectrum, specifically the  $\text{CH}(\text{OH})$  and methyl signals (Fig. 6.28). The  $-\text{CH}_2-$  signal (b) changes very little on cooling and is therefore not shown.

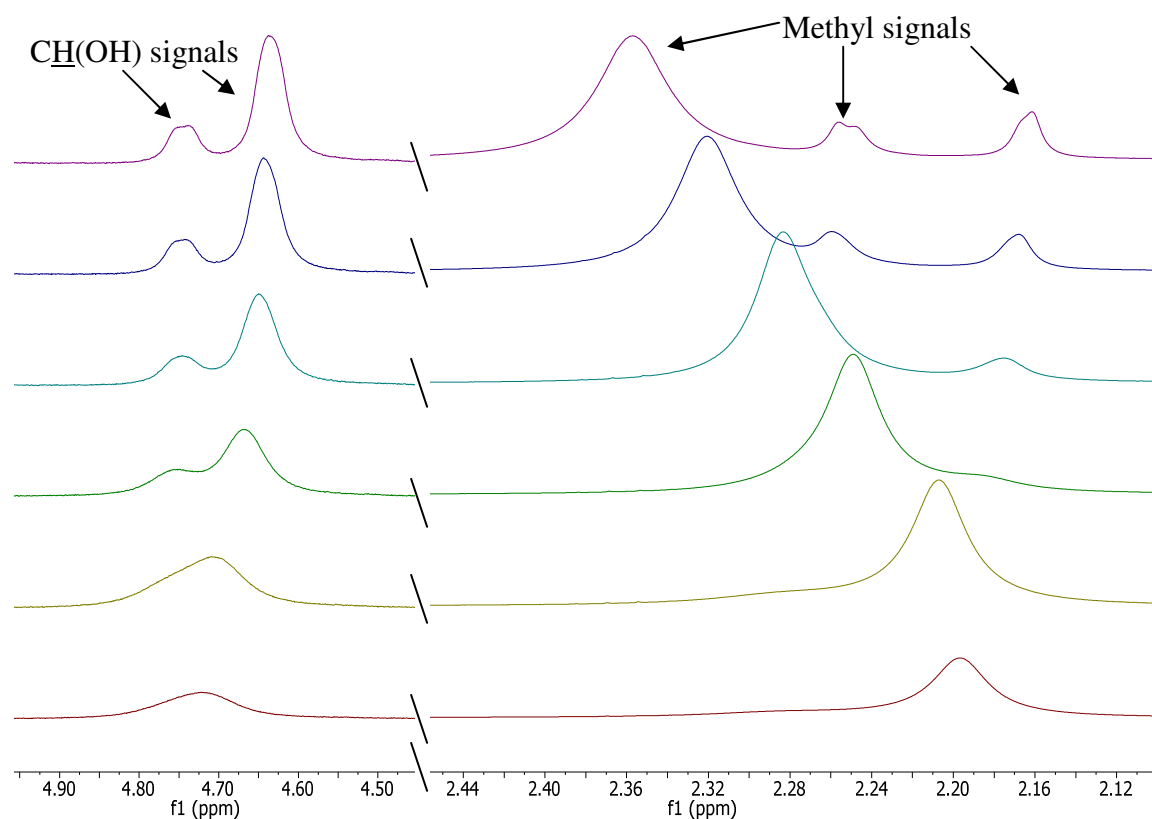


Fig. 6.28 Variable temperature  $^1\text{H}$  NMR (500 MHz,  $\text{CD}_3\text{CN}$ , TMS) of  $[\text{Cu}(\mathbf{15})_2][\text{PF}_6]$ , (red) 298 K, (yellow) 295 K, (green) 283 K, (light blue) 273 K, (royal blue) 263 K, (purple) 253 K. Only the aliphatic region is shown.

On cooling it is possible to observe the broad signal at  $\delta$  4.71 separating into two signals and the broad signal at  $\delta$  2.89 ppm becomes at least three signals. Contrary to the methyl signal of  $[\text{Cu}(\mathbf{15})_2][\text{PF}_6]$ , which does not change on cooling, the methyl signal of  $[\text{Cu}(\mathbf{14})_2][\text{PF}_6]$  appears to split. Overall, the signals remain broad at 253 K, and lower temperature spectra need to be recorded if this investigation is to be expanded. It has not yet been possible to fully elucidate the processes that involve the interconversion of diastereoisomers and the interconversion of enantiomers (ie. the same process as in  $[\text{Cu}(\mathbf{15})_2][\text{PF}_6]$ <sup>10</sup>).

Future work should include further investigation of the NMR spectra by changing the solvent to deuterated dichloromethane and cooling the sample further.

The enantiomerically pure NMR solvating agent  $\Delta$ -TRISPHAT was added, as  $[\text{NBu}_4][\Delta\text{-TRISPHAT}]$ , to the NMR sample of  $[\text{Cu}(\mathbf{14})_2][\text{PF}_6]$  to separate out the enantiomers by making them diastereoisomers, which are individually distinguishable in the NMR spectrum as, for example,  $[\Delta\text{-R,R-Cu}(\mathbf{14})_2]^+[\Delta\text{-X}]^-$  is chemically different to  $[\Lambda\text{-R,R-Cu}(\mathbf{14})_2]^+[\Delta\text{-X}]^-$ . Six sets of signals were then expected in the  $^1\text{H}$  NMR spectrum.

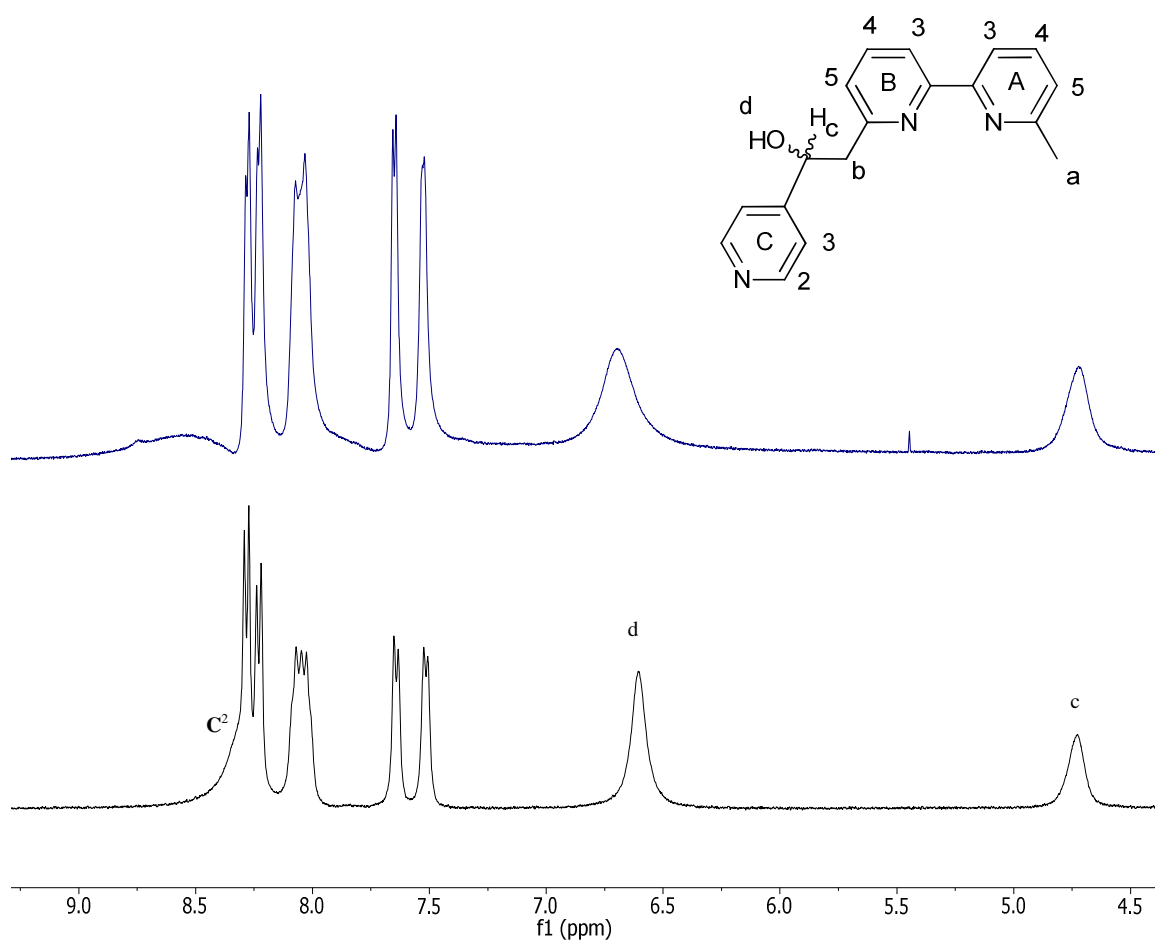


Fig. 6.29 Bottom,  $^1\text{H}$  NMR spectrum of  $[\text{Cu}(\mathbf{14})_2][\text{PF}_6]$  with added  $\Delta$ -TRISPHAT (400 MHz,  $\text{CD}_3\text{CN}$ , TMS,  $25^\circ\text{C}$ ), Top,  $^1\text{H}$  NMR spectrum of  $[\text{Cu}(\mathbf{14})_2][\text{PF}_6]$  without  $\Delta$ -TRISPHAT (500 MHz,  $\text{CD}_3\text{CN}$ , TMS,  $25^\circ\text{C}$ ).

On addition of the  $\Delta$ -TRISPHAT the broad signal at  $\delta$  8.54 ppm in the spectrum with no added  $\Delta$ -TRISPHAT is shifted upfield to  $\delta$  8.35 ppm, where it overlaps with the doublet of doublets at  $\delta$  8.25 ppm. The broad signal at  $\delta$  8.05 ppm is split into a multiplet on

addition of the  $\Delta$ -TRISPHAT and the signal at  $\delta$  7.52 ppm becomes a well defined doublet. The signals due to the aliphatic protons at  $\delta$  6.60, 4.72, 3.56 and 2.89 ppm also become sharper on addition of the  $\Delta$ -TRISPHAT. However, no significant changes are observed on addition of the  $\Delta$ -TRISPHAT, which is consistent with previously reported copper(I) complexes at room temperature<sup>12</sup>.

### 6.5.3 Mass Spectrometry

Both Cu(I) complexes were characterised using ESI-MS and the main peak in the spectrum was due to  $[M-PF_6]^+$ . Initially both complexes were measured in acetonitrile but in this solvent the  $[M-PF_6]^+$  peak was not observed for  $[Cu(\mathbf{15})_2][PF_6]$ . On changing the solvent to a mixture of dichloromethane and methanol it was possible to observe the  $[M-PF_6]^+$  peak at  $m/z$  609.2. A base peak at  $m/z$  274.1, which was assigned to protonated ligand  $[\mathbf{15}+H]^+$ , was also observed.

### 6.5.4 Absorption Spectroscopy

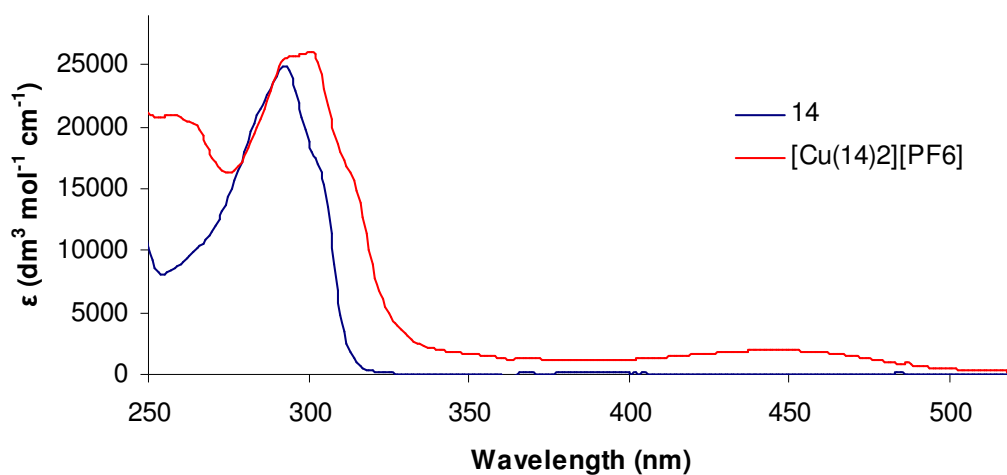


Fig. 6.30 The absorption spectra of ligand **14** (measured in dichloromethane at  $10^{-5} \text{ mol dm}^{-3}$ ) and its corresponding Cu(I) complex (measured in acetonitrile at  $10^{-5} \text{ mol dm}^{-3}$ ).

Compared to the absorption spectrum of the ligand, a new peak, centred at 450 nm, is observed in the spectrum of  $[Cu(\mathbf{14})_2][PF_6]$  (Fig. 6.30). This is an MLCT band, which gives rise to the orange-red colour of the complex. The high energy region of the spectrum is very similar for both the ligand and the complex. A small amount of red-

shifting is observed for the high energy absorptions of the complex but this could be attributed to the change in solvent.

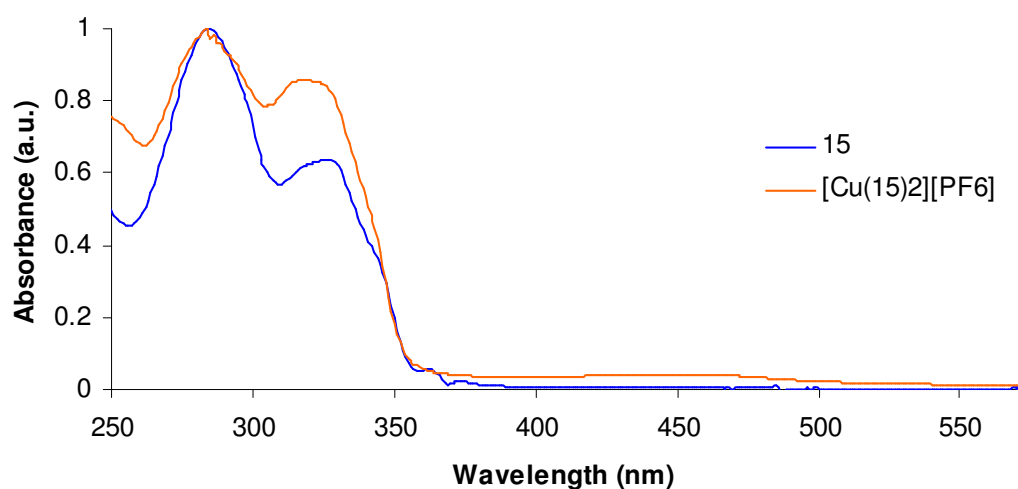


Fig. 6.31 The absorption spectra of ligand **15** (measured in dichloromethane) and its corresponding Cu(I) complex (measured in acetonitrile).

Due to the incomplete characterisation of  $[\text{Cu}(\mathbf{15})_2][\text{PF}_6]$  the concentration of the solution could not be accurately established. For this reason, the ligand and complex absorption spectra have been normalised for comparison (Fig. 6.31).

It was thought that coordination of a ligand with extended  $\pi$ -conjugation would affect the MLCT band of the complex, however, the MLCT  $\lambda_{\text{max}}$  of both  $[\text{Cu}(\mathbf{14})_2][\text{PF}_6]$  and  $[\text{Cu}(\mathbf{15})_2][\text{PF}_6]$  are at 450 nm. The extended  $\pi$ -conjugation from  $[\text{Cu}(\mathbf{14})_2][\text{PF}_6]$  to  $[\text{Cu}(\mathbf{15})_2][\text{PF}_6]$  does affect the high energy absorptions as  $[\text{Cu}(\mathbf{15})_2][\text{PF}_6]$  absorbs a broader range of UV light compared to  $[\text{Cu}(\mathbf{14})_2][\text{PF}_6]$ .

Compound	MLCT	$\lambda_{\text{max}}$			
	$\lambda_{\text{max}}$ ( $\epsilon$ , $10^3 \text{ dm}^3 \text{ mol}^{-1} \text{ cm}^{-1}$ )	( $\epsilon$ , $10^3 \text{ dm}^3 \text{ mol}^{-1} \text{ cm}^{-1}$ )			
$[\text{Cu}(\mathbf{14})_2][\text{PF}_6]$	450 (1.9)	312 sh (16.8)	301 (26.1)	295 (25.7)	265 sh (20.1)
$[\text{Cu}(\mathbf{15})_2][\text{PF}_6]$	450	326	318	284	

Table 6.3 A summary of the absorption data, recorded in dichloromethane, for  $[\text{Cu}(L)_2][\text{PF}_6]$  ( $L = \mathbf{14}, \mathbf{15}$ )

### 6.5.5 Emission Data

Excitation into the MLCT band of  $[\text{Cu}(\mathbf{14})_2][\text{PF}_6]$  gave rise to an emission at 521 nm. This emission had a lifetime of 4.6 ns, which is almost the same as the lifetime of the related  $[\text{Cu}(\mathbf{8})_2][\text{PF}_6]$  complex (4.0 ns).

Due to the possibility of impurities in the  $[\text{Cu}(\mathbf{15})_2][\text{PF}_6]$  complex, emission and excitation spectra were not measured.

### 6.5.6 Crystal Structures - Complexes

Red plates of  $[\text{Cu}(\mathbf{15})_2][\text{PF}_6]$  were grown by evaporation of a dichloromethane-methanol solution of the complex. The crystal solved in the triclinic P-1 space group with a reasonable R factor of 7.69%. The asymmetric unit contains one cation, two half hexafluoridophosphate counter-anions and three water molecules. The cation is depicted in Fig. 6.32.

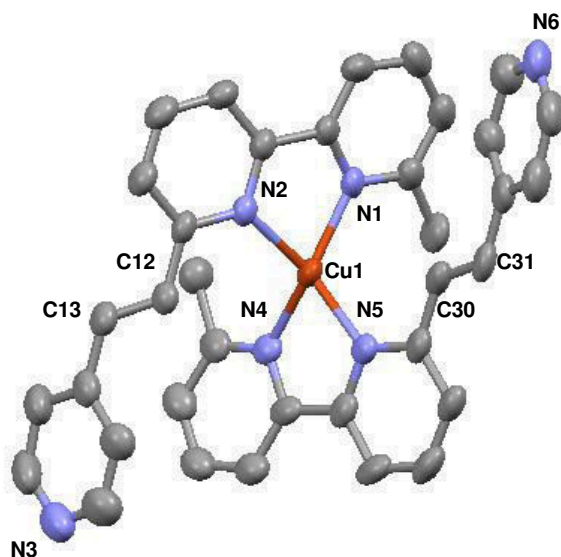


Fig. 6.32 The cation  $[\text{Cu}(\mathbf{15})_2]^+$  with ellipsoids plotted at 50% probability and hydrogens omitted for clarity. Selected bond parameters:  $\text{Cu1-N1} = 2.017(3)$ ,  $\text{Cu1-N2} = 2.045(4)$ ,  $\text{Cu1-N4} = 2.002(3)$ ,  $\text{Cu1-N5} = 2.039(4)$ ,  $\text{C12-C13} = 1.338(5)$ ,  $\text{C30-C31} = 1.345(6)$  Å;  $\text{N1-Cu1-N2} = 80.7(1)$ ,  $\text{N1-Cu1-N5} = 121.0(1)$ ,  $\text{N2-Cu1-N4} = 115.6(1)$ ,  $\text{N4-Cu1-N5} = 81.2(1)^\circ$ .

As expected, the ligand coordinates to the metal through the bipyridine nitrogen donor atoms. The bond lengths and angles are as expected. The geometry of the complex is



neither square planar nor tetrahedral with the angle between the two bipyridine planes being  $70.09^\circ$ .

The lengths of the alkene bonds C12-C13 and C30-C31 are both the same as each other (within experimental error) and the same as the length of the alkene bond in the crystal structure of the ligand. Of note are the intramolecular face-to-edge and face-to-face interactions in the cation (Fig. 6.33).

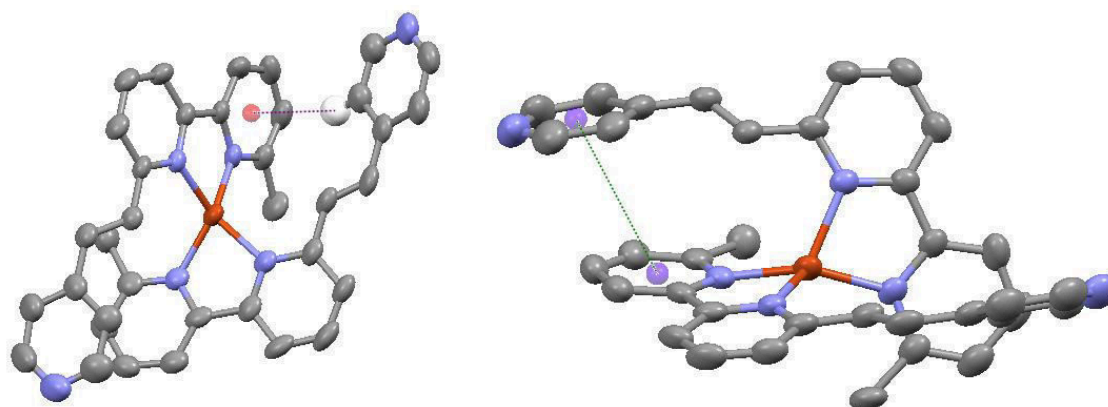


*Fig. 6.33 (Left) Intramolecular face-to-edge interaction between H35A and the bipyridine ring containing N1, (Right) Intramolecular face-to-face interaction between the pendant pyridyl ring containing N3 and the bipyridine ring containing N4.*

The packing also consists of multiple face-to-edge and face-to-face interactions between the chains of the cations (Fig. 6.34). Contrary to the packing of the ligand there is no intercation hydrogen bonding network through the pendant pyridyl nitrogens. This is because it is hydrogen bonding with water molecules present in the lattice instead. The water molecules surround the pendant pyridine sites preventing chains from forming along the *c* axis (Fig. 6.35).

Both enantiomers are present in the structure and are related to one another by an inversion centre (marked by a blue dot in Fig. 6.35).

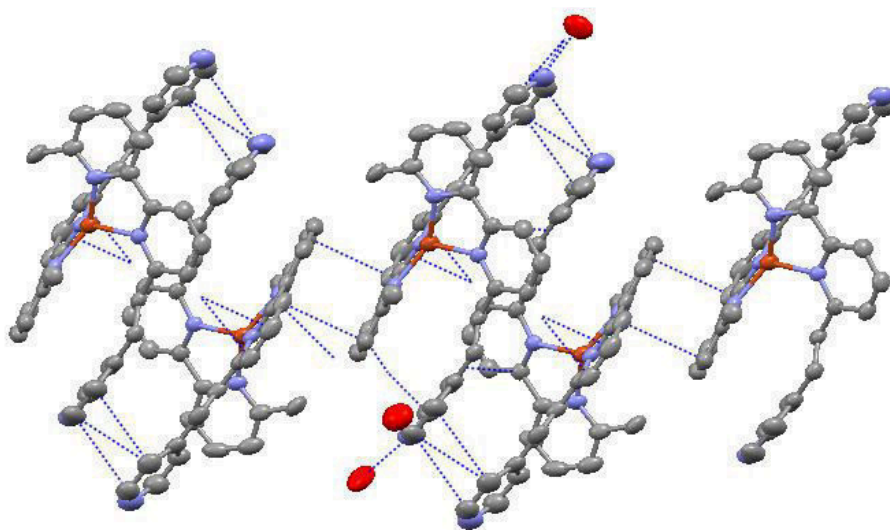


Fig. 6.34 Packing of the  $[\text{Cu}(\mathbf{15})_2]^+$  cations with interactions between the cations denoted by dashed blue lines. Hydrogen bonding between the pendant pyridyl nitrogens and water also shown.

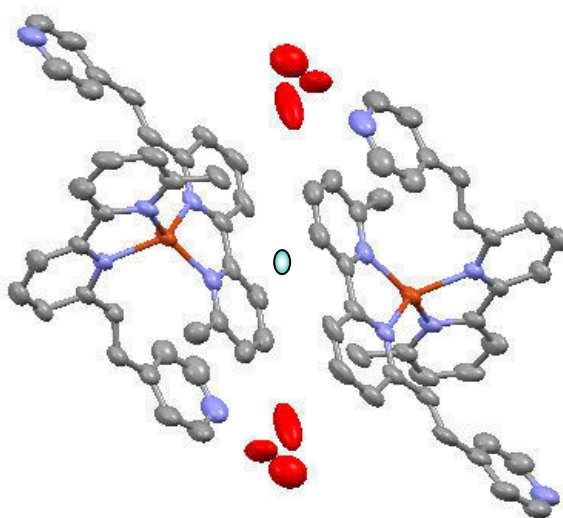


Fig. 6.35 The two enantiomers of the  $[\text{Cu}(\mathbf{15})_2]^+$  cation with water molecules blocking the pendant pyridine sites. Hydrogens are omitted for clarity and the blue dot marks the centre of inversion.

## 6.6 Conclusions

Two chiral copper(I) complexes have been synthesised as racemates and characterised using a variety of techniques. Further investigation into the photophysical properties of  $[\text{Cu}(\mathbf{15})_2][\text{PF}_6]$  and the electrochemical properties of both  $[\text{Cu}(\mathbf{14})_2][\text{PF}_6]$  and  $[\text{Cu}(\mathbf{15})_2][\text{PF}_6]$  is necessary to decide whether the complexes are suitable for application in dye sensitised solar cells. If this is the case then a higher-yielding synthesis of the ligand should also be developed to enable a more efficient and cost-effective overall synthesis of both complexes.

## 6.7 Experimental

### 14

#### Synthesis:

Under nitrogen, **8** (300 mg, 1.63 mmol) was dissolved in dry THF (30 cm<sup>3</sup>) and cooled to -78 °C. LDA (1.2 equivalents) was added, upon which the solution turned from colourless to black. The solution was left to stir for 30 minutes after which pyridine-4-carbaldehyde (0.18 cm<sup>3</sup>, 1.2 eq., 1.95 mmol) was added. The solution turned from black to golden yellow. The reaction mixture was left to stir for 12 hours, during which time it warmed to room temperature. The reaction was then quenched with water (10 cm<sup>3</sup>) and extracted three times with DCM (3 x 15 cm<sup>3</sup>). The solvent was removed *in vacuo*, which resulted in a brown oil. The oil was purified by chromatography (SiO<sub>2</sub>, ethyl acetate: hexane: triethylamine, 48:33:2).

Yield: 64.5 %

<sup>1</sup>H NMR: (500 MHz, CDCl<sub>3</sub>, 25 °C, TMS)  $\delta$ /ppm: 8.57 (2H, dd, J = 6.1, 2.9 Hz, **C**<sup>2</sup>), 8.34 (1H, d, J = 7.9 Hz, **B**<sup>3</sup>), 8.07 (1H, d, J = 7.8 Hz, **A**<sup>3</sup>), 7.76 (1H, t, J = 7.4 Hz, **B**<sup>4</sup>), 7.72 (1H, t, J = 7.4 Hz, **A**<sup>4</sup>), 7.36 (2H, dd, J = 4.5, 1.5 Hz, **C**<sup>3</sup>), 7.21 (1H, d, J = 7.6 Hz, **A**<sup>5</sup>), 7.10 (1H, d, J = 7.6 Hz, **B**<sup>5</sup>), 6.55 (1H, br s, H<sup>d</sup>), 5.26 (1H, dd, J = 8.6, 2.9 Hz, H<sup>c</sup>), 3.20 (2H, m, H<sup>b</sup>), 2.64 (3H, s, H<sup>a</sup>);

<sup>13</sup>C NMR (126 MHz, CDCl<sub>3</sub>, 25 °C, TMS)  $\delta$ /ppm: 158.4 (**A**<sup>6</sup>), 158.3 (**B**<sup>6</sup>), 155.7 (**B**<sup>2</sup>), 154.8 (**A**<sup>2</sup>), 152.9 (**C**<sup>1</sup>), 150.0 (**C**<sup>2</sup>), 138.3 (**B**<sup>4</sup>), 137.4 (**A**<sup>4</sup>), 123.8 (**B**<sup>5</sup>+**A**<sup>5</sup>), 121.0 (**C**<sup>3</sup>), 119.8 (**B**<sup>3</sup>), 118.0 (**A**<sup>3</sup>), 72.1 (c), 44.4 (b), 24.8 (a);

ESI-MS: m/z 314.2 [M+Na]<sup>+</sup> (calc. 314.13)

Found: C, 73.92; H, 6.15; N, 13.99; C<sub>18</sub>H<sub>17</sub>N<sub>3</sub>O requires C, 74.20; H, 5.88; N, 14.42;

Melting Point: 116.4 °C

IR (solid,  $\nu$ /cm<sup>-1</sup>): 551 (m), 579 (m), 611 (m), 615 (m), 624 (m), 632 (s), 652 (m), 663 (m), 744 (m), 750 (m), 789 (s), 807 (s), 826 (m), 976 (w), 999 (m), 1028 (w), 1035 (w), 1060 (s), 1082 (m), 1093 (m), 1152 (m), 1225 (w), 1259 (w), 1295 (w), 1326 (w), 1342 (w), 1381 (w), 1413 (m), 1435 (s), 1488 (w), 1557 (m), 1572 (s), 1603 (m), 2846 (w), 2928 (w), 3021 (w), 3064 (w), 3180 (w).

## 15

### Synthesis:

Under nitrogen, **14** (100 mg, 0.34 mmol) was refluxed in acetic acid (4 cm<sup>3</sup>) overnight, during which time the solution turned orange. The solution was then poured over ice and neutralised using a saturated NaHCO<sub>3</sub> solution. The product was extracted four times with dichloromethane (4 x 15 cm<sup>3</sup>) and the solvent was removed *in vacuo* to give a brown oil. The product was purified by chromatography (SiO<sub>2</sub>, Ethyl acetate: Hexane: NEt<sub>3</sub>, 15:1:0.5).

Yield: 27.7 mg, 29.5%

<sup>1</sup>H NMR: (500 MHz, CDCl<sub>3</sub>, 25 °C, TMS)  $\delta$ /ppm: 8.62 (2H, d, J = 6.1, 3.0 Hz, **C**<sup>2</sup>), 8.38 (1H, dd, J = 7.9, 0.9 Hz, **B**<sup>3</sup>), 8.34 (1H, d, J = 7.7 Hz, **A**<sup>3</sup>), 7.83 (1H, t, J = 7.8 Hz, **B**<sup>4</sup>), 7.75 (1H, t, J = 7.7 Hz, **A**<sup>4</sup>), 7.71 (1H, br d, J = 16 Hz, H<sup>c</sup>), 7.47 (2H, dd, **C**<sup>3</sup>), 7.42 (1H, br d, J = 16 Hz, H<sup>b</sup>), 7.42 (1H, dd, J = 7.7, 0.9 Hz, **B**<sup>5</sup>), 7.21 (1H, d, J = 7.6 Hz, **A**<sup>5</sup>), 2.65 (3H, s, H<sup>a</sup>);

<sup>13</sup>C NMR (126 MHz, CDCl<sub>3</sub>, 25 °C, TMS)  $\delta$ /ppm: 158.0 (**A**<sup>6</sup>), 156.6 (**B**<sup>2</sup>), 155.5 (**A**<sup>5</sup>), 153.7 (**B**<sup>6</sup>), 150.3 (**C**<sup>2</sup>), 144.3 (**C**<sup>1</sup>), 137.7 (**B**<sup>4</sup>), 137.0 (**A**<sup>4</sup>), 132.7 (**C**<sup>a</sup>), 129.9 (**C**<sup>b</sup>), 123.6 (**A**<sup>5</sup>), 122.8 (**B**<sup>5</sup>), 120.7 (**B**<sup>3</sup>), 118.4 (**A**<sup>3</sup>);

ESI-MS: m/z 296.2 [M+Na]<sup>+</sup> (calc. 296.12), 312.1 [M+K]<sup>+</sup> (calc. 312.09)

Found: C, 78.67; H, 5.38; N, 15.17; C<sub>18</sub>H<sub>15</sub>N<sub>3</sub> requires C, 79.10; H, 5.53; N, 15.37

IR (solid,  $\nu$ /cm<sup>-1</sup>): 551 (s), 572 (m), 632 (s), 652 (m), 668 (m), 729 (m), 739 (m), 761 (w), 781 (s), 807 (s), 821 (m), 829 (m), 863 (w), 874 (w), 903 (w), 954 (s), 973 (m), 989 (m), 1082 (m), 1109 (w), 1151 (w), 1168 (w), 1235 (w), 1256 (w), 1279 (w), 1369 (w), 1387 (w), 1411 (s), 1435 (s), 1532 (w), 1552 (s), 1564 (s), 1575 (s), 1591 (s), 2913 (w), 3032 (w), 3069 (w), 3999 (m).

### [Cu(**14**)<sub>2</sub>][PF<sub>6</sub>]

#### Synthesis:

[Cu(MeCN)<sub>4</sub>][PF<sub>6</sub>] (64.0 mg, 0.17 mmol) was dissolved in MeCN (2 cm<sup>3</sup>) and the solution was added to a solution of compound **14** (100 mg, 0.34 mmol) in CHCl<sub>3</sub> (5 cm<sup>3</sup>). The solution immediately became red in colour and was stirred for 30 min. Addition of Et<sub>2</sub>O (10 cm<sup>3</sup>) afforded a red precipitate, which was collected by filtration over Celite. The product was washed with H<sub>2</sub>O and Et<sub>2</sub>O and removed from the Celite by dissolution in MeCN. Solvent was removed *in vacuo* and [Cu(**14**)<sub>2</sub>][PF<sub>6</sub>] was isolated as a red powder.

Yield: 94.4 mg, 69.6 %

<sup>1</sup>H NMR: (500 MHz, CD<sub>2</sub>Cl<sub>2</sub>, 298 K, TMS) δ/ppm: 8.52, 8.27, 8.22, 8.03, 7.66, 7.53, 6.71,

4.71, 3.58, 2.90 (all signals were broad, see text).

ESI-MS: m/z 645.3 [M-PF<sub>6</sub>]<sup>+</sup> (calc 645.2)

Found C, 52.33; H, 4.45; N, 10.33; C<sub>36</sub>H<sub>34</sub>N<sub>6</sub>CuPF<sub>6</sub>•2H<sub>2</sub>O requires C, 52.27; H, 4.63; N, 10.16.

### [Cu(**15**)<sub>2</sub>][PF<sub>6</sub>]

[Cu(MeCN)<sub>4</sub>][PF<sub>6</sub>] (17.7 mg, 0.047 mmol) was dissolved in MeCN (2 cm<sup>3</sup>) and the solution was added to a solution of compound **15** (26 mg, 0.095 mmol) in CHCl<sub>3</sub> (5 cm<sup>3</sup>). The solution immediately became red in colour and was stirred for 30 min after which the solvents were removed *in vacuo* to leave a red powder.

Yield: 30.6 mg, 85.0 %

<sup>1</sup>H NMR: (500 MHz, CD<sub>2</sub>Cl<sub>2</sub>, 205 K, TMS) δ/ppm: 8.34 (4H, br s, **C**<sup>2</sup>), 8.25 (2H, d, J = 7.9 Hz, **B**<sup>3</sup>), 8.22 (2H, d, J = 8.1 Hz, **A**<sup>3</sup>), 8.10 (2H, t, J = 7.8 Hz, **B**<sup>4</sup>), 8.00 (2H, t, J = 7.8 Hz, **A**<sup>4</sup>), 7.90 (2H, d, J = 7.8 Hz, **B**<sup>5</sup>), 7.47 (1H, d, J = 7.6 Hz, **A**<sup>5</sup>), 7.04 (4H, m, overlapping b+c), 6.56 (4H, br s, **C**<sup>3</sup>), 2.25 (6H, s, a)

$^1\text{H}$  NMR: (500 MHz,  $\text{CD}_3\text{CN}$ , 298 K, TMS)  $\delta/\text{ppm}$ : 8.47 (3H, br s,  $\text{C}^2$ ), 8.30 (4H, br t, overlapping  $\text{B}^3+\text{A}^3$ ), 8.10 (2H, t,  $J = 7.9$  Hz,  $\text{B}^4$ ), 8.04 (2H, t,  $J = 7.8$  Hz,  $\text{A}^4$ ), 7.92 (2H, d,  $J = 7.8$  Hz,  $\text{B}^5$ ), 7.54 (2H, d,  $J = 7.6$  Hz,  $\text{A}^5$ ), 7.22 (2H, br d,  $J = 16.4$  Hz, b), 7.13 (2H, br d,  $J = 16.5$  Hz, c), 6.75 (3H, br s,  $\text{C}^3$ ), 2.33 (6H, s, a)

$^{13}\text{C}$  NMR: (500 MHz,  $\text{CD}_3\text{CN}$ , 298 K, TMS)  $\delta/\text{ppm}$ : 158.6 ( $\text{A}^6$ ), 155.1 ( $\text{B}^6$ ), 154.9 ( $\text{C}^4$ ), 153.2 ( $\text{A}^2/\text{B}^2$ ), 152.3 ( $\text{A}^2/\text{B}^2$ ), 139.7 ( $\text{B}^4$ ), 139.5 ( $\text{A}^4$ ), 132.9 (b), 132.3 (c), 127.2 ( $\text{A}^5$ ), 123.6 ( $\text{B}^5$ ), 122.4 ( $\text{A}^3/\text{B}^3$ ), 121.7 ( $\text{C}^3$ ), 102.8 ( $\text{A}^3/\text{B}^3$ ), 25.5 (a)

ESI-MS:  $m/z$  609.2 [ $\text{M-PF}_6$ ] $^+$  (calc 609.2), 274.1 [ $\text{15+H}$ ] $^+$  (calc. 274.2)

## 6.8 References

1. B. J. Coe, J. A. Harris, L. A. Jones, B. S. Brunshwig, K. Song, K. Clays, J. Garín, J. Orduna, S. J. Coles and M. B. Hursthouse, *J. Am. Chem. Soc.*, 2005, **127**, 4845-4859.
2. B. J. Coe, E. C. Harper, M. Helliwell and Y. T. Ta, *Polyhedron*, 2011, **30**, 1830-1841.
3. F. Fabrizi de Biani, E. Grigiotti, F. Laschi, P. Zanello, A. Juris, L. Prodi, K. S. Chichak and N. R. Branda, *Inorg. Chem.*, 2008, **47**, 5425-5440.
4. B. J. Coe, J. Fielden, S. P. Foxon, B. S. Brunshwig, I. Asselberghs, K. Clays, A. Samoc and M. Samoc, *J. Am. Chem. Soc.*, 2010, **132**, 3496-3513.
5. P. K. A. Shonfield, A. Behrendt, J. C. Jeffery, J. P. Maher, J. A. McCleverty, E. Psillakis, M. D. Ward and C. Western, *J. Chem. Soc. Dalton Trans.*, 1999, 4341-4347.
6. M. Yamada, K. Araki and S. Shiraishi, *Bull. Chem. Soc. Jpn.*, 1988, **61**, 2208-2210.
7. E. Riesgo, Y.-Z. Hu, F. Bouvier and R. P. Thummel, *Inorg. Chem.*, 2001, **40**, 2541-2546.
8. V. Hebbe-Viton, V. Desvergnés, J. J. Jodry, C. Dietrich-Buchecker, J.-P. Sauvage and J. Lacour, *Dalton Trans.*, 2006, 2058-2065.
9. E. C. Constable, *Chem. Soc. Rev.*, DOI: 10.1039/C2CS35270B.
10. P. Kopecky, PhD Thesis, University of Basel, 2012.
11. R. S. Cahn, C. Ingold and V. Prelog, *Angew. Chem. Int. Edit.*, 1966, **5**, 385-415.
12. B. Bozic-Weber, E. C. Constable, C. E. Housecroft, P. Kopecky, M. Neuburger and J. A. Zampese, *Dalton Trans.*, 2011, **40**, 12584-12594.



## Conclusions and Outlook

The first part of this thesis explored the substitution of a bis{4'-(4-pyridyl)-2,2':6',2''-terpyridine}ruthenium(II) complex with different electron donating and electron withdrawing moieties. It was found that regardless of the substituent the photophysical and electrochemical properties of the resulting complexes changed very little. DFT was used to investigate this finding and it was determined that the bridging  $-\text{CH}_2-$  group of the substituent broke the conjugation between the electronically active part of the substituent and the pyridyl terpyridine moiety. This resulted in the LUMO of the complex being confined to the pyridyl terpyridine ligand for all complexes. In the TD-DFT calculations, use of the split LANL2DZ/6-31G\* basis set resulted in the prediction of the absorption spectra of the complexes to within 20 nm of the experimental results.

The alkylated bis{4'-(4-pyridyl)-2,2':6',2''-terpyridine}ruthenium(II) complexes were made water soluble by means of an anion exchange reaction and the photophysical and electrochemical properties of this set of complexes was found to be very similar to those of their hexafluoridophosphate pre-cursors. Use of these complexes as water-splitting co-catalysts resulted in differing activities. This was explained in terms of the susceptibility of the complex to basic attack at the C2 proton. Further studies into the kinetics of the water splitting reaction and stability tests on the ruthenium(II) complexes themselves are underway at Emory University. These results will lead to a better understanding of the properties required from the dye sensitisers, which will, in turn, lead to better dye design.

The second part of this thesis detailed the development of copper(I) complexes for use in dye-sensitised solar cells. Initially two homoleptic Cu(I) complexes were synthesised, one with a simple structure,  $[\text{Cu}(\mathbf{8})_2][\text{PF}_6]$  and one utilising a ligand bearing triphenylamine units, bonded to the 6'-position of bipyridine through a double bond,  $[\text{Cu}(\mathbf{9})_2][\text{PF}_6]$ . It was found that that the complex incorporating triphenylamine groups lead to increases in the absorption coefficient and quantum yield of the complex, compared to the more simple complex.

A recently developed approach to making TiO<sub>2</sub> surface-bound heteroleptic Cu(I) complexes incorporating carboxylate or phosphonic acid groups was used. The dyes were screened for their efficiency in DSSCs and it was found that dyes with ligand **9** had an enhanced performance. The best performing cell, which included the phosphonate anchor, gave an efficiency of 2.35 %, compared to 7.29 % for N719 under the same conditions. Research into substituting bipyridine with triphenylamine groups at different positions is now underway.

DFT and TD-DFT calculations were used to investigate the properties of the homoleptic and heteroleptic Cu(I) complexes. A number of basis sets were screened and it was found that use of either the split basis set LANL2DZ/6-31G\* or 6-311++G\*\*/6-31G\* resulted in a good prediction of the absorption spectrum of [Cu(**8**)<sub>2</sub>]<sup>+</sup>. Using the split basis set 6-311++G\*\*/6-31G\*, TD-DFT calculations have been carried out to predict the electronic absorption spectra of the heteroleptic complexes [Cu(**8**)(L')]<sup>+</sup> and [Cu(**9**)(L')]<sup>+</sup> (L' = **10**, **11**, **12**). For [Cu(**8**)(**11**)]<sup>+</sup> and [Cu(**8**)(**12**)]<sup>+</sup>, metal-to-anchoring ligand transitions contribute significantly to the absorption bands, whereas for [Cu(**8**)(**10**)]<sup>+</sup> there is little anchoring ligand involvement. This is consistent with the DSSC data, where use of [Cu(**8**)(**10**)]<sup>+</sup> results in a DSSC with a poor efficiency. Use of [Cu(**9**)(**11**)]<sup>+</sup> resulted in a DSSC with a high efficiency and, correspondingly, the calculations predict dominant phosphonate ligand character in the LUMO, which is necessary for efficient dye injection. Further calculations on a variety of Cu(I) complexes should be carried out to test the robustness of the choice of basis set.

Finally, two chiral homoleptic Cu(I) complexes were synthesised as racemates. Development of the ligand synthesis is necessary to improve the yields and it may be possible to synthesise bis-substituted bipyridine compounds using the Ullmann procedure. Further investigations into the electrochemical properties of the Cu(I) complexes should be carried out, alongside testing of the dyes as sensitisers in DSSCs. As the complexes bear pendant pyridyl groups it would also be sensible to look at the effect of protonation and methylation on the properties of the complexes.

## Crystallographic Data

Compound	[Ru(1) <sub>2</sub> ][PF <sub>6</sub> ] <sub>4</sub>
Empirical Formula	C <sub>54</sub> H <sub>42</sub> N <sub>8</sub> Ru·4(F <sub>6</sub> P)·H <sub>2</sub> O
Formula Weight	1501.93
Temperature / K	173(2)
Crystal System	Triclinic
Space Group	P-1
Unit cell dimensions:	
a / Å	13.488(3)
b / Å	16.934(3)
c / Å	27.758(6)
α / °	94.43(3)
β / °	103.78(3)
γ / °	98.27(3)
Volume / Å <sup>3</sup>	6053(2)
Z	4
Crystal Description	red block
Crystal Size / mm <sup>3</sup>	0.03 × 0.12 × 0.30
Density / Mg m <sup>-3</sup>	1.646
Absorption Coefficient / mm <sup>-1</sup>	0.486
Theta range for data collection / °	1.51 – 26.00
Reflections collected	111421
Independent reflections	23797
R(int)	0.2214
Completeness to theta / ° (%)	26.00 (0.999)
Parameters	1660
Goodness of fit	1.096
wR <sub>2</sub>	0.3677
Final R <sub>1</sub> [I>2σ(I)]	0.1499

Compound	[Ru(3) <sub>2</sub> ][PF <sub>6</sub> ] <sub>4</sub>
Empirical Formula	C <sub>476</sub> H <sub>0</sub> N <sub>70</sub> Ru <sub>8</sub> O <sub>58</sub> F <sub>242</sub> P <sub>46</sub>
Formula Weight	14456.64
Temperature / K	173(2)
Crystal System	Triclinic
Space Group	P -1
Unit cell dimensions:	
a / Å	17.279(3)
b / Å	17.415(3)
c / Å	50.947(10)
α / °	98.35(3)
β / °	93.85(3)
γ / °	90.77(3)
Volume / Å <sup>3</sup>	15130(5)
Z	1
Crystal Description	Red blocks
Crystal Size / mm <sup>3</sup>	0.05 × 0.25 × 0.40
Density / Mg m <sup>-3</sup>	1.587
Absorption Coefficient / mm <sup>-1</sup>	0.457
Theta range for data collection / °	0.8383 – 0.9775
Reflections collected	294313
Independent reflections	64172
R(int)	0.1260
Completeness to theta / ° (%)	26.88 (0.985)
Parameters	2470
Goodness of fit	0.937
wR <sub>2</sub>	0.2809
Final R <sub>1</sub> [I>2sigma(I)]	0.1061

<b>Compound</b>		<b>[Ru(4)<sub>2</sub>][PF<sub>6</sub>]<sub>4</sub></b>
<b>Empirical Formula</b>		C <sub>44</sub> H <sub>38</sub> N <sub>8</sub> Ru·4(F <sub>6</sub> P)·H <sub>2</sub> O
<b>Formula Weight</b>		1377.79
<b>Temperature / K</b>		173(2)
<b>Crystal System</b>		Monoclinic
<b>Space Group</b>		P2 <sub>1</sub> /c
<b>Unit cell dimensions:</b>	<b>a / Å</b>	18.322(4)
	<b>b / Å</b>	8.8509(18)
	<b>c / Å</b>	31.688(6)
	<b>α / °</b>	90.00
	<b>β / °</b>	95.16(3)
	<b>γ / °</b>	90.00
<b>Volume / Å<sup>3</sup></b>		5117.9(18)
<b>Z</b>		4
<b>Crystal Description</b>		red needle
<b>Crystal Size / mm<sup>3</sup></b>		0.03 × 0.04 × 0.35
<b>Density / Mg m<sup>-3</sup></b>		1.786
<b>Absorption Coefficient / mm<sup>-1</sup></b>		0.565
<b>Theta range for data collection / °</b>		2.39 – 27.00
<b>Reflections collected</b>		84418
<b>Independent reflections</b>		11159
<b>R(int)</b>		0.1627
<b>Completeness to theta / ° (%)</b>		27.00 (0.998)
<b>Parameters</b>		925
<b>Goodness of fit</b>		1.161
<b>wR<sub>2</sub></b>		0.1385
<b>Final R<sub>1</sub> [I&gt;2sigma(I)]</b>		0.0664

<b>Compound</b>		<b>[Ru(6)<sub>2</sub>][PF<sub>6</sub>]<sub>4</sub></b>
<b>Empirical Formula</b>	4(C <sub>46</sub> H <sub>38</sub> N <sub>8</sub> Ru)·16(F <sub>6</sub> P)· 5 (C <sub>2</sub> H <sub>3</sub> N)·3(H <sub>2</sub> O)	
<b>Formula Weight</b>	5795.09	
<b>Temperature / K</b>	173(2)	
<b>Crystal System</b>	Monoclinic	
<b>Space Group</b>	Cc	
<b>Unit cell dimensions:</b>	<b>a / Å</b>	25.5529(9)
	<b>b / Å</b>	15.1322(7)
	<b>c / Å</b>	16.2770(7)
	<b>α / °</b>	90.00
	<b>β / °</b>	117.0660(10)
	<b>γ / °</b>	90.00
<b>Volume / Å<sup>3</sup></b>	5604.6(4)	
<b>Z</b>	1	
<b>Crystal Description</b>	red block	
<b>Crystal Size / mm<sup>3</sup></b>	0.15 × 0.25 × 0.45	
<b>Density / Mg m<sup>-3</sup></b>	1.715	
<b>Absorption Coefficient / mm<sup>-1</sup></b>	0.521	
<b>Theta range for data collection / °</b>		
<b>Reflections collected</b>	47951	
<b>Independent reflections</b>	12829	
<b>R(int)</b>	0.0372	
<b>Completeness to theta / ° (%)</b>	27.50 (0.998)	
<b>Parameters</b>	942	
<b>Goodness of fit</b>	1.049	
<b>wR<sub>2</sub></b>	0.1132	
<b>Final R<sub>1</sub> [I&gt;2sigma(I)]</b>	0.0467	

<b>Compound</b>	<b>[Ru(7)<sub>2</sub>][PF<sub>6</sub>]<sub>4</sub></b>	
<b>Empirical Formula</b>	C <sub>56</sub> H <sub>62</sub> F <sub>24</sub> N <sub>8</sub> OP <sub>4</sub> Ru	
<b>Formula Weight</b>	1544.09	
<b>Temperature / K</b>	123(2)	
<b>Crystal System</b>	Triclinic	
<b>Space Group</b>	P -1	
<b>Unit cell dimensions:</b>	<b>a / Å</b>	8.7018(7)
	<b>b / Å</b>	12.5549(10)
	<b>c / Å</b>	30.067(3)
	<b>α / °</b>	91.770(6)
	<b>β / °</b>	95.442(6)
	<b>γ / °</b>	98.367(6)
<b>Volume / Å<sup>3</sup></b>	3231.88	
<b>Z</b>	2	
<b>Crystal Description</b>	red needle	
<b>Crystal Size / mm<sup>3</sup></b>	0.03 × 0.08 × 0.45	
<b>Density / Mg m<sup>-3</sup></b>	1.587	
<b>Absorption Coefficient / mm<sup>-1</sup></b>	0.457	
<b>Theta range for data collection / °</b>	0.8207 to 0.9864	
<b>Reflections collected</b>	42067	
<b>Independent reflections</b>	11406	
<b>R(int)</b>	0.1005	
<b>Completeness to theta / ° (%)</b>	25.05 (0.996)	
<b>Parameters</b>	1060	
<b>Goodness of fit</b>	1.118	
<b>wR<sub>2</sub></b>	0.3352	
<b>Final R<sub>1</sub> [I&gt;2sigma(I)]</b>	0.1312	

<b>Compound</b>	<b>9</b>
<b>Empirical Formula</b>	C <sub>50</sub> H <sub>38</sub> N <sub>4</sub>
<b>Formula Weight</b>	694.88
<b>Temperature / K</b>	100
<b>Crystal System</b>	Orthorhombic
<b>Space Group</b>	Pbca
<b>Unit cell dimensions:</b>	
<b>a / Å</b>	8.9360(3)
<b>b / Å</b>	15.3904(5)
<b>c / Å</b>	26.8164(9)
<b>α / °</b>	90
<b>β / °</b>	90
<b>γ / °</b>	90
<b>Volume / Å<sup>3</sup></b>	3688.0(2)
<b>Z</b>	4
<b>Crystal Description</b>	yellow plate
<b>Crystal Size / mm<sup>3</sup></b>	0.020 × 0.100 × 0.220
<b>Density / Mg m<sup>-3</sup></b>	1.251
<b>Absorption Coefficient / mm<sup>-1</sup></b>	0.565
<b>Theta range for data collection / °</b>	3.296 to 68.471
<b>Reflections collected</b>	35364
<b>Independent reflections</b>	3377
<b>R(int)</b>	0.068
<b>Completeness to theta / ° (%)</b>	67.102 (0.998)
<b>Parameters</b>	244
<b>Goodness of fit</b>	1.0410
<b>wR<sub>2</sub></b>	0.0384
<b>Final R<sub>1</sub> [I&gt;2sigma(I)]</b>	0.0478



<b>Compound</b>	[Cu( <b>8</b> ) <sub>2</sub> ][PF <sub>6</sub> ]
<b>Empirical Formula</b>	C <sub>24</sub> H <sub>24</sub> Cu <sub>1</sub> F <sub>6</sub> N <sub>4</sub> P <sub>1</sub>
<b>Formula Weight</b>	576.99
<b>Temperature / K</b>	123
<b>Crystal System</b>	Monoclinic
<b>Space Group</b>	P21/c
<b>Unit cell dimensions:</b>	
<b>a / Å</b>	12.7104(6)
<b>b / Å</b>	21.9632(11)
<b>c / Å</b>	8.7001(5)
<b>α / °</b>	90
<b>β / °</b>	94.692(2)
<b>γ / °</b>	90
<b>Volume / Å<sup>3</sup></b>	2420.6(2)
<b>Z</b>	4
<b>Crystal Description</b>	red block
<b>Crystal Size / mm<sup>3</sup></b>	0.060 × 0.130 × 0.210
<b>Density / Mg m<sup>-3</sup></b>	1.583
<b>Absorption Coefficient / mm<sup>-1</sup></b>	1.036
<b>Theta range for data collection / °</b>	1.856 to 32.588
<b>Reflections collected</b>	35645
<b>Independent reflections</b>	8817
<b>R(int)</b>	0.030
<b>Completeness to theta / ° (%)</b>	32.588 (0.999)
<b>Parameters</b>	325
<b>Goodness of fit</b>	1.0891
<b>wR<sub>2</sub></b>	0.0312
<b>Final R<sub>1</sub> [I&gt;2sigma(I)]</b>	0.0301

<b>Compound</b>	[Cu(9) <sub>2</sub> ][PF <sub>6</sub> ]
<b>Empirical Formula</b>	C <sub>100</sub> H <sub>76</sub> Cu <sub>1</sub> F <sub>6</sub> N <sub>8</sub> P <sub>1</sub>
<b>Formula Weight</b>	1666.32
<b>Temperature / K</b>	123
<b>Crystal System</b>	Tetragonal
<b>Space Group</b>	P4/n
<b>Unit cell dimensions:</b>	
<b>a / Å</b>	15.1209(2)
<b>b / Å</b>	15.1209(2)
<b>c / Å</b>	18.2971(4)
<b>α / °</b>	90
<b>β / °</b>	90
<b>γ / °</b>	90
<b>Volume / Å<sup>3</sup></b>	4183.48(12)
<b>Z</b>	2
<b>Crystal Description</b>	orange plate
<b>Crystal Size / mm<sup>3</sup></b>	0.030 × 0.170 × 0.210
<b>Density / Mg m<sup>-3</sup></b>	1.316
<b>Absorption Coefficient / mm<sup>-1</sup></b>	0.352
<b>Theta range for data collection / °</b>	1.747 to 31.714
<b>Reflections collected</b>	49103
<b>Independent reflections</b>	7090
<b>R(int)</b>	0.062
<b>Completeness to theta / ° (%)</b>	31.714 (0.997)
<b>Parameters</b>	276
<b>Goodness of fit</b>	1.0236
<b>wR<sub>2</sub></b>	0.0524
<b>Final R<sub>1</sub> [I&gt;2sigma(I)]</b>	0.0494

<b>Compound</b>	<b>14</b>
<b>Empirical Formula</b>	C <sub>18</sub> H <sub>17</sub> N <sub>3</sub> O
<b>Formula Weight</b>	291.35
<b>Temperature / K</b>	123(2)
<b>Crystal System</b>	Monoclinic
<b>Space Group</b>	P21/c
<b>Unit cell dimensions:</b>	
<b>a / Å</b>	7.6803(19)
<b>b / Å</b>	11.193(3)
<b>c / Å</b>	17.011(5)
<b>α / °</b>	90.00
<b>β / °</b>	90.329(10)
<b>γ / °</b>	90.00
<b>Volume / Å<sup>3</sup></b>	1462.3(7)
<b>Z</b>	4
<b>Crystal Description</b>	colourless needle
<b>Crystal Size / mm<sup>3</sup></b>	0.04 × 0.04 × 0.25
<b>Density / Mg m<sup>-3</sup></b>	1.323
<b>Absorption Coefficient / mm<sup>-1</sup></b>	0.084
<b>Theta range for data collection / °</b>	3.43 to 22.81
<b>Reflections collected</b>	10463
<b>Independent reflections</b>	3006
<b>R(int)</b>	0.0589
<b>Completeness to theta / ° (%)</b>	26.50 (0.992)
<b>Parameters</b>	202
<b>Goodness of fit</b>	1.023
<b>wR<sub>2</sub></b>	0.1903
<b>Final R<sub>1</sub> [I&gt;2sigma(I)]</b>	0.0780

<b>Compound</b>		<b>15</b>
<b>Empirical Formula</b>		C <sub>18</sub> H <sub>15</sub> N <sub>3</sub>
<b>Formula Weight</b>		273.33
<b>Temperature / K</b>		123(2)
<b>Crystal System</b>		Monoclinic
<b>Space Group</b>		C2/c
<b>Unit cell dimensions:</b>	<b>a / Å</b>	31.0692(17)
	<b>b / Å</b>	6.5480(4)
	<b>c / Å</b>	13.7053(8)
	<b>α / °</b>	90.00
	<b>β / °</b>	100.287(3)
	<b>γ / °</b>	90.00
<b>Volume / Å<sup>3</sup></b>		2743.4(3)
<b>Z</b>		8
<b>Crystal Description</b>		colourless block
<b>Crystal Size / mm<sup>3</sup></b>		0.05 × 0.30 × 0.30
<b>Density / Mg m<sup>-3</sup></b>		1.324
<b>Absorption Coefficient / mm<sup>-1</sup></b>		0.080
<b>Theta range for data collection / °</b>		3.08 to 27.49
<b>Reflections collected</b>		32903
<b>Independent reflections</b>		3144
<b>R(int)</b>		0.0271
<b>Completeness to theta / ° (%)</b>		27.49 (0.996)
<b>Parameters</b>		191
<b>Goodness of fit</b>		1.032
<b>wR<sub>2</sub></b>		0.0955
<b>Final R<sub>1</sub> [I&gt;2sigma(I)]</b>		0.0360

<b>Compound</b>		<b>Co-crystallised 15 and 17</b>
<b>Empirical Formula</b>		$C_{18}H_{15}N_3O_{0.31}$
<b>Formula Weight</b>		278.31
<b>Temperature / K</b>		123(2)
<b>Crystal System</b>		Monoclinic
<b>Space Group</b>		$P2_1/c$
<b>Unit cell dimensions:</b>	<b>a / Å</b>	6.2417(2)
	<b>b / Å</b>	8.6472(3)
	<b>c / Å</b>	26.2360(10)
	<b><math>\alpha</math> / °</b>	90.00
	<b><math>\beta</math> / °</b>	92.017(2)
	<b><math>\gamma</math> / °</b>	90.00
<b>Volume / Å<sup>3</sup></b>		1415.16(9)
<b>Z</b>		4
<b>Crystal Description</b>		yellow block
<b>Crystal Size / mm<sup>3</sup></b>		0.15×0.20×0.40
<b>Density / Mg m<sup>-3</sup></b>		1.306
<b>Absorption Coefficient / mm<sup>-1</sup></b>		0.081
<b>Theta range for data collection / °</b>		3.11 to 33.07
<b>Reflections collected</b>		12728
<b>Independent reflections</b>		3101
<b>R(int)</b>		0.0210
<b>Completeness to theta / ° (%)</b>		27.10(0.996)
<b>Parameters</b>		202
<b>Goodness of fit</b>		1.047
<b>wR<sub>2</sub></b>		0.1053
<b>Final R<sub>1</sub> [I&gt;2sigma(I)]</b>		0.0398

<b>Compound</b>	<b>16</b>
<b>Empirical Formula</b>	C <sub>12</sub> H <sub>10</sub> N <sub>2</sub> O <sub>2</sub>
<b>Formula Weight</b>	214.22
<b>Temperature / K</b>	123
<b>Crystal System</b>	Monoclinic
<b>Space Group</b>	P2 <sub>1</sub> /c
<b>Unit cell dimensions:</b>	
<b>a / Å</b>	3.8672(14)
<b>b / Å</b>	10.873(4)
<b>c / Å</b>	23.976(9)
<b>α / °</b>	90.00
<b>β / °</b>	93.974(4)
<b>γ / °</b>	90.00
<b>Volume / Å<sup>3</sup></b>	1005.7(6)
<b>Z</b>	4
<b>Crystal Description</b>	colourless needle
<b>Crystal Size / mm<sup>3</sup></b>	0.020 × 0.030 × 0.310
<b>Density / Mg m<sup>-3</sup></b>	1.415
<b>Absorption Coefficient / mm<sup>-1</sup></b>	0.099
<b>Theta range for data collection / °</b>	2.058 to 26.371
<b>Reflections collected</b>	6134
<b>Independent reflections</b>	2053
<b>R(int)</b>	0.108
<b>Completeness to theta / ° (%)</b>	26.371(1.000)
<b>Parameters</b>	145
<b>Goodness of fit</b>	1.1003
<b>wR<sub>2</sub></b>	0.0688
<b>Final R<sub>1</sub> [I&gt;2sigma(I)]</b>	0.0626

<b>Compound</b>		<b>[Cu(15)<sub>2</sub>][PF<sub>6</sub>]</b>
<b>Empirical Formula</b>		C <sub>72</sub> H <sub>69</sub> Cu <sub>2</sub> F <sub>12</sub> N <sub>12</sub> O <sub>4.50</sub> P <sub>2</sub>
<b>Formula Weight</b>		1591.44
<b>Temperature / K</b>		123(2)
<b>Crystal System</b>		Triclinic
<b>Space Group</b>		P-1
<b>Unit cell dimensions:</b>	<b>a / Å</b>	11.497(2)
	<b>b / Å</b>	12.283(2)
	<b>c / Å</b>	14.749(3)
	<b>α / °</b>	96.949(11)
	<b>β / °</b>	112.804(10)
	<b>γ / °</b>	103.550(12)
<b>Volume / Å<sup>3</sup></b>		1813.6(6)
<b>Z</b>		1
<b>Crystal Description</b>		Red plate
<b>Crystal Size / mm<sup>3</sup></b>		0.02 × 0.10 × 0.45
<b>Density / Mg m<sup>-3</sup></b>		1.452
<b>Absorption Coefficient / mm<sup>-1</sup></b>		0.719
<b>Theta range for data collection / °</b>		2.02 to 25.05
<b>Reflections collected</b>		23159
<b>Independent reflections</b>		6379
<b>R(int)</b>		0.0916
<b>Completeness to theta / ° (%)</b>		25.05 (0.991)
<b>Parameters</b>		490
<b>Goodness of fit</b>		1.029
<b>wR<sub>2</sub></b>		0.2050
<b>Final R<sub>1</sub> [I&gt;2sigma(I)]</b>		0.0769

## Jennifer Amy Rudd (née Paley) MChem Hons AMRSC

Email: [jpaley530@googlemail.com](mailto:jpaley530@googlemail.com)

Date of Birth: 12<sup>th</sup> August 1987

### Education and Qualifications:

- Oct. 2009 – **Universität Basel, Basel, Switzerland**  
Nov. 2012 Studied for a PhD in coordination chemistry in the Housecroft/Constable research group. Techniques used include UV-vis and emission spectroscopy, lifetime measurements, spectroelectrochemistry, cyclic voltammetry (inc. square wave and DPV), NMR, DFT and TD-DFT. Have supervised two Wahlpraktikum students and assisted in the First Year undergraduate teaching laboratories for three years. Proficient in the use of Microsoft Office applications. Basic Linux experience. Familiar with DFT tools: Gaussian 09, GaussSum, Molekel, Molden, GaussView.
- 2005 – 2009 **University of York, York, UK**  
MChem Year Abroad (2:2) inc. Option Modules in Natural Environment, Clean Technology, Radicals in Synthesis, Catalysis. Final year at **Münster Universität, Germany** working in the Hahn research group on N-heterocyclic carbenes which included the use of air sensitive compounds, glove box techniques and a Schlenk line.
- 1998-2005 **Hayesfield School Technology College, Bath**  
A Levels: Chemistry (C), Mathematics (C), German (D), Music (B)  
GCSEs: 8(A); 2(B); 1(C)

### Technical Experience

- 2008 **Student Researcher, University of York, York (7 weeks)**
- Worked in Prof. Perutz's research group synthesising organometallic iridium catalysts for asymmetric hydrogenation.
  - Synthesised two novel iridium complexes and characterised them using <sup>1</sup>H, <sup>13</sup>C and <sup>19</sup>F NMR, ESI Mass spectrometry, IR spectroscopy, UV-vis spectroscopy and X-ray crystallography.
- 2006 **Student Scientist, Vectura Plc, Chippenham (8 weeks)**
- Worked as part of a team on a project researching dry powder inhalers.
  - Job was split between secretarial work and work in the laboratory.
  - Laboratory work included making up solutions, cleaning glassware and making up solutions for the HPLC machine.
- 2005 **Work Experience, Hunstman Petrochemicals, ICI Plant, Teeside (1 week)**
- Shadowed chemists working on petroleum purity and zeolite catalysts.
  - Went on 2 site visits to see the production of paraxylene and cyclohexane.



## Interests and Activities

- **Secretary for the Swiss Young Chemist's Association:** responsibilities include taking the minutes of the meetings, aiding organization of the Snow Symposium with a particular responsibility for the speakers.
- Associate member of the Royal Society of Chemistry.
- Student member of the Swiss Chemical Society, affiliate of the Photochemistry section.
- Responsible for running a youth group called Rock Solid for 11-14 year olds at the International School Basel in Reinach, Baselland.
- Worship Leader and singer at Anglican Church Basel

## Additional Skills

- Attained LFA Level 5 (highest offered) German through the University of York and retain a working knowledge of the language.

## Referees

Prof. Dr. E. C. Constable, University of Basel, Basel, Switzerland

Tel: (0041) 61 2671001

Email: edwin.constable@unibas.ch

Prof. Dr. C. E. Housecroft, University of Basel, Switzerland

Tel: (0041) 61 2671018

Email: catherine.housecroft@unibas.ch

## Publications:

B. Bozic-Weber, V. Chaurin, E.C. Constable, C.E. Housecroft, M. Meuwly, M. Neuburger, J.A. Rudd, E. Schönhofer, L. Siegfried, "Exploring copper(I)-based dye-sensitized solar cells: a complementary experimental and TD-DFT investigation" *Dalton Trans.*, **2012**, *41*, 14157-14169

E.C. Constable, M. Devereux, E.L. Dunphy, C.E. Housecroft, J.A. Rudd, J.A. Zampese, "Water-soluble alkylated bis{4'-(4-pyridyl)-2,2':6',2''}-terpyridine}ruthenium(II) complexes for use as photosensitizers in water oxidation: a complementary experimental and TD-DFT investigation" *Dalton Trans.*, **2011**, *40*, 5505-5515

M. C. Jahnke, J. Paley, F. Hupka, J. J. Weigand, F. E. Hahn, "Silver and Gold Complexes with Benzimidazolin-2-ylidene Ligands", *Z. Naturforsch.* **2009**, *64b*, 1458 – 1462

## Poster and Oral Presentations:

*"Copper(I) Complexes for Application in Dye-Sensitised Solar Cells: A Comparative Experimental and TD-DFT Investigation"*

Nov. 2012 Oral presentation at the 1<sup>st</sup> Clariant Chemistry Day, University of Basel (CH)

June 2012 Poster and Flash Poster presentation presented at the Dalton Summer School on Electronic Structural Methods in Inorganic Chemistry, University of Edinburgh, UK.

February 2012 Poster Presentation at the Central European Conference on Photochemistry 2012, Bad Hofgastein, Austria

*“Water-soluble alkylated bis{4'-(4-pyridyl)-2,2':6',2''-terpyridine}ruthenium(II) complexes for use as photosensitizers in water oxidation: a complementary experimental and TD-DFT investigation”*

September 2011 Poster Presentation at the 5<sup>th</sup> EuCheMS Nitrogen Ligands conference, Granada, E

September 2011 Poster presentation at the SCS Fall Meeting, Lausanne, CH

*“Photophysical and electrochemical investigations of functionalised bis 4'-pyridyl-2,2':6',2''-terpyridine Ru(II) complexes”*

February 2011 Oral Presentation at the 9<sup>th</sup> Swiss Snow Symposium, Lenk, CH

September 2010 Poster Presentation at the SCS Fall Meeting, Zurich, CH

August 2010 Poster Presentation at the 3<sup>rd</sup> EuCheMS Conference, Nuernberg, DE  
An oral presentation of the poster was then featured in the Wiley electronic magazine “Chemistry Views” (05.10.10)

June 2010 Poster and Flash Poster presentation presented at the Dalton Summer School on Electronic Structural Methods in Inorganic Chemistry, University of Edinburgh, UK.